Incorporation of LEO GNSS observations into global network solutions

Inaugural dissertation
of the Faculty of Science,
University of Bern

presented by

Cyril Kobel

from Lauperswil (BE)

Supervisor of the doctoral thesis:

Prof. Dr. Adrian Jäggi
Astronomical Institute, University of Bern, Switzerland

Incorporation of LEO GNSS observations into global network solutions

Inaugural dissertation
of the Faculty of Science,
University of Bern

presented by

Cyril Kobel

from Lauperswil (BE)

Supervisor of the doctoral thesis:

Prof. Dr. Adrian Jäggi
Astronomical Institute, University of Bern, Switzerland

Accepted by the Faculty of Science.

Bern, 14.12.2023

The Dean

Prof. Dr. Marco Herwegh

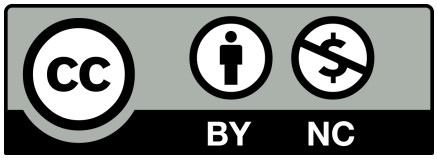

Acknowledgments

I want to thank all who contributed to this work, especially Prof. Dr. Adrian Jäggi for the opportunity and support to conduct this research.

This research was funded by the European Research Council under the grant agreement No. 817919 (project SPACE TIE). The computations were carried out using the Bernese GNSS software version 5.4 (Dach and Walser, 2015), partly performed on UBELIX (http://www.id.unibe.ch/hpc), the HPC cluster at the University of Bern.

We acknowledge the support from Spire Global and the provision of Spire data by ESA.

Contents

List of Figures

List of Tables

Acronyms

ADS-B Automatic Dependent Surveillance.

AIR Aerodynamic force.

AIS Automatic Identification System.

AIUB Astronomical Institute of the University of Bern.

AMR-C Advanced microwave radiometer-climate quality.

AO Announcement of Opportunity Project.

ARP Antenna Reference Point.

BDS BeiDou Navigation Satellite System.

CERES Clouds and the Earth's Radiant Energy System.

CNES Centre National d'Etudes Spatiales.

CODE Center for Orbit Determination in Europe.

DORIS Doppler Orbitography and Radiopositioning Integrated by Satellite.

DOY Day of Year.

EARP Earth Radiation Pressure.

ERP Earth Rotation Parameter.

ESA European Space Agency.

EUMETSAT European Organization for the Exploitation of Meteorological Satellites.

FTP File Transfer Protocol.

FYB Fixed-yaw backward.

FYF Fixed-yaw forward.

GF-C Gravity Recovery and Climate Experiment Follow-On C.

GF-D Gravity Recovery and Climate Experiment Follow-On D.

GLONASS Global Navigation Satellite System.

GNSS Global Navigation Satellite Systems.

GPS Global Positioning System.

GRACE Gravity Recovery and Climate Experiment.

GRACE-A Gravity Recovery and Climate Experiment A.

GRACE-B Gravity Recovery and Climate Experiment B.

GRACE-FO Gravity Recovery and Climate Experiment Follow-On.

IGS International GNSS Service.

ILRS International Laser Ranging Service.

IR Infrared light.

ITRF International Terrestrial Reference Frame.

JPL Jet Propulsion Laboratory.

KBR K-band Range.

LAGEOS Laser Geodynamic Satellite.

LC Linear Combination.

LEMUR Low Earth Multi-Use Receiver.

LEO Low Earth Orbiter.

LOD Length of Day.

LRI Laser Ranging Interferometry.

LSQA Least-squares Adjustement.

MJD Modified Julian Date.

MWR Microwave Radiometer.

NASA National Aeronautics and Space Administration.

NEQ Normal Equation System.

NEU North/East/Up.

NG Reduced-dynamic, explicit non-gravitational force modeling.

NL Narrow-lane.

NNR No-net-rotation.

NNS No-net-scale.

NNT No-net-translation.

OLCI Ocean and Land Colour Instrument.

OSB Observable Specific Biases.

OSTM Ocean Surface Topography Mission.

PCA Piecewise Constant Acceleration.

PCC Phase Center Correction.

PCO Phase Center Offset.

PCV Phase Center Variation.

POD Precise Orbit Determination.

RD Reduced-dynamic, no non-gravitational force modeling.

RINEX Receiver Independent Exchange Format.

RMS Root Mean Square.

RO Radio Occultation.

RSW Local orbital frame.

S3A Sentinel-3A.

SBFF Satellite Body-Fixed Frame.

SLEO LEO with scientific mission goal.

SLR Satellite Laser Ranging.

SLSTR Sea and Land Surface Temperature Radiometer.

SRAL SAR Radar Altimeter.

SRF Satellite Reference Frame.

SRP Solar Radiation Pressure.

TRF Terrestrial Reference Frame.

VI Visible light.

VLBI Very Long Baseline Interferometry.

WL Wide-lane.

YSB Yaw-steering backward.

YSF Yaw-steering forward.

Chapter 1

Introduction

Over the course of the last hundred years, we have advanced our understanding of the planet Earth. Since ancient times, humans have set themselves the task of describing their home as accurately as possible. During the last few decades, knowledge about the Earth has grown rapidly as a result of the increasing capabilities to perform experiments designed to test various hypotheses regarding the worldview.

Geodesy, the science of the measurement and mapping of the Earth (Torge, Wolfgang, 2002; Teunissen and Montenbruck, 2017), grew in importance over time, and has gained a wide range of applications in the present day. Among others, important information can be retrieved serving the purpose of forecasting and surveying natural disasters like earthquakes and tsunamis. In the last decades, navigation has become one of the most used applications where geodesy plays a key role. In focus is hereby often the accurate determination of precise positions of points on the Earth's surface (Morton et al., 2021). Due to the relevance of the applications, the development of strategies to retrieve superior information is of outstanding importance. To achieve this, the size, shape, and orientation of the planet have to be known with high accuracy. A major part consists of determining several physical quantities, such as where the Earth's center-of-mass lies, as well as the orientation of the Earth's rotation axis at the current time (Flury et al., 2006). A possible approach to gaining this knowledge is to make use of measurements made between satellites in orbit around the Earth and ground stations on its surface. A widely used method is to use observations from Global Navigation Satellite Systems (GNSS). For one or more GNSS constellations the positions of the satellites and their clocks are determined along with exact coordinates of the globally distributed ground stations on the Earth's surface, which are equipped with GNSS receivers, whereby also the geodetic properties of the Earth like the location of the center-of-mass and the orientation of the rotation axis may be determined. This common estimation process is called the determination of a global network solution.

The surveying of the Earth, for example, the determination of sea surface height, has become the mission goal of several altimetry satellites in the past decades. These satellites typically orbit the Earth at much lower altitudes than satellites that are part of GNSS and are therefore called Low Earth Orbiters (LEOs). To make use of the measurements performed from the different devices onboard these satellites, the position of the LEO has to be known with high precision. The related field of research, therefore, focuses on the Precise Orbit Determination (POD) for LEOs. The approach that leads to results with the highest precision for LEOs is to carry out a POD by making use of measurements between GNSS satellites and corresponding receivers onboard the LEOs (Yunck, 1996).

Terrestrial Reference Frames (TRFs) constitute the fundamental framework for measuring changes in the Earth's system. As a key discipline, geodesy measures not only changes in space and over time but also provides the indispensable standard by which these changes are measured (Altamimi et al., 2016). The "three pillars" of geodesy, encompassing alterations in Earth's form, rotation, and gravity field, are intrinsically linked and establish the conceptual and observation-driven basis necessary for Earth observation (Rummel et al., 2000).

Highly precise and stable TRFs are crucial to capture the smallest variations in Earth system components. The realization of TRFs involves a combination of space geodesy techniques such as Very Long Baseline Interferometry (VLBI), GNSS, Satellite Laser Ranging (SLR), and Doppler Orbitography and Radiopositioning Integrated by Satellite (DORIS). The International Terrestrial Reference Frame (ITRF, Altamimi et al., 2016), as the current standard, is achieved through regular updates and a combination of these different techniques using so-called local ties at stations where several space geodetic techniques are co-located. Although the ITRF is currently the most accurate TRF, an improvement of about an order of magnitude is needed to meet scientific requirements for observing Earth system variability with low uncertainty. The implementation of the ITRF2014 exhibits stability of about 0.5 mm/year, which is one of the most significant sources of uncertainty for phenomena such as global sea-level rise (Blewitt et al., 2010).

The current state of realizing terrestrial reference frames (TRFs) has conceptual weaknesses, as they are not based on all three pillars of geodesy. In particular, the time-variable gravity field of the Earth is only considered through its center-of-mass contribution via translation vectors for TRF determination. The present work is part of the SPACE TIE project, funded by the European Research Council (ERC), which addresses this gap, by proposing the consistent derivation of the time-variable gravity field of the Earth along with the Earth's form and rotation. Satellites in low Earth orbits are intended to serve as keys in this process, as they are particularly sensitive to the gravity field and can act as tie points in space (Space Ties) for various satellite geodetic techniques.

The results of SPACE TIE are of great interest in various scientific disciplines such as hydrology, climate modeling, ice observation, and environmental sciences. The consistent connection of gravimetric and geometric data enables a more accurate understanding of complex geophysical processes, such as glacier dynamics and sea-level rise. Furthermore, SPACE TIE contributes to exploring future perspectives in gravity field determination. The present work focuses on the combined solution of GNSS and several LEO satellites, based on undifferenced ambiguity-fixing techniques. The key aspect of this work is linking the high sensitivity of LEOs to the Earth's gravity field with GNSS.

Typically, the process of POD of LEOs and the computation of global network solutions for GNSS are separate processes. As part of a LEO POD, traditionally the approach is to introduce and fix the orbits and clocks of GNSS satellites that were previously determined as part of a network solution (Kobel et al., 2023b). Many studies have demonstrated the potential for GNSS observations of LEOs to contribute to global network solutions, particularly when it comes to computing geodetic parameters such as the Earth's center-of-mass coordinates. In this work, GNSS observations from specific LEOs were utilized to determine a global network solution. By combining observations collected from GNSS receivers aboard selected LEOs and those from ground stations together, a GNSS-LEO solution may be obtained. The orbits of LEO and GNSS satellites are determined together with geodetic parameters, such as the Earth's rotation axis orientation and center-of-mass coordinates. Nearly three decades ago Rim et al. (1995) already stated that the combination of station-Topex/Poseidon double-differences observables with station-station double-differences observables yields superior coverage in a Global Positioning System (GPS) network solution, consequently leading to improved GPS orbit solutions. Nevertheless, the improvement in the Topex/Poseidon orbit accuracy remains marginal. One major hurdle in the LEO-integrated approach is the identification and interpretation of inherited modeling errors due to the high degree of freedom by means of the number of parameters (Hugentobler and Beutler, 2003).

The chosen scientific approach serves to find answers to different aspects of the key question: How does the integration of GNSS observations collected by satellite-based receivers contribute to the computation of a global network solution in terms of the determination of LEO and GNSS satellite trajectories, and particularly, the determination of geodetic parameters, like the Earth's center-of-mass coordinates, Earth rotation parameters, and station coordinates.

This thesis is structured as follows:

Chapter 2 contains important information about the GNSS ground station network, Earth rotation parameters (ERPs), Earth's center-of-mass coordinates, and GNSS systems. Detailed information about GNSS observations, LEO missions, and data availability is provided. The current state-of-the-art is described by analyzing previous studies in this field.

Chapter 3 describes theoretical and mathematical concepts together with applied procedures for the POD of LEOs. This includes the description of the modeling of background forces which are of central importance for the adopted strategy. Information about crucial properties of the LEO satellites is described together with the strategy of the adopted ambiguity resolution. The experimental setup is explained, regarding introduced a priori information, the list of estimated parameters, and the processing chain. Additionally, an overview of the used quality metrics is provided.

Chapter 4 shows the special focus of this work adopted to the POD of LEOs. For this purpose, detailed information and results of the POD of the LEO Jason-3 are shown in this section.

Chapter 5 describes an analysis of possible error sources resulting from erroneous information on LEO-specific properties, concerning integrating observations from LEOs into the computation of a global network solution. Potential corrections to LEO satellite-specific properties are investigated.

Chapter 6 details the results of the LEO-integrated experiments carried out. It is analyzed, how the proposed approach of LEO-integrated global network solutions influences the resulting solutions. Dedicated experiments are shown to answer specific aspects of the key question.

Chapter 7 concludes and summarizes the findings, whereby the advantages and drawbacks of the procedure are analyzed.

Recall: How does the incorporation of observations collected by GNSS receivers onboard LEOs help in the computation of a global network solution, with regard to the determination of the trajectories of LEO and GNSS satellites, as well as the determination of geodetic parameters such as the center-of-mass coordinates, the ERPs and station coordinates?

Chapter 2

Background information

2.1 Global Navigation Satellite Systems

Data from satellites of a GNSS allow for the determination of the location and time of the collector, e.g., the antenna's point on the Earth's surface (Teunissen and Montenbruck, 2017). The United States government developed and operates the GPS. There are also GNSS systems developed and operated by other countries, including the Global Navigation Satellite System (GLONASS) of the Russian Federation, the Galileo system of the European Union, and the Chinese BeiDou Navigation Satellite System (BDS). A GNSS satellite orbiting around the Earth transmits signals that are collected by receivers on the ground or in space. By receiving the signals, the receiver determines its position, as well as the receiver's clock offset w.r.t. GNSS system time. By determining the change of the position, also the velocity of the receiver can be determined. Navigation, tracking, surveying, and other applications can be performed using this information. In order to exploit the data emitted from the GNSS satellites, the trajectories and the clock readings of these satellites have to be known, in this work done via the determination of a global network solution. Further information about GNSS can be found in Remondi (1984), Strang and Borre (1997), Hofmann-Wellenhof et al. (2012), and Xu and Xu (2016).

2.1.1 Global Positioning System

Initially, GPS was used primarily for military purposes, but nowadays it is indispensable to geodesy. In order to determine the precise orbit solutions of LEO satellites, GPS receivers are crucial. POD requirements of cm accuracy (Fernández et al., 2020) can be met through GPS tracking. Today's receivers of most LEO satellites can still receive solely GPS signals, whereas very recent missions, e.g., Sentinel-6A, are equipped with multi-GNSS receivers. GPS satellites constantly transmit their current position and the exact time of the signal transmission. Three satellites are sufficient for determining the exact position of the receiver at any measured epoch based on the signal propagation times. In order to determine the exact time of the receiver, a signal from a fourth GPS satellite is required since the receivers lack an accurate clock and synchronization to GPS time (Noureldin et al., 2012). In 1978 the first GPS satellite was launched, whereby the system of a constellation of 24 satellites was operational by the mid-1990s. Today there are 32 active satellites, to enable a GPS receiver to collect signals from at least four satellites at the same time (Fig. 2.1). The GPS satellites are arranged in six orbital planes, inclined 55° w.r.t. the equator (Beutler, 2005), and evenly distributed around the equator by 60° according to

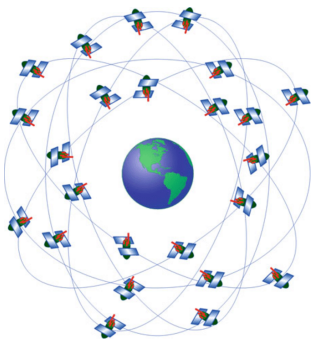

Figure 2.1: GPS constellation (image credit: Tamazin (2015))

$$\Omega_n = \Omega_0 + n \cdot 60°, \tag{2.1}$$

whereby Ω_n describes the longitude of the ascending node of the n-th orbital plane (see Fig. 3.1). As stated in Blewitt (1997), it takes a GPS satellite 11 hours and 58 minutes to orbit the Earth at a semi-major axis of 26 578 km on a nearly circular orbit. The satellites continuously rotate to ensure that the antennas are always pointing towards the Earth while the solar panels are pointing in the direction of the sun (e.g., Sośnica, 2015). The GPS satellites are equipped with atomic clocks which produce the fundamental L-band frequency of 10.23 MHz (Xu and Xu, 2016). The signals are transmitted on three different carrier frequencies, which are multiples of the fundamental frequency: 1575.42 MHz (L1), 1227.60 MHz (L2), and 1176.45 MHz (L5). The signal consists of pseudo-random noise codes, along with satellite ephemerides, clock corrections, and ionospheric models. The receiver detects, decodes, and processes the signals to create code and phase observables. The knowledge about the positions of the GPS satellites stems either from the transmitter broadcast (real-time) information or from the International GNSS Service (IGS, Johnston et al., 2017), whereby IGS orbits result from near-real-time or post-processing. International organizations formed the IGS in the 1990s to make the GPS satellite orbit and clock correction determination more accurate and comparable between different contributing institutions (Johnston et al., 2017). Detailed information about GPS Broadcast ephemerides and IGS precise ephemerides can be found in Xu and Xu (2016).

2.1.2 Galileo

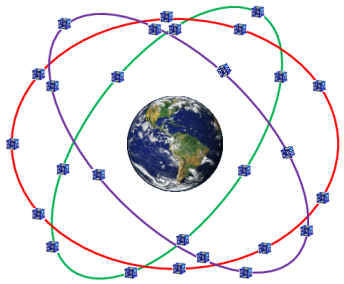

Figure 2.2: Galileo constellation (image credit: Saeed et al., 2020)

The Galileo System, operated by the European Space Agency (ESA), provides accurate positioning and contributes to significant advances in aerospace technology and a wide range of scientific research. The first satellite of the Galileo constellation was launched in 2005, and nowadays there are 24 satellites (plus spares) orbiting the Earth. The signal is transmitted on three different frequencies: 1575.42 MHz (E1), 1278.75 MHz (E6), and 1191.80 MHz (E5)[1]. The satellites are arranged in three orbital planes with an inclination of 56° (Spits, 2012), whereby the ascending nodes are equally spaced in three orbital planes according to:

$$\Omega_n = \Omega_0 + n \cdot 120°. \tag{2.2}$$

The Galileo satellites orbit the Earth on nearly circular orbits with semi-major axis of about 29 600 km (Xu and Xu, 2016) with an inertial velocity of 3.6 km/s and with a revolution period around the Earth of approximately 14 hours[2].

2.2 Ground station network

More than 500 IGS stations are located across the globe today. However, due to geographical constraints, there are some regions that are not covered, such as the oceans, whereas other regions have a dense cluster of stations, e.g., Europe (Kobel et al., 2022c). Several ground stations were selected for this work. Only GNSS observations from stations that contributed to the repro3 product series provided by CODE (Center for Orbit Determination in Europe, Dach et al., 2009) (Selmke et al., 2020) were used. Reduced ground station networks drastically reduce computation times and increase the effect of including LEO GNSS data in the processing (Kobel et al., 2022c). Until now, only studies that have used a less dense ground station network to integrate LEO observations have been published. By integrating GNSS observations from LEOs into a global GNSS network solution, this type of experimental setup can be used to demonstrate the effect. For example, Huang et al. (2020) performed an analysis including 26 ground stations plus integrated LEOs and compared it to a reference solution consisting of 33 ground stations with no integrated LEOs. Huang (2022) analyzed a scenario consisting of 62 ground stations in terms of a LEO-integrated global network solution. Männel and Rothacher (2017) used a ground station network of 53 well-distributed stations. 46

[1] https://www.gsc-europa.eu/sites/default/files/sites/all/files/Galileo-OS-SIS-ICD.pdf (Accessed: 4 September 2023)

[2] https://www.esa.int/Applications/Navigation/Galileo/Galileo_a_constellation_of_navigation_satellites (Accessed: 24 August 2023)

ground stations were included in the study performed by Haines et al. (2015). Despite this, a reduced network of ground stations might not be the best possible status quo and makes GNSS orbital elements, ERPs, and the center-of-mass of the Earth harder to determine. In this work, a much larger ground station network has been used in order to be as close to real-world applications, e.g., processings performed by IGS analysis centers, as possible and to compete with results derived from other geodetic techniques, e.g., the estimation of the Earth's-center-of-mass coordinates via SLR data processing. A subset of 240 ground stations is selected as shown in Fig. 2.3. The average number of stations providing data to a one-day solution was 212 for the period 14 January 2022 - 13 February 2022 (see Table 6.1).

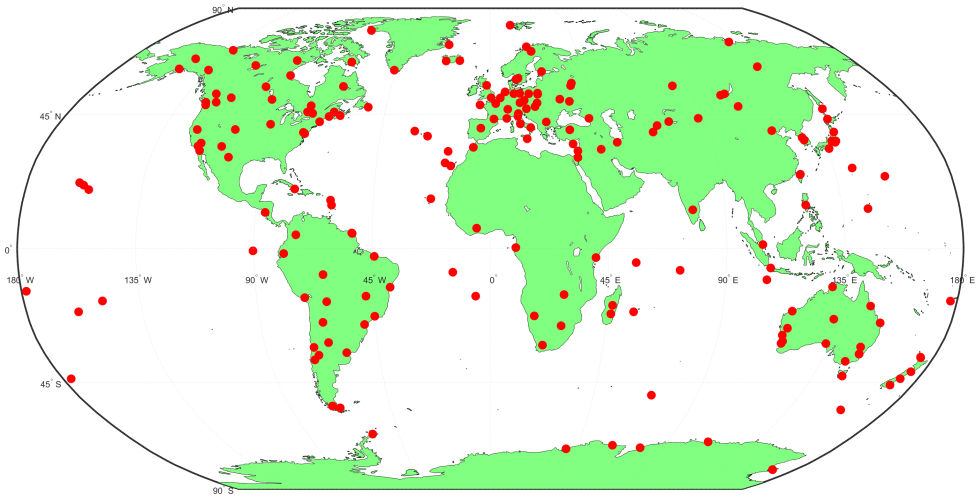

Figure 2.3: Selected ground station network (DOY 22/016)

It is evident in Fig. 2.3 that the distribution of the ground station network is not homogeneous. This is, as already mentioned, due to geographical constraints, but also demographic reasons play a role. An interesting quantity of a selected ground station network is the distribution in terms of distances from one station to the other stations. It can help identify the most dominant, important, and therefore crucial sites. This allows to identification of potential weaknesses in the processing regarding global coverage.

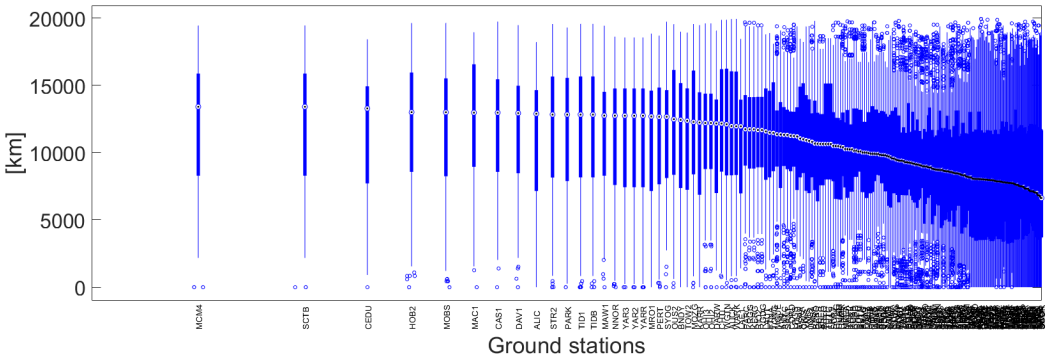

Figure 2.4: Distances of ground stations to each other

Figure 2.4 illustrates the median and the 95th percentile of the ground stations' distances from each other. A clear signature is evident. The stations with the highest median values are MCM4 (Ross Island, Antarctica), SCTB (Scott Base, Antarctica), CEDU (Ceduna, South Australia), and HOB2 (Hobart, Australia). It is of special interest to ensure that these stations provide observations for the processed time span. Another approach to assess the inhomogeneity of the ground station distribution over the globe is to represent the

stations' latitudes as a histogram.

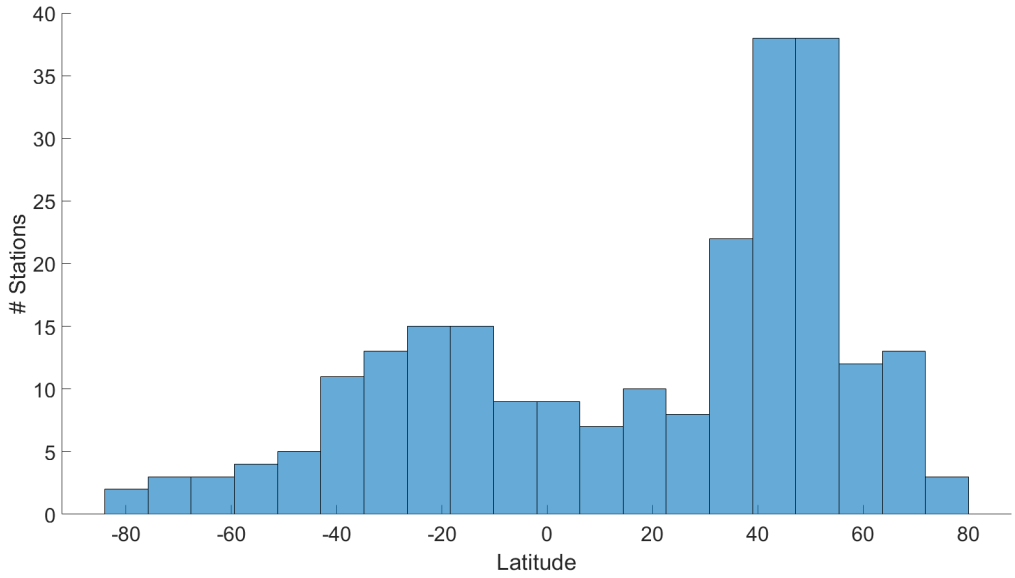

Figure 2.5: Histogram station latitudes

From Fig. 2.5 one can conclude that a large amount of stations is located between 40° and 60° latitude. Due to the information provided in Figs. 2.3, 2.4 and 2.5 it is of special interest how integrating LEOs, acting as fast-moving stations, can improve the coverage and therefore also the determination of geodetic parameters.

2.3 Earth rotation parameters

To assess the movement of the Earth in terms of rotation, the key is to study the ERPs. The transformation of a position vector between the Earth-fixed coordinate system ($\mathbf{r}_E$) and the inertial (celestial) coordinate system ($\mathbf{r}_I$) can be performed by computing:

$$\mathbf{r}_I = \mathbf{P}^T(t) \cdot \mathbf{R}_1(\Delta\epsilon) \cdot \mathbf{R}_2(-\Delta\psi \sin\epsilon_0) \cdot \mathbf{R}_3(-\theta_{GM}) \cdot \mathbf{R}_1(y_p) \cdot \mathbf{R}_2(x_p) \cdot \mathbf{r}_E. \tag{2.3}$$

Equation (2.3) requires the knowledge of the ERPs. $\Delta\psi$ and $\Delta\epsilon$ describe the nutation in longitude and obliquity, whereby ϵ_0 denotes the mean obliquity of the ecliptic (Dach and Walser, 2015). Precession ($\mathbf{P}(t)$) refers to the circular motion in inertial space of the Earth's rotation axis and is mainly caused by the gravitational forces of the Moon and Sun. It has a period of about 26000 years and can also affect the distribution of solar radiation on Earth's surface (Buis, 2020). θ_{GM} is the Greenwich mean sidereal time, whereby the ERP ΔUT = UT1 - UTC is the analyzed quantity in this work. Since this parameter is highly correlated with the satellite's ascending nodes, it cannot be determined along with orbit parameters from satellite geodetic techniques. A drift in ΔUT can, however, be estimated, which is equivalent to estimating the length of day (LOD) (Zumberge et al., 1994), which is the time it takes the Earth to complete one complete rotation around its rotation axis. This parameter has been measured for many decades and small variations have been found (Lambeck and Cazenave, 1976). Several factors are responsible for these variations, including changes in the distribution of Earth's mass and changes in the wind and ocean currents. The X- and Y-Pole (x_p, y_p) describe the rotation angles between the Celestial Intermediate Pole and the Pole in the Earth-fixed coordinate system (Dach and Walser, 2015). The determination and further understanding of the ERPs asks for continuous and rigorous monitoring of the Earth, for example via GNSS and Satellite Laser Ranging (SLR) to dedicated satellites, or Very Long Baseline Interferometry (VLBI) as a unique technique to determine the ERPs, because it is the only method which can provide the complete set of all ERPs (Malkin, 2009).

2.4 Earth's center-of-mass coordinates

The knowledge of the Earth's center-of-mass is very important for a wide range of scientific applications, e.g., geodesy, orbital mechanics, gravitational studies, climate and oceanography, etc., and therefore a key geodetic parameter. To describe the mass distribution of the Earth, a rigorous determination of the Earth's center-of-mass coordinates is essential, for which many different approaches have been used in the past. A challenging task is to properly take into account the influence of the Earth's rotation for the determination of the Earth's center-of-mass (Altamimi et al., 2011). The estimation of the Earth's center-of-mass with terrestrial GNSS data only is an approach that has been investigated in the past (Meindl et al., 2013). The space geodetic technique of SLR is used for estimating the center-of-mass motion with the nowadays highest quality (Cheng et al., 2013). VLBI measurements are made in a reference frame linked to distant quasars or extragalactic radio sources, which causes them to not be sensitive to the Earth's center-of-mass. The reference frame for VLBI observations is defined by the positions of these fixed sources in the sky. The relative positions of these distant sources in the sky are not affected by the position of the Earth's center-of-mass. However, there is a proposal from Blewitt (2003) of the use of Very Long Baseline VLBI to determine the Earth's center-of-mass via deformations, using quasar sources, where no satellite orbit determination is necessary. The combination of these techniques allows for the determination of the International Terrestrial Reference Frame (ITRF) (Altamimi et al., 2011), whereby the estimation of the Earth's center-of-mass plays a central role. For further details and explanations about the Earth's center-of-mass estimations, the reader is referred to Lavallée et al. (2006).

Climate events, weather patterns, and seasonal changes can cause temporary shifts in the Earth's center-of-mass (Altamimi et al., 2001). Also, the accumulation of snow and ice in the polar regions during the winter causes the center-of-mass to shift. The Earth's center-of-mass can also change as a result of the movement of water throughout its hydrological cycle, including rainfall, evaporation, and groundwater flow. Also, a rebound of the Earth's crust may happen when glaciers and ice sheets melt due to climate change, causing its mass distribution to change. The center-of-mass of the Earth can gradually shift as a result of this process. The Earth's center-of-mass can also vary due to seismic activity, such as earthquakes and volcanic eruptions. Additionally, anthropogenic factors such as mining, dam construction, and the extraction of groundwater can redistribute mass within the Earth, leading to changes in the Earth's center-of-mass, whereby these changes can have both short-term and long-term effects.

2.5 Low Earth Orbiters

A LEO is an object that orbits the Earth at low altitudes between 250 km and 2000 km (Jäggi, 2007). Since many decades, it is of wide interest to place artificial satellites in orbits at low altitudes, whereby various scientific and commercial mission goals are addressed. Many of these LEO satellites are nowadays equipped with GPS receivers (Wang, 2021). The received observation data can be used for the POD of the satellites, which is one of the main topics in this work. Generally, precise orbit solutions for a LEO satellite are computed by more than one institution, allowing for comparison and determination of the orbit precision. For this purpose, most of the provided solutions are given in the specific "SP3-C" data format (Hilla, 2010), whereby the positions are given in the Earth-fixed frame. The processing of GNSS data follows a convention regarding the GNSS product and especially the data distribution, namely the data format, which is given by the Receiver Independent Exchange Format (RINEX), whereby for most LEOs either format version 2 (Gurtner and Mader, 1990) or version 3 (Gurtner and Estey, 2006) is used at the time of writing. More detailed information can be found in Hatanaka (2008). GNSS observation data (and other POD-related products) are either available on mission-specific FTP servers or on request from mission operators. The experiments performed in this work are based on GNSS observations collected by dedicated GNSS receivers onboard 13 selected scientific LEO missions. Additionally, GPS observations collected onboard nano-satellites (CubeSats) from the Spire constellation are analyzed and included in parts of the experiments. In this section, an overview of all the LEOs processed in this work is provided.

2.5.1 Sentinel-3

Figure 2.6: Sentinel-3 (image credit: ESA)

The Sentinel-3 A and B satellites are a pair of Earth observation satellites that are jointly operated by the European Space Agency (ESA) and the European Organization for the Exploitation of Meteorological Satellites (EUMETSAT) (Yang et al., 2019). They belong to the space segment of the Copernicus program, which builds infrastructure for Earth observation and was founded by the European Commission and ESA in 1998 (Aschbacher and Milagro-Pérez, 2012). The satellites were launched on 16 February 2016 (A) and 28 April 2018 (B) from the spaceport Plessezk with a Rockot skyrocket (Donlon et al., 2021). They orbit the Earth at an altitude of ∼811km in a sun-synchronous orbit with an inclination of 98.6°. With the aim to monitor long-term and large-scale global dynamics, they perform systematic measurements in the Earth's oceans, land ice, sea ice, rivers, and lakes. The main purpose of this scientific LEO mission is to monitor climate change, increase maritime safety and security, and support European security, humanitarian, and emergency services[1]. For this purpose, they are equipped with dedicated instruments (ESA, 2017):

- OLCI (Ocean and Land Colour Instrument)
- SLSTR (Sea and Land Surface Temperature Radiometer)
- SRAL (SAR Radar Altimeter)
- MWR (Microwave Radiometer)

Apart from these instruments, the satellites are equipped with two GPS receivers and a Doppler Orbitography and Radiopositioning Integrated by Satellite (DORIS) (Auriol and Tourain, 2010) receiver each, allowing for a POD. Additionally, the two satellites carry a SLR retroreflector, which is mainly used for independent validation of the determined trajectories. For more detailed information about the POD package onboard Sentinel-3 A and B the reader is referred to Montenbruck et al. (2018a).

2.5.2 Sentinel-2

Figure 2.7: Sentinel-2 (image credit: ESA)

Also part of the space segment of the Copernicus program are the two identical Sentinel-2 Earth observation satellites. Sentinel-2A was launched on 23 June 2015 from Kourou, from where also Sentinel-2B was launched on 7 March 2017, both onboard a Vega skyrocket[2]. They orbit the Earth at an altitude of ∼790 km. The two satellites are separated by 180° in the argument of latitude in their sun-synchronous orbits with an inclination of 98.6°. They collect data serving the purposes of climate protection, land survey, and catastrophe and crisis management on Earth. This is carried out by performing imaging of land and coastal areas at high spatial resolution in the optical domain and land ecosystems monitoring as well as inland and coastal water quality monitoring (Fernández-Sánchez et al., 2016). The main scientific instrument onboard the two satellites is a multi-spectral instrument that operates from visible to shortwave infrared (ESA, 2013). In order to enable POD, each satellite is equipped with two GPS receivers, an operational and a spare receiver.

[1] https://sentinel.esa.int/web/sentinel/missions/sentinel-3 (Accessed: 13 September 2023)
[2] https://sentinel.esa.int/web/sentinel/missions/sentinel-2 (Accessed: 13 September 2023)

2.5.3 Sentinel-6

The Sentinel-6 mission is designed to take over the data collection performed by the Jason-3 satellite (see sect. 2.5.4) and is therefore also called Jason Continuity of Service (Jason-CS) mission. The goal is to extend the climate record of sea level measurements from 2020 to beyond 2030 (Scharroo et al., 2016), by carrying out sea surface altimetry (Donlon et al., 2021). The first satellite of this mission, Sentinel-6A "Michael Freilich" was launched on the 21 November 2020 from the Vandenberg Air Force Base in California, US, with a SpaceX Falcon 9 rocket[1], into an orbit at 1336 km altitude[2] and 66° inclination. The specific data collection includes the measurement of sea surface height, wave height, wind speed, atmospheric pressure, temperature, water vapor, and ionospheric data (Scharroo et al., 2016). Dedicated instruments are carried on board the Sentinel-6A satellite:

Figure 2.8: Sentinel-6 (image credit: ESA)

- Poseidon-4 Ku/C-band altimeter (Cullen and Francis, 2014; Donlon et al., 2021) which represents a major evolution over the altimeter onboard of the Jason-3 satellite (Montenbruck et al., 2021)
- Advanced microwave radiometer-climate quality (AMR-C) (Maiwald et al., 2020)
- GNSS radio occultation (RO) receiver (Young, 2017)

For further information on these instruments, the reader is referred to Donlon et al. (2021). To allow for a POD, the satellite is equipped with two GNSS receivers and a DORIS receiver. This satellite is the only one from which data is analyzed in this work whose receiver collects observations from GPS and Galileo. Measurements made using the SLR reflector on board can serve for orbit validation purposes. The second satellite of this mission, Sentinel-6B is planned to be launched in 2026 (Scharroo et al., 2016).

2.5.4 Jason-3

Altimetry is the primary mission of Jason-3. Designed as a follow-up mission to Jason-2, it follows the same ground track. The satellite was launched on 17 January 2016 (Liu et al., 2019) from the Vandenberg Air Force Base in California, US, with a Falcon-9 skyrocket (Dumont et al., 2015) into an orbit of 1336 km altitude and 66.0° inclination. The main mission goal is to provide highly accurate radar altimeter measurements for global ocean circulation and sea surface studies. The data collected onboard Jason-3 provides information for deriving marine nowcasting, numerical prediction of sea state, ocean circulation, and weather[3]. To assess the mission goals, the satellite is equipped with corresponding instrumentations: Poseidon-3B radar altimeter, Microwave radiometer (AMR), and two additional non-core mission experiments for the radiations effect measurement. Also part of the instrumentation are two GPS and a DORIS receiver, to allow for a POD. The SLR measurements made to the retroreflector can serve for orbit validation purposes. Compared to the other LEOs presented in this section, the Jason-3 satellite is orbiting the Earth in a more complicated attitude behavior. While the

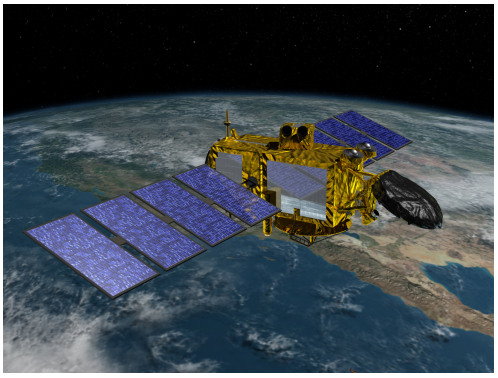

Figure 2.9: Jason-3 (image credit: NASA Jet Propulsion Laboratory)

[1] https://www.eoportal.org/satellite-missions/copernicus-sentinel-6-michael-freilich (Accessed: 24 August 2023)
[2] https://sentinels.copernicus.eu/web/sentinel/missions/sentinel-6 (Accessed: 24 August 2023)
[3] https://www.nesdis.noaa.gov/current-satellite-missions/currently-flying/jason-3/jason-3-mission (Accessed: 31 August 2023)

attitude is controlled by reaction wheels and magnetotorquer bars, the satellite changes its attitude mode depending on the β-angle, which is defined as the angle between the orbital plane of the satellite and the vector from the Sun to the satellite, i.e., the direction from which the Sun is shining (see Sect. 4.1.1). The POD of Jason-3 is of special focus in this work and is described in detail in Sect. 4, especially with regard to obtained orbit precision. An extract of the performed investigations can be found in Kobel et al. (2022a) and Kobel et al. (2021).

2.5.5 GRACE Follow-On

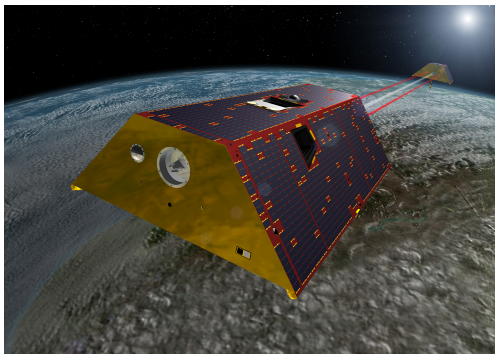

Figure 2.10: GRACE Follow-On (image credit: NASA)

The GRACE (Gravity Recovery And Climate Experiment) Follow-On mission, the successor of the GRACE mission, consists of two LEO satellites GF-C and GF-D[1]. They were launched with a SpaceX Falcon 9 rocket on 22 May 2018 from Vandenberg Air Force Base in California, US, into a polar orbit of about 480 km altitude and 89.0° inclination. The mission goal is the continuation of the GRACE mission in terms of measuring the time-variable gravity field of the Earth. For this, the separation of the two satellites orbiting the Earth is actively controlled to be 170 km-270 km all the time (Landerer et al., 2020). The two satellites perform the following measurements:

- To monitor the Earth's time-varying gravity field with high precision, K-band range (KBR) measurements are used (see sect. 3.7.4),
- Determining the inter-satellite distance using Laser Ranging Interferometry (LRI) serves as a technology demonstrator instrument for optical interferometry between two satellites with an outstanding precision of 10 nm (Abich et al., 2019),
- The accelerometers provide measurements of perturbations acting on the satellites caused by non-gravitational forces,
- An onboard GPS receiver allows for POD, which is essential for a gravity field recovery mission.

More specific information about the instruments can be found in Kornfeld et al. (2019). Detailed specifications about the GRACE Follow-On mission and its satellites are described in Wen et al. (2019).

2.5.6 Swarm

Figure 2.11: Swarm (image credit: ESA)

The Swarm mission is part of ESA's Living Planet Programme. The mission goal is to provide a survey of the Earth's geomagnetic field and its temporal evolution (Friis-Christensen et al., 2008). With a single-satellite magnetic mission, it is not possible to make full use of the onboard instrumentation because separation of the contributions from various sources of the geomagnetic field is not possible. This issue can be solved by designing a mission that makes use of a satellite constellation, which in the case of Swarm consists of three satellites, Swarm-A, Swarm-B, and Swarm-C. All three satellites were launched on 22 November 2013 from the Plessezk spaceport onboard a Rockot skyrocket (Viertel et al., 2014). The research objectives include studies of core dynamics, geodynamic processes, core-mantle interaction, mapping of the lithospheric magnetization, determination of the 3-D electrical conductivity of the mantle, and investigation of the electric currents

[1] https://space.skyrocket.de/doc_sdat/grace-fo.html (Accessed: 31 August 2023)

flowing in the magnetosphere and ionosphere (Haagmans et al., 2004; Kelly, 2013). The satellites are equipped with dedicated instruments: A scalar magnetometer, a vector magnetometer, and an instrument to measure the electric field. To allow for a POD, each Swarm satellite is equipped with a GPS receiver. The design of the ideal orbit constellation to achieve all research objectives is a difficult task and has been determined to be:

- Swarm-A and Swarm-C orbiting the Earth in tandem, with a separation of $1° - 1.5°$ in longitude, in a near-polar orbit at an altitude of 450 km and an inclination of 87.3° (Hackel, 2019)
- Swarm-B in a polar orbit at an altitude of 530 km and an inclination of 87.8°

While the data from the different satellites must be treated as an entity for purposes of the scientific mission goal (Friis-Christensen et al., 2008), this mission provides three individual LEOs to be integrated into the processing in the frame of this work.

2.5.7 Spire

All LEO satellites described previously are designed to achieve scientific mission goals. The recent developments in micro-electronics allow for the production of nano-satellites, which are of comparably low costs, for commercial purposes. Spire Global Incorporated is a data and analytics company, which operates a mega constellation of over 100 CubeSats, which are nano-satellites of 10 cm × 10 cm× 34 cm size (Angling et al., 2021). The CubeSats are lighter than 10 kg and have the primary purpose of tracking aircraft via ADS-B (Automatic Dependent Surveillance) and sea vessels via AIS (Automatic Identification System), together with GNSS-based measurements of radio occultation (Cappaert, 2020). A large number of satellites allow for a drastic increase in global coverage, which leads to the question of whether the collected data can also be used for scientific purposes. The bus of the satellites, from which data have been analyzed in this work, are all very similar and are based on the Low Earth Mulit-Use Receiver (LEMUR) 3U CubeSat platform developed by Spire Global, Inc.(Johnstone, 2020). The main instrumentation of the satellites is two GNSS antennas for radio occultation (RO) which are mounted at the side of the satellite bus, one heading in forward- and one heading in backward velocity direction. The satellites are also equipped with a STRATOS-dual-frequency GPS receiver (Angling et al., 2021) to allow for POD. For a subset of these satellites, GPS data is analyzed in the frame of this work. Table 2.1 provides specific detailed information about the CubeSats from which data has been processed.

Figure 2.12: Spire satellite (image credit: ESA)

Table 2.1: Processed Spire CubeSats

Spire	Name	Launch	Satellite Bus version	Altitude	Inclination
FM 099	JohanLoran	01/04/2019	LEMUR2_3.4	505 km	97.36°
FM 101	Elham	01/04/2019	LEMUR2_3.4	505 km	97.36°
FM 102	Victor-Andrew	01/04/2019	LEMUR2_3.4	505 km	97.35°
FM 103	Wanli	05/07/2019	LEMUR2_3.4	530 km	97.64°
FM 104	LillyJo	05/07/2019	LEMUR2_3.4	530 km	97.64°
FM 106	Ejatta	05/07/2019	LEMUR2_3.4	530 km	97.63°
FM 107	Morag	05/07/2019	LEMUR2_3.6	530 km	97.64°
FM 108	GregRobinson	05/07/2019	LEMUR2_3.6	530 km	97.63°
FM 115	JpgSquared	11/12/2019	LEMUR2_3.4	550 km	36.92°

Table 2.1 contains, among other details, the orbit altitudes and inclinations (Kobel et al., 2023a). It is evident that FM 115 has an altitude of 550 km, while the other orbit the Earth at either 505 km or 530 km. Unlike the others, FM 115 has a very low inclination of 36.92°.

2.6 LEO GNSS observation data availability

To rigorously determine the impact of integrating GNSS observations received from LEOs into the computation of a global network solution, it is crucial that for the investigated time period for as many LEOs as possible, this data is available. The beginning of the missions, namely the points in time, where the LEOs have been placed in the orbit, is named in the corresponding sections. Nevertheless, data availability may not be identical to these dates, since at the beginning of a mission, certain steps must be completed before routine data processing can begin. These initial steps depend on the satellite mission but in general, they include:

- In order to perform the mission-specific measurements while also maintaining a stable connection with the on-Earth mission base, the satellite needs some time to stabilize in orbit and reach the appropriate orientation.
- Instruments dedicated to the mission must be activated, which is not typically done before launch for safety reasons.
- Before accurate data can be analyzed, the instruments on board the satellite must be calibrated and checked for functionality.
- It is the mission operator's responsibility to ensure the correct functioning of the instrumentation, especially in terms of data transfer, and to ensure maneuvering can take place if necessary.

These initial steps lead to a delay between begin of the mission and data availability for scientific purposes. To select accurate time periods for the experiments carried out in this work, an overview of the GNSS observation data availability for the processed LEO satellites is needed.

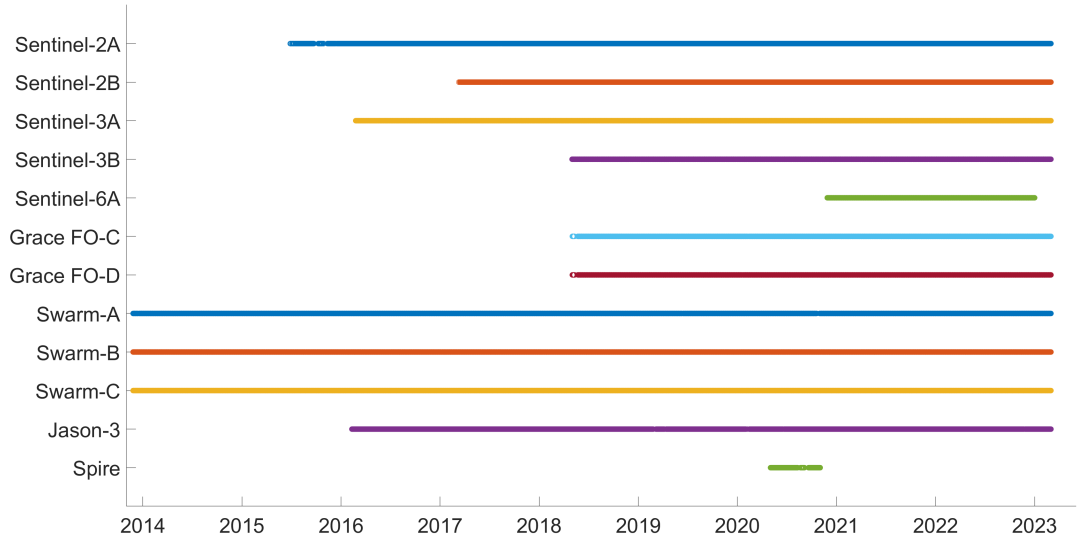

Figure 2.13: LEO data availability

Figure 2.13 shows that observations are available for most of the processed LEO satellites from mid-2018 onwards, with the exception of Sentinel-6A, which was launched more recently (see sect. 2.5.3). Since the GPS observation data from the Spire satellites was not publicly available at the time of writing, the possible processing time period is much shorter than for the LEO satellites with scientific mission goals and covers the period from 1 May 2020 to 31 October 2020 where data access has been granted in the frame of an ESA Announcement of Opportunity Project (AO).

2.6.1 Ground tracks of LEOs

As visible in Fig. 2.3, the global distribution of ground stations used in this work is not homogeneous, and large areas remain uncovered. An increase in global coverage due to the integration of observations from LEOs can potentially lead to a higher quality of the derived global network solution. To illustrate the improvement of global coverage with available GNSS observations, ground tracks from LEOs with different orbit characteristics are shown in Fig. 2.14 over one day.

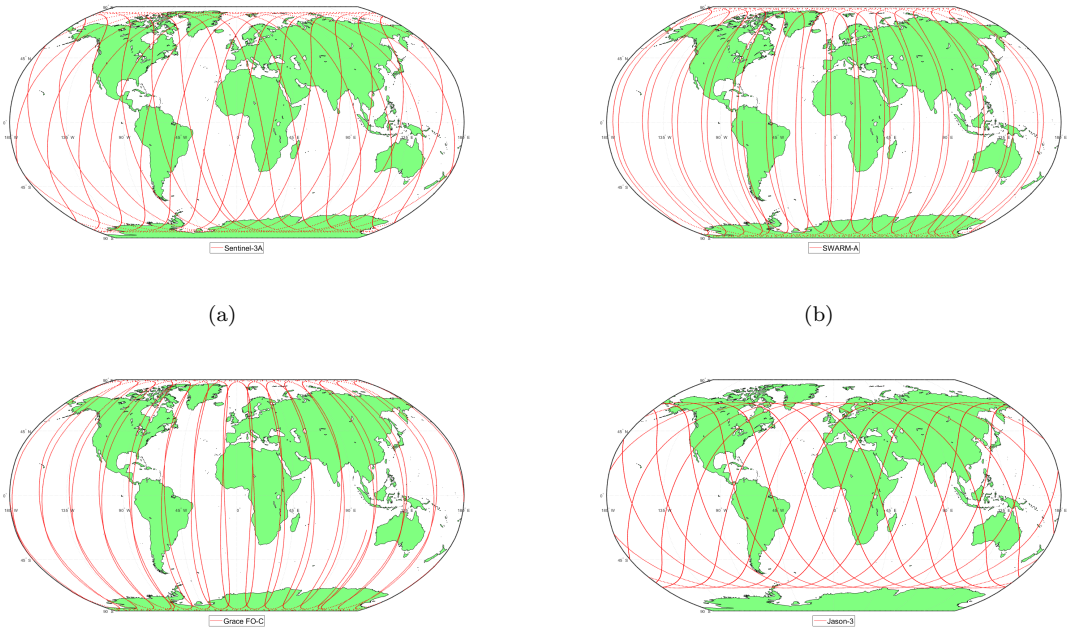

(a) (b)

(c) (d)

Figure 2.14: (a) Sentinel-3A (b) Swarm-A (c) GRACE FO-C (d) Jason-3

A comparison of the orbit characteristics of different LEOs is shown in Fig. 2.14 in which the ground tracks are clearly distinguishable. Whenever the integrated LEOs are interchanged, variability in the global network solutions may result due to the different ground tracks of the LEOs, determined by their orbit characteristics.

2.7 Literature review

The key questions of this work have already been partly addressed by several studies. This section provides an overview of selected investigations. The most important findings are described together with the main differences in terms of experimental setups with regard to the present work.

Hugentobler et al. (2005) analyzed LEO-integrated GPS network solutions, including the estimation of ground station coordinates, GPS orbits, LEO orbits, ERPs, and troposphere parameters using double difference observations. For this purpose, one single space-ground baseline was added per epoch to baselines built from a subset of 120 IGS ground stations. The strategy was defined to include observations from a single LEO, namely Jason-1. The ambiguities for the ground stations were introduced as determined in the frame of the computation of the final solution from CODE. The solutions were computed on a 24-hour arc basis, whereby 6 days were processed in total. For the observations from ground stations, a data sampling of 180 sec was used, whereas for the LEO GPS observation a 30 sec sampling was adapted. The LEO orbit was modeled by six initial osculating elements, nine radiation pressure parameters according to the CODE extended radiation pressure model (Beutler et al., 1994), and stochastic pulses every 12 min (Hugentobler et al., 2005). Orbit overlaps at arc boundaries for the LEO showed a discrepancy of 3-5 cm. Orbit comparisons to external solutions showed differences of the same magnitude. A SLR validation

revealed residuals with a RMS of 2-5 cm. The resulting GPS orbits were shifted in the order of 1 cm compared to the ground station-only solution. The impact on the determined ground station coordinates was on the sub-millimeter level, whereby a general translation of 1 cm was observed, and eliminated by a Helmert transformation previous to the comparison of the ground station coordinates. The impact on the estimated ERPs was of minor significance in the order of a few μas for the pole coordinates and up to 10 μs/day for the LOD estimate (Hugentobler et al., 2005). The largest error sources were the inhomogeneous ground station network and the modeling errors in the LEO orbit determination. The observed effects in the determined GPS orbits and Earth's center-of-mass coordinates (obtained via Helmert transformation) due to the integrated LEO observations were larger than adding a ground station to the network. The differences between the applied strategy to the one used in this work are:

- Only one LEO (Jason-1)
- Double-difference approach
- Orbit model (no non-gravitational force modeling)
- No ambiguity resolution for LEO
- Short investigated time span (6 days)

The study from Haines et al. (2015) addressed whether a network solution determined using only GPS data can compete with current TRF realizations. For this purpose, a long-arc approach for the determination of the network solution has been used. 7-day arc solutions were determined, using zero-difference observations, to potentially overcome problems related to the usage of observations from GPS only. For the GPS observations from ground stations and the LEO a 300 sec sampling was used. The LEO orbit was parametrized by six initial osculating elements, one drag coefficient, and one set (sine and cosine) of once-per-rev empirical accelerations in along- and cross-track directions plus one constant acceleration over one arc in along-track direction. The finding was, that using this approach it is possible, in terms of long-term stability, to reach high accordance with the ITRF2008, in particular in terms of the scale rate and the variability in Earth's center-of-mass coordinates along the equatorial plane (X and Y-coordinates). The estimation of the Z-coordinate in this approach was not robust in terms of annual motion. The most dominant errors are highly correlated to the draconitic period of the GPS satellites. The approach was to overcome these difficulties by integrating GRACE-A into the network computation, whereby for the LEO a 3-day arc was used. This strategy allowed for an improvement of the Z-coordinate post-fit RMS residual from 11 mm to 5 mm. It was stated that this represents a reduction of 80% of the variance. The drawback of this improvement was newly introduced errors which are linked to the GRACE-A β-angle period. The conclusion of this study was that the inclusion of data from LEOs is likely the best approach for improving the realization of the TRF using GPS data only, especially regarding the estimation of the Earth's center-of-mass. This study differs from the present investigation in the following points:

- Arc length (7 days for GPS/3 days for LEO)
- Number of integrated LEOs (1)
- LEO orbit parametrization (less stochastic parameters)
- Investigated period length (10 years)
- Fewer ground stations (varying, about 46)
- Ambiguity resolution (none)
- Weights of LEO observations (5$\times$ weight of station observations)
- Background force models (see Haines et al. (2015))

Kuang et al. (2015) carried out a simulation study to investigate the determination of the Earth's center-of-mass coordinates using different experimental setups in terms of integrated satellites. The main focus was to determine the formal errors of estimated Earth's center-of-mass coordinates when using GPS data. The approach was to combine GPS data from LEOs and observations from ground stations, adopting the

zero-difference observation approach, whereby it was investigated whether the additional observations from the LEOs could lead to an improvement in the determination of the Earth's center-of-mass coordinates of a GPS-only solution. The chosen sampling for the observations from ground stations and from the LEO was 300 sec. The LEO orbit was modeled by six initial osculating elements, one drag coefficient, and one scaling factor for solar radiation pressure. One outcome was that the resulting formal errors (more precisely the square root of the cofactors, see Sect 3.1) were not sensitive to the chosen arc length, and therefore a long arc solution (more than 24h) was used. In the simulation setup, the ground station coordinates were kept fixed, which may lead to a rather optimistic formal error estimation. It was shown that the estimation of Earth's center-of-mass coordinates is heavily influenced by integrating dynamically defined orbital planes. The determination of the Earth's center-of-mass Z-coordinate was weaker than an estimation via SLR tracking because of the need for the estimation of several other parameters like satellite and receiver clocks, tropospheric delay, and others. It was also shown that with a sufficiently high number of ground stations in the network, it was feasible to determine Earth's center-of-mass coordinates from GPS only. The integration of LEOs into the network has led to an improvement in the observability of the Earth's center-of-mass Z-coordinate, evidenced by decreased formal errors. It was stated that adding multiple LEOs in different orbital planes (different inclinations) can further improve the formal errors. It was pointed out that accurate modeling of non-gravitational forces is necessary to improve the estimation of the Earth's center-of-mass coordinates by integrating LEO GPS observations into the computation of a global network solution (Kuang et al., 2015). The most important differences to the present work are:

- Simulation study (no real data)
- Smaller ground station network (40 stations)
- No station coordinates estimated
- Chosen LEO orbit characteristics not in line with real missions

Männel and Rothacher (2017) put the focus on the estimation of the Earth's center-of-mass coordinates. The approach is similar to the present work, whereby observations from a set of ground stations were processed together with observations from LEO satellites in zero-difference mode to obtain a network solution including the geodetic parameters. Special regard has been put to the influence of empirical one-per-revolution orbit parameters in the direction towards the Sun (D-component) and parallel to the solar panel rotation axis (Y-component), used for the GPS satellites. For the observations from ground stations, a data sampling of 30 sec was used, whereas for the LEO GPS observation a 10 sec sampling was adapted. The LEO orbit was modeled by six initial osculating elements, nine radiation pressure parameters, and stochastic pulses every 6 min. The conclusion has been drawn that these types of parameters have to be constrained to retrieve appropriate results for the estimated Earth's center-of-mass coordinates. It has also been shown that the usage of modeled non-tidal corrections is crucial for this estimation. The integration of observations from LEOs to a ground station network showed a clear benefit in terms of formal errors, which decreased by about 20%. The comparisons of the resulting Earth's center-of-mass coordinates to reference values showed clear discrepancies in terms of amplitudes and phases of an annual signal, whereby phase shifts in the X- and Z-component appeared. The authors claimed that resolving the ambiguities to their integer values has the potential to further improve the resulting network solution, especially the estimation of the geodetic parameters. The conclusion was drawn that the integration of LEO-GPS observations to a ground station network worked well (in the zero-difference mode), whereby an improvement was found when compared to a ground station-only processing. This study is similar to the present work, whereby potentially crucial differences are:

- Small ground station network (53 stations)
- 4 LEOs (GRACE-A/B, Jason-2, GOCE)
- No single-receiver ambiguity resolution
- Different LEO orbit parametrization (different stochastic orbit parameters)
- 7-day arc for Earth's center-of-mass estimates
- Different observation sampling for ground stations and LEOs (LEO: 10 sec, Stations: 30 sec)

The last point indicates that no GPS clock corrections for the epochs where only LEO-GPS observations have been used have been estimated since this would have resulted in singularities or poorly determined values (too few observations for the parameters). In the present work, the sampling for observations from ground stations and from LEOs is chosen to be equal.

The study carried out by Huang (2022) investigated the impact of adding seven LEOs to a sparse ground station network. The integrated LEO-GPS observations stem from GRACE-A/B, Jason-2/3, and Swarm-A/B/C, whereby zero-difference observables have been used. The orbit characteristics and the number of integrated LEOs were therefore similar to the setup chosen in the present work. The author focused on the quality of the derived orbit solutions for the GPS satellites. The approach was to successfully integrate LEOs into the ground station network and determine the impact in terms of the resulting GPS orbits, whereby orbit comparisons and orbit overlaps at arc boundaries have been used as quality indications. A special focus was put on how the integration of different numbers of LEOs in different orbital planes influences the resulting solution. For the GPS observations from ground stations and LEOs, a data sampling of 300 sec was used. The LEO orbits were modeled by six initial osculating elements, drag parameters (always valid for 5 h), and piecewise constant accelerations valid for 90 min. The conclusion was drawn that the resulting GPS orbits were of superior quality when observations from LEOs were included in the processing of a small ground station network, especially due to the larger number of observations and the additional global coverage with observations. For a sparse ground station network, the resulting GPS orbits improved more when LEOs were integrated compared to additional ground stations integrated (the same number as LEOs) (Huang, 2022). The varying constellation of integrated LEOs allowed for the conclusion that including LEOs in different orbital planes (different orbit inclinations) allows for the largest improvements in the GPS orbits. The observations from the LEOs also have to potential to decrease the effect of outliers resulting from observations from specific ground station observations by providing more redundancy. The main differences between this study and the present investigations are:

- Small ground station network (26/33)
- No single-receiver ambiguity resolution for the LEO-GPS observations
- Ground station coordinates estimates highly constrained

All the studies which were briefly discussed in this section have a similar approach to answering dedicated questions which can be aligned with the key questions which are addressed in the present work. Throughout the sections describing the findings of the performed experiments, whenever possible the results will be compared, whereby it's being attempted to identify the causes for differences, potentially generated by the crucial differences in the approaches.

Recall: The global distribution of ground stations used in this work is not homogeneous, but incorporating GNSS observations from LEO satellites with different orbit characteristics can drastically improve global coverage.

Chapter 3

Theoretical fundamentals

3.1 Least-squares adjustment

A physical model can be verified by performing an adequate experiment. Generally, an experiment includes the observation of specific parameters in a system. To determine whether the performed observations are explained by the model, the a priori unknown parameters have to be determined. A well-known mathematical approach for this estimation is the method of least-squares, developed by Carl Friedrich Gauss (Gauss, 1809). The procedure consists of the definition of a functional model $\mathbf{f}(\mathbf{x})$, which shall describe subsequently the linear relationship between the observations $\mathbf{l}$ and the parameters $\mathbf{x}$ in the way that

$$\mathbf{l} = \mathbf{f}(\mathbf{x}) + \mathbf{e} = \mathbf{A}\mathbf{x} + \mathbf{e} \tag{3.1}$$

whereby the term $\mathbf{e}$ describes the residuals, and a stochastic model

$$\mathbf{C}_{\mathbf{ll}} = \sigma_0^2 \mathbf{P}^{-1}. \tag{3.2}$$

Variances and covariances of the observations are described by the stochastic model. $\mathbf{C}_{\mathbf{ll}}$ represents the covariance matrix of the observations, composed by the general variance factor σ_0^2 and the weight matrix $\mathbf{P}$. Detailed information can be found in Koch (1980). Considering the weight matrix $\mathbf{P}$, the least-squares adjustment (LSQA) minimizes the sum of the (weighted) squared residuals by adjusting the parameters $\mathbf{x}$:

$$\mathbf{e}^T \mathbf{P} \mathbf{e} = min \tag{3.3}$$

The weight matrix $\mathbf{P}$ is used to assign the precision of the individual observations, e.g., higher weights to more precise observations. The functional model of a linearized LSQA can mathematically be described by the first design matrix $\mathbf{A}$, indicated in eqn. (3.1). According to equation (3.1), the dimensions of matrix $\mathbf{A}$ are N rows (number of observations) and M columns (number of parameters to be estimated). To carry out an LSQA in a meaningful way $N \geq M$ has to hold true. To obtain $\mathbf{x}$ by fulfilling eqn. (3.3) one uses the normal equation matrix $\mathbf{N}$

$$\mathbf{N} := \mathbf{A}^T \mathbf{P} \mathbf{A} \tag{3.4}$$

together with

$$\mathbf{b} := \mathbf{A}^T \mathbf{P} \mathbf{l} \tag{3.5}$$

to derive the normal equation system (NEQ)

$$\mathbf{N}\mathbf{x} = \mathbf{b}, \tag{3.6}$$

and to solve for $\mathbf{x}$, provided that $\mathbf{N}$ is regular, by

$$\mathbf{x} = \mathbf{N}^{-1}\mathbf{b} = (\mathbf{A}^T \mathbf{P} \mathbf{A})^{-1} \cdot \mathbf{A}^T \mathbf{P} \mathbf{l}. \tag{3.7}$$

Since the system is over-determined (more observations than parameters), not all observations can be described perfectly, and therefore the residuals $\mathbf{e}$ result, which can be computed by

$$\mathbf{e} = \mathbf{l} - \mathbf{A}\mathbf{x}. \tag{3.8}$$

To evaluate the goodness of the adjustment process, the sum of the weighted residual squares can be derived by

$$\Omega := \mathbf{e}^T \mathbf{P} \mathbf{e} \tag{3.9}$$

and computing

$$m_0 = \sqrt{\frac{\Omega}{N - M}} \tag{3.10}$$

also known as the estimated a posteriori Root Mean Square (RMS) error of unit weight. It is of interest to determine the uncertainty (formal errors) of the resulting parameters. This can be addressed by computing the cofactor matrix

$$\mathbf{Q_{xx}} = \mathbf{N}^{-1}. \tag{3.11}$$

The standard deviation (the uncertainty) of parameter i is given by the corresponding diagonal element of $\mathbf{Q_{xx}}$ and m_0 as

$$m_i = \sqrt{q_{ii}} \cdot m_0. \tag{3.12}$$

If more than one unknown parameter is to be determined, then they are potentially correlated. The off-diagonal elements of the matrix $\mathbf{Q_{xx}}$, again multiplied by m_0^2, describe the covariances between the parameter i and k:

$$m_{ik} = q_{ik} \cdot m_0^2 \tag{3.13}$$

Observations and the unknown parameters lead in general to a non-linear equation system (Dahmen and Reusken, 2008). To use the method described, the observation equations have to be linearized by using a Taylor series about the a priori parameter values $\mathbf{x_0}$, truncated after first order (Weisstein, 2004).

$$\mathbf{F}(\mathbf{f}, \mathbf{x_0}) = \mathbf{f}(\mathbf{x_0}) + \frac{\partial \mathbf{f}(\mathbf{x_0})}{\partial \mathbf{x}} (\mathbf{x} - \mathbf{x_0}) \tag{3.14}$$

The design matrix $\mathbf{A}$ is the Jacobian and first design-matrix

$$\mathbf{A} = \begin{pmatrix} \frac{\partial f_1(\mathbf{x_0})}{\partial x_1} & \cdots & \frac{f_1(\mathbf{x_0})}{\partial x_M} \\ \vdots & \ddots & \vdots \\ \frac{\partial f_N(\mathbf{x_0})}{\partial x_1} & \cdots & \frac{f_N(\mathbf{x_0})}{\partial x_M} \end{pmatrix} \tag{3.15}$$

evaluated at the a priori values $\mathbf{x_0}$ for the unknown parameters. Instead of using the observations directly as in eqn. (3.7), one uses the "observed-minus-computed" term

$$\delta \mathbf{l} := \mathbf{l} - \mathbf{f}(\mathbf{x_0}) \tag{3.16}$$

whereby the functional model is evaluated at $\mathbf{x_0}$. Equation (3.7) then transforms to

$$\delta \mathbf{x} = (\mathbf{A}^T \mathbf{P} \mathbf{A})^{-1} \cdot \mathbf{A}^T \mathbf{P} \delta \mathbf{l}. \tag{3.17}$$

Based on the a priori values and corrections, the final estimate for the unknown parameters is computed:

$$\mathbf{x} = \mathbf{x_0} + \delta \mathbf{x} \tag{3.18}$$

Since the non-linear observation equations were represented as truncated Taylor series' it might be that the solution is not yet appropriate, which causes the need for an iterative procedure, by always adding the estimated corrections $\delta \mathbf{x}$ of the unknown parameters to the a priori values $\mathbf{x_0}$, whereby the stopping criterion for the iterations have to be set depending on the conditions of the experimental setup and the quality of the observations.

3.1.1 Constraining of parameters

If a subset of unknown parameters cannot be sufficiently described by the observations it may be of interest to avoid large errors of the estimates for these parameters. It may also be of interest to reduce strong correlations between different parameters. In the LSQA, an approach to address these difficulties is to constrain (some) of the unknown parameters. The procedure is to introduce artificial observations $\mathbf{h}$, so-called pseudo-observations, in addition to the real (authentic) observations. In line with the procedure of the LSQA, the design matrix $\mathbf{H}$ contains the information about the relation between the pseudo-observations and the unknown parameters (Koch, 1999):

$$\mathbf{Hx} = \mathbf{h} \tag{3.19}$$

In analogy to the quadratic weight matrix $\mathbf{P}$ of the authentic observations, the quadratic matrix $\mathbf{W}$, with dimensions $P=$ number of constraining equations (number of rows), is designed (Dach and Walser, 2015):

$$\mathbf{W} = \begin{pmatrix} \frac{\sigma_0^2}{\hat{\sigma}_{11}} & \cdots & \frac{\sigma_0^2}{\hat{\sigma}_{1M}} \\ \vdots & \ddots & \vdots \\ \frac{\sigma_0^2}{\hat{\sigma}_{P1}} & \cdots & \frac{\sigma_0^2}{\hat{\sigma}_{PM}} \end{pmatrix} \tag{3.20}$$

The elements of this matrix $\hat{\sigma}_{ik}$ are the a priori variances of the constraining equations. Including this information in the parameter estimation process, a constrained normal equation system is created. The normal equation matrix $\hat{\mathbf{N}}$

$$\hat{\mathbf{N}} := \mathbf{A}^T\mathbf{PA} + \mathbf{H}^T\mathbf{WH} = \mathbf{N} + \mathbf{H}^T\mathbf{WH} \tag{3.21}$$

together with $\hat{\mathbf{b}}$

$$\hat{\mathbf{b}} := \mathbf{A}^T\mathbf{Pl} + \mathbf{H}^T\mathbf{Wh} = \mathbf{b} + \mathbf{H}^T\mathbf{Wh} \tag{3.22}$$

is used to find the constrained solution for the unknown parameters $\hat{\mathbf{x}}$

$$\hat{\mathbf{x}} = \hat{\mathbf{N}}^{-1}\hat{\mathbf{b}}. \tag{3.23}$$

3.1.2 Absolute and relative constraining

Certain specific parameters are needed to be constrained to their a priori values (Dach and Walser, 2015). For this purpose, the parameter improvement in a non-linear least-squares adjustment is constrained to zero, which is called an absolute constraint. This can be achieved by adding the pseudo-observation

$$h = 0 \tag{3.24}$$

to the system. In some practical applications, it may also be of interest to constrain the improvements of two parameters with respect to each other (Dach and Walser, 2015). Such a relative constraint can be achieved by adding the pseudo-observation

$$h = x_i - x_j = 0 \tag{3.25}$$

to the system. To elucidate the absolute and relative constraining of parameters an example is given, in which three parameters ($\mathbf{x_e} = (x_1, x_2, x_3)$) are to be constrained:

$$\mathbf{H_e} = \begin{pmatrix} 0 & 1 & 0 \\ 1 & 0 & -1 \end{pmatrix}, \mathbf{h_e} = \begin{pmatrix} 0 \\ 0 \end{pmatrix}$$

$$\mathbf{H_e x_e} = \begin{pmatrix} 0 & 1 & 0 \\ 1 & 0 & -1 \end{pmatrix} \cdot \begin{pmatrix} x_1 \\ x_2 \\ x_3 \end{pmatrix} = \begin{pmatrix} 0 \\ 0 \end{pmatrix} = \mathbf{h_e}$$

$$\begin{pmatrix} x_2 \\ x_1 - x_3 \end{pmatrix} = \begin{pmatrix} 0 \\ 0 \end{pmatrix}$$

In this example for x_2 an absolute constraint is applied and for x_1 and x_3 a relative constraint is used.

3.1.3 Free-network constraints

The free-network constraint method explained in this section follows the descriptions given by Thaller (2008). It offers the opportunity to align the estimated network solution with a predefined reference frame. This alignment is achieved through the use of a Helmert transformation, which characterizes the relationship between the network solution derived from observations and the coordinates of the a priori reference network. Specifically, the Helmert transformation is formulated for each station, denoted by the index i, within the network. This transformation involves the coordinate estimates, $\mathbf{X_i} = (X, Y, Z)$, and the reference coordinates, $\mathbf{X_{i_0}} = (X_0, Y_0, Z_0)$:

$$\begin{pmatrix} X \\ Y \\ Z \end{pmatrix} = (1+\mu) \cdot \begin{pmatrix} 1 & \gamma & -\beta \\ -\gamma & 1 & \alpha \\ \beta & -\alpha & 1 \end{pmatrix} \cdot \begin{pmatrix} X_0 \\ Y_0 \\ Z_0 \end{pmatrix} + \begin{pmatrix} T_X \\ T_Y \\ T_Z \end{pmatrix} \tag{3.26}$$

Here, the parameters describe translations in the X, Y, and Z directions (T_X, T_Y, T_Z), rotations around the X, Y, and Z axes approximated by small angles (α, β, γ), and a scaling factor $(1+\mu)$. By rearranging variables and assuming small values for the transformation parameters, the equation simplifies to:

$$\begin{pmatrix} X \\ Y \\ Z \end{pmatrix} = \begin{pmatrix} X_0 \\ Y_0 \\ Z_0 \end{pmatrix} + \begin{pmatrix} 1 & 0 & 0 & 0 & -Z_0 & Y_0 & X_0 \\ 0 & 1 & 0 & Z_0 & 0 & -X_0 & Y_0 \\ 0 & 0 & 1 & -Y_0 & X_0 & 0 & Z_0 \end{pmatrix} \cdot \begin{pmatrix} T_X \\ T_Y \\ T_Z \\ \alpha \\ \beta \\ \gamma \\ \mu \end{pmatrix} \tag{3.27}$$

In matrix notation for station i, this transformation is expressed as:

$$\mathbf{X_i} = \mathbf{X_{i_0}} + \mathbf{B_i} \cdot \boldsymbol{\zeta} \tag{3.28}$$

To account for all stations (in total n_{sta}) contributing to the free-network constraint, the expression is organized as follows:

$$\mathbf{X} = \begin{pmatrix} \mathbf{X_1} \\ \mathbf{X_2} \\ \vdots \\ \mathbf{X_{n_{sta}}} \end{pmatrix}, \mathbf{X_0} = \begin{pmatrix} \mathbf{X_{1_0}} \\ \mathbf{X_{2_0}} \\ \vdots \\ \mathbf{X_{n_{sta_0}}} \end{pmatrix}, \mathbf{B} = \begin{pmatrix} \mathbf{B_1} \\ \mathbf{B_2} \\ \vdots \\ \mathbf{B_{n_{sta}}} \end{pmatrix} \tag{3.29}$$

The fundamental residual equation for solving for the Helmert parameters, denoted as $\boldsymbol{\zeta}$, is expressed as:

$$\mathbf{e} = \mathbf{B} \cdot \boldsymbol{\zeta} - (\mathbf{X} - \mathbf{X_0}) = \mathbf{B} \cdot \boldsymbol{\zeta} - \hat{\mathbf{x}} \tag{3.30}$$

Thus, the Helmert parameters are determined by:

$$\boldsymbol{\zeta} = (\mathbf{B^T} \cdot \mathbf{B})^{-1} \cdot \mathbf{B^T} \cdot \hat{\mathbf{x}} \tag{3.31}$$

The free-network constraint itself is established based on the last equation by setting certain Helmert parameters to zero. This requirement leads to the observation equation for the free-network constraint:

$$\boldsymbol{\zeta} = (\mathbf{B^T} \cdot \mathbf{B})^{-1} \cdot \mathbf{B^T} \cdot \hat{\mathbf{x}} = \mathbf{0} \tag{3.32}$$

Comparing this equation with the general equation for constraints, it becomes evident that $\mathbf{h} = \mathbf{0}$, and the Jacobian matrix $\mathbf{H}$ is determined as:

$$\mathbf{H} = (\mathbf{B^T} \cdot \mathbf{B})^{-1} \cdot \mathbf{B^T} \tag{3.33}$$

For free-network constraints, the weight matrix $\mathbf{W}$ is constructed using the variances of the individual transformation parameters. Finally, the system of normal equations that incorporates free-network constraints takes the form:

$$(\mathbf{A^T P A} + \mathbf{H^T W H}) \cdot \hat{\mathbf{x}} = \mathbf{A^T P l} \tag{3.34}$$

Compared to absolute constraints on station coordinates, the application of free-network constraints offers the advantage that the network itself remains undistorted, provided that only datum defects (e.g., rotations, translations, and scale) are constrained. When only Helmert parameters corresponding to the network's degree of freedom are constrained, they are referred to as minimum constraints. Constraints involving only the three rotations are termed as the no-net-rotation (NNR) condition. Similarly, constraining only the three translations results in the no-net-translation (NNT) constraint, while a no-net-scale (NNS) condition constrains only the scaling factor.

3.1.4 Zero-mean condition

Apart from an absolute or relative constraint of parameters, a zero-mean condition can be introduced, which is always applied to a group of unknown parameters (x_i,...,x_k). The needed additional pseudo-observations are designed the way that the sum of the estimated corrections of this group of parameters is zero, and therefore also the mean:

$$\sum_{n=i}^{k} x_n = 0 \tag{3.35}$$

Mathematically it is also possible to fix (delete) specific parameters in the normal equation system (Cordelli et al., 2017). Whenever the a priori parameters are to be retained as estimates or if the computational effort should be minimized, this can be useful.

3.1.5 Parameter pre-elimination

In the normal equation system, certain parameters may also be pre-eliminated without losing their information, in order to reduce the computational effort. To formulate this procedure mathematically, the NEQ is represented as follows:

$$\begin{pmatrix} \mathbf{N_{ab}} & \mathbf{N_{ba}}^T \\ \mathbf{N_{ba}} & \mathbf{N_{bb}} \end{pmatrix} \begin{pmatrix} \mathbf{x_a} \\ \mathbf{x_b} \end{pmatrix} = \begin{pmatrix} \mathbf{b_a} \\ \mathbf{b_b} \end{pmatrix} \tag{3.36}$$

The NEQ is subdivided such that the parameters to be pre-eliminated ($\mathbf{x_b}$) are "at the end" of the parameter vector $\mathbf{x}$ (Dach and Walser, 2015). This equation system's second row equals

$$\mathbf{N_{ba}x_a} + \mathbf{N_{bb}x_b} = \mathbf{b_b} \tag{3.37}$$

and can be transformed to

$$\mathbf{x_b} = \mathbf{N_{bb}}^{-1}(\mathbf{b_b} - \mathbf{N_{ba}x_a}), \tag{3.38}$$

provided that $\mathbf{N_{bb}}$ is regular. Equation (3.36) can be reformulated by substitution of the to-be pre-eliminated parameters $\mathbf{x_b}$ from eqn. (3.38):

$$\begin{pmatrix} \mathbf{N_{aa}} & \mathbf{N_{ba}}^T \\ \mathbf{N_{ba}} & \mathbf{N_{bb}} \end{pmatrix} \begin{pmatrix} \mathbf{x_a} \\ \mathbf{N_{bb}}^{-1}(\mathbf{b_b} - \mathbf{N_{ba}x_a}) \end{pmatrix} = \begin{pmatrix} \mathbf{b_a} \\ \mathbf{b_b} \end{pmatrix} \tag{3.39}$$

The manipulated normal equation system can be solved for the unknown parameters $\mathbf{x_a}$:

$$\begin{aligned} \mathbf{N_{aa}x_a} + \mathbf{N_{ba}}^T(\mathbf{N_{bb}}^{-1}(\mathbf{b_b} - \mathbf{N_{ba}x_a})) &= \mathbf{b_a} \\ \mathbf{N_{aa}x_a} + \mathbf{N_{ba}}^T\mathbf{N_{bb}}^{-1}\mathbf{b_b} - \mathbf{N_{ba}}^T\mathbf{N_{bb}}^{-1}\mathbf{N_{ba}x_a} &= \mathbf{b_a} \\ (\mathbf{N_{aa}} - \mathbf{N_{ba}}^T\mathbf{N_{bb}}^{-1}\mathbf{N_{ba}})\mathbf{x_a} &= \mathbf{b_a} - \mathbf{N_{ba}}^T\mathbf{N_{bb}}^{-1}\mathbf{b_b} \\ (\mathbf{N_{aa}} - \mathbf{N_{ba}}^T\mathbf{N_{bb}}^{-1}\mathbf{N_{ba}})^{-1}(\mathbf{b_a} - \mathbf{N_{ba}}^T\mathbf{N_{bb}}^{-1}\mathbf{b_b}) &= \mathbf{x_a} \end{aligned} \tag{3.40}$$

The derivation of the pre-elimination already reveals that no information can get lost, the resulting parameter estimates $\mathbf{x_a}$ are identical as without pre-eliminating the parameters $\mathbf{x_b}$, but to solve for the parameters $\mathbf{x_b}$ a re-substitution is necessary. If constraints are applied to the parameters to be pre-eliminated, they remain implicitly in the resulting NEQ.

3.1.6 Normal equation system stacking

The derivation of the least-squares adjustment was based so far on the creation of one normal equation system for all observations to be included. As soon as the numbers of the unknown parameters and the observations become large, it is of interest to perform a sequential least-squares adjustment. The procedure is to create separate NEQs for different observation (and parameter) blocks (i,...,k), whereby $\mathbf{l}$, $\mathbf{A}$ and $\mathbf{P}$ can be written as

$$\mathbf{l} = \begin{pmatrix} \mathbf{l_1} \\ \vdots \\ \mathbf{l_k} \end{pmatrix}, \mathbf{A} = \begin{pmatrix} \mathbf{A_1} \\ \vdots \\ \mathbf{A_k} \end{pmatrix}, \mathbf{P} = \begin{pmatrix} \mathbf{P_1} & & \mathbf{0} \\ & \ddots & \\ \mathbf{0} & & \mathbf{P_k} \end{pmatrix}. \tag{3.41}$$

For each observation block j the contribution to the full normal equation system can be derived by computing the corresponding normal equation matrix

$$\mathbf{N_j} = \mathbf{A_j}^T \mathbf{P_j} \mathbf{A_j} \tag{3.42}$$

and the right-hand side vector

$$\mathbf{b_j} = \mathbf{A_j}^T \mathbf{P_j} \mathbf{l_j}. \tag{3.43}$$

The representation of matrix $\mathbf{P}$ in eqn. (3.41) indicates that in the aforementioned approach, it is assumed that the observations from different blocks are uncorrelated. The solution of the parameters from the (stacked) normal equation system is obtained by computing

$$\mathbf{x} = \left(\sum_{j=i}^{k} \mathbf{N_j} \right)^{-1} \cdot \sum_{j=i}^{k} \mathbf{b_j}. \tag{3.44}$$

In real physical experimental setups, it may be the case that some of the unknown parameters are only observed by one of the observation blocks ($\mathbf{x_u}$, u=unique), while others are common parameters ($\mathbf{x_c}$). In this case, the approach is to sort each of the individual normal equation system parameter lists $\mathbf{x_j}$ for these two types:

$$\mathbf{x_j} = \begin{pmatrix} \mathbf{x_c} \\ \mathbf{x_{u_j}} \end{pmatrix} \tag{3.45}$$

In the case of two sets of observation blocks (or NEQs) (indicated by the subscripts *1* and *2*), the two normal equation systems are:

$$\begin{pmatrix} \mathbf{N_{1_{cc}}} & \mathbf{N_{1_{cu_1}}} \\ \mathbf{N_{1_{cu_1}}}^T & \mathbf{N_{1_{u_1u_1}}} \end{pmatrix} \begin{pmatrix} \mathbf{x_c} \\ \mathbf{x_{u_1}} \end{pmatrix} = \begin{pmatrix} \mathbf{b_{1_c}} \\ \mathbf{b_{1_{u_1}}} \end{pmatrix} \tag{3.46}$$

and

$$\begin{pmatrix} \mathbf{N_{2_{cc}}} & \mathbf{N_{2_{cu_2}}} \\ \mathbf{N_{2_{cu_2}}}^T & \mathbf{N_{2_{u_2u_2}}} \end{pmatrix} \begin{pmatrix} \mathbf{x_c} \\ \mathbf{x_{u_2}} \end{pmatrix} = \begin{pmatrix} \mathbf{b_{2_c}} \\ \mathbf{b_{2_{u_2}}} \end{pmatrix}. \tag{3.47}$$

The stacking of these individual NEQs results to

$$\begin{pmatrix} \mathbf{N_{1_{cc}}} + \mathbf{N_{2_{cc}}} & \mathbf{N_{1_{cu_1}}} & \mathbf{N_{2_{cu_2}}} \\ \mathbf{N_{1_{cu_1}}}^T & \mathbf{N_{1_{u_1u_1}}} & 0 \\ \mathbf{N_{2_{cu_2}}}^T & 0 & \mathbf{N_{2_{u_2u_2}}} \end{pmatrix} \begin{pmatrix} \mathbf{x_c} \\ \mathbf{x_{u_1}} \\ \mathbf{x_{u_2}} \end{pmatrix} = \begin{pmatrix} \mathbf{b_{1_c}} + \mathbf{b_{2_c}} \\ \mathbf{b_{1_{u_1}}} \\ \mathbf{b_{2_{u_2}}} \end{pmatrix}. \tag{3.48}$$

As evident from comparing eqns. (3.46) and (3.47) to eqn. (3.48), the resulting stacked systems dimensions have to be adapted. Very important to note is that such a superposition of parameters stemming from different observation blocks is only valid, if the a priori information, namely $\mathbf{x_{0_c}}$, is identical in all included individual NEQs. Otherwise, blocks with erroneous a priori information may introduce systematic biases into the stacked system. This can affect the overall quality and reliability of the final solution. Detailed information about NEQ manipulations, e.g. transformation of a priori values, is described in Brockmann (1997).

3.2 Orbit determination

The determination of a satellite's trajectory is a challenging task, which has been investigated and improved for many decades. In theory, if one knows all forces ($\mathbf{F_i}$) acting on a satellite with mass m, the motion can be derived via Newton's second law

$$\sum_i \mathbf{F_i} = m\ddot{\mathbf{r}}, \tag{3.49}$$

whereby $\ddot{\mathbf{r}}$ describes the acceleration of the satellite. The trajectory, called orbit solution hereafter, can be described by the equation of motion

$$\ddot{\mathbf{r}}(t) = \mathbf{f}(t, \mathbf{r}, \dot{\mathbf{r}}), \tag{3.50}$$

where $\mathbf{f}$ describes all forces acting on the satellite. If a satellite is in a Keplerian orbit around the Earth (central body with mass M), where only two objects with point masses are taken into account and numerous effects, including gravitational interactions with other objects, atmospheric drag, solar radiation pressure, and relativistic effects, are ignored, the equation of motion is represented by

$$\ddot{\mathbf{r}}(t) = -\frac{G(M+m)\mathbf{r}}{r^3} \tag{3.51}$$

with G being the gravitational constant, $\mathbf{r}$ the geocentric position vector of the satellite, and $r = |\mathbf{r}|$. The orbit solution (position and velocity)

$$\begin{aligned} \mathbf{r}(t) &= \mathbf{r}(t, a, e, i, \Omega, \omega, u_0) \\ \dot{\mathbf{r}}(t) &= \dot{\mathbf{r}}(t, a, e, i, \Omega, \omega, u_0) \end{aligned} \tag{3.52}$$

can be described by six initial osculating elements:

- a The semi-major axis is defined as the sum of the periapsis and apoapsis distance divided by two.
- e The eccentricity describes the shape of the orbit.
- i The inclination describes the tilt of the orbital plane with respect to the reference (equatorial) plane.
- Ω The right ascension of the ascending node is the angle between the reference direction and the point where the orbit passes the reference plane from south to north.
- ω The argument of perigee is defined to be the angle between the nodal line and the point of the orbital plane where the satellite is closest to the Earth.
- u_0 The argument of latitude describes the angle between the position of the satellite at a specific epoch t_0 and the nodal line.

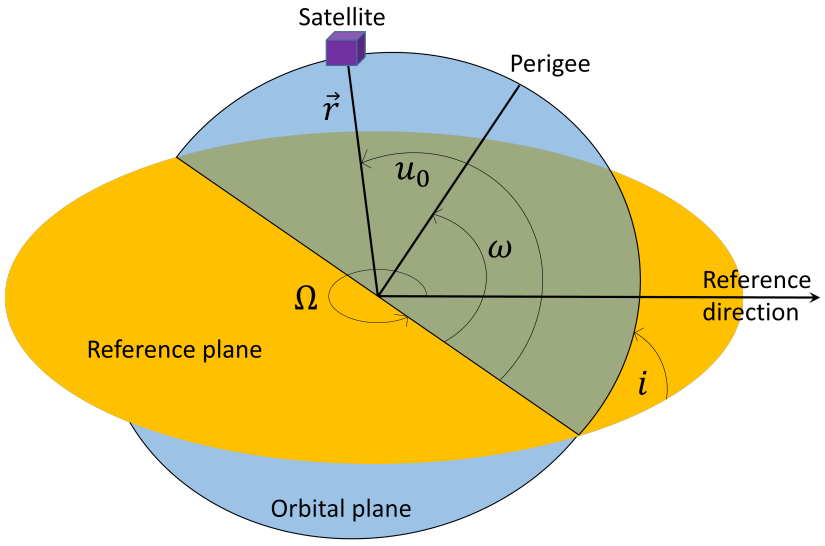

Figure 3.1: The initial osculating elements

3.2.1 Observation equations

As a prelude to describing the different types of orbit representations, it is important to state the GNSS observation equations that result from the various observation types, as well as the linear combinations of these equations that are used for POD. The following information is extracted from Jäggi and Arnold (2017).

3.2.1.1 Code measurements

In this section, it is decisive that information stemming from the GNSS signal emitter (indicated by superscript k) and the receiver (indicated by subscript i) are distinguished. The formulation of the observation equation using code measurements is eventually given by

$$P_i^k = c(T_i - T^k) = \rho_i^k + c(\Delta t_i - \Delta t^k) + \Delta\rho_{i,trop}^k + \Delta\rho_{i,ion}^k + \tilde{\epsilon}_i^k. \tag{3.53}$$

Quantities included are:

P_i^k	=	Code pseudo-range observation
c	=	Speed of light
T_i	=	Observation time of the signal at the receiver, measured by its clock
T^k	=	Transmission time of the signal at the emitter, measured by its clock
ρ_i^k	=	Geometric distance between emitter and receiver
Δt_i	=	Clock offset of the receiver with respect to GPS time
Δt^k	=	Clock offset of the emitter with respect to GPS time
$\Delta\rho_{i,trop}^k$	=	Signal delay due to tropospheric refraction
$\Delta\rho_{i,ion}^k$	=	Signal delay due to ionospheric dispersion
$\tilde{\epsilon}_i^k$	=	Residual

It is important to note here, that for the computation of ρ_i^k also the relativistic effects have to be taken into account.

3.2.1.2 Phase measurements

Along with the code observations, also for the phase measurements, the observation equation can be stated:

$$L_i^k = \lambda(\phi_i - \phi^k + N_i^k) = \rho_i^k + c(\Delta t_i - \Delta t^k) + \Delta\rho_{i,trop}^k - \Delta\rho_{i,ion}^k + \lambda \cdot B_i^k + \epsilon_i^k, \tag{3.54}$$

whereby the quantities are:

L_i^k	=	Phase observation
λ	=	Wavelength of the signal
ϕ	=	Carrier phase of the signal
N_i^k	=	Constant initial phase ambiguity
B_i^k	=	Constant bias related to the initial phase ambiguity
ϵ_i^k	=	Residual

When comparing eqn. (3.53) and eqn. (3.54) it is evident that the signal delay due to ionospheric dispersion has an opposite sign. The major difference between the code and phase observation equations is the additional B_i^k-term which is the sum of:

- N_i^k being the initial phase ambiguity
- Emitter-specific hardware delay
- Receiver-specific hardware delay

Any time the receiver starts tracking an incoming signal, particularly when regaining after losing the lock of a signal, a new ambiguity term N_i^k must be set up. Given the nature of the observations, namely that phase measurements are defined by numbers of wave cycles and code measurements are based on the time taken for the signal to travel, whereby phase measurements have higher precision compared to code measurements, different noise levels result. The drawback of phase measurements is that the sensitivity is much higher for signal interruptions and multipath propagation. This leads to a higher noise level for phase measurements.

3.2.1.3 Linear combinations of observations

Equations (3.53) and (3.54) indicate that it may be useful to generate information from the received signal, which allows the elimination of certain terms. Since the received phase and code observations are available on (at least) two frequencies a combination of two observables (*1* and *2*) can be carried out. In the following, the two linear combinations (LC) are presented which are used in this work. The ionosphere-free LC, L_3, is derived by using the phase measurements L_1 and L_2 collected on the frequencies f_1 and f_2:

$$L_3 = \frac{1}{f_1^2 - f_2^2}(f_1^2 L_1 - f_2^2 L_2) \tag{3.55}$$

The use of this LC results in the elimination of the first order of ionospheric signal advance for phase measurements. This LC can also be formed from code observations:

$$P_3 = \frac{1}{f_1^2 - f_2^2}(f_1^2 P_1 - f_2^2 P_2) \tag{3.56}$$

The corresponding (narrow-lane) wavelength λ_3 can be derived by computing

$$\lambda_3 = \frac{c}{f_1 + f_2} \tag{3.57}$$

In the case of phase measurements, the observation equation reads as:

$$L_i^k = \rho_i^k + c(\Delta t_i - \Delta t^k) + \Delta\rho_{i,trop}^k + \lambda \cdot B_i^k + \epsilon_i^k \tag{3.58}$$

The observation equation for the code measurements can be formed analogously. In L_3 the two measurement types code and phase are not mixed, whereby the Melbourne-Wübbena LC, L_6, described by Melbourne (1985) and Wubbena (1985) is a combination of code and phase measurements:

$$L_6 = \frac{1}{f_1 - f_2}(f_1 L_1 - f_2 L_2) - \frac{1}{f_1 + f_2}(f_1 P_1 + f_2 P_2) \tag{3.59}$$

with the corresponding (wide-lane) wavelength

$$\lambda_6 = \frac{c}{f_1 - f_2}. \tag{3.60}$$

When this LC is formed, the signal delay due to ionospheric dispersion $\Delta\rho_{i,ion}^k$, the signal delay due to tropospheric refraction $\Delta\rho_{i,trop}^k$, the clock offsets Δt and the geometric distance ρ_i^k are eliminated. This results in the observation equation

$$L_{6_i}^k = \lambda_6 \cdot B_i^k + \epsilon_i^k. \tag{3.61}$$

It is evident from the equation (3.61) that the Melbourne-Wübbena LC is well-suited for solving (wide-lane) ambiguities.

3.2.2 Single-receiver integer ambiguity resolution

The observation equation for phase measurements (3.54) includes the unknown term B_i^k, which consists, among others, of N_i^k. The determination of N_i^k, being the initial phase ambiguity, plays an important role in the process of the precise orbit determination of a LEO. This process is referred to as integer ambiguity resolution or ambiguity-fixing. By applying this resolution, ambiguity-fixed solutions are computed instead of so-called ambiguity-float solutions. To describe the procedure, the observation equation (3.54) is rewritten to be

$$L_i^k = (\rho_i^k + \theta_i^k) + c(\Delta t_i - \Delta t^k) - \Delta\rho_{i,ion}^k + c(\xi_i - \xi^k) + \lambda \cdot N_i^k + \lambda \cdot \omega_i^k + \epsilon_i^k. \tag{3.62}$$

Along with (3.62) the observation equation for code measurements is also restated as follows:

$$P_i^k = (\rho_i^k + \eta_i^k) + c(\Delta t_i - \Delta t^k) + \Delta\rho_{i,ion}^k + c(\zeta_i - \zeta^k), + \epsilon_i^k, \tag{3.63}$$

whereby the newly appearing terms are:

θ_i^k, η_i^k = Sum of phase center offset and variations of emitter and receiver (see sect. 3.4)
ξ_i^k, ζ_i^k = Signal specific range biases related to emitter and receiver
ω_i^k = Phase windup effect (see Montenbruck et al. (2018a))

It is assumed, that the signal-specific range biases related to the emitter and the receiver are independent of each other and can therefore be split. Using this notation, and taking into account that a signal delay due to tropospheric refraction is not present when the signal propagates from a GNSS satellite to a LEO satellite, the L_3 LC for phase observations can be written as

$$L_i^k = (\rho_i^k + \theta_i^k) + c(\Delta t_i - \Delta t^k) + c(\xi_{i,L_3} - \xi_{L_3}^k) + \lambda_3(N_i^k + \frac{\lambda_6}{\lambda_2} N_{i,WL}^k) + \lambda_3 \cdot \omega_i^k + \epsilon_i^k. \tag{3.64}$$

In eqn. (3.64) the ambiguities (NL = narrow-lane, WL = wide-lane) are now separated from the signal-specific range biases. When the Melbourne-Wübbena LC is formed, the observable is a function of only the wide-lane ambiguity, the signal-specific range biases, and the phase center offsets and variations of emitter and receiver:

$$L_6 = \lambda_6 N_{i,WL}^k + L_6(\eta_i^k, \theta_i^k) + c \cdot L_6(\xi_i, \zeta_i) - c \cdot L_6(\xi^k, \zeta^k) + \epsilon_i^k \tag{3.65}$$

Let's now assume that the phase center offset and variations of emitter and receiver are known from external sources. If additionally, the signal-specific range biases are known for every observation type and emitter/receiver, eqn. (3.65) allows the estimation of the WL ambiguities. Introducing them to eqn. (3.64) yields the process of ambiguity resolution. Throughout this work single-receiver ambiguity resolution has to be performed which demands the consideration of single-difference ambiguities between pairs of satellites, which allows for the elimination of the receiver bias terms. The observation equations have to be reformulated accordingly for equivalent single differences (see Schaer et al., 2021). The determination of signal-specific range biases, also known as observable specific biases (OSB), is a highly sophisticated process, e.g., carried out by CODE. The reader is referred to Villiger et al. (2019) and Schaer et al. (2021) for a detailed explanation of the generation and properties of OSB products generated by CODE.

3.2.3 Orbit representations

An explanation of the different orbit representations used to describe LEO trajectories is given in this section. The content and the structure shown in this section follow the detailed explanations given in Jäggi and Arnold (2017). In eqn. (3.53) the geometric distance between emitter and receiver ρ_i^k has been introduced. This term describes the geometric relation between the emitter (GNSS satellite k) at signal emission time and the receiver (LEO satellite leo) at signal reception time. Strictly speaking, the quantity refers to the phase center position of the emitter of the GNSS satellite and the phase center position of the receiving antenna onboard the LEO.

$$\rho_{leo}^k = |\mathbf{r}_{leo}(t_{leo}) - \mathbf{r}^k(t_{leo} - \tau_{leo}^k)| \tag{3.66}$$

The quantities describe:

$\mathbf{r}_{leo}$ = Position of the antenna phase center of LEO in the inertial system
t_{leo} = Receiving time (in GPS time)
$\mathbf{r}^k$ = Position of the phase center of the GNSS satellite k
τ_{leo}^k = Signal propagation time between the two phase centers

To understand the different orbit representations it is important to define the different reference systems which are used in practical applications in the field of geodesy and specifically in satellite POD. The Earth-fixed system, namely the International Terrestrial Reference System (ITRS) is a reference system whose origin is defined to be at the center-of-mass of the Earth (Petit et al., 2010). A realization of the ITRS is the International Terrestrial Reference Frame (ITRF) (Altamimi et al., 2011, which is based on observations performed from globally distributed ground stations. In this system, the coordinates of a point on the Earth in relation to a reference point on the Earth remain constant. In satellite POD this system refers to a specific point on the Earth, whereby the motion of the satellite relative to this point is described. In contrast, an inertial system moves relative to a fixed background in the sky. In an inertial system, the

motion of a satellite remains constant if it is not influenced by an external force. Therefore, an inertial system is independent of the movement of the Earth.

3.2.3.1 Kinematic orbit representation

The kinematic orbit representation describes the trajectory at discrete measurement epochs by three Cartesian coordinates. The positions are derived using only pure geometric information stemming from the GNSS observations, whereby the inertial phase center position of the LEO's receiver antenna is given by

$$\mathbf{r}_{leo}(t_{leo}) = \mathbf{R}(t_{leo}) \cdot (\mathbf{r}_{leo,e,0}(t_{leo}; x_1, y_1, z_1, ..., x_n, y_n, z_n) + \delta\mathbf{r}_{leo,e,ant}(t_{leo})), \tag{3.67}$$

whereby

$\mathbf{R}$	=	Transformation matrix from Earth-fixed to inertial frame
$\mathbf{r}_{leo,e,0}$	=	LEO center-of-mass position in Earth-fixed frame
$\delta\mathbf{r}_{leo,e,ant}$	=	Vector $\mathbf{r}_{leo,e,0} \rightarrow$ antenna phase center in Earth-fixed frame
x_i, y_i, z_i	=	Kinematic coordinates of LEO at epoch t_{leo} in Earth-fixed frame

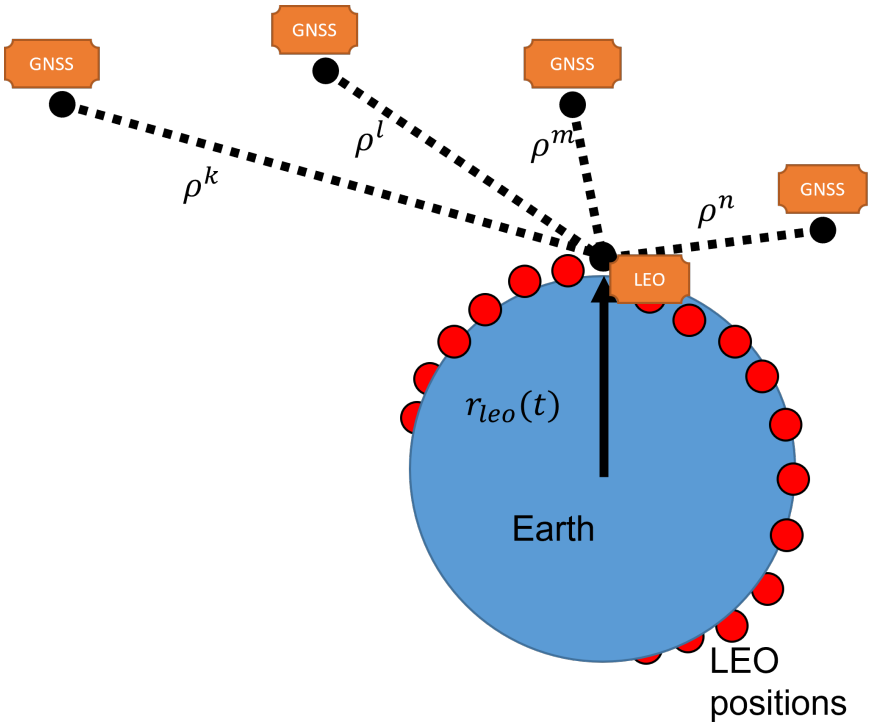

Figure 3.2: Kinematic orbit representation

Figure 3.2 illustrates the basic principle of a kinematic orbit representation, where the positions are estimated for each measurement epoch. Due to the small degree of freedom, outliers can significantly affect the results. A kinematic orbit solution solely relies on observations and is independent of the LEO orbital dynamics causing the resulting positions to be very sensitive to bad GNSS data and erroneous information of satellite-specific properties, e.g., the vector pointing from center-of-mass to antenna phase center ($\delta\mathbf{r}_{leo,e,ant}$).

3.2.3.2 Dynamic orbit representation

In contrast to the kinematic orbit representation, the dynamic orbit representation fully depends on the force models used. It is the physical description of the trajectory of the LEO. The inertial phase center position of the LEO's receiver antenna is given by

$$\mathbf{r}_{leo}(t_{leo}) = \mathbf{r}_{leo,0}(t_{leo}; a, e, i, \Omega, \omega, u_0; Q_1, ..., Q_d) + \delta\mathbf{r}_{leo,ant}(t_{leo}), \tag{3.68}$$

whereby the quantities are

$\mathbf{r}_{leo,0}$	=	LEO center-of-mass position in inertial frame
$\delta\mathbf{r}_{leo,ant}$	=	Vector pointing from the LEO center-of-mass to the antenna phase center in the inertial frame
$a, e, i, \Omega, \omega, u_0$	=	Initial osculating elements
$Q_1, ..., Q_d$	=	Dynamical parameters (e.g., scaling factors)

The orbit trajectory can be derived by solving the equation of motion

$$\ddot{\mathbf{r}} = -GM\frac{\mathbf{r}}{r^3} + \mathbf{f_p}(t, \mathbf{r}, \dot{\mathbf{r}}, Q_1, ..., Q_d) \tag{3.69}$$

by numerical integration techniques (Beutler, 2005) with $\mathbf{f_p}$ being the accelerations due to perturbing forces which act on the satellite. The initial conditions for the position and velocity at the reference epoch t_0 may be expressed as

$$\begin{aligned} \mathbf{r}(t_0) &= \mathbf{r}(t_0; a, e, i, \Omega, \omega, u_0) \\ \dot{\mathbf{r}}(t_0) &= \dot{\mathbf{r}}(t_0; a, e, i, \Omega, \omega, u_0) \end{aligned} \tag{3.70}$$

where one set of initial orbital elements is estimated per orbital arc. Equation (3.70) goes in line with eqn. (3.51). Since in reality the celestial bodies, in our application the Earth, are not point masses and apart from gravitational forces also non-gravitational forces act on the satellite, the trajectory cannot be described by a Keplerian orbit. Especially the inhomogeneous mass distribution of the Earth leads to a significant perturbation. Since some LEOs are orbiting the Earth at low orbital altitudes where the atmosphere is noticeable also air drag becomes important. Other important perturbation forces result from solar radiation pressure, Earth radiation pressure, and attraction by other celestial bodies. The additional term $\mathbf{f_p}$ consists of all these gravitational and non-gravitational forces acting on the satellite. Also empirical accelerations $Q_q, ..., Q_d$ may appear in the equation of motion. More details about the modeling of selected non-gravitational forces are given in sect. 3.3.

3.2.3.3 Reduced-dynamic orbit representation

The dynamic orbit representation approach fully depends on the underlying force models. These force models, however, never perfectly reflect the real physical conditions. Additionally, it is an almost impossible task to include all existing forces acting on a satellite. These circumstances demand an approach where mismodeled or not explicitly modeled forces can be compensated. The reduced-dynamic orbit representation approach addresses these problems by including a set of additional (pseudo-stochastic) parameters $(P_1, ..., P_s)$. The equation of motion to be solved is adapted to be

$$\ddot{\mathbf{r}} = -GM\frac{\mathbf{r}}{r^3} + \mathbf{f_p}(t, \mathbf{r}, \dot{\mathbf{r}}, Q_1, ..., Q_d, P_1, ..., P_s). \tag{3.71}$$

The parameters $P_1, ..., P_s$ can be setup in the Bernese GNSS Software (Dach and Walser, 2015) as follows:

- Instantaneous velocity changes, so-called pulses, in three spatial directions, which are applied at certain epochs
- Piecewise constant accelerations, in three spatial directions, which are applied over intervals with a specified length

In a reduced-dynamic orbit representation, piecewise constant accelerations ensure an orbit that is continuous and differentiable at any time and are therefore well suited for an orbit estimation process. These additional parameters are co-estimated along with the dynamic orbit parameters. Pseudo-stochastic refers to a system's apparent randomness that is not caused by real randomness but rather by complex interactions and dependencies. In the POD process, unpredictability may occur, which can be controlled deterministically. For further information, the reader is referred to Jäggi (2007).

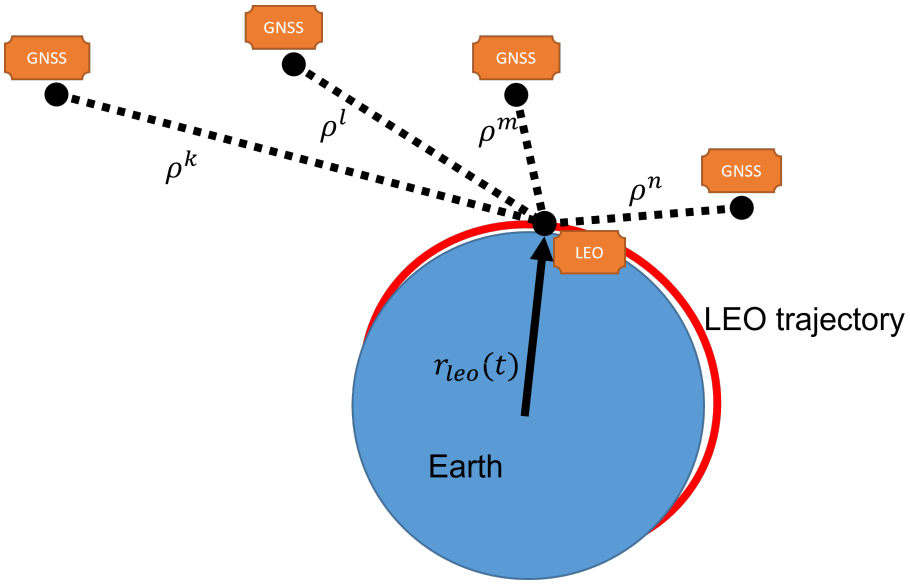

Figure 3.3: Reduced-dynamic orbit representation

While reduced-dynamic orbits still heavily depend on the force models used (Jäggi et al., 2008), their strength can be reduced by the additional pseudo-stochastic parameters, allowing for a close following of the orbit to the observations (see illustration 3.3). Therefore, the reduced-dynamic approach is widely used and allows for the computation of LEO orbits of highest quality (Arnold et al., 2023a; Fernández et al., 2022; Mao et al., 2021; Lasser et al., 2020; Meyer et al., 2019; Montenbruck et al., 2018a).

3.2.4 Precise orbit determination

To obtain an orbit solution of a satellite, mathematical descriptions of the satellite's center-of-mass motion were defined, which allow an orbit estimation and improvement using a LSQA (sect. 3.1). Numerical integration of the equation of motion (eqn. 3.70) for a specific time interval yields $\mathbf{r}$ and $\dot{\mathbf{r}}$. Using a sophisticated numerical integration method is a prerequisite to fulfilling the accuracy requirements, e.g., the collocation method (Beutler, 2005). The full model for the equation of motion is parameterized by M unknowns consisting of 6 initial osculating elements plus D parameters describing the additional gravitational and non-gravitational forces. If it is assumed that an a priori orbit $\mathbf{r_0}$ is available, resulting from the numerical integration of the equation of motion, it is possible to define improvements to the orbit in the form of a truncated Taylor series

$$\mathbf{r}(t) = \mathbf{r_0}(t) + \sum_{i=1}^{6+D} \frac{\partial \mathbf{r}_0(t)}{\partial p_i}(p_i - p_{i,0}), \tag{3.72}$$

whereby p_i and $p_{i,0}$ describe the orbit parameters (either the initial osculating elements or the additional dynamical parameters) and the corresponding initial values, respectively. The partial derivatives of the orbit with respect to the parameters, abbreviated by

$$\mathbf{z}_{p_i} := \frac{\partial \mathbf{r}_0(t)}{\partial p_i}, \tag{3.73}$$

describe the change in orbit for a change in parameter p_i (Dach and Walser, 2015). To solve the initial value problem, the integration of a linear second-order differential equation system known as the variational equations, has to be carried out, for example by numerical quadrature (Beutler et al., 2010). The variational equations can be derived by setting the sum of all accelerations in the equation of motion to be $\mathbf{f^{tot}}$

$$\ddot{\mathbf{r}} = -GM\frac{\mathbf{r}}{r^3} + \mathbf{f_p}(t, \mathbf{r}, \dot{\mathbf{r}}, Q_1, ..., Q_d) = \mathbf{f^{tot}} \tag{3.74}$$

which yields

$$\ddot{\mathbf{r}} = \mathbf{f^{tot}}. \tag{3.75}$$

Since $\mathbf{f^{tot}}$ is dependent of $\mathbf{r}$ and $\dot{\mathbf{r}}$, the orbit improvements are formulated by:

$$\ddot{\mathbf{z}}_{p_i} = \frac{\partial \mathbf{f^{tot}}}{\partial \mathbf{r}_0}\frac{\partial \mathbf{r}_0}{\partial p_i} + \frac{\partial \mathbf{f^{tot}}}{\partial \dot{\mathbf{r}}_0}\frac{\partial \dot{\mathbf{r}}_0}{\partial p_i} + \frac{\partial \mathbf{f_p}}{\partial p_i} \tag{3.76}$$

The variational equations result in a homogeneous, linear differential system of second order for the initial conditions:

- $\mathbf{z_{p_i}}(t_0) \neq \mathbf{0}$
- $\dot{\mathbf{z}}_{\mathbf{p_i}}(t_0) \neq \mathbf{0}$

If p_i is one of the parameters $Q_1, ..., Q_d$, the variational equations are inhomogeneous with initial conditions:

- $\mathbf{z_{p_i}}(t_0) = \mathbf{0}$
- $\dot{\mathbf{z}}_{\mathbf{p_i}}(t_0) = \mathbf{0}$

because the initial state and velocity vectors do not depend on the parameters $Q_1, ..., Q_d$.

3.2.5 Orbit improvement

A LSQA orbit improvement requires the first design matrix $\mathbf{A}$ connecting the observations and the parameters of the functional model. The relationship between the observations and the satellites' position can be represented as $\mathbf{F}(\cdot)$ because there are different observables (or linear combinations of these observables) available. Therefore, in line with eqn. (3.1),

$$\mathbf{l} = \mathbf{F}(\mathbf{r}) + \mathbf{e} \tag{3.77}$$

can be stated. Using the approach for $\mathbf{r}$ from eqn. (3.72) , whereby $\mathbf{F}(\mathbf{r})$ is linearized as well, results in

$$\begin{aligned}\mathbf{l} &= \mathbf{F}\left(\mathbf{r_0}(t) + \sum_{i=1}^{6+D}\frac{\partial \mathbf{r_0}(t)}{\partial p_i}(p_i - p_{i,0})\right) + \mathbf{e} \\ &= \mathbf{F}(\mathbf{r_0}(t)) + \frac{\partial \mathbf{F}(\mathbf{r_0}(t))}{\partial \mathbf{r_0}(t)}\sum_{i=1}^{6+D}\frac{\partial \mathbf{r_0}(t)}{\partial p_i}(p_i - p_{i,0}) + \mathbf{e}.\end{aligned} \tag{3.78}$$

Having identified the term $F(\mathbf{r_0}(t))$ as the term "computed" ($\mathbf{l_0}$) at initial values $\mathbf{p_0}$, eqn. (3.78) can be rewritten as follows:

$$\mathbf{l} - \mathbf{l_0} = \left(\frac{\partial \mathbf{l_0}}{\partial \mathbf{r}_0}\right)\left(\frac{\partial \mathbf{r_0}}{\partial \mathbf{p}}\right)\delta\mathbf{p} + \mathbf{e} \tag{3.79}$$

When setting

$$A = \begin{pmatrix} \sum_{u=1}^{3}\frac{\partial l_1}{\partial r_{0,u}}\frac{\partial r_{0,u}}{\partial p_1} & \cdots & \sum_{u=1}^{3}\frac{\partial l_1}{\partial r_{0,u}}\frac{\partial r_{0,u}}{\partial p_{6+D}} \\ \vdots & \ddots & \vdots \\ \sum_{u=1}^{3}\frac{\partial l_N}{\partial r_{0,u}}\frac{\partial r_{0,u}}{\partial p_1} & \cdots & \sum_{u=1}^{3}\frac{\partial l_N}{\partial r_{0,u}}\frac{\partial r_{0,u}}{\partial p_{6+D}} \end{pmatrix} \tag{3.80}$$

presuming N observations are present, one ends up with the observation equation

$$\delta\mathbf{l} = A \cdot \delta\mathbf{p} + \mathbf{e}, \tag{3.81}$$

whereby $\delta\mathbf{l} = \mathbf{l} - \mathbf{l_0}$ and $\delta\mathbf{p}$ are the corrections to be estimated for the unknown orbit parameters $\mathbf{p}$.

3.3 Non-gravitational force modeling

In Sects. 3.2.3.2 and 3.2.3.3 it was described that the dynamic and reduced-dynamic orbit representation requires the modeling of forces acting on a satellite in orbit. Of special interest in the frame of LEO-integrated global network solution computation is the modeling of specific non-gravitational forces for LEOs, namely:

- Solar radiation pressure (SRP)
- Earth radiation pressure (EARP)
- Aerodynamic force (AIR)

Since LEOs are orbiting the Earth at lower altitudes than e.g., GNSS satellites, the perturbations due to non-gravitational forces are much more complex. These perturbations can be numerically computed, based on sophisticated models (Girardin, 2016; Mao et al., 2021). The computation of the forces is based on the description of the satellite by a macro model, which describes the surfaces of the satellite bus and solar panels. For example, the macro model used in this work describing the Sentinel-3 satellites is defined by an 8-plate model (Fernández, 2019), whereas for Swarm the macro model is described by a more complex 15-plate macro model (Montenbruck et al., 2018b). The details of a macro model include the size of the plates, the 3-dimensional (X,Y,Z) normal vectors expressed in the Satellite Body-Fixed Frame (SBFF), and the material-dependent properties, exemplarily shown for Jason-3 in Table 3.1. In macro model descriptions, it is distinguished between infrared (IR) and visible (VI) light.

Table 3.1: Jason-3 macro model

Surface [m^2]	Normal vector (SBFF)	IR spec.	IR diff.	VI spec.	VI diff.
0.783	(-1, 0, 0)	0.000	0.987	0.341	0.646
0.783	(1, 0, 0)	0.000	1.000	0.149	0.851
2.040	(0,-1, 0)	0.104	0.569	0.573	0.384
2.040	(0, 1, 0)	0.089	0.627	0.539	0.424
3.105	(0, 0,-1)	0.005	0.977	0.246	0.752
3.105	(0, 0, 1)	0.037	0.287	0.213	0.453
9.800	(1, 0, 0)	0.097	0.098	0.060	0.407
9.800	(-1, 0, 0)	0.035	0.035	0.004	0.298

For the solar radiation pressure and the Earth radiation pressure, it is important to take into account that photons incoming at non-solar plates can be spontaneously re-emitted (Cerri et al., 2010). To appropriately model the Earth's radiation pressure the Clouds and the Earth's Radiant Energy System (CERES) S4 monthly grid products can be linearly interpolated (Wielicki et al., 1996). Since all these models can never represent the real physical conditions in perfection, there are often scaling factors co-estimated in the precise orbit determination. The resulting sum of all non-gravitational forces taken into account in the orbit determination process (3.2.3.3) is described by:

$$\mathbf{f_{NG}} = s_{SRP} \cdot \mathbf{f_{SRP}} + \mathbf{f_{REF}} + \mathbf{f_{EMI}} + s_{AIR} \cdot \mathbf{f_{AIR}}, \tag{3.82}$$

whereby

s_{SRP} = Scaling factor for Solar radiation pressure
$\mathbf{f_{SRP}}$ = Solar radiation pressure force
$\mathbf{f_{REF}}$ = Earth radiation pressure force (reflectivity)
$\mathbf{f_{EMI}}$ = Earth radiation pressure force (emissivity)
s_{AIR} = Scaling factor for aerodynamic force
$\mathbf{f_{AIR}}$ = Aerodynamic force

The solar radiation pressure results from the interaction between incoming photons on the satellite and its surface materials (Girardin, 2016), where they are absorbed or reflected, either specular (spec.) or diffuse (diff.), whereby the split between these three behaviors depends on the material, which is described

by the macro model. The acceleration describing the solar radiation pressure can be derived by computing

$$\mathbf{f_{SRP}} = \sum_{i=1}^{n} \frac{\mathbf{C_{s,i}}}{m} \left(\frac{1AU}{r_{Sun,s}} \right)^2 f_s P_{1AU}. \tag{3.83}$$

The coefficients appearing in eqn. (3.83) are:

i	=	All plates $1, ..., n$, described by the macro model
$\mathbf{C_{s,i}}$	=	Vectorial radiation pressure coefficient
m	=	Mass of satellite
$r_{Sun,s}$	=	Distance between sun and satellite
f_s	=	Geometric shadowing factor
P_{1AU}	=	Solar radiation pressure at $1AU$

The factor f_s describes the proportions of the sun's radiation which is absorbed by the atmosphere, the satellite and Earth shadowing, and others. For more information, the reader is referred to Hackel (2019) and Doornbos (2012). In computing the solar radiation pressure, it is difficult to derive $\mathbf{C_{s,i}}$ since incoming photons can either be absorbed or reflected (specular or diffuse). A more detailed description can be found in Montenbruck and Gill (2000) and Doornbos (2012). The Earth radiation pressure is the sum of two distinguishable components (Mao et al., 2021):

- Scattered short-wavelength visible solar radiation
- Emitted long-wavelength thermal infrared radiation

As already mentioned, to model the reflectivity and emissivity the CERES-S4 data (Wielicki et al., 1996) has been used. The data is described by a grid with a resolution of $2.5° \times 2.5°$ ($N = 72 \times 144$ bins) which strongly varies from month to month but is rather stable for the same months of different years as pointed out by Mao et al. (2021). The total Earth radiation pressure acting on a satellite can be computed by

$$\mathbf{f_{ERP}} = \sum_{j=1}^{N} \sum_{i=1}^{n} \frac{1}{m} (\mathbf{C_{R,i}} f_s P_{REF,j} + \mathbf{C_{E,i}} P_{EMI,j}). \tag{3.84}$$

The coefficients of eqn. (3.84) can be described in analogy to eqn. (3.83) with special regard to $P_{REF,j}$ and $P_{EMI,j}$ which originate from the top of the atmosphere instead of the sun. It is important to mention here, that usually for none of the components of the Earth radiation a scaling factor is estimated because it would particularly highly correlate with the radial positioning of the satellite, which is of crucial interest for altimetry satellites (Montenbruck et al., 2018a; Hackel, 2019). The aerodynamic force can be separated into two parts:

- Atmospheric drag = Projection of force to velocity direction
- Atmospheric lift = Perpendicular to velocity direction

Generally for satellites orbiting the Earth at low altitudes the atmospheric drag is roughly 50 times larger than the atmospheric lift in terms of force acting on the satellite. Since these forces depend on the area of the satellite (plates in the macro model), they are heavily dependent on the attitude of the satellite. The total aerodynamic acceleration is described by:

$$\mathbf{f_{AIR}} = -\frac{\rho}{2m} \sum_{i=1}^{n} A_i \mathbf{v_i}^2 (C_{D,i} \mathbf{e_{D,i}} + C_{L,i} \mathbf{e_{L,i}}) \tag{3.85}$$

Along with the coefficients for eqn. (3.83) the components of eqn. (3.85) are:

ρ	=	Atmospheric density
A_i	=	Projected area of plate i along the velocity direction
$\mathbf{v_i}$	=	Relative velocity of satellite plate to the atmosphere in the Earth-fixed system
$C_{D,L,i}$	=	Coefficient for drag/lift
$\mathbf{e_{D,L,i}}$	=	Unit vector in direction of drag/lift

To compute reliable relative velocities $\mathbf{v_i}$, highly sophisticated horizontal wind models are needed, which describe the time-varying atmospheric circulation dynamics (Drob et al., 2015). Also, the knowledge about the atmospheric density ρ stems from models which are state-of-the-art. For more detailed information about non-gravitational force modeling, with special regard to the technical implementations the reader is referred to Girardin (2016). Detailed analysis on the impact of making use of non-gravitational force modeling in terms of LEO POD can be found in Mao et al. (2021).

3.4 Receiver antenna phase center offset and variation

The determination of the three different orbit representation types, explained in sects. 3.2.3.1, 3.2.3.2, and 3.2.3.3, all rely to different extents on the exact knowledge of the vector pointing from the center-of-mass of the satellite to the antenna phase center (Montenbruck et al., 2009). The corresponding vector $\delta\mathbf{r}_{leo,ant}$ appears in the central eqns. (3.68 and 3.67). A determined orbit using the kinematic orbit representation type would suffer most from imprecisely known exact antenna phase center because it purely relies on geometric information without any physical modeling of the reality, which would cause a direct mapping of erroneous antenna phase center to the LEOs trajectory. Depending on the specific orbit parametrization in terms of additional pseudo-stochastic parameters and their constraints in a reduced-dynamic orbit representation, the knowledge of the exact signal-receiving point in the antenna may be crucial, as well. An orbit solution using the dynamic representation is the least sensitive to errors in the exact position of the signal-receiving point because it solely relies on dynamical models. This may then in turn lead to larger observation residuals. The exact phase center location in terms of the vector $\delta\mathbf{r}_{leo,ant}$ is conventionally defined as the sum of the vector pointing to the antenna reference point (ARP), the vector describing the phase center offset (PCO), and the azimuth- and elevation/nadir-dependent phase center variation (PCV). Other conventions are to combine the PCO and PCV to a single quantity called phase center correction (PCC) or to combine the ARP and the PCO to a single quantity which is identified as the "true" antenna reference point. Note that not only ARP, PCO and PCV can be erroneous, also the position of the Center-of-mass (CoM) may be affected by uncertainties. Since in the present applications the vector from CoM to signal-receiving point is the decisive quantity, an error in the PCO or ARP information can also be aligned with an erroneous information of the CoM. In this work we follow the first mentioned convention for the constituents of the signal-receiving point, also described in Montenbruck et al. (2009), and define:

- ARP: Physical mounting point of the antenna on the satellite bus, which is defined by the construction plan and realized by the manufacturer of the satellite bus. For this purpose, a satellite body-fixed right-handed coordinate system (X, Y, Z) is defined, whereby the origin usually does not coincide with the CoM of the satellite, because the CoM may vary depending on the aging of the satellite, e.g., by fuel usage. This constituent of this vector is (usually) assumed to be known with perfect precision.
- PCO: The difference between the ARP and the mean electrical antenna phase center (in this convention) (Morton et al., 2021). The information about the PCO of a receiver antenna is usually provided by the mission operator in the case of a LEO GNSS antenna. The information about the PCO is given in a separate antenna system, whose components are defined by North/East/Up in analogy to terrestrial GNSS antennas, whereas the corresponding unit vectors need to be given in the SBBF. The PCO (in this convention) may need to be improved (Peter et al., 2017; Kobel et al., 2022b).
- PCV: An additional offset which depends on the azimuth (α) and elevation (β) angle of the incoming beam of the signal. For LEO missions, often only a pre-launch phase pattern is available, which does not represent the real conditions sufficiently. This is because the PCV highly depends on the influence of near-field multipath effects, which are in general not determined before the launch of the satellite. Many studies have been carried out to determine accurate phase patterns for GNSS antennas of various LEO missions. Kobel et al. (2021) describes different antenna patterns for Jason-3. Jäggi et al. (2009) and Montenbruck et al. (2009) describe the derivation of phase patterns for the GPS antennas of the GRACE and TerraSAR-X missions and their influence on POD. The determination of a phase pattern for the satellite of the Sentinel-1A mission is described in Peter et al. (2017).

Figure 3.4 illustrates the constituents of the exact phase center location. A widely used terminology is to call the phase pattern a PCV map. This is because a suitable way to graphically represent a phase

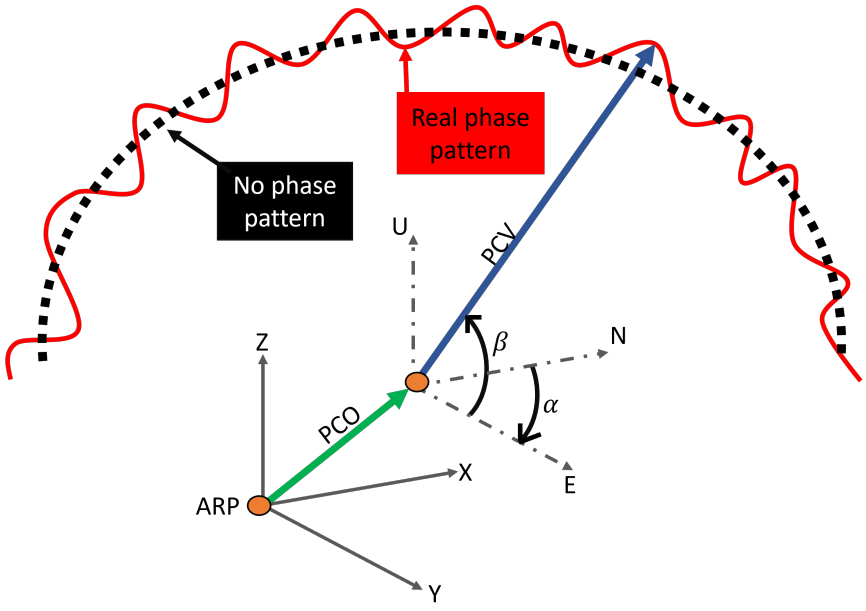

Figure 3.4: Exact antenna phase center

pattern is to plot the α- and β-dependent variations in an antenna diagram (map). An example of a PCV map is shown in Fig. 3.5 for the GPS antenna of the LEO satellite Sentinel-3A. Different approaches are possible for the in-flight determination of PCV maps for LEO satellites. Within this work, use is made of the residual stacking approach (Jäggi et al., 2009) solely. The procedure consists of the following steps:

1. POD using a reduced-dynamic orbit representation including the estimation of one constant acceleration per spatial direction per arc, or a dynamic orbit representation, and additional empirical accelerations valid for specified time lengths.

2. Categorizing the negative observation residuals of the final orbit parameter estimation step of the POD into a binned grid with specific resolution (usually $1° \times 1°$) according to the azimuth and elevation angles of the corresponding observations. This results in a first PCV map with a size of 360×90.

3. A second POD is carried out, whereby the previously (preliminary) determined PCV map is applied.

4. By repeating the binning of the resulting observation residuals and reintroducing a corrected PCV map, an iterative procedure results. A sufficient number of iterations has to be performed to obtain a converged phase pattern (e.g., see Fig. 4.18 from sect. 4.2.5.1).

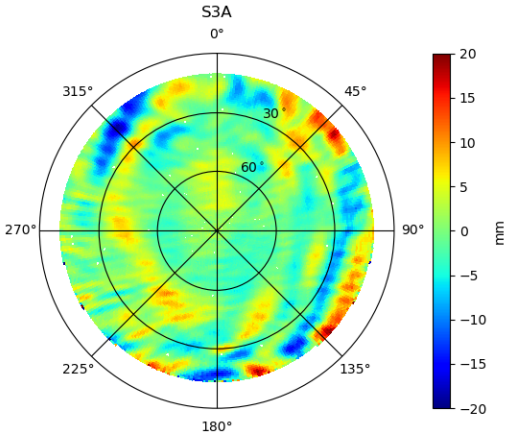

Figure 3.5: Antenna phase center variations map

For PCV map determination purposes, a longer processing period is generally associated with a higher level of accuracy due to a better averaging of the residuals. For most LEO missions 0° azimuth corresponds to the nominal direction of flight.

Being aware that the empirically derived PCV maps of LEO receiver antennas contain inherited information of the transmitter patterns, causing LEO PCVs to contain the terrestrial reference frame's fingerprints, for the LEO-integrated processing performed in this work it is always made use of the receiver and transmitter patterns.

3.5 Transmitter antenna phase center offset and variation

In GNSS systems, the uncertainty associated with the effective transmission point (Zhu et al., 2003) is the primary constraint to determining geodetic parameters. Identifying the vector pointing from the satellite's mass center to the transmit antenna phase center is crucial. The PCO can vary due to complex antenna designs and multipath effects, which require the determination of GNSS PCV maps for transmit antennas. In undifferenced GPS solution approaches, part of the false information about PCO and PCV is absorbed by the co-estimated clock offsets, so it is not directly mapped into the estimation of geodetic parameters. Mismodeling of phase center location, however, has been shown to have a significant effect. For example, Cardellach et al. (2007) showed a possible network shift of several millimeters in simulations. In a LEO POD parts of erroneous transmit antenna information may also be absorbed in the derived LEO PCVs.

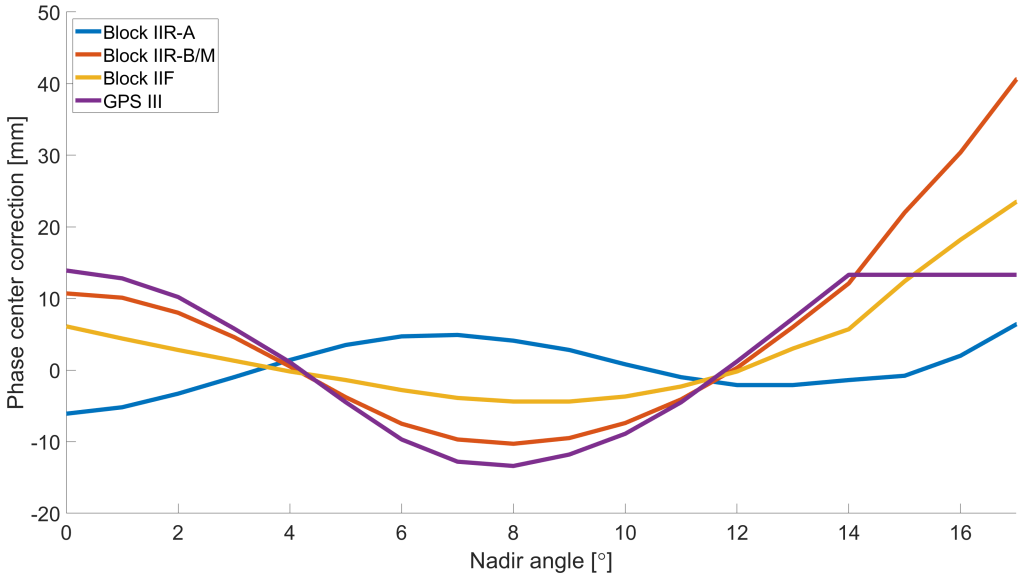

Figure 3.6: GPS transmitter antenna phase center variations of the igs14.atx model

Based on the recommended values of the IGS (Rebischung et al., 2016), which are consistent with the ITRF14[1], Fig. 3.6 shows the nadir-dependent phase center corrections of the GPS satellites used in this work. The phase center variations are only shown for currently active satellite blocks[2]. Particularly interesting is the visible cut-off of the patterns at certain nadir-angles. For the GPS III satellites, the corrections are constant above a nadir-angle of 14°, because at the time the igs14. atx model was determined, none of these satellites were in orbit yet. The igs14.atx model has been constructed (extended) by adding LEO data to the igs08.atx model (Schmid et al., 2016). Recent results from Conrad et al. (2023) demonstrate an extension of the PCV for GPS III satellites above a nadir-angle of 14°. Different approaches have been used in the past to determine the PCOs and PCVs of GPS transmit antennas. Ground calibration has been attempted (Wubbena et al., 2007), however, it is difficult to determine whether multipath effects will result from the antenna mounted on the satellite bus. In-flight calibration nowadays leads to PCVs of desirable accuracy (Schmid and Rothacher, 2003; Schmid et al., 2005; Haines et al., 2005). The determination of the PCV patterns using in-flight data is again dependent on the PCV maps of the receiving antennas, which are usually calibrated using observations to ground stations. By using GPS observations from LEOs to enhance PCV determination of GPS satellites, Haines et al. (2015) demonstrates a promising approach. Regarding the present work, the usage of PCO and PCV information of GPS signal emitter and receiver (ground stations and LEOs) is one major obstacle, because the currently used values were determined (estimated) based on the underlying terrestrial reference frame. This causes a large correlation between the determined PCOs and PCVs of emitters and receivers. For the Galileo system, the situation differs, because the European GNSS Agency provides satellite antenna calibrations (GSA, 2019). Detailed information about the different calibration methods for emitter and receiver antennas and the impact on global GNSS

[1]https://igs.org/wg/reference-frame/ (Accessed: 13 September 2023)
[2]https://www.gps.gov/systems/gps/space/ (Accessed: 13 September 2023)

network determination based on fixed Galileo emitter PCOs are described by Villiger et al. (2020). One large advantage of having antenna calibrations is the possibility to determine the scale of the reference frame from GNSS solely. This allows for the independent estimation of PCOs and PCVs corrections for other GNSS and may therefore be a game-changer in the determination of global GNSS network solutions.

3.6 LEO attitude representation

In satellite POD, different coordinate frames are used. The origin of the satellite reference frame (SRF) is the satellite's mass center. Equation (3.68) and (3.70) specify that the integration of the equation of motion (in a dynamic or reduced-dynamic orbit representation) must be performed in an inertial frame. $J2000.0$ is the most commonly used celestial reference frame (Xia et al., 2021). SRF and inertial frame differ, so there is a need for a transformation to align the orientation of the frames. The attitude of the satellite needs to be known for this purpose. A POD can be distorted to the centimeter level by false attitude information as shown by Hwang et al. (2009), where the magnitude of the distortion depends on the distance between the receiver antenna and the CoM of the satellite. The orientation of a satellite is typically represented by quaternions:

$$\mathbf{q} = \begin{pmatrix} q_0 \\ q_1 \\ q_2 \\ q_3 \end{pmatrix}, \tag{3.86}$$

whereby q_0 describes an angle of rotation about the axis defined by (q_1, q_2, q_3). By using

$$\mathbf{R}(\mathbf{q}) = \begin{pmatrix} 2(q_0^2 + q_1^2) - 1 & 2(q_1 q_2 - q_0 q_3) & 2(q_1 q_3 + q_0 q_2) \\ 2(q_1 q_2 + q_0 q_3) & 2(q_0^2 + q_2^2) - 1 & 2(q_2 q_3 - q_0 q_1) \\ 2(q_1 q_3 - q_0 q_2) & 2(q_2 q_3 + q_0 q_1) & 2(q_0^2 + q_3^2) - 1 \end{pmatrix} \tag{3.87}$$

one can convert a quaternion to a three-dimensional rotation matrix (Kuipers, 1999). It is important to note that all satellites are designed to perform a certain attitude movement, which is known as nominal attitude. Each satellite can have a different nominal attitude. Based on the nominal attitude, it is possible to also model the attitude. Satellites with dedicated attitude sensors such as star cameras can, however, be used to compare POD processes based on nominal or measured attitude data. Within this work, measured attitudes were used for all processed LEO satellites.

3.7 Quality metrics

Since an orbit solution cannot be directly observed or evaluated in-situ for a satellite orbiting the Earth, quality metrics are required for determining its accuracy and precision. The purpose of this section is to present a brief overview of the most commonly used quality measures used to determine the quality of precise orbit solutions.

3.7.1 Orbit comparisons

In general, different institutions compute a range of solutions for scientific satellite missions, by using various software packages. In doing so, it is possible to compare different orbit solutions and therefore evaluate whether the procedures and modeling approaches employed for the POD result in orbits that are consistent with other institutions' solutions. Satellite positions are compared at common epochs for this purpose. Orbit differences are often expressed in the local orbital frame (RSW). The RSW system is a right-handed three-dimensional system, where R represents the direction from the center-of-mass of the Earth to the center-of-mass of the satellite. S points approximately in the direction of motion and W, also

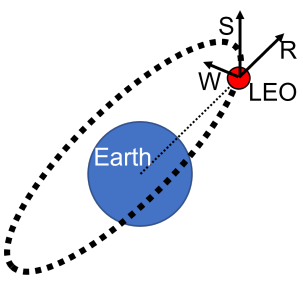

Figure 3.7: RSW local orbital frame

called out-of-plane direction, completes the coordinate system. Figure 3.7 illustrates the local orbital frame. In order to display orbit differences in the RSW system, position and velocity information in the inertial system have to be provided for each epoch. The unit vectors needed for the transformation of orbit differences $\mathbf{r_1} - \mathbf{r_2} = \epsilon$, computed in the inertial system, to the RSW system are given by

$$\begin{aligned}
\mathbf{e_r} &= \frac{\mathbf{r}}{|\mathbf{r}|} \\
\mathbf{e_v} &= \frac{\mathbf{v}}{|\mathbf{v}|} \\
\mathbf{e_w} &= \frac{\mathbf{e_r} \times \mathbf{e_v}}{|\mathbf{e_r} \times \mathbf{e_v}|} \\
\mathbf{e_s} &= \frac{\mathbf{e_r} \times -\mathbf{e_w}}{|\mathbf{e_r} \times -\mathbf{e_w}|}.
\end{aligned} \tag{3.88}$$

The orbit differences can then be projected to the RSW system by

$$\epsilon_i = \mathbf{e}_i \cdot \epsilon. \tag{3.89}$$

Figure 3.8 shows exemplarily orbit differences of an orbit comparison for Jason-3 to a solution provided by JPL for 19 July 2019. In particular, once-per-revolution differences are visible, which are probably due to different modeling of forces acting on the satellite. A high-frequency noise is evident in the along-track direction. The problem is related to Bernese GNSS Software's use of Modified Julian Date (MJD) as the time argument when accessing numerically integrated reduced-dynamic orbit positions (Kobel et al., 2019), which is needed to compare orbit position provided in the "SP3-C" file format. It appears when positions are accessed at non-integer seconds. In the present comparison, this is necessary, because the positions of the satellite in the orbit solutions provided by JPL are given at non-integer seconds. This problem could be solved by rigorously separating the MJD time argument into days and fractional parts.

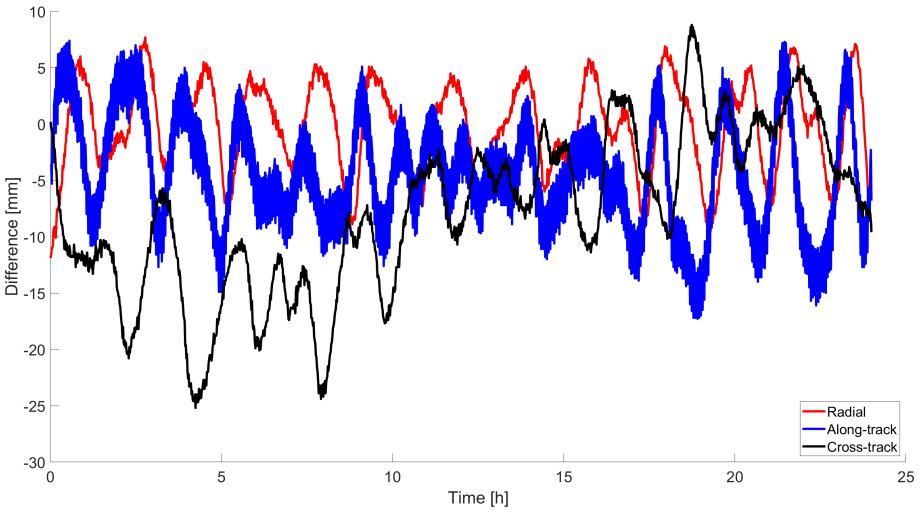

Figure 3.8: Orbit differences Jason-3 in local orbital frame

A special case of orbit comparison for LEO satellites is differences between orbit solutions of different orbit representation types, namely between reduced-dynamic and kinematic orbit solutions. Such comparisons provide a consistency test for these orbit representations. It also allows for identifying deficiencies in the modeling of forces acting on the satellite and identifying problematic epochs in kinematic orbits induced by outliers.

3.7.2 Orbit overlaps at arc boundaries

A quality measure for validating orbit solutions is the computation of orbit overlaps at arc boundaries, also called orbit misclosures. For this purpose, orbit overlaps can either be computed in the Earth-fixed or in the inertial system (Lutz et al., 2016a). It is important to analyze orbit misclosures for long time periods, where many arcs of satellites are computed since only one common epoch is computed for two subsequent arcs. Mean values and standard deviation of orbit misclosures (illustrated in Fig. 3.9 can be analyzed to assess the quality of the derived orbit solutions (Peter et al., 2022). The purpose of this quality metric is to assess the consistency between consecutive arcs. Absolute orbit accuracy cannot be determined using orbit misclosures.

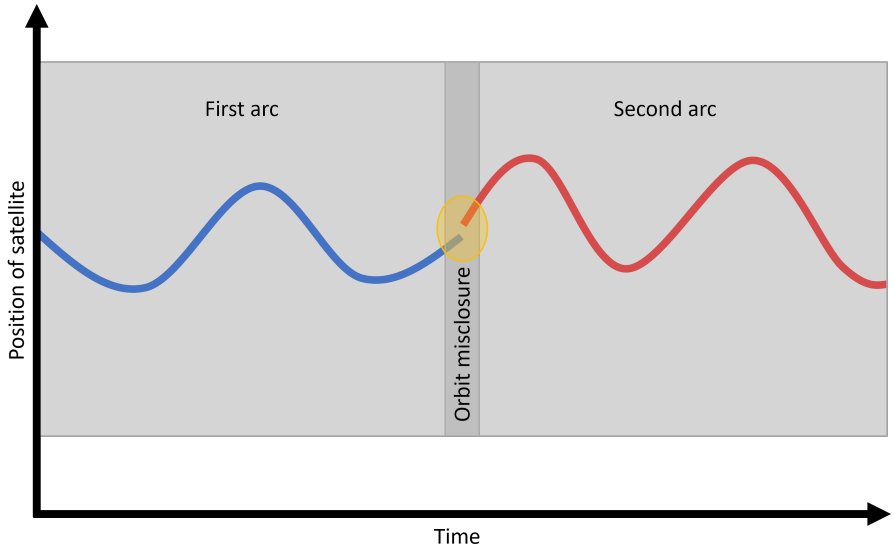

Figure 3.9: Illustrative orbit misclosure

3.7.3 Satellite laser ranging validation

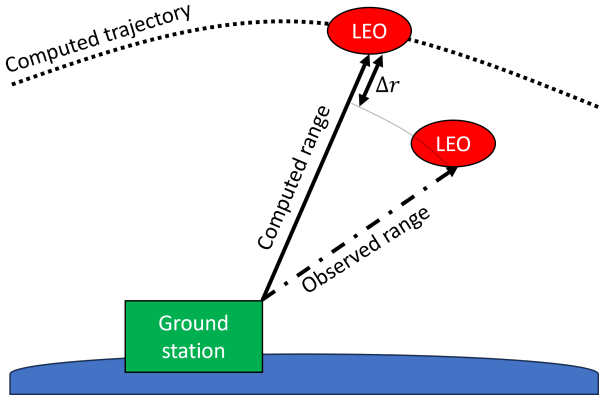

Figure 3.10: Principle of SLR validation. According to Flohrer (2008)

Orbit comparisons and misclosures always only reflect relative measures, since common mismodeling cannot be detected. Furthermore, it is impossible to determine which of the compared solutions is more accurate when only orbit differences are examined. This demands a technique that allows for independent validation. Satellite Laser Ranging (SLR) represents a high-precision method to track a satellite in orbit (Combrinck, 2010). This tool is widely used in satellite geodesy, especially also for LEO orbit validation (Arnold et al., 2019). The principle is to send a short laser pulse from an optical system at a ground station to a satellite and simultaneously start a high-precision clock. The laser pulse is reflected at the satellite's Laser retroreflector and travels back to be detected in a dedicated optical system at the ground station (Degnan, 1993). The incoming laser pulse gets registered, amplified, analyzed, and induces the stopping of the electronic clock. This two-way measuring principle makes it possible to derive a geometric distance from the ground station to the satellite by computing in first-order approximation

$$d = \frac{\delta t}{2} \cdot c + \epsilon, \tag{3.90}$$

whereby

d = Computed distance

δt = Travel time

c = Speed of light

ϵ = Corrections to be applied.

The sum of all corrections to be applied to the derived distance d consists of atmospheric signal delay, relativistic effects, laser system offsets, and phase center offsets of the Laser retroreflector onboard the satellite. The measured distance d can be compared with the computed distance resulting from the GPS-based precise orbit solution at the measuring time. Figure 3.10 illustrates the resulting difference Δr, which is a scalar quantity to characterize one-dimensional orbit determination errors, errors in the station coordinates, errors in the optical system or electronic chronometer or a combination of all those (Arnold et al., 2019). To carry out an SLR validation, the satellite has to be equipped with a Laser retroreflector which must fulfill certain requirements, like being capable of collecting enough light while not allowing for pulse deformations due to signal superposition. The coordination and evaluation of the laser ranging measurements, performed by the ground stations, is carried out by the International Laser Ranging Service (ILRS) (Pearlman et al., 2002). The development of standards and strategies for measurements and analysis, to ensure high, consistent data quality, is the purpose of the ILRS.

3.7.4 K-band validation

The two GRACE-FO satellites are equipped with a K- and Ka-band ranging system. The inter-satellite phase tracking measurements are mainly used for gravity field recovery, but they can also serve as an orbit validation method, whereby the precision of the measurements is 10 μm (Abich et al., 2019). The two LEOs following each other are exchanging microwave signals from which a pseudo-range between the K-Band antennas can be derived. It is not a direct range measurement, because an ambiguity has to be resolved since the measurement is derived from comparing the incoming phase signals with a reference phase signal created onboard the satellites. The pseudo-range has to be corrected for ionospheric effects and light travel time and describes the Euclidean distance which can be compared to the instantaneous range derived from the GPS-determined orbit solution for both GRACE-FO satellites. It is important to correct the measurements due to the different reference points that are used, whereby the determined orbit positions refer to the center-of-mass of the satellites, while the K- and Ka-band range measurements are performed for the distance between the locations of the antennas.

3.7.5 Analysis of time series of parameters

Along with orbit parameters, also other unknowns are to be determined in this work. For some of these parameters, only one value is estimated for one processed batch of observations. In the frame of this work, these are the Earth's center-of-mass coordinates, station coordinates, and Earth rotation parameters. These parameters may show periodic behavior when analyzing longer time periods. This demands a frequency analysis of the resulting parameters with respect to time. Fourier series (Lighthill, 1958) represents a way of describing periodic piecewise continuous functions by a series of sine and cosine functions:

$$f(t) = \frac{a_0}{2} + \sum_{k=1}^{\infty}(a_k \cos(k\omega t) + b_k \sin(k\omega t)), \tag{3.91}$$

whereby the frequencies of the sine- and cosine functions are integer multiples of the basic frequency ω. The unknown coefficients a_0, a_k, and b_k are to be estimated. The magnitudes of the a_k and b_k coefficients give access to the amplitude and phase of a signal with the frequency $k \cdot \omega$ in the analyzed time series.

3.8 Integrated processing scheme

The integrated processing used in this work requires estimating a large number of parameters, including geodetic and orbital parameters for GNSS and LEO satellites, as well as clock corrections and ground station coordinates. For a one-day (24-hour arc) solution, Table 3.2 provides comprehensive information on the parametrization of the determined solutions in terms of the total number of parameters and corresponding constraints.

Table 3.2: Estimated parameters and their contraints

Parameter	Number	Constraint
Station coordinates	3/station (X/Y/Z)	No-Net-Translation
(Datum definition)		No-Net-Rotation
Station clocks	288/station	zero-mean
Zenith path delay	12/station	relative: 1 m
Horizontal gradient	1 set (N/E)/station	-
Earth rotation	2 sets/day (X,Y-pole,dT)	dT_1:10^{-4} ms
Earth's center-of-mass	3	-
GNSS orbital elements	6/satellite	-
GNSS dynamical parameters	7/satellite	-
GNSS stoch.param.(Pulses)	3/satellite	R:10^{-6} m/s,A:10^{-5} m/s,C:10^{-8} m/s
GNSS satellite clocks	288/satellite	-
LEO orbital elements	6/satellite	-
LEO dynamical parameters	3 or 0/satellite	-
LEO stoch. param. (PCA)	3·48/satellite	(R/A/C):$5 \cdot (10^{-9}$ or $10^{-10})$ m/s^2
LEO satellite clocks	288/satellite	-
Ambiguities	∼9000	-

There are no constraints applied to many of the estimated parameters given in Table 3.2. Two sets of ERPs (indicated by subscripts) are estimated per day whereby the first one belongs to the beginning of the day, and the second to the end of the day, whereby continuity at the polynomial boundaries between the subsequent sets is enforced and dT_1 is heavily constrained to a priori (Table 3.3) because of the large correlation with the ascending nodes of the GNSS satellites. A set of velocity pulses (in radial/along-track/cross-track) is set up at orbit noon for each GNSS satellite. The GNSS orbit solutions are parametrized as described in Selmke et al. (2020). As described in sect. 3.2, for the LEO orbits piecewise constant accelerations (PCA) are estimated together with six initial osculating elements. For some of the solutions, constant accelerations over one arc in the radial (R), along-track (S), and cross-track (W) directions are estimated to account for modeling errors in the LEO POD, especially when neglecting the explicit modeling of non-gravitational forces such as solar radiation pressure and air drag. For the observations from terrestrial GNSS stations, an elevation-dependent weighting is applied, according to:

$$w(z) = \cos^2(z), \tag{3.92}$$

with $w(z)$ being the weight and z the zenith angle of the respective GNSS observation. For the LEO observations, no elevation-dependent weighting is applied, whereby the weights equal the station observation weights at 0° zenith angle. This weighting strategy is applied to decrease potential problems due to mismodeling of tropospheric refraction for ground stations. The GNSS data sampling for the ground station and LEO observations in the integrated processing was chosen to be 5 minutes (300 sec) in order to keep an appropriate balance between accuracy and computation time. It has been shown by Huang et al. (2020) that this observation sampling is adequate to lead to an increase in the consistency of derived GPS orbit solutions with the IGS orbit solutions using the LEO-integrated approach.

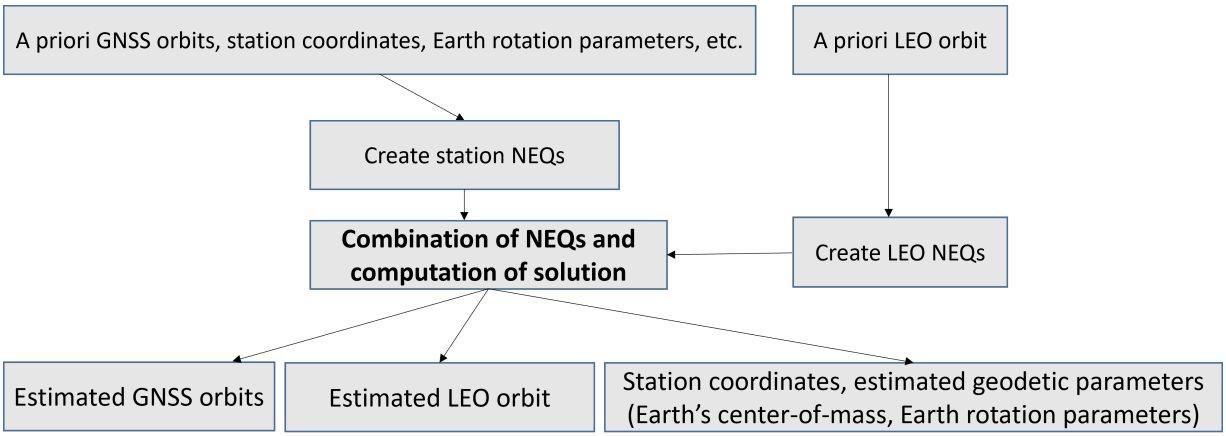

Figure 3.11: Integrated processing scheme (1)

In Fig. 3.11 the scheme of the integrated processing is provided. First, using a priori GNSS orbits and a priori station coordinates, NEQs are set up for the chosen ground stations. On the other hand, using a priori LEO orbits, NEQs are set up for each LEO individually. Both NEQ-types (ground station and LEO) contain all common parameters. The next step is the combination of all the NEQs and the computation of the final solution.

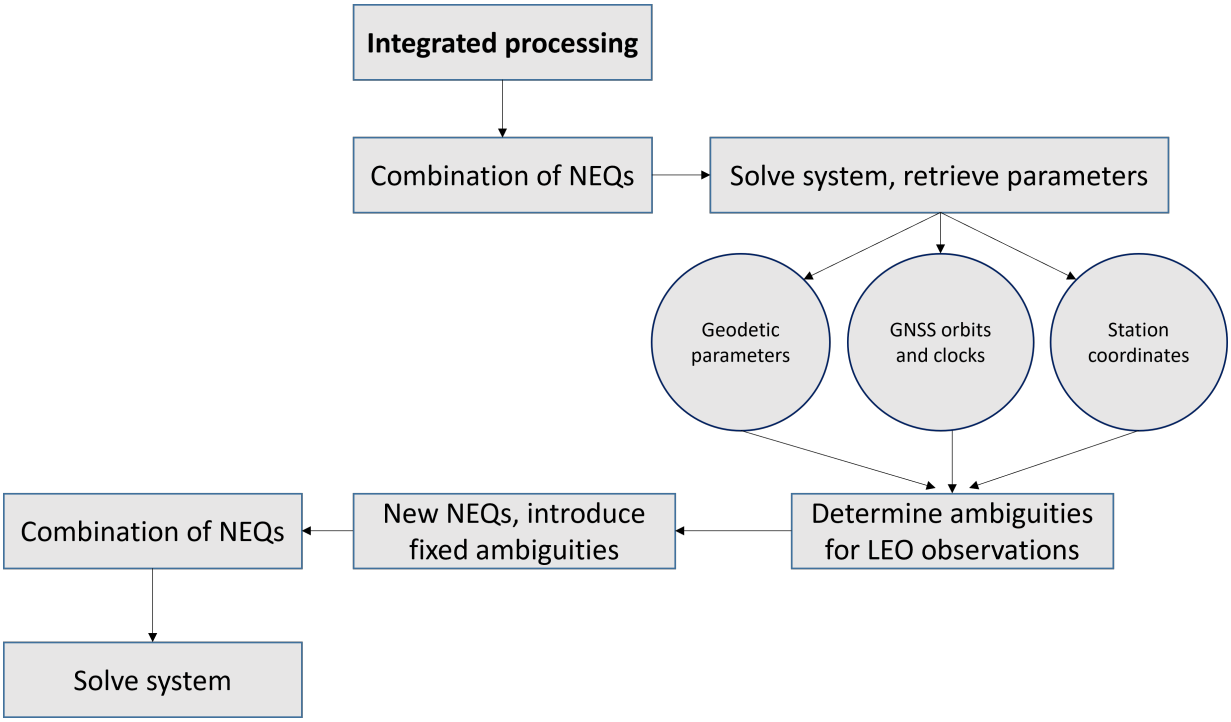

Figure 3.12: Integrated processing scheme (2)

This step consists of the sub-steps indicated in Fig. 3.12 which includes the combination of the NEQs, the estimation of ambiguities for the LEO GNSS observations based on the first (ambiguity-float) solution, a recreation of the NEQs, whereby the determined integer ambiguities are introduced as known, and the computation of the final solution (ambiguity-fixed). The ambiguities of the ground station observations are not resolved within the procedure but are introduced as known from a ground station-only processing. From the combined solution, GNSS orbits, LEO orbits, ground station coordinates, and the geodetic parameters result.

3.8.1 A priori information and models

As introduced in sect. 3.1 about the LSQA, for all parameters to be estimated an a priori value is needed. Table 3.3 describes the a priori information used in this work, along with applied models. The LEO a priori orbits are derived by performing a POD following the strategy described in Jäggi (2007). The LEO orbit parametrization contains six initial osculating elements, constant accelerations over one arc in three spatial directions (R/S/W), and piecewise constant accelerations (PCAs) in R/S/W, constrained to $5{\cdot}10^{-9}$m/s^2. This parametrization is adapted when non-gravitational forces are explicitly modeled, whereby no constant accelerations are estimated and the constraints of the PCAs are set to $5{\cdot}10^{-10}$m/s^2. It is evident in Table 3.3 that for some of the parameters (troposphere, Earth's center-of-mass, GNSS and LEO stochastic parameters, and ambiguities), a priori values of zero have been used.

Table 3.3: A priori information and models

Parameter/Model	A priori Information
Ground station coordinates	CODE final products[1]
Ground station clocks	CODE final products[1]
Troposphere	Zero
Earth rotation	CODE final products[1]
Earth's center-of-mass	Zero
GNSS orbits	CODE final products[1]
GNSS stochastic parameters	Zero
GNSS clocks	CODE final products[1]
LEO orbits	Own processing (LEO POD only)
LEO stochastic parameters	Zero
LEO clocks	LEO GNSS Observation files
Ambiguities	Zero
Pole model	IERS2010 Conventions[2]
Precession/Nutation	IERS2010 Conventions[2]
Gravity field (static)	GOCO06s[3] (120x120)
Gravity field (time-varying)	IERS2010 Conventions[2]
Solid Earth tides	IERS 2010 Conventions[2]
Ocean tides	EOT11a[4] (50x50)
Earth/Ocean pole tide	IERS 2010 Conventions[2]
Third bodies	Sun, Moon, Planets DE421[5]
GNSS satellite PCO/PCV	igs14.atx[6]
Observation sampling	300 sec
A priori σ_0 (L1,L2)	1 mm
Software	Bernese GNSS Software v5.4[7]

3.8.1.1 Observation data

To reduce the errors in a determined global network solution, the outlier screening of the observation data plays a crucial role. Highly sophisticated methods have been developed to perform an accurate pre-processing of the data. In this work the handling of observation data from ground-based receivers and from space-borne receivers are different. The observations from ground stations are used in the form of observation files stemming from the reprocessing campaign (Selmke et al., 2020) described by Dach et al. (2021). This data is used without further outlier screening. The observations collected by space-borne receivers, the LEOs used in the processing, are treated in a different manner. Beginning with the raw observation data a

[1] Dach et al. (2023)
[2] Petit et al. (2010)
[3] Kvas et al. (2021)
[4] Savcenko and Bosch (2012)
[5] Folkner et al. (2009)
[6] Rebischung and Schmid (2016)
[7] Dach and Walser (2015)

POD is carried out, whereby an outlier screening is performed, as described in Jäggi (2007). The screened observation files resulting from the LEO POD are introduced in the integrated processing to set up the NEQ (see Fig. 3.11).

3.8.1.2 Computational aspects

The computation time is a decisive factor in computer technology. It defines the amount of time it takes a computer or an algorithm to carry out a specific computation. The efficiency of the computation time is of high importance whenever large data sets are handled. The determination of a global network solution, as carried out in this work, has therefore to be analyzed in terms of computation time, with special regard to an increase due to the integration of LEO observations. In Fig. 3.13 the percentual composition of the computation time is shown for the adopted integrated global network determination, whereby one LEO has been integrated.

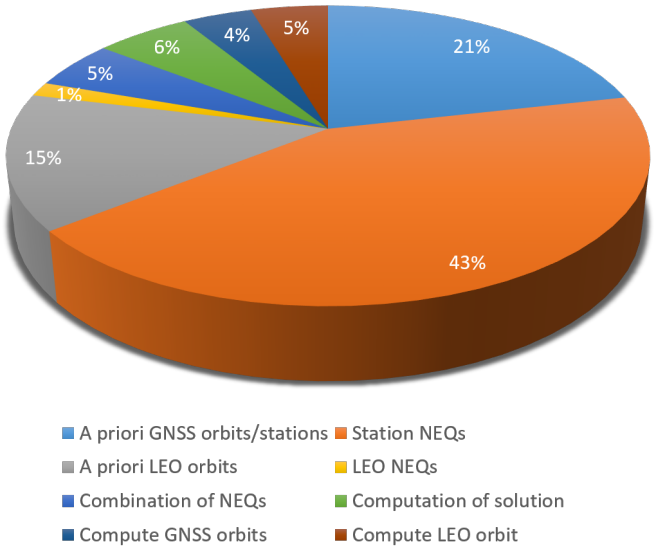

Figure 3.13: Percentual computation time per task in LEO-integrated processing

For one 1-day solution, including one LEO, the total computation time for the tasks shown in Fig. 3.13 is about 3 hours[1] when a 300 sec sampling is used. Important to note that these tasks have to be carried out twice, according to the processing scheme shown in Fig. 3.12 to compute the final, ambiguity-fixed, solution. It is evident that the largest amount of computation time is needed for the creation of the ground station NEQs, due to their large number. The integration of an additional LEO satellite leads to an increase in the computation time of about 19%.

Recall: The method of least-squares is used to estimate unknown parameters by minimizing the sum of weighted squared errors using the design matrix A and the normal equation matrix. The determination of a satellite's trajectory involves understanding all forces acting on it, whereby the experiments of this work require modeling of forces including solar radiation pressure, Earth radiation pressure, and aerodynamic force. Additionally, the process referred to as integer ambiguity resolution or ambiguity-fixing plays an important role in the process of the POD of a LEO. The determination of the quality of a global network solution in terms of satellites' precise orbit solutions requires quality metrics, including orbit comparisons in the RSW system, SLR validation, and orbit overlaps at arc boundaries. In this work, geodetic and orbit parameters for GNSS and LEO satellites are estimated, by using an integrated processing scheme consisting of setting up normal equations for stations and LEOs, the combination of NEQs, estimation of ambiguities, and computation of final solutions.

[1] performed on UBELIX (http://www.id.unibe.ch/hpc)

Chapter 4

Precise orbit determination of Jason-3

4.1 Jason-3 satellite properties

In this section, various steps, experiments, and findings related to the POD of Jason-3 are discussed. In this work, the Bernese GNSS software was used for the first time to perform a POD for Jason-3. In the following, the POD process of Jason-3 will be discussed with a focus on the challenges associated with its satellite design. In order to ensure that the GPS observations collected by Jason-3 can be incorporated into a global GNSS network solution and improve the estimated parameters, a rigorous investigation of the quality of the POD was performed.

4.1.1 Attitude of Jason-3

One of the characteristics of Jason-3 is that the satellite changes its attitude, depending on the β-angle, i.e., the angle between the satellite's orbital plane and the sun's geocentric position vector. The LEO is in either yaw-steering or fixed-yaw attitude mode, whereby either the positive or negative x-axis of the Satellite Body-Fixed Frame (SBFF) is pointing in the direction of flight (Fig. 4.1), therefore four different attitude modes results. As for the Jason-1 and Jason-2/OSTM satellites (Cerri et al., 2010), the attitude of Jason-3 (Couderc, 2015) changes according to:

- $|\beta| > 15° \rightarrow$ Yaw-steering mode (YS)
- $|\beta| \leq 15° \rightarrow$ Fixed yaw mode (FY)
- $\beta = 0° \rightarrow$ Yaw flip

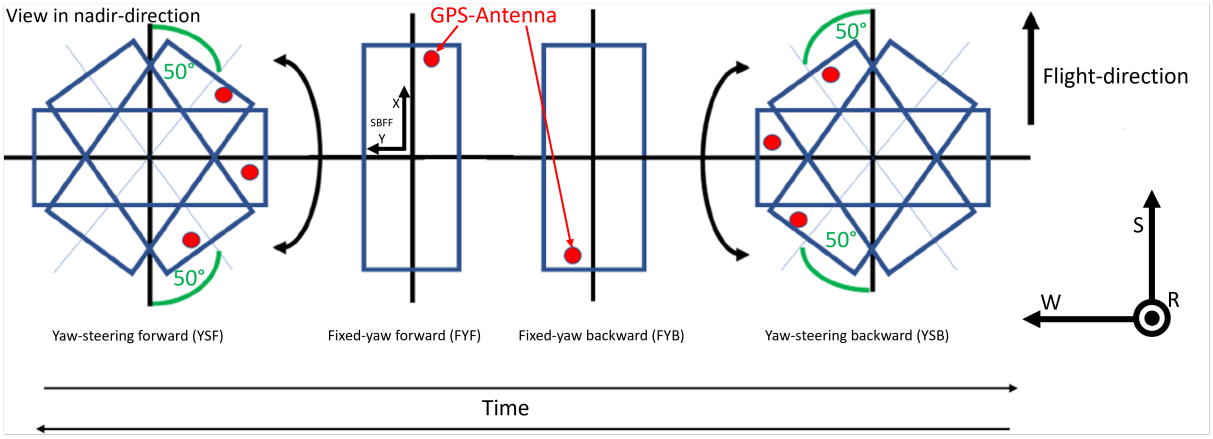

Figure 4.1: Jason-3 Attitude modes

When $\beta = 0°$ a yaw flip takes place. Fig. 4.1 illustrates the different attitude modes, highlighting the position of the GPS antenna and the range of the satellite bus' rotation, including its maximum elongation.

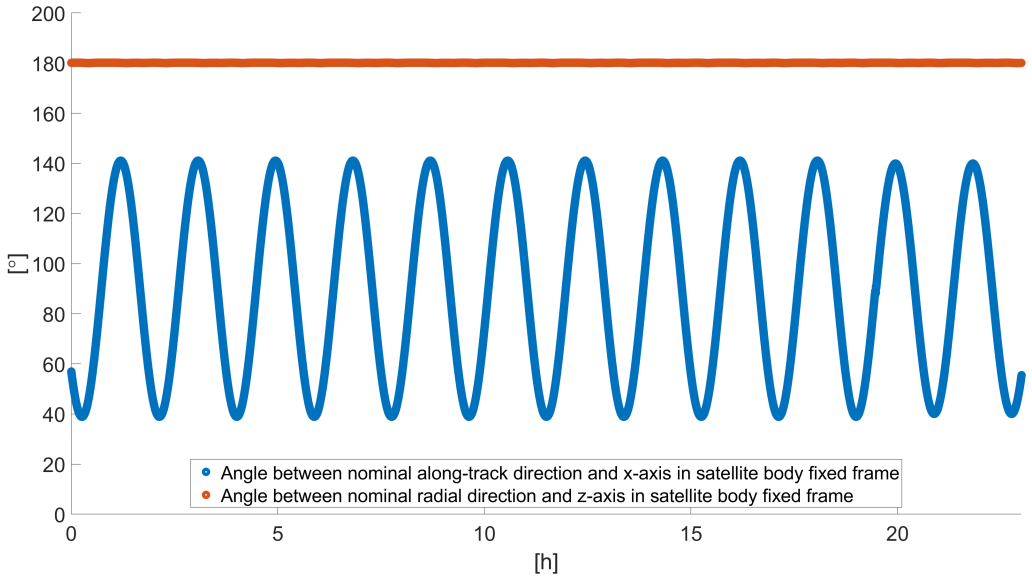

Figure 4.2: Jason-3 yaw-steering rotation

To illustrate the rotation of the satellite in a yaw steering attitude mode, Fig. 4.2 shows the angles between the R/S/W attitude and the axes of the SBFF for 1 January 2019. The maximum elongations from Fig. 4.1 are well recognizable. The angle between the radial direction and the Z-axis of the satellite body-fixed frame is always close to 180°. The two time axes show the sequence of the different attitude modes.

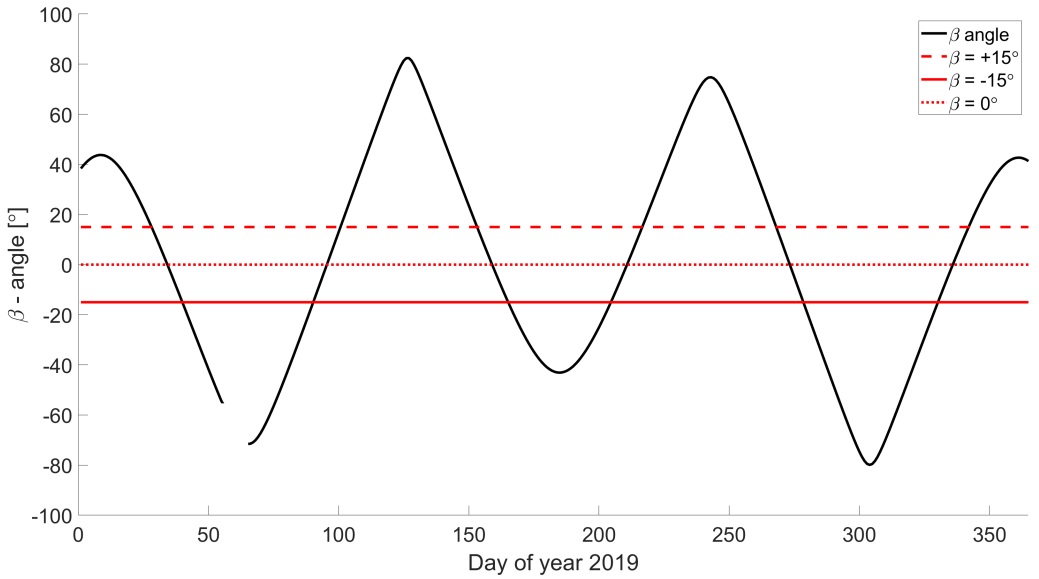

Figure 4.3: β-angle of Jason-3

The yaw-steering attitude modes last for about 35 days, whereas the fixed-yaw attitude modes last for about 10 days (Kobel et al., 2022a). This is visible in Fig. 4.3, which displays the β-angle for Jason-3 for the year 2019. For the time period 24 February 2019 - 6 March 2019, no GPS observation data is available.

4.1.2 Jason-3 GPS antenna orientation and coverage

According to Couderc (2015), the boresight vector of the GPS antennas of the Jason-3 satellite are not zenith pointing but 15° tilted towards the $+X$ axis in the SBFF and perpendicular to the Y-axis. The boresight vector in the antenna system reads $\mathbf{b_A} = (0, 0, 1)^T$. Using the rotation matrix

$$\mathbf{R} = \mathbf{R_1}(0) \cdot \mathbf{R_2}(15°) \cdot \mathbf{R_3}(0) \tag{4.1}$$

the boresight vector in the SBFF frame reads as:

$$\mathbf{b_{SBFF}} = \mathbf{R} \cdot \mathbf{b_A} = \begin{pmatrix} 0.259 \\ 0 \\ -0.966 \end{pmatrix} \tag{4.2}$$

In analogy, the azimuth vector can be computed to be

$$\mathbf{a_{SBFF}} = \mathbf{R} \cdot \mathbf{a_A} = \begin{pmatrix} 0.996 \\ 0 \\ 0.259 \end{pmatrix} \tag{4.3}$$

using $\mathbf{a_A} = (1, 0, 0)^T$. The antenna tilt causes an incomplete coverage in the antenna frame depending on the attitude mode (evident in Fig. 4.21). This is mainly visible when comparing forward and backward orientations. This results from the differences in the acquisition or loss of the signal at the beginning or end of a pass of a GPS satellite (Kobel et al., 2021).

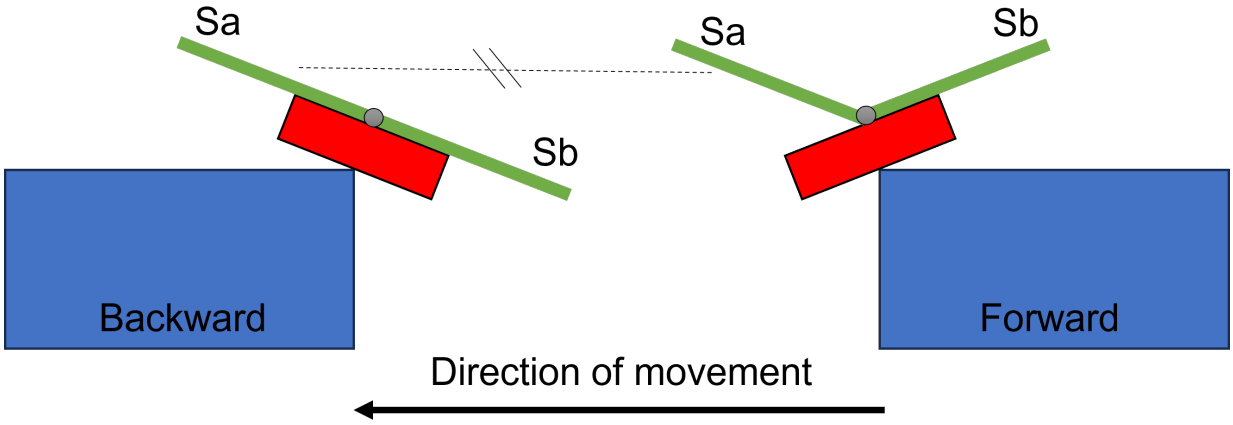

Figure 4.4: Jason-3 GPS receiver signal acquisition

Figure 4.4 describes schematically the two different signal-to-noise ratio thresholds, whereby one value S_a for acquisition and another value S_b for loss is indicated, and $S_a > S_b$. It is evident in Fig. 4.4 that due to geometry, the visibility cone for the acquisition is smaller for the forward orientation than for the backward orientation. Some added delays in the acquisition, as the receiver needs a certain time to lock correctly (Flavien Mercier, personal communication) additionally lead to different antenna coverages with GPS measurements for varying attitude modes.

4.1.3 Jason-3 solar panel rotation

The POD requires accurate modeling of the radiation pressure acting on the LEO. For this purpose, the optical properties of the LEO's surface are given in the form of a macro model (see Table 3.1). Information about macro models for Jason-3 and other LEO satellites is given in Cerri et al. (2018). An important feature of the Jason-3 LEO satellite is its rotating solar panels. In Cerri et al. (2018) it is stated that the solar array is rotating along the Y axis in order to be pointed towards the sun. The actual rotation angle relative to the central body is provided in a dedicated file. This opens the opportunity to assess the difference between the modeled and the measured rotation of the solar panel and the resulting influence on the POD. Dedicated experiments and their results are shown in sect. 4.2.4.

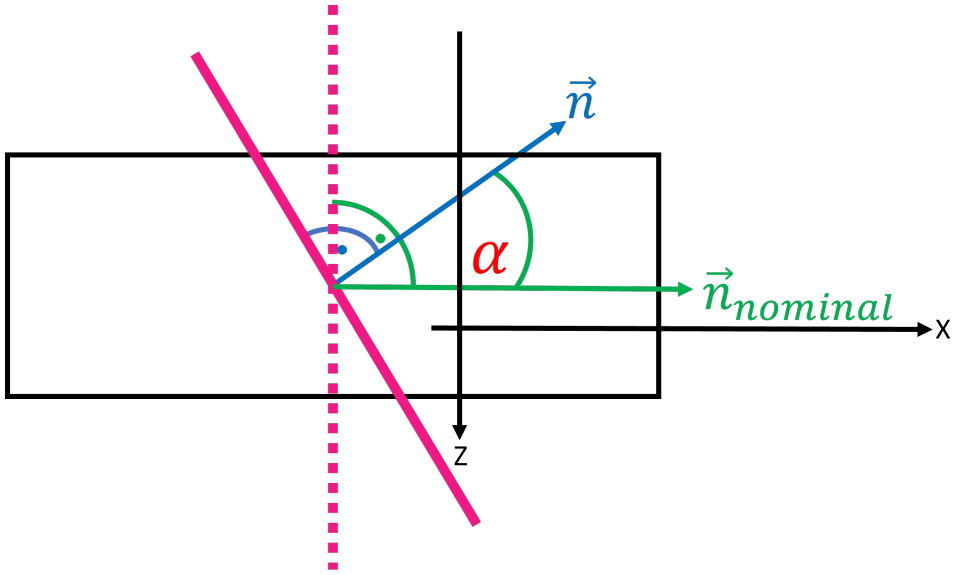

Figure 4.5: Jason-3 solar panel rotation

In Fig. 4.5 the pink color indicates the solar panels. The orientation of the solar panels is characterized by the normal vector on its surface. The solar panel's nominal orientation, as given from the macro model (Table 3.1), is indicated in green ($\vec{n}_{nominal}$). Another arbitrary orientation is characterized by the normal vector ($\vec{n}$), α describes the actual rotation angle that can either be modeled according to the intended solar panel orientation or is given in the dedicated files.

4.2 Experiments

Several key results regarding the POD of Jason-3 are presented in this section. Orbit validations are shown in terms of orbit comparisons. The influence of using measured solar panel orientation is investigated. The effect of non-gravitational force modeling is examined. The influence of single-receiver ambiguity resolution is also analyzed. An orbit validation based on SLR measurements is shown. A description of how PCO corrections and PCV maps were determined is described. It is specifically examined how many ambiguities are resolved as part of the data quality analysis.

4.2.1 Data quality of Jason-3 GPS observations

A prerequisite for a POD with high precision is good data quality of GPS observations received onboard the LEO. To assess the data quality of Jason-3 GPS observations, dedicated results are described in this section.

4.2.1.1 Code and phase measurements

First, we investigate the quality of the code observations. For this purpose, code residuals for 1 January 2022 are shown in Fig. 4.6. The results are quantified by analyzing code residuals from Sentinel-3A's POD of the same day. It is evident that the ionosphere-free code observations of Jason-3 exhibit larger noise than for Sentinel-3A, evidenced by the larger standard deviation (σ) of the observation residuals. A detailed analysis reveals that no GPS block-specific features (code patterns) are distinguishable. Important to note is that for GPS observations of Sentinel-3A an elevation cutoff of 10° due to receiver settings is present. The same cut-off has been used for Jason-3 for the comparison of the code observation residuals. It is important to note that whenever Jason-3 is processed, no elevation cut-off has been used unless specifically noted. In the POD processes carried out in the frame of this work, the code observations are only used for the first a priori orbit determination and the resolution of wide-lane ambiguities. Since the first a priori orbit is generally not critical for the final solution, the data quality in terms of noise is solely crucial for integer ambiguity resolution. An informative quantity to assess the quality of a LEO POD is the analysis of phase residuals. For this purpose, the ionosphere-free phase residuals from the final Jason-3 orbit adjustment

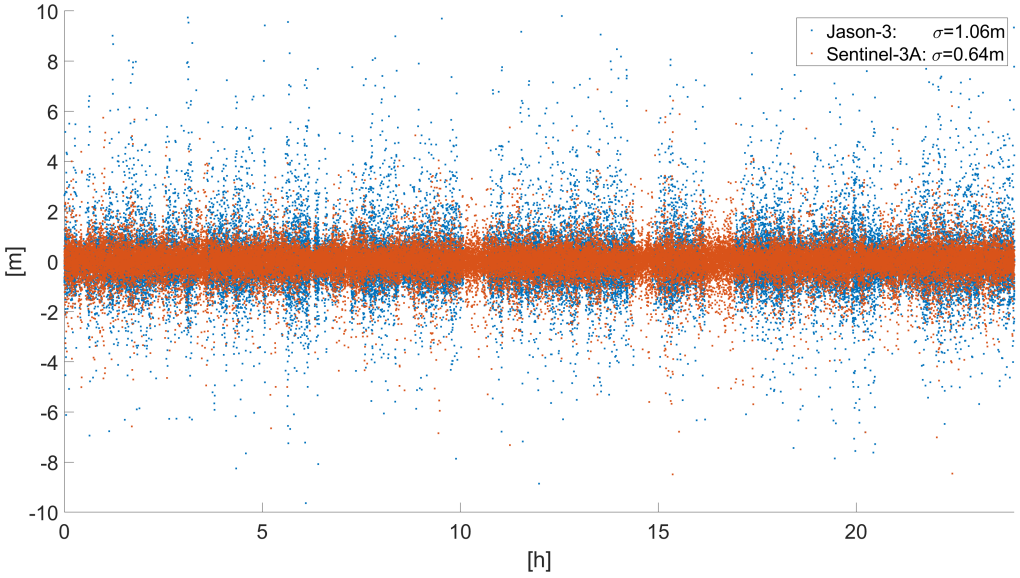

Figure 4.6: Ionosphere-free code residuals, Jason-3 and Sentinel-3A, 1 January 2022

process are illustrated in Fig. 4.7, again together with the residuals from a Sentinel-3A POD. For both receiving antennas (Jason-3 and Sentinel-3A) empirically derived PCV maps were applied in the processing.

Figure 4.7 reveals that the phase residuals resulting from the POD process are generally larger for Jason-3 than for Sentinel-3A, as it is indicated by the standard deviation (σ). It appears that the Jason-3 GPS receiver has larger residuals than the Sentinel-3A GPS receiver. For the PODs carried out to compute the phase residuals shown, PCV maps were applied, which were determined using the residual stacking approach (see sect. 3.4). The resulting RMS of the phase observation residuals indicates a superior orbit fit to the observations for Sentinel-3A. A possible reason for the larger code and phase noise of the Jason-3 GPS observations compared to Sentinel-3A could be the different types of GPS receivers mounted on the satellites. While Jason-3 is equipped with a blackjack reciever[1] developed by NASA, Sentinel-3A is equipped with a GPS receiver developed by RUAG Space (Montenbruck et al., 2018a).

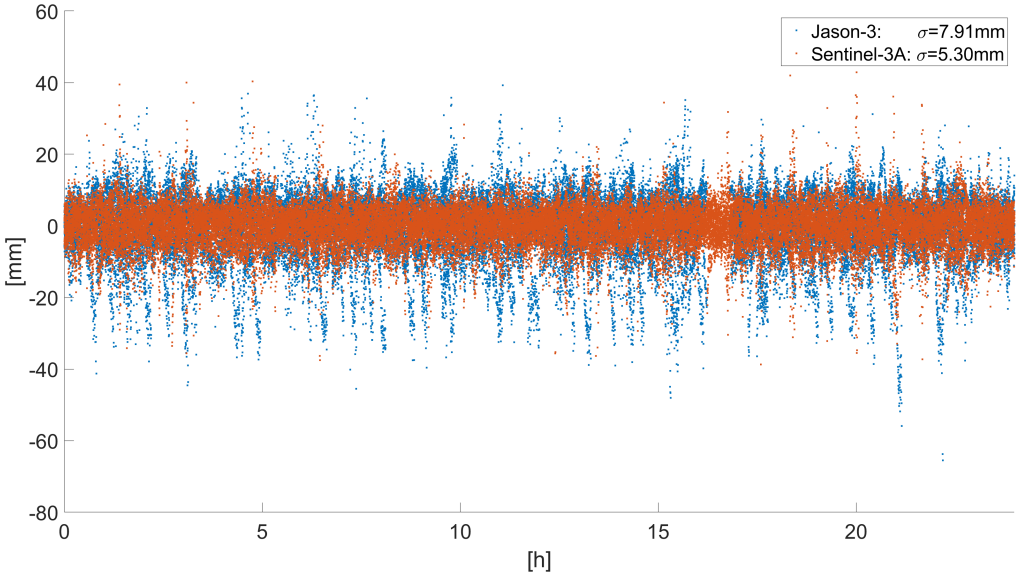

Figure 4.7: Ionosphere-free phase residuals, Jason-3 and Sentinel-3A, 1 January 2022

[1] https://www.aviso.altimetry.fr/en/missions/current-missions/jason-3/instruments.html (Accessed: 24 August 2023)

4.2.1.2 Single-receiver ambiguity resolution for Jason-3

To assess the quality of the ambiguity-fixing process, different measures can be analyzed. Figure 4.8 shows the Melbourne-Wübbena linear combination (see sect. 3.2.1.3) for 4 GPS satellites, shown by different colors, for 1 January 2019. The different passes of each individual GPS satellite can be seen.

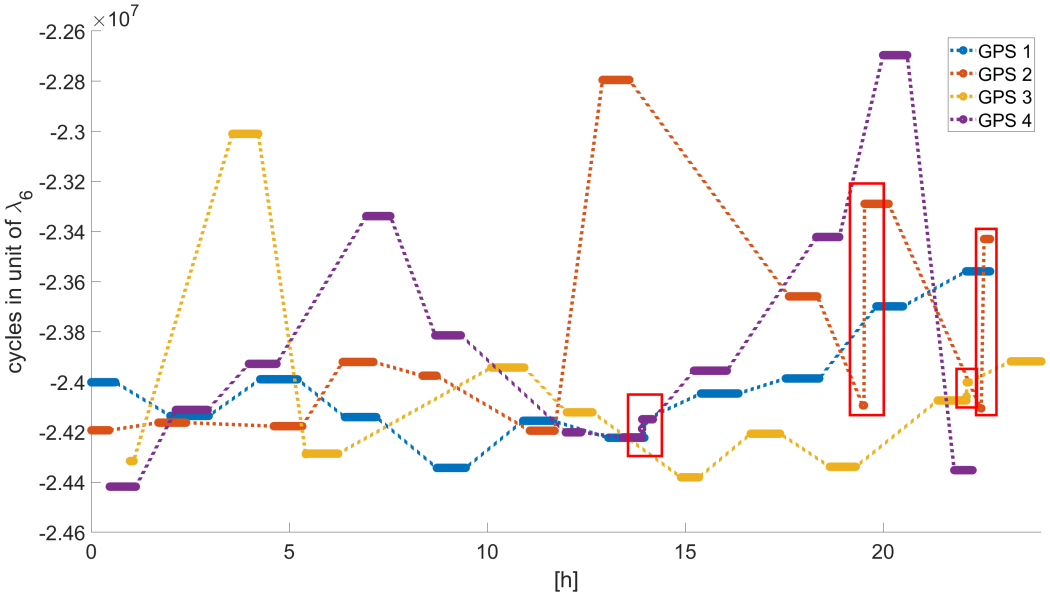

Figure 4.8: Melbourne-Wübbena LC Jason-3, 1 January 2019, for a selection of GPS satellites

In theory for every pass of a GPS satellite, the Melbourne-Wübbena LC should remain constant, if no cycle slip occurs, since it represents the wide-lane ambiguity. However, in Fig. 4.8 passes are visible for which this does not hold (marked in red boxes). The first box represents a cycle slip, caused by e.g., signal obstruction, multipath interference, or receiver noise, whereas the others result from bad observations at the beginning or end of a pass. This may lead to an incomplete or wrong resolution of integer ambiguities. For the shown examples, the ambiguities cannot be resolved to integer numbers and remain to be estimated as float numbers. Therefore, it is crucial that for the code observations, along with the phase observations, an outlier screening is performed.

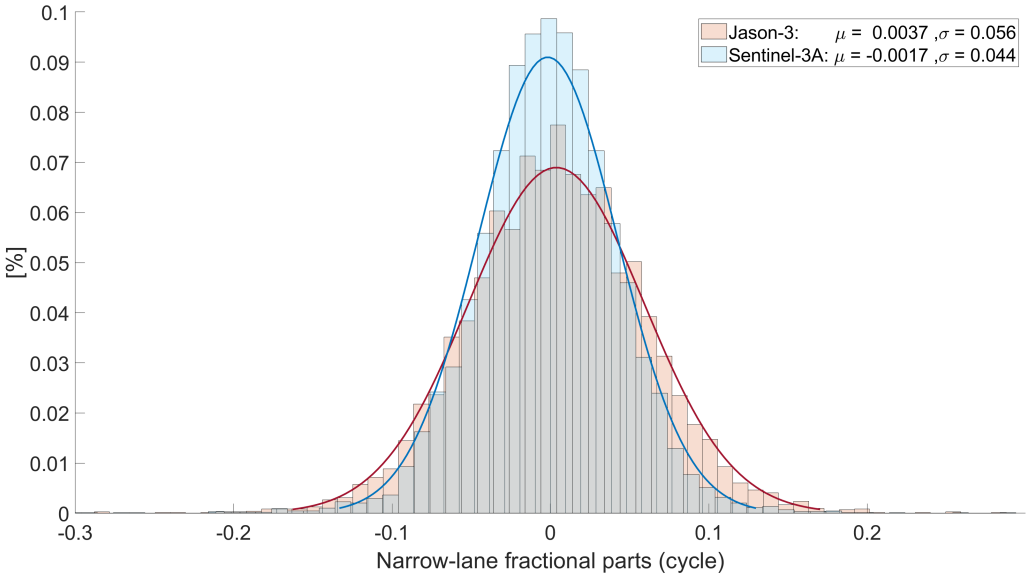

Figure 4.9: Narrow-lane fractional parts, Jason-3 and Sentinel-3A, 1 January 2019

In particular, the fractional parts of narrow-lane ambiguities provide an indication of the quality of the ambiguity-fixing. There is an obvious difference between the fractional parts for Jason-3 and Sentinel-3A when we examine Fig. 4.9. This indicates that the single-receiver ambiguity resolution of Jason-3 may be of poorer quality than for Sentinel-3A. The percentage of fixed ambiguities is shown in Fig. 4.10.

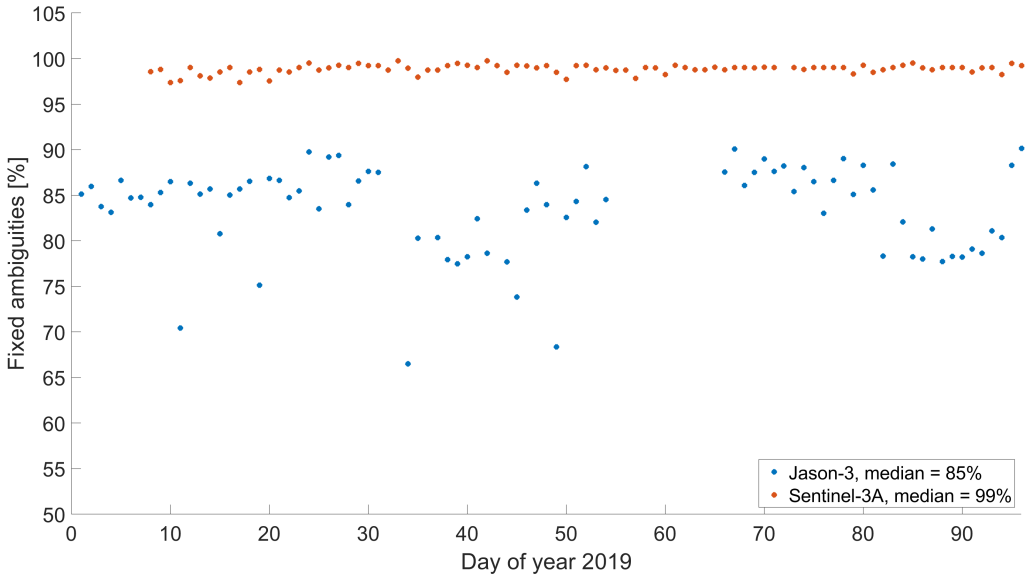

Figure 4.10: Ambiguity resolution, Jason-3 and Sentinel-3A

Jason-3 has a lower success rate in integer ambiguity resolution than Sentinel-3A, as shown in Fig. 4.10. This means that for a one-day orbit solution of Jason-3, more ambiguities remain float than for a Sentinel-3A orbit solution. For the precursor mission Jason-1 Laurichesse et al. (2009) stated an ambiguity-fixing rate of 95%, while for the Jason-2/OSTM Bertiger et al. (2010) notes issues with half-cycle carrier phase identification. In this work, the major reason for the comparably low ambiguity-fixing rate is the relatively large amount of wide-lane ambiguities that cannot be fixed, caused by the feature shown in Fig. 4.8.

4.2.2 Comparison of orbit solutions

Since it was the first time, that a POD of Jason-3 was conducted using the Bernese GNSS software, it is of central importance to compare the orbit solution to an externally determined reference solution, which is provided by the Centre National d'Etudes Spatiales (CNES). The derived orbit solution is parameterized by the six initial osculating elements (see Fig. 3.1) and three additional constant accelerations (one per spatial direction) over one arc, and piecewise constant accelerations, over 6 minutes, constrained to $5 \cdot 10^{-9}\mathrm{m/s^2}$. Figure 4.11 shows the daily mean values of an orbit comparison between the reduced-dynamic orbit solution, including ambiguity-fixing, and the reference orbit solution provided by CNES. For the reduced-dynamic orbit solution, non-gravitational forces were not explicitly modeled but absorbed by the PCAs. CNES's POD strategy includes the modeling of non-gravitational accelerations, which is the main difference between the compared solutions apart from different parametrizations. It is evident that in cross-track direction systematic orbit differences are present, whereby different offsets are visible for the satellite being in different attitude modes. Since the solar radiation pressure highly affects the satellites leveling in the cross-track direction (depending on the β-angle), a possible cause for the offsets evident can be the different handling of this force in the POD. The parametrization of the reduced-dynamic orbit solution includes the estimation of a constant acceleration in the cross-track direction which allows for a compensation of not modeling the SRP and consequently shifting the orbits. The cross-track leveling of the CNES solution is highly dominated by the explicit modeling of the SRP, whereby false information in the macro model can potentially lead to orbit shifts. Also, different information about the PCO can lead to systematic orbit shifts, especially when the orbit parametrization includes the estimation of constant accelerations, because a better fit of the trajectory to the observations (aligned to false PCO information) is possible. This causes an orbit shift of magnitude similar to the PCO error. Additionally, when the attitude mode changes, false information of

the PCO, would lead to orbit shifts in different directions, as evident in Fig. 4.11. Also, a general offset in the radial direction is present in the comparison of these two orbit solutions.

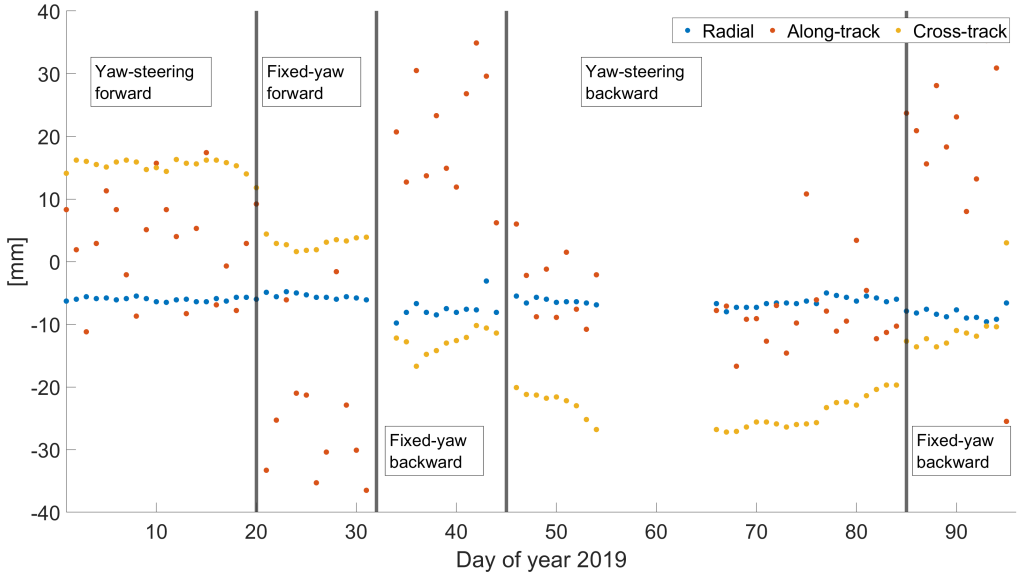

Figure 4.11: Daily mean values of comparison of Jason-3, reduced-dynamic orbit solution vs. CNES orbit solution

Apart from gravity, the major force influencing the satellites' radial leveling is the Earth's radiation pressure. A possible cause of the systematic offset in the orbit comparison could therefore point to inaccurate modeling of the Earth's radiation pressure, again compensated in the reduced-dynamic orbit solution by the co-estimated constant acceleration in the radial direction. However, this systematics may also point to false information in the PCO, whereby in the antenna frame the radial direction corresponds nearly to the Up direction (not exactly, because of the antennas' tilt). As explained, whenever systematic differences are visible in orbit comparisons, it is not possible to assign an error with one of the solutions by assessing only the orbit differences. It is only feasible to detect inconsistencies. However, it is clearly evident in the orbit differences in Fig. 4.11 that the explicit modeling of non-gravitational forces in CNES' POD or the PCO information are potentially incorrect. The most probable scenario is a composition of these two error sources.

4.2.2.1 POD including non-gravitational force modeling

A comparison of two solutions is carried out, whereby one represents the approach without non-gravitational force modeling and the other includes the modeling of solar radiation pressure, Earth radiation pressure, and air drag. The orbit is parameterized by the six initial osculating elements (see Fig. 3.1) plus piecewise constant accelerations which are constrained more tightly: 0.5 nm/s^2 instead of 5 nm/s^2, which is used for the solution where explicit non-gravitational force modeling is not applied, because the main purpose of estimating PCAs is to compensate for errors due to not modeling non-gravitational accelerations. For SRP and air drag a scaling factor was estimated each. In Fig. 4.12 daily mean values of orbit differences are displayed, showing the influence of non-gravitational force modeling on orbit levelling. It is evident that the attitude-mode systematic differences in cross-track direction shown in Fig. 4.11 are reduced to a large extent, however still present. This clearly points to a attitude-mode dependent systematic erroneous SRP modeling or PCO information. A systematic offset in the radial direction is present which has a similar magnitude as in the comparison to the CNES solution (Fig. 4.11). Since in both comparisons, the same offset is evident, it can be concluded that the radial leveling of the CNES orbit solution and the solution computed in the frame of this work using explicit non-gravitational force modeling are consistent. It is therefore important to explore potentially false information in the PCO to assess the inconsistency between the solutions compared in Fig. 4.12 in the radial direction. Since the systematics in the cross-track direction, which are shown in Fig. 4.12 are centered around zero for the different attitude modes, PCO corrections

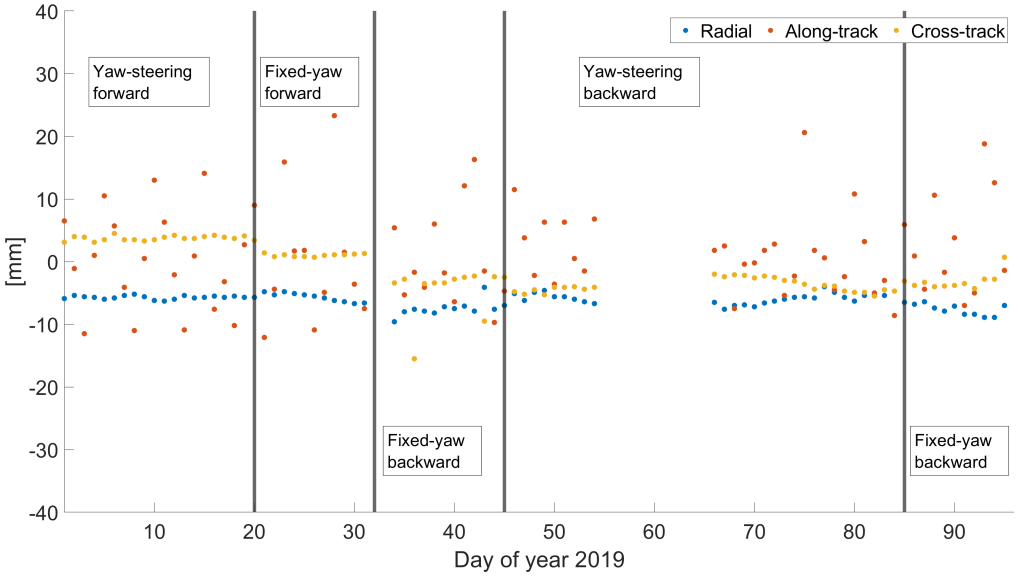

Figure 4.12: Daily mean values of comparison of Jason-3 orbit solutions using different orbit representation types

have the potential to further decrease the inconsistencies. The differences in along-track direction in both comparisons show comparably large mean values, whereby no systematics, like for the cross-track direction, is evident. Moyard et al. (2019) stated an along-track bias for Jason-3, revealed by SLR, whereby an error in the information of the ARP is assumed. Such an error is not possible to detect by using only GPS data, because the satellites' along-track leveling is highly correlated with the estimated receiver clock. Also Arnold et al. (2022) found an along-track error of 12.9 mm for the Jason-3 orbit solutions. Since Jason-3 orbits the Earth at a high orbital altitude where the air density is comparably small, it is of interest to investigate the influence of explicitly modeling the air drag. Since in eqn. (3.85) the air density plays a key role, it might be that the modeling of the air drag is prone to errors and should therefore not be applied in the POD of Jason-3. The derived orbit differences are, however, very small. A slight offset in the along-track direction of about 0.5 mm results, which indicates that the explicit modeling of air drag for Jason-3 is not crucial.

4.2.2.2 Influence of single-receiver ambiguity resolution

The strategy introduced in sect. 3.2.2 allows for the resolution of single-receiver ambiguities in the POD process. Montenbruck et al. (2018a) stated for Sentinel-3A that single-receiver ambiguity resolution leads to significantly smaller orbit misclosures. To determine the impact on the final orbit solutions when single-receiver ambiguity resolution is performed, in line with Montenbruck et al. (2018a), orbit misclosures are computed for two different solutions, one representing an ambiguity-float and the other one representing an ambiguity-fixed solution. Figure 4.13 shows the statistics of the orbit misclosure results in terms of median, 25th and 75th percentile, maximum and minimum, and outliers.

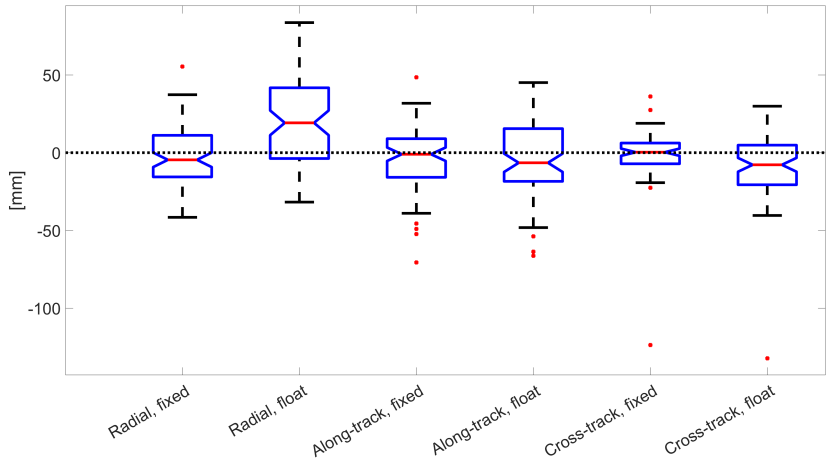

Figure 4.13: Jason-3, statistics of orbit misclosures for ambiguity-fixed/ambiguity-float solutions

It is evident that in all three spatial directions, the median and the interquartile range notably improve when single-receiver ambiguity resolution is applied. This result clearly indicates that single-receiver ambiguity resolution is crucial for Jason-3 POD and the derived orbit solutions are of superior quality. Therefore, for all experiments, where a Jason-3 POD is conducted, ambiguity-fixing is applied.

4.2.3 SLR validation of Jason-3 orbit solutions

An independent validation is necessary to determine the precision of the computed Jason-3 orbit solutions, which cannot be provided by orbit comparisons. A SLR validation, as a one-dimensional accuracy measure introduced in sect. 3.7.3, is carried out for different orbit solutions of Jason-3. To minimize the impact of bad SLR observations, a subset of SLR stations is chosen. A set of 10 stations was used, which are all well-performing stations according to GMV (2018). SLR residuals larger than 10 cm were identified as outliers and rejected from the analysis, resulting in 0.3% of the SLR data being rejected in average. Because the CNES orbit solutions are provided in the "sp3" format, the positions, given at integer second epochs, were extrapolated to the observations epochs of the SLR observations.

Table 4.1: SLR stations used in the processing[1]

Monument	Location
7090	Yarragadee, Australia
7105	Greenbelt, Maryland
7119	Haleakala, Hawaii
7501	Hartebeesthoek, South Africa
7810	Zimmerwald, Switzerland
7839	Graz, Austria
7840	Herstmonceux, United Kingdom
7841	Potsdam, Germany
7941	Matera, Italy
8834	Wettzell, Germany

A validation is carried out for orbit solutions for 1 January 2019 - 10 April 2019. The validated solutions are:

- Reduced-dynamic, no non-gravitational force modeling, ambiguity-fixed (RD)
- Reduced-dynamic, non-gravitational force modeling, ambiguity-fixed (NG)
- Reference solution from CNES (CNES)

[1] https://ilrs.gsfc.nasa.gov/network/stations/active/index.html (Accessed: 3 July 2023)

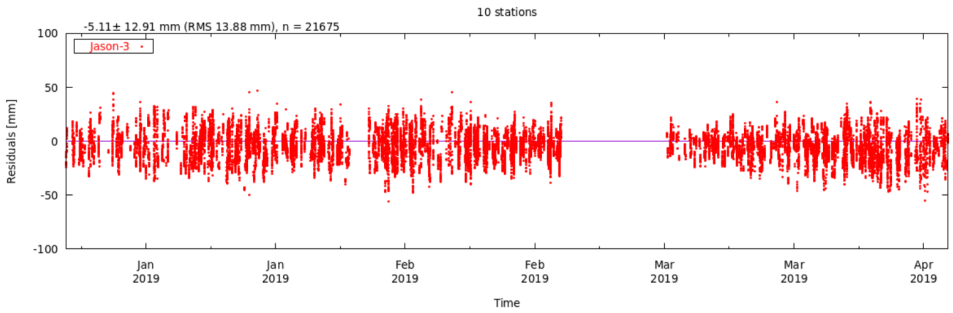

(a)

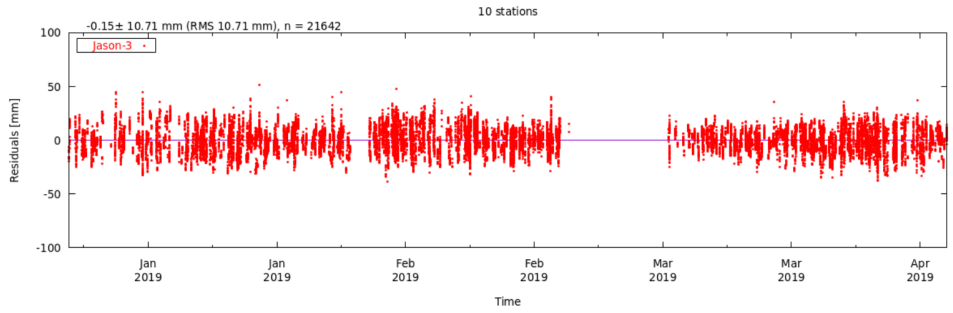

(b)

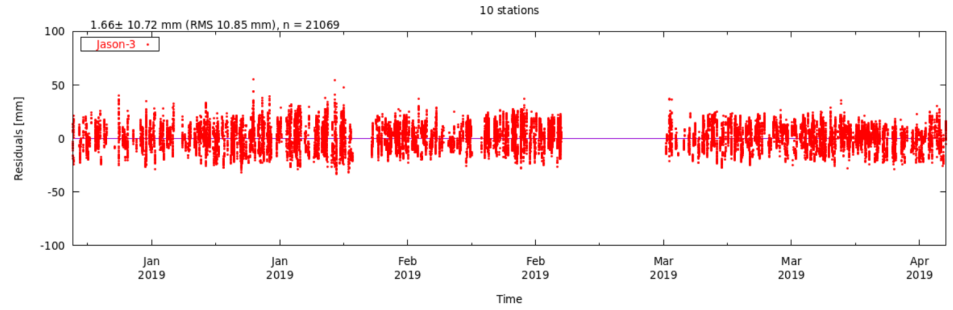

(c)

Figure 4.14: SLR validation of solution RD(a), NG(b), CNES(c)

It is evident in Fig. 4.14 that the SLR validation of the solution including non-gravitational force modeling has a smaller mean and standard deviation than the solution, where these accelerations are not explicitly modeled. The CNES solution shows a slightly larger mean value and standard deviation than the solution including non-gravitational force modeling. For the time period 24 February 2019 - 6 March 2019, no GPS observation data, and therefore no orbit solutions, are available.

Table 4.2: SLR validation Jason-3 orbit solutions

Solution	Mean	RMS
RD	-5.11mm	13.88mm
NG	-0.15mm	10.71mm
CNES	1.66mm	10.85mm

From the statistics shown in Table 4.2 one can conclude that the orbit quality of the derived orbit solution including explicit non-gravitational force modeling outperforms the reference solution from CNES in terms of a SLR validation. Additionally, it is evident that the RD solution, where no explicit non-gravitational force modeling was applied, shows larger mean and RMS values. This is an important indication that non-gravitational forces should be explicitly modeled in the Jason-3 POD.

4.2.4 Influence of using measured solar panel orientation

Cerri et al. (2010) stated that for Jason-2 the difference between measured (obtained from telemetry) and modeled orientation of solar panel orientation may amount up to 8°. Since Jason-3 is designed identical to Jason-2, the discrepancies are expected to have a similar magnitude. The comparison between the modeled and the measured rotation angle of the solar panels is carried out by making use of the Bernese GNSS Software. Figure 4.15 shows the differences for a period of 100 days. It is visible (in the upper plot) that for specific days, the differences are up to 180°, which means the modeled normal vector of the solar panel is in no consensus to the measured normal vector. Therefore, either the modeled or the measured rotation angle is erroneous. Additionally, for the periods where Jason-3 operates in fixed-yaw attitude mode (small β-angle), the differences show large variations. This is due to the fact that the rotation axis is nearly parallel to the satellite-sun vector and makes correct modeling almost impossible because the solar array is rotating in order to point towards the sun.

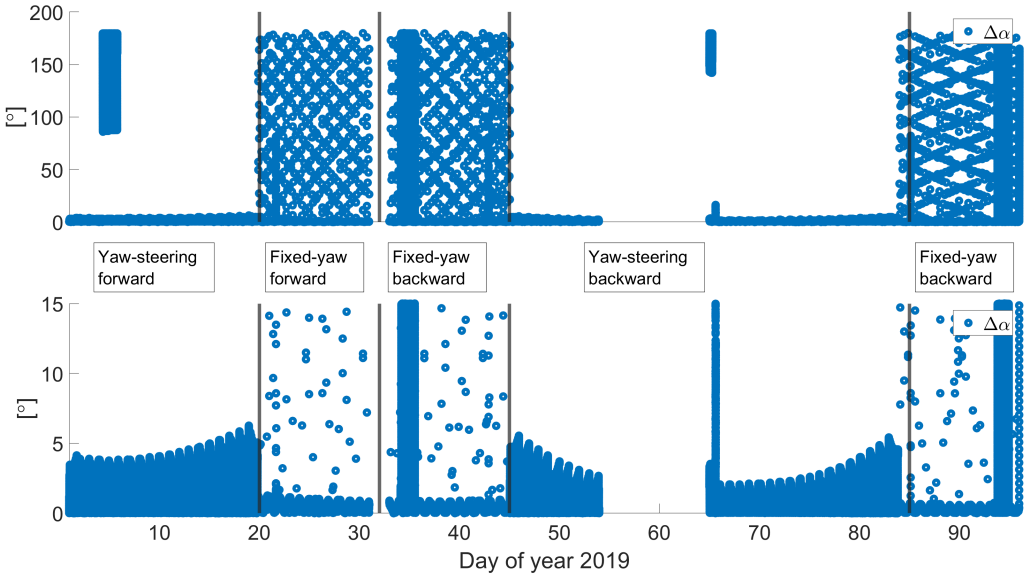

Figure 4.15: Jason-3, differences of measured and modeled rotation angles of solar panel

To clarify whether the findings match with the ones from Cerri et al. (2010), in Fig, 4.15 the differences are shown with a cut-off of 15° (lower plot). It is evident that during a yaw-steering attitude period, the amplitude of the differences is growing towards the beginning and the end. During a fixed-yaw period, the differences are generally smaller than during a yaw-steering period, apart from the previously mentioned large discrepancies, which are evident by the single points which reach much larger values. These large discrepancies occur because of numerical problems in the modeling of the rotation using the Bernese GNSS software. The maximum amplitude (about 6°) seems to be smaller as shown by Cerri et al. (2010). To investigate the influence of the usage of the measured rotation angles on the POD processing, two results are shown in the following; the estimated scaling factor for solar radiation pressure (Fig. 4.16) and the orbit differences of a comparison of two solutions with either solar panel orientation modeled or measured. In theory, when the modeling of the solar radiation pressure is accurate, the estimated scaling factor should be equal to one. It is evident in Fig. 4.16, that for the two solutions the estimated scaling factors for solar radiation pressure modeling are nearly identical, but a clear β-dependency is visible.

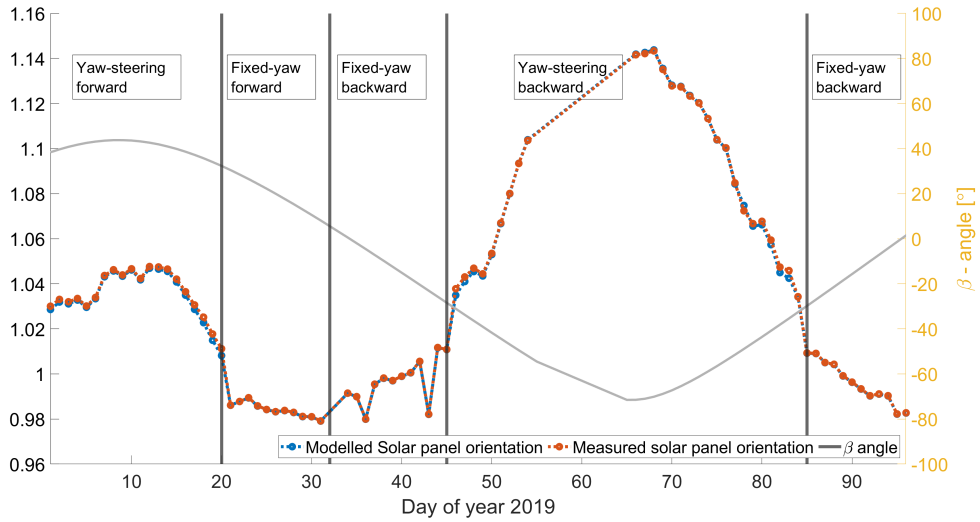

Figure 4.16: Jason-3, estimated scaling factors for solar radiation pressure

The orbit comparison, shown in Fig. 4.17, between the two different solutions reveals that the orbit differences between the two solutions, with modeled and measured solar panel orientation are negligible. Therefore, the usage of measured solar panel orientation in the POD process of Jason-3 is not critical. Regarding the large values at specific days during a yaw-steering period (see Fig. 4.15), it is important to note that whenever the angle between modeled and measured solar panel orientation is larger than 15°, the modeled values are used in the processing.

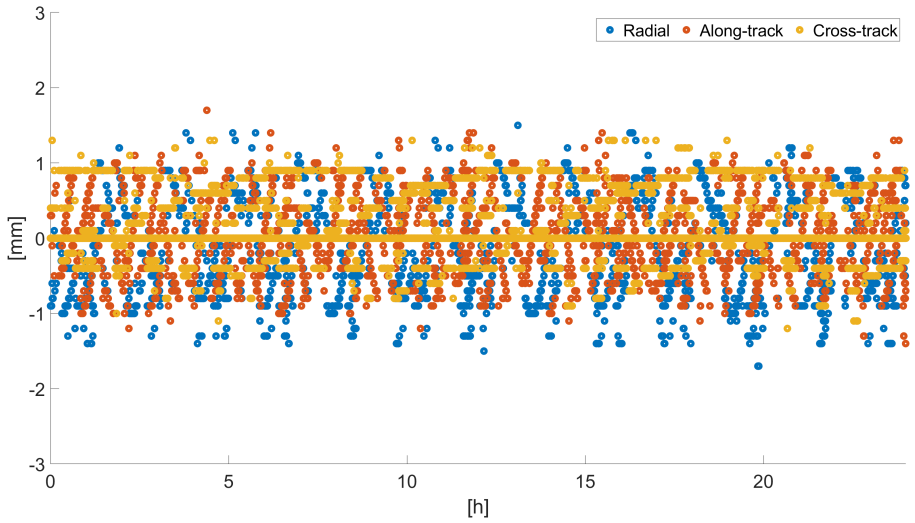

Figure 4.17: Jason-3, comparison of orbit solutions, with measured and modeled solar panel orientation, 1 January 2019

4.2.5 Estimation of PCO corrections and PCV map for Jason-3

The systematic attitude mode-dependent differences evident in Fig. 4.11 and 4.12 indicate that satellite-specific properties, namely the PCO, might not be as accurate as required. To exploit the potential to further increase the quality of the Jason-3 POD, corrections of satellite properties are estimated. This is done by estimating PCO corrections by different approaches, as well as the determination of a PCV map.

4.2.5.1 PCV map for Jason-3 GPS antenna

As described in sect. 3.4, accurate knowledge of the phase center variations of a LEOs' GPS antenna is eminently important (Jäggi et al., 2009). A PCV map for Jason-3 was derived using the approach described in sect. 3.4.

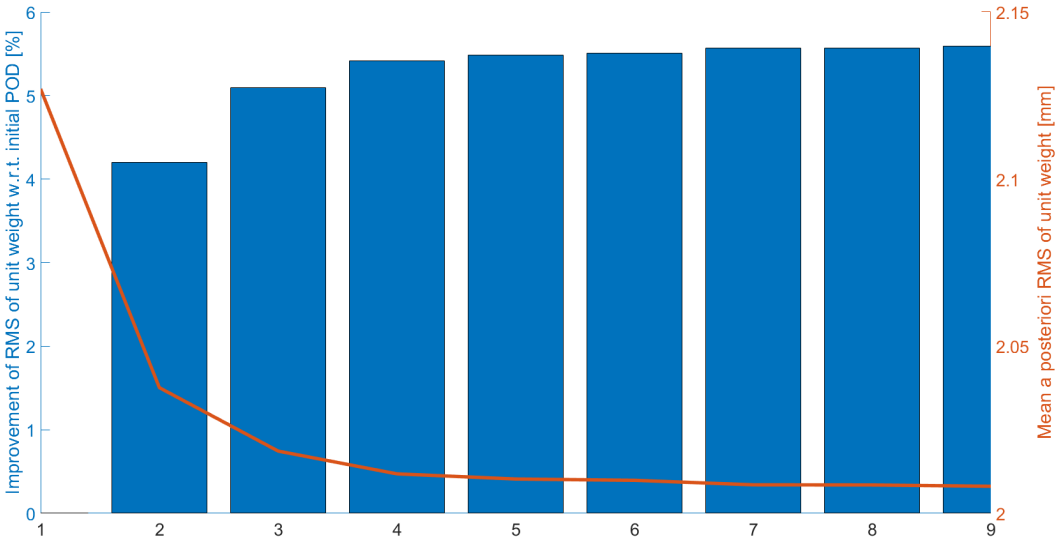

Figure 4.18: Jason-3, PCV determination, iterative improvement

Figure 4.18 shows the improvement of the a posteriori RMS of unit weight and its change for the iterative PCV determination procedure. It is visible that the determination of the PCV map converges after a few iterations. A total number of 10 iterations is sufficient to determine a PCV map of appropriate quality for Jason-3. The availability of an externally determined PCV map by CNES provides the possibility for comparison. For the Jason-3 satellite also a pre-launch PCV map is available.

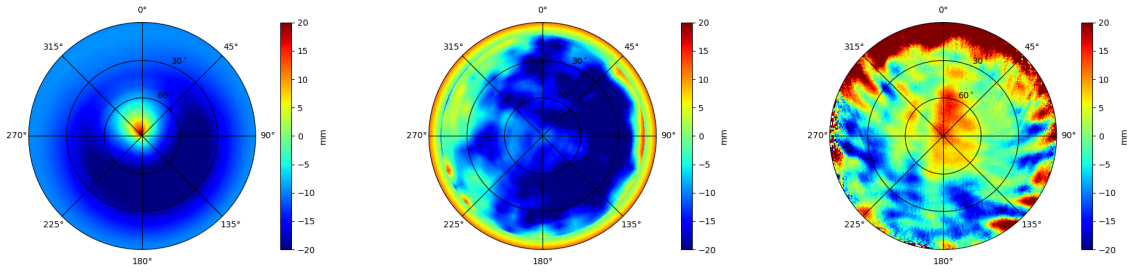

(a) (b) (c)

Figure 4.19: (a) Pre-Launch PCV (b) CNES PCV (c) Computed PCV

The comparison of the PCV maps in Fig. 4.19 shows clearly that for the derivation of the pre-Launch PCV map the satellite environment was not taken into account in terms of multipath effects. The PCV map provided by CNES shows no similarity with the PCV derived in the frame of this work. In contrast to the CNES PCV map, the computed PCV (from this work) map shows patterns that stem most probably from multipath effects. Possible reasons for this could be another approach for the generation of the PCV map, another orbit parametrization, or a different PCV definition (as described in sect. 3.4). It is therefore important that the LEO POD processing is always consistent with the generation of the PCV map used. An internal comparison of two orbit solutions, whereby the determined PCV correction was either applied or not, reveals the influence on the orbit level.

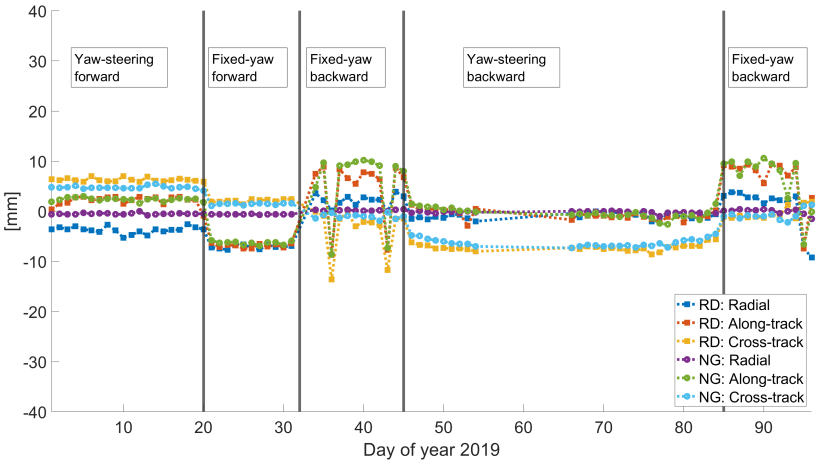

Figure 4.20: Influence of PCV map on orbit level for Jason-3, daily mean values of orbit comparisons

It is evident in Fig. 4.20 that applying a PCV map in the POD process influences the resulting orbit solution notably. Daily mean values of orbit differences between solutions which differ by either applying the derived PCV corrections or not applying them in the orbit determination, are shown. The results are shown for two orbit representation types: a reduced-dynamic orbit parametrization with no explicit non-gravitational force modeling (RD) and a more dynamic orbit determination with modeling radiation pressure and air drag (NG). The identical PCV map was applied for the RD and NG solution. The results mainly differ with respect to the radial direction. The NG solution is insensitive to the application of a PCV map on orbit level, which is evident by a nearly zero mean of the differences, in contrast to the RD solution. Figures 4.11, 4.12 and 4.20 reveal systematic differences depending on the attitude mode. This opens the question of whether for different attitude mode regimes, different PCV maps result. To assess this question, four different PCV maps were determined, whereby for each of them only observations were taken into account which stem from a specific attitude mode. A reduced-dynamic orbit parametrization with no explicit non-gravitational force modeling was used for this purpose. The processing was carried out for 1 January 2019 - 31 December 2019. The time periods (in DOY) for the different attitude modes are given in Table 4.3.

Table 4.3: Jason-3 attitude mode regimes in the year 2019

Yaw-steering forward	19/001-19/019
	19/106-19/146
	19/223-19/261
	19/349-19/365
Yaw-steering backward	19/047-19/083
	19/172-19/195
	19/285-19/323
Fixed-yaw forward	19/021-19/031
	19/103-19/104
	19/148-19/158
	19/211-19/221
	19/263-19/271
	19/336-19/347
Fixed-yaw backward	19/034-19/045
	19/085-19/094
	19/160-19/170
	19/197-19/209
	19/273-19/283
	19/325-19/334

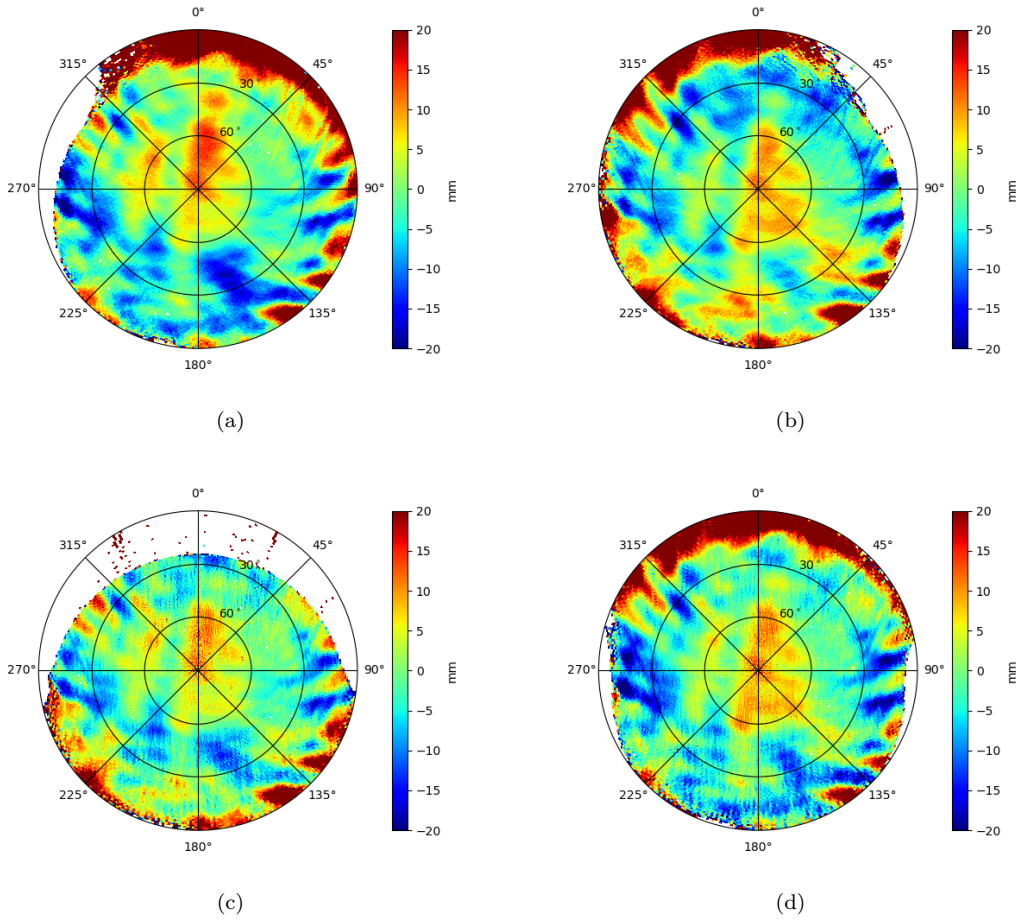

Figure 4.21: (a) PCV Yaw-steering forward (b) PCV Yaw-steering backward (c) PCV Fixed-yaw forward (d) PCV Fixed-yaw backward

Figure 4.21 reveals that the four determined PCV maps show similar patterns, whereby the magnitudes differ. The PCV map derived from GPS observations stemming from the fixed-yaw forward attitude mode clearly shows the incomplete coverage of the antenna as described in Fig. 4.4.

4.2.5.2 Estimate PCO from PCV

It is possible to estimate the induced phase center offsets from a PCV map using least-squares adjustment (sect. 3.1) with the model function (from Peter et al. (2017)) being:

$$\phi'(\alpha, z) = -\sin(\alpha) \cdot \sin(z) \cdot E - \cos(\alpha) \cdot \sin(z) \cdot N - \cos(z) \cdot U + \Delta\phi \tag{4.4}$$

$\phi'(\alpha, z)$ describes the PCV map, whereby α and z are azimuth and zenith angles respectively. The offset vector consists of three components: East (E), North (N), and Up (U). $\Delta\phi$ represents an arbitrary offset that is strongly correlated to the estimated receiver clock and is therefore not of interest for this analysis and not estimated. To estimate potential offsets from the determined PCV maps, a 30° elevation cut-off was applied, to account for the different incomplete coverages (Kobel et al., 2021). The estimations are based on the different attitude modes illustrated in Fig. 4.21.

Table 4.4: Extracted PCO corrections from PCV maps

	E	N	U
Yaw-steering forward	0.0 ± 0.01 mm	6.7 ± 0.01 mm	4.3 ± 0.002 mm
Yaw-steering backward	2.7 ± 0.01 mm	-3.6± 0.01 mm	3.3 ± 0.002 mm
Fixed-yaw forward	0.7 ± 0.01 mm	3.0 ± 0.01 mm	2.9 ± 0.002 mm
Fixed-yaw backward	1.9 ± 0.01 mm	0.6 ± 0.01 mm	4.1 ± 0.002 mm

Table 4.4 contains the estimated PCOs from the determined PCV maps for the different attitude modes. For all three directions in the antenna frame, the values differ notably for the different attitude modes. Since the PCO itself does not change depending on the attitude mode, this reveals systematic attitude-mode dependent orbit modeling issues. Remarkable is that in U-direction for all attitude modes an offset is revealed. In order to determine whether the usage of attitude mode-specific PCV maps in the POD process is beneficial in terms of orbit precision, a SLR validation (see sect. 3.7.3) is carried out.

The SLR validation (Table 4.5), carried out for the time period 1 January 2019 - 10 April 2019, shows that for the yaw-steering attitude modes, the usage of specific PCV maps leads to an improved orbit precision. The statistics for the fixed-yaw attitude modes do not show conclusive results, the mean value for the forward mode improves but the standard deviation does not. For the fixed-yaw backward mode, a deterioration of the mean value appears when using the attitude mode-specific PCV map while the standard deviation slightly improves.

Table 4.5: SLR validation of Jason-3 orbit solutions using attitude mode-specific PCV maps

	No specific PCV map	Specific PCV map
Yaw-steering forward	-2.91±14.26 mm	-1.51±13.86 mm
Yaw-steering backward	-4.95±10.65 mm	-3.94± 9.13 mm
Fixed-yaw forward	-4.50±11.44 mm	0.02±11.46 mm
Fixed-yaw backward	-6.60±15.85 mm	-9.73±14.61 mm

4.2.5.3 PCO correction from LEO POD and SLR

Due to the different attitude modes, the direction of flight coincides either with the positive or negative x-axis in the SBFF (Fig.4.1). Instead of determining PCO offsets from PCV maps, LEO antenna phase center offsets can be estimated by setting up corresponding parameters in the dynamic POD process. All three spatial directions can be corrected using data from the different attitude modes. The offsets in the local orbital frame can also be estimated using long time spans of SLR data as an independent measurement technique (Arnold et al., 2019). The results shown here follow Kobel et al. (2022a). A critical point to note is that in the orbit determination in this analysis, non-gravitational forces were explicitly modeled. However, unlike typical parametrization, no scaling coefficient for solar radiation pressure was estimated to prevent strong correlations between estimated PCO corrections and the SRP scaling factor (Kobel et al., 2022a). The relationship between the SLR validation and the estimated PCO corrections for the various attitude modes is shown in Fig. 4.22. The PCO corrections are estimated in the antenna frame: North (N), East (E), and Up (U). According to this information, modification of the PCO has the potential to change the leveling of

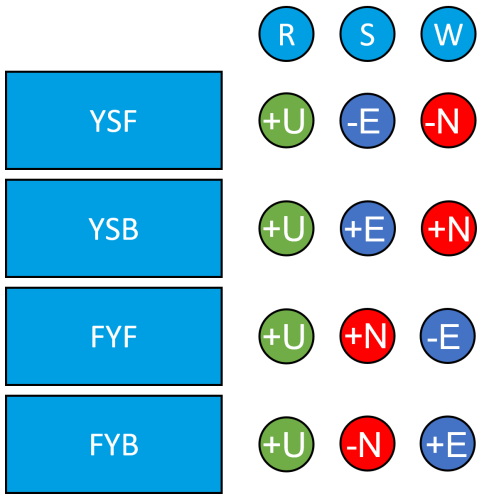

Figure 4.22: Relations N/E/U and R/S/W

the resulting orbits of Jason-3, as eventually revealed by a SLR validation. The relations shown in Fig. 4.22 can be derived from the knowledge about the orientation of the satellite in the different attitude modes as shown in Fig. 4.1. Note that the GPS antenna is tilted by 15° towards the +X axis (Fig. 4.4) which causes that estimated corrections in N and U direction do not perfectly align with the spatial directions (radial/along-track) in the local orbital frame.

An estimation of PCO correction and SLR validation were performed in an iterative manner. Based on the mean values of the initially estimated PCO corrections, adapted PCO information is used for the preceding iteration step. After the correction of the PCO values based on the initial PCO correction estimates, a further orbit determination is made, and a subsequent SLR validation with PCO correction estimation is carried out. To enhance the PCO correction, a second iteration is conducted, where PCO correction and reestimation (including SLR validation) are repeated. To mitigate any adverse effects on the solution due to the systematic differences observed in FYF/FYB attitude modes, as presented in Table 4.5, only the estimates derived from YSF/YSB were utilized for the applied correction in the U direction, because the major part of an SLR residual can be aligned with the radial leveling of the orbit, which in turn is mainly reflected by the U direction in the antenna frame. Figure 4.23 gives the results of the iterative procedure. According to the SLR validation, the applied corrections after the first iteration have exhibited inconclusive changes for the radial direction, namely in general larger offsets together with different signs for YSF and YSB. Consequently, the correction initially applied to PCO estimation for the U direction has been reverted (-9.3 mm). In the N direction, the correction is computed based on the offsets determined in the W direction for YSF and YSB, resulting in a correction of (-(-6.1 mm)+(6.7 mm)/2 = 6.4 mm, considering the relationship illustrated in Fig. 4.22 (accounting for the reverse sign of YSF). A general cross-track offset is identified for the E direction, which amounts to (((-3.1 mm)+(-4.6 mm))/2 = -3.85 mm). This offset is likely attributable to deficiencies in modeling solar radiation pressure. The applied correction is E =(-(-3.1 mm)+(-4.6 mm))/2 = -0.75 mm. It is worth noting that corrections derived from SLR validation must be applied with a change of sign. Particularly noteworthy is the difference in the estimated corrections in the U component between the two fixed yaw attitude modes. Based on the SLR validation results from the first iteration, it is evident that the correction applied to the PCO in the North direction, for instance, in the along-track direction (S), exhibits opposite signs for forward and backward orientation in the fixed yaw attitude modes. A similar observation is made for the correction applied to the East direction when comparing SLR validation results between the initial and first iterations of the yaw-steering modes.

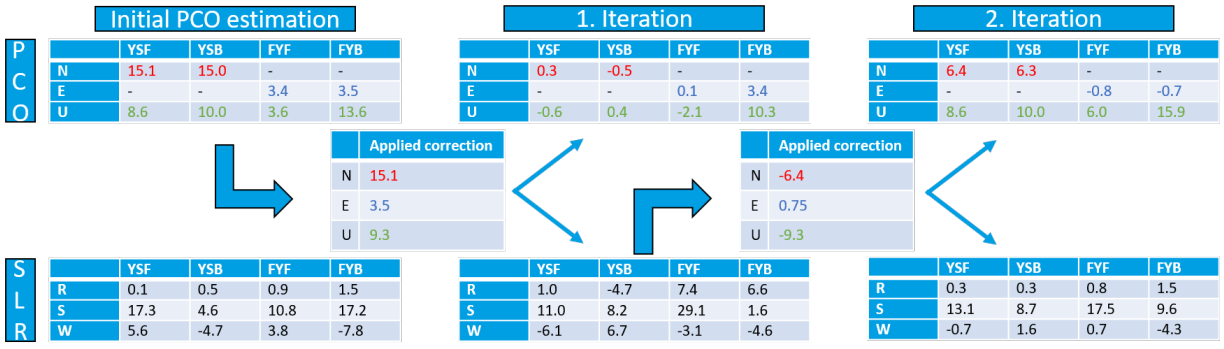

Figure 4.23: PCO estimation and SLR validation results

Subsequently, based on the first and second iterations, it becomes apparent that applying the estimated PCO correction in the U direction can impact the radial leveling of Jason-3 but does not enhance it. The results suggest that if the estimated offsets for the fixed-yaw steering attitude mode and yaw steering attitude mode are similar, including an opposite sign, an error in the PCO (center-of-mass) information is present. In the local orbital frame, the presence of mean offset estimates differing from zero, e.g., for cross-track directions in the fixed yaw attitude modes, suggests potential mismodeling of the POD, possibly due to an inappropriate SRP modeling resulting from the large area-to-mass ratio (Lemoine et al., 2019). According to the results shown in Fig. 4.23, by adding the applied corrections from the two iterations, a PCO correction is needed: N =(15.1-6.4) mm = +8.7 mm, and E = (3.5+0.75) mm = +4.25 mm. When

applying these corrections, the SLR validation reveals a small mean for all attitude modes in the radial and cross-track directions. It is highly likely that the observed offsets in SLR validation after the PCO correction are attributable to orbit modeling issues. A bias is detected in the fixed yaw attitude modes when a yaw flip occurs, consistent with the findings of Moyard et al. (2019), where the error source may be imprecise information regarding the distance between the GPS antenna and the SLR retroreflector.

Recall: In the POD of Jason-3, special focus must be put on difficulties associated with its satellite design such as changes in attitude mode depending on the β-angle, incomplete GPS antenna coverage, and rotating solar panels. The Jason-3 POD results indicate poorer GPS data quality compared to Sentinel-3A, whereby receiver ambiguity resolution has a lower success rate, and code and phase observations show larger residuals. The computed Jason-3 orbit solutions show systematic differences to a reference solution, while different strategies such as ambiguity resolution, and explicit non-gravitational force modeling notably improve the accuracy of the orbit solutions. A SLR validation of different orbit solutions of Jason-3 showed that the quality of the computed orbits outperforms the reference solution. Different approaches for the determination of a PCV map and for PCO corrections showed significant variations for different attitude modes, while a SLR validation indicated that an iterative manner of PCO estimation allows for further improvement in the precision of the resulting orbits.

Chapter 5

Phase center offset correction estimation

With recent advancements in scientific research aimed at enhancing orbit determination precision, it has become increasingly important to know the satellite's specific properties to improve resulting orbit solutions. The experiments shown in this section address potentially needed corrections of these properties, as any inaccuracies in the provided information may lead to a degradation in the computation of a global network solution derived from the LEO-integrated approach. One of the most essential satellite properties within this research domain is the PCO information. Pre-launch determination of LEO receiver antennas PCO (and PCV) information is known to often show discrepancies to in-flight analyses. Consequently, in-flight PCO corrections may be needed, based on the original pre-launch values.

All Sentinel satellites collect measurements transmitted from GPS satellites, with Sentinel-6A additionally collecting measurements from the Galileo system. Previous studies from Montenbruck et al. (2018a), Peter et al. (2020), and Montenbruck et al. (2021), have highlighted deficiencies in the PCOs of the Sentinel GNSS antennas, evidenced by different empirical orbit parameters for similar satellites. The experiments shown in this section aim to estimate corrections for the existing PCOs of Sentinel-1, Sentinel-2, Sentinel-3, and Sentinel-6A satellites while investigating their variability and reliability. The estimation of PCO corrections is carried out as an integral part of the POD process, necessitating the application of single-receiver ambiguity resolution to enhance the stability of the estimated PCOs. Accurate modeling of non-gravitational forces acting on the satellite is essential to achieve precise PCO estimates. To assess the impact of such modeling deficiencies on PCO estimation, a specific experiment has been conducted. By determining PCO corrections, it becomes possible not only to improve the accuracy of observation modeling but also to identify potential modeling deficits related to non-gravitational forces.

In pairs (A and B), the Sentinel-1,2,3 satellites are identical in construction, making it possible to compare their estimated corrections for the PCOs directly. The plausibility of the PCO correction can be determined by this method. Using that the Sentinel-3 and Sentinel-6A satellites are equipped with SLR retroreflectors, SLR validations are carried out to investigate possible changes in (radial) leveling after applying the derived corrections to the PCO, which serves as a reliability test of the PCO correction estimations. In this work, the PCO correction estimation consists of two steps:

1. POD including single-receiver ambiguity resolution
2. POD with estimation of PCO corrections, reintroducing solved ambiguities from step 1

Through the use of the nominal attitude of the LEO and the relationship between the satellite body-fixed frame and the antenna frame, it is possible to reconstruct which direction (N/E/U) roughly corresponds to the along-track direction in the local orbital frame, since this direction cannot be corrected, because it is highly correlated with the orbit parameter u_0 (see sect. 3.2) and the estimated receiver clock.

5.1 Orbit parametrization in PCO correction estimation

Using explicit non-gravitational force modeling, such as solar radiation pressure, Earth radiation pressure, and air drag, reduced-dynamic orbit solutions are computed in this work. It is important to note that no scaling factors are estimated for these forces as this would potentially affect the estimation of PCO corrections. As part of the parametrization, PCAs are also estimated for along- and cross-track directions, always valid for 30 minutes. In order to estimate PCO corrections reliably and meaningfully, it is necessary to fix integer ambiguities (Peter et al., 2020). No PCV maps were applied in order not to influence the PCO estimation.

Table 5.1: LEO orbit parametrization and models in PCO correction estimation

Parameter/Model	
Radiation pressure model	Macromodel
Earth radiation	Albedo and infrared
Atmospheric density model	DTM2013 (Bruinsma, 2015)
Orbit parametrization	6 initial osculating elements Piecewise constant accelerations in Along-/Cross-track directions every 30 min, constrained to zero with $5 \cdot 10^{-10} m/s^2$
Observation sampling	10s
Antenna PCV	Not Applied
Ambiguities	Introduced (integer)

Table 5.1 provides detailed information on the parametrization and force modeling in the PCO estimation process for the LEO receivers. It may be possible that co-estimated PCAs interfere with the PCO correction estimation. The relationship between an incorrect ARP and the acceleration necessary to compensate for it is given in Montenbruck et al. (2018a). Consequently, in light of the fact that PCO correction can also be aligned to a wrongly given ARP, the relationship also holds for the purpose of these experiments. For the cross-track direction the (linearized) relation

$$\Delta a_C = \frac{GM}{r^2} \cdot \frac{\Delta r_C}{r} \tag{5.1}$$

holds, when Δr_C is the ARP inconsistency in cross-track direction. For the radial direction the relation

$$\Delta a_R = -3\frac{GM}{r^2} \cdot \frac{\Delta r_R}{r}, \tag{5.2}$$

holds, whereby Δr_R is the ARP inconsistency in the radial direction.

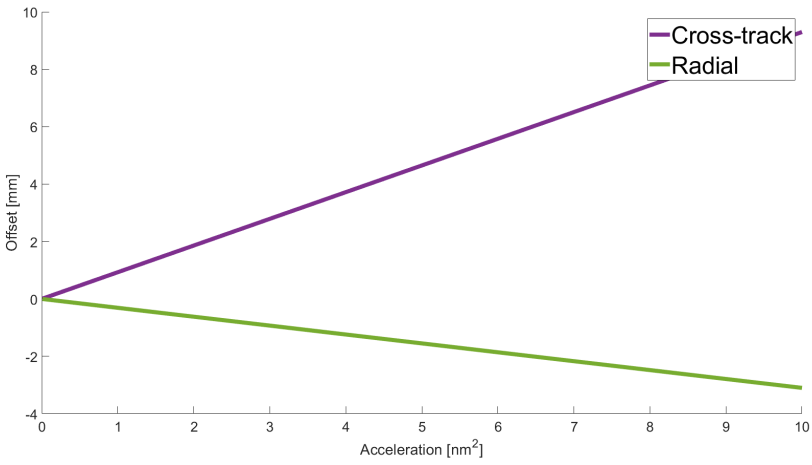

Figure 5.1: Linearized relation between wrong ARP and induced empirical acceleration

According to Fig. 5.1, the parametrization given in Table 5.1 causes a possible disturbance smaller than 1 mm from the PCAs on the estimated PCOs. For the experiments shown hereafter, only PCAs in along- and cross-track directions have been estimated, since, for the altimetry missions investigated in this work, it is of special importance to perform POD resulting in a superior radial leveling of the orbit. This requires that PCO correction estimation and PCAs do not interfere with one another, which is only possible when PCAs are not set up in radial direction.

5.2 PCO correction estimation results

The results of PCO correction estimation for Sentinel-1, 2, and 3 are presented in this section. Daily PCO correction estimations were computed for all six satellites for one year (2020), resulting in estimates in the Up direction or either in the North or East direction in the antenna frame, depending on the satellite's nominal attitude.

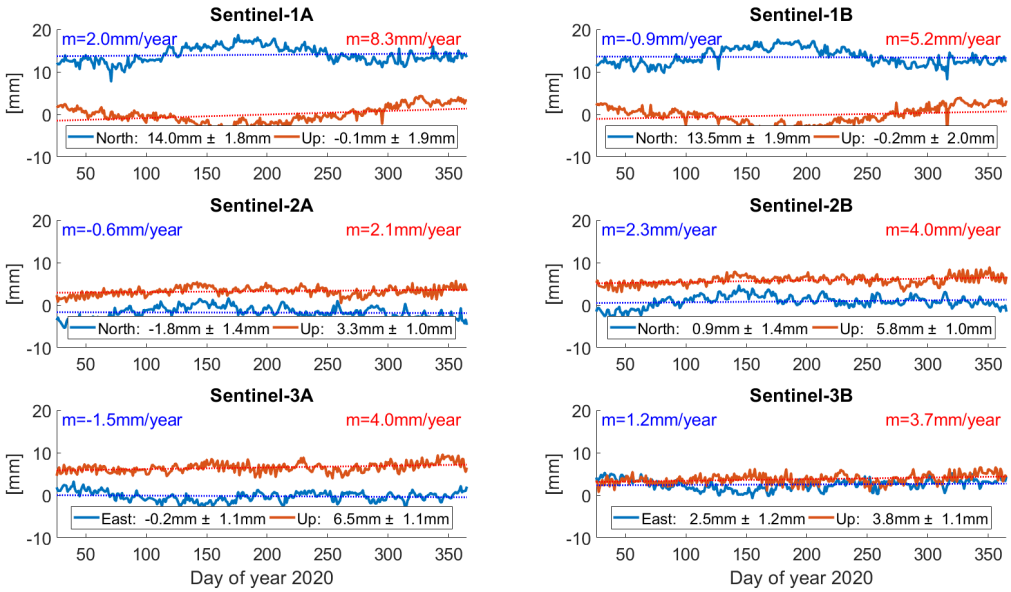

Figure 5.2: PCO correction estimations for Sentinel satellites

In Fig. 5.2 the PCO estimates are shown, whereby corresponding mean values and standard deviations are given, together with an estimated trend including the corresponding slope. What is evident at first is the periodicity of the estimation for the Sentinel-1 estimates, whereby the systematics for both (A and B) are very similar. The period of this systematics is related to the variations of the β-angle of the satellites. It is in accordance with the findings by Peter et al. (2020), where this systematics is evident in the estimation of scaling factors for solar radiation pressure when no PCO correction was estimated, but also when the scaling factor was fixed to 1.0 and a PCO correction estimation was carried out. As pointed out by Peter et al. (2020), the use of highly accurate macro models is crucial for modeling non-gravitational forces, particularly with regard to the SRP. Since the shape of the Sentinel-1 satellites is more complex than for other LEOs, it is also of interest to investigate the influence of self-shadowing on the POD and especially on PCO correction estimation. The model developed and applied for this purpose can be found in Table 5.2 (from Peter et al. (2020)).

It is important to note, that for the estimates shown in Fig. 5.2 for the Sentinel-1 satellites no quaternions were used, but the attitude was modeled according to the nominal attitude. This allows for a comparison to a dedicated experiment, where the measured attitude is processed and used from an external source, as it is usually done whenever a LEO was processed in the frame of this work. It is evident that for all estimates shown in Fig. 5.2, a positive gradient for the estimated U component between 2.1 mm/year and 8.3 mm/year can be seen. For the Sentinel-2 satellites similar results are obtained, whereby the mean values are comparably small, -1.8/0.9 mm for Sentinel-2A and 3.3/5.8 mm for Sentinel-2B, respectively, in N and

U directions. Furthermore, the very small standard deviation of a maximum of 1.4 mm indicates that the estimates are very stable over the investigated time period. The Sentinel-3 satellite PCO estimates are similar to those of Sentinel-2 satellites. There is an even smaller standard deviation of 1.2 mm and below for the estimates, indicating that the estimates of PCO corrections are very stable.

Table 5.2: Self-shadowing model for Sentinel-1

Surface	Sun incident angle	Surface correction factor
-z	$\theta(-z) = [30°...60°[$	$1 - \frac{\cos(\theta(-z)) - \cos(60°)}{\cos(30°) - \cos(60°)} \cdot 0.4286$
-x	$\theta(-x) = [53.13°...90°[$	$1 - \frac{\cos(\theta(-x))}{\cos(53.13°)} \cdot 0.1481$
Solar panel	$\theta(-x) = [53.13°...90°[$	$1 - \left(1 - \frac{\cos(\theta(-x))}{\cos(53.13°)}\right) \cdot 0.1614$

5.2.1 PCO correction estimation special case: Sentinel-1A

The experiments shown in this section were designed to address and investigate the potential pitfalls described in the previous section, from which some have been already pointed out by Peter et al. (2020). These are namely:

- Attitude: Nominal model versus quaternions
- Effect of applying a self-shadowing model (see Table 5.2)
- Trend in estimated PCO corrections
- Potentially insufficient macro model

To address these points, results from five different experiments are shown here, in terms of estimated PCO corrections, together with the result already shown in Fig. 5.2 for Sentinel-1A as a reference.

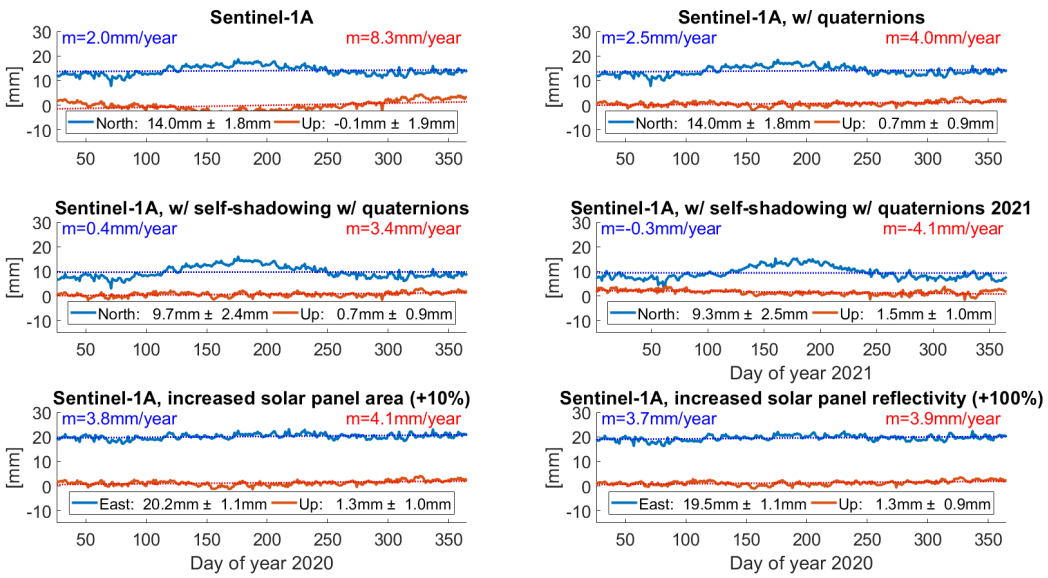

Figure 5.3: PCO correction estimations for Sentinel-1A

The comparison of the results in the plots of the top row from Fig. 5.3 reveals the influence of either modeling the attitude or using the quaternions. It is clearly visible that the estimated corrections in the U component show notably less periodic behavior, whereby also the standard deviation drops from 1.9 mm to 0.9 mm. This indicates that the usage of measured quaternions is important for the estimation of PCOs. It can be anticipated that the use of quaternions in the POD for Sentinel-1 leads to an improvement compared

to using modeled attitude information. The influence of using the self-shadowing model, as described in Table 5.2, can be seen from the top right plot and the middle row left plot. The comparison of these results reveals a deviation in the N component since the estimated corrections result in a smaller mean value when self-shadowing modeling is used. As the self-shadowing model is a more sophisticated approach, it can be assumed that the SRP modeling is more accurate, which influences the cross-track leveling, and, therefore, also the PCO correction estimation in N-direction. However, the periodicity of the estimates remains in the estimates. In order to examine the trends in PCO correction estimations, the PCOs of Sentinel-1A are also examined for 2021. Considering the results shown in the middle row, it is clear that this trend does not appear to continue with the same slope in the following period, but rather shows an opposite sign. As a result, it can be concluded that the trend is not due to any change in satellite properties as a result of aging. Possible explanations for the trends, visible for all examined Sentinel satellites, are annual signals in the Earth's center-of-mass coordinates or ERPs. The last tests for Sentinel-1 shown here served to investigate the periodic behavior of the estimated corrections in the N component. Two results are shown in the lower row of Fig. 5.3, whereby the used macro model, was modified. The left plot shows the result when the solar panel area is increased by 10 percent. The plot on the right-hand side shows the results when the solar panel reflectivity is doubled. In both of these scenarios, the periodic signature of the estimated corrections in the N component visible in all the other plots vanishes. This indicates that the macro model for the Sentinel-1 satellites is not as accurate as it is for the other sentinel satellites that were investigated in this work. The applied corrections to the macro model of both scenarios, however, tend to represent unrealistically extreme cases. It is more likely that a combination, possibly together with corrections to other satellite-specific properties, is accurate.

5.2.2 Impact of parametrization/models on PCO correction estimation

To assess the influence of orbit parametrization in terms of estimated PCAs to the PCO estimation, three experiments were carried out, whereby the number of PCAs per day is varied and the need for PCAs in radial direction is investigated. Together with these experiments, a solution is computed to address the question about the influence of explicitly modeling the Earth's albedo, since this force has the potential to influence the radial leveling of an orbit solution to a large extent.

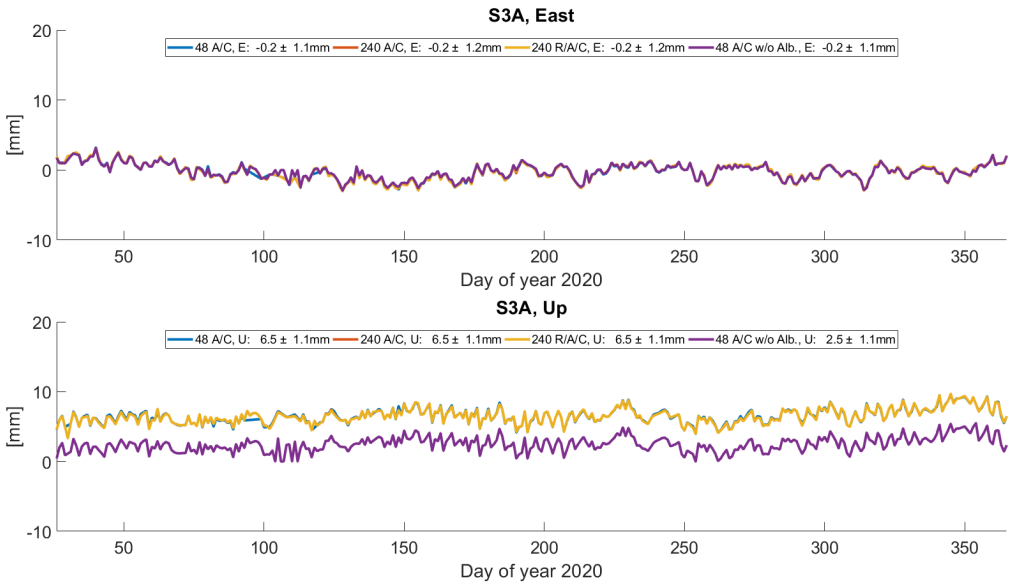

Figure 5.4: PCO correction estimations for Sentinel-3

The results of these experiments, as shown in Fig. 5.4 reveal, that the number of PCAs estimated in the process is not crucial for the estimated PCO corrections, since the values do not vary notably for the three solutions (blue, red and yellow) in both, N and U, components. Additionally, no notable difference results when en-or disabling PCAs in the radial direction, which is an important finding since it is desired to estimate as few PCAs as possible as long as the result is not deteriorated. This goes in line with

the theoretical analysis shown in Fig. 5.1. This result serves as validation of the choice of the orbit parametrization adapted in the PCO estimation processes shown in this section (see Table 5.1). The purple line represents the estimates from a solution where the Earth's albedo was not explicitly modeled. The shift in the estimates evident in the lower plot of Fig. 5.4 is clear evidence of the importance of properly modeling non-gravitational forces since the impact on the PCO correction estimation is notable. From this result itself, it cannot be concluded if the Earth's albedo modeling is erroneous. An independent validation, e.g., an SLR validation, has to be performed to assess the absolute orbit quality. It is evident in Table 5.3 that the PCO correction estimation, where the Earth's albedo was explicitly modeled, leads to orbit solutions of superior quality. This finding confirms the assumption that whenever a LEO is processed, of course also in the frame of the computation of a global network solution with LEOs integrated, accurate modeling on non-gravitational forces is crucial.

5.2.3 PCO correction estimation for Sentinel-6A

For Sentinel-6A the analysis of PCO correction estimation was carried out for the time period of one year (2021). It's not the same time period as for the other Sentinel satellites, because Sentinel-6A was not in orbit for this period (see sect. 2.5.3). The processing also differs from the previously shown results in the way that two PCO corrections have been estimated, since Sentinel-6A, as the only Sentinel satellite processed in this work, can also collect observations from the Galileo system.

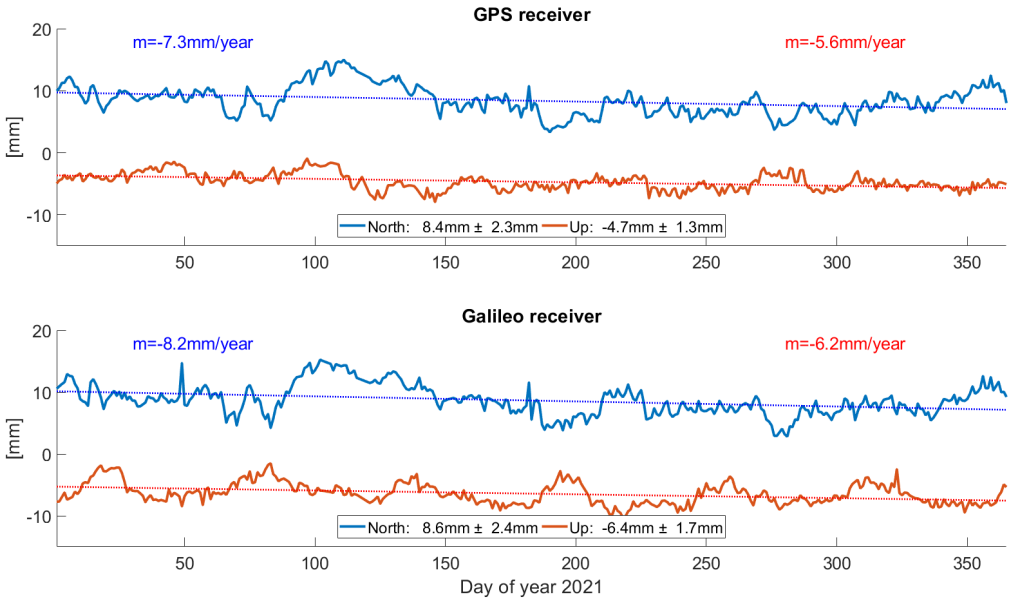

Figure 5.5: PCO correction estimations for Sentinel-6A

Figure 5.5 shows the daily estimates of the PCO corrections of the two Sentinel-6A receivers. For the determination of each of these always only data from the specific system has been used, in order to not deteriorate the solution by introducing a stiffness due to fixed PCO values of the other system. When comparing the estimates from Fig. 5.5 to the estimates in Fig. 5.2 it is evident that a larger variation results for the Sentinel-6A case. The estimates for the PCOs show similarities in terms of systematics, which leads to the conclusion, that this is probably due to errors/problems in the POD approach itself. Similar offsets (mean values) in the N and U components of the estimates result for both PCOs, whereby for the N component a correction of about 8.5 mm is the consequence. This could potentially point out incorrect information about the vector from center-of-mass of the satellite and its antenna. This result is in line with the finding of Montenbruck et al. (2021), where a correction for the antenna reference point in the Y-direction in the SBFF of roughly 8 mm was estimated.

5.2.4 Validation of PCO correction estimations

The parametrization of determined orbit solutions has the potential to influence the sensitivity to the PCO in terms of radial leveling of the resulting trajectories. If no constant accelerations over one arc are estimated, the resulting orbit is barely shifted in the radial direction by introducing a change in the PCO, whereby also the estimation of PCAs can not compete with such a change according to eqn. (5.2). To carry out a quality control for the estimated PCO corrections a POD is needed where a constant acceleration (in radial direction) over one arc is included in the parametrization. By performing a SLR validation, as an independent technique, it is possible to verify the correctness of the applied PCO corrections assuming that SLR offsets are correct. Since the Sentinel-3 and Sentinel-6A satellites are equipped with SLR retroreflectors, this validation has been performed. The validation was carried out for the processed time period for two solutions each, whereby for one the original and for the other the modified (estimated) PCO information was used in the POD.

Table 5.3: SLR validation of orbit solutions using modified PCO

Satellite	Original PCO	Updated PCO
Sentinel-3A	-3.17 mm±8.62 mm	1.15 mm±8.56 mm
Sentinel-6A	3.08 mm±9.13 mm	-0.84 mm±9.02 mm

According to the statistics of the SLR validation, shown in Table 5.3, applying estimated PCO offset corrections leads to reduced-dynamic orbit solutions of improved quality, since mean and standard deviation are smaller when using a corrected PCO in the POD process (Kobel et al., 2022b). This finding has the important consequence that information about satellite-specific properties, like the PCO or the macro model, may be erroneous. Unfortunately, such incorrect information has the potential to map into the computation of a global network solution using the LEO-integrated approach.

Recall: Aiming to improve the precision of orbit determination, PCO corrections for specific Sentinel satellites were estimated. These experiments use non-gravitational force modeling such as solar radiation and Earth radiation pressure to compute reduced-dynamic orbit solutions while estimating PCO corrections for LEO receivers with integer ambiguities fixed during the POD process. The PCO correction estimation results showed comparably small offsets in the U component for the Sentinel-2 and 3 satellites, while for the Sentinel-1 satellites a significant dependency on the β-angle has been identified. Dedicated experiments of estimating PCO corrections for the Sentinel-1 satellites imply that an inaccurate macro model was used. The application of estimated PCO corrections results in reduced-dynamic orbit solutions of superior quality as assessed by SLR validations.

Chapter 6

LEO integrated processing results

This section describes the experiments carried out to address specific parts of the key questions of this work. Following the description of the experiments, detailed results of these experiments are presented, in which specific quality characteristics are discussed. In Sect. 3.7, the analyzed quantities are presented, whereby not all of the quality checks are possible depending on the specific setup. Other studies, e.g., Huang et al. (2020), investigated the influence of various different combinations of integrated LEOs, whereby in the previous studies (shown in Sect. 2.7) the number of integrated LEOs is always smaller than in the present work. This approach is not followed in this work, because of a total of 511 possible combinations. When taking into account the possible Spire satellites, this number increases even to 262143. This number, however, does not include specific experiments where the influence of specific modeling selections, e.g., explicit modeling of non-gravitational forces, are investigated. Therefore, setups were chosen, designed to address specific aspects of the key questions of this work. The chosen experimental designs, including the processed time period, the number of integrated LEOs, and specific modeling applied for the experiments, are shown in Table 6.1.

Given the selection of a comparatively large ground station network, it is plausible that several stations do not contribute observations to a one-day solution due to a range of possible factors, including system failures, power outages, the upload of new software, or the installation of new hardware components. This may result in a notably less dense coverage, leading to a potential bias in the resulting solution. In order to not deteriorate the statistical outcome of the results, particular days showing such characteristics have been identified as outliers and omitted from the analytical procedures. Additionally, for all LEO-integrated solutions, a resulting one-day solution was not taken into account in the statistical analyses if the POD of an integrated LEO failed. This may be caused by data problems, e.g., missing GNSS observations or attitude information, maneuvers, etc.

Table 6.1: Performed experiments: LEO integrated processing

Time period		Integrated LEOs		ID	Specialities
14.01.2022 - 13.02.2022	(31 days)	-	(0)	R	Reference solution
14.01.2022 - 13.02.2022	(31 days)	Sentinel-3A	(1)	A	
14.01.2022 - 13.02.2022	(31 days)	Sentinel-3A, Sentinel-3B	(2)	B	
14.01.2022 - 13.02.2022 13.02.2022	(31 days)	Sentinel-3A, Jason-3	(2)	C	
14.01.2022 - 13.02.2022	(31 days)	Sentinel-3A, Jason-3 GRACE FO-C	(3)	D	
14.01.2022 - 13.02.2022	(31 days)	Sentinel-3A, Sentinel-3B GRACE FO-C, GRACE FO-D Swarm-A, Swarm-B, Swarm-C Jason-3, Sentinel-6A	(9)	E	
14.01.2022 - 13.02.2022	(31 days)	Sentinel-3A, Jason-3 GRACE FO-C	(3)	G	No integer ambiguity resolution for LEOs
14.01.2022 - 13.02.2022	(31 days)	Sentinel-3A, Jason-3 GRACE FO-C	(3)	H	No explicit modeling of non-gravitational forces for LEOs
14.01.2022 - 13.02.2022	(31 days)	-	(0)		GPS + Galileo
14.01.2022 - 13.02.2022	(31 days)	Sentinel-6A	(1)		GPS + Galileo
20.05.2020 - 19.06.2020	(31 days)	-	(0)		Reference solution
20.05.2020 - 19.06.2020	(31 days)	Sentinel-3A, Sentinel-3B GRACE FO-C, GRACE FO-D Swarm-A, Swarm-B, Swarm-C Jason-3, Sentinel-6A	(9)		
20.05.2020 - 19.06.2020	(31 days)	Spire	(9)		All (Table 2.1)
20.05.2020 - 19.06.2020	(31 days)	Sentinel-3A, Sentinel-3B GRACE FO-C, GRACE FO-D Swarm-A, Swarm-B, Swarm-C Jason-3, Sentinel-6A, Spire	(18)		
01.01.2020 - 31.12.2022	(1096 days)	-	(0)		Reference solution
01.01.2020 - 31.12.2022	(1096 days)	Sentinel-3A, GRACE FO-C Jason-3	(3)		Parametrization as D

6.1 Influence of incorporation of LEO observations

In this section, results are shown for the experiments which were carried out for the time period 14 January 2022 - 13 February 2022. The aspects of the key question which are addressed by the specific experimental setups are:

- What is the impact of integrating different numbers of LEOs (in different orbital planes) on the resulting global network solution?
- Is the applied procedure for the single-receiver ambiguity resolution for the LEO-GPS observations beneficial for the integrated processing?
- How does the orbit modeling of the integrated LEOs, especially in terms of explicitly modeling non-gravitational forces, influence the determination of a global network solution?

6.1.1 Observation residuals and noise

The first quantity analyzed is the RMS of the observation residuals referring to the observations on L1 and L2 used from the ionosphere-free linear combination. This value represents the noise level and therefore the goodness of the fit of the model parameters to represent the observations. Figure 6.1 shows the result for the experiments analyzed in this section in terms of mean values and standard deviations of daily observation RMS values. Note that the legend is adapted according to the IDs of the experiments given in Table 6.1.

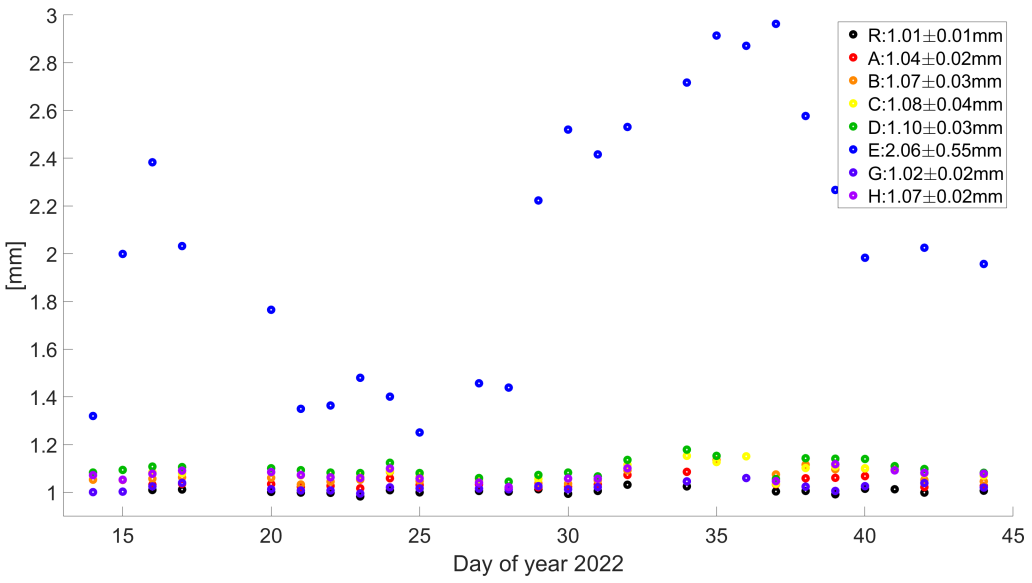

Figure 6.1: RMS of observation residuals in integrated processing of L1 phase observations

It is evident that the solution providing the smallest mean value of the daily RMS of the observation residuals (stated in the legend of Fig. 6.1) is the reference solution, where no observations from LEOs have been included in the processing, as well as the solution G with an almost identical mean value. The comparison of solutions A, B, C, D, and E clearly reveals the influence of including different numbers of LEOs in the processing on the resulting RMS of observation residuals. Solution A, where only one LEO (Sentinel-3A) is incorporated shows the smallest RMS of these solutions. When more LEOs are added to the system (B, C = 2 LEOs, D = 3 LEOs), the resulting mean RMS increases. When the number of incorporated LEOs reaches a large number (9 in the case of scenario E), the resulting RMS of observation residuals is heavily increased by the LEO observations, compared to the experiments where fewer LEOs are integrated into the processing.

The solution G differs from solution D by a larger mean value of daily RMS of observation residuals, caused by the handling of integer ambiguities for the LEO observations. The average ambiguity-fixing rate for the LEO GPS observations is 77%, and therefore generally smaller than for the LEO-only POD

case (see sect. 4.2.1.2). For the ground station GPS observations, the amount of fixed ambiguities is larger than 90%. It can be stated that adopting the procedure of fixing ambiguities of the LEO GPS observations leads to larger observation residuals in the LEO-integrated approach. This can be explained by the fact that float ambiguities can absorb modeling errors (to some extent) in contrast to fixed ambiguities, which then in turn may lead to larger residuals when single-receiver ambiguity resolution is applied for the LEO observations.

When comparing the results for solutions H and D the effect of explicitly modeling non-gravitational forces, as described in Sect. 3.3, on the resulting observation residuals can be explored. The different parametrizations of the LEO orbit for these two experiments, namely the estimation of constant accelerations over one arc in the radial, along-track, and cross-track directions and the looser constraints for the PCAs ($5{\cdot}10^{-9}$ m/s^2 instead of $5{\cdot}10^{-10}$ m/s^2), lead to distinguishable capabilities of absorbing modeling errors. The parametrization of the LEO orbits in solution H leads therefore to smaller observation residuals as for solution D.

In the LSQA the a posteriori RMS of unit weight m_0 is computed, which represents an estimation of the observation noise. The relation of observation RMS and a posteriori m_0 is given by eqn. 3.10. The estimated observation noise in a GPS-only global network solution determined in this work is at the level of 1 mm of L1 phase observations. The a posteriori RMS of LEO-only POD results depends on the satellite, whereby the typical range is from 1.5 mm (GRACE FO-C) to 2.6 mm (Swarm-C). Table 6.2 provides the mean values and standard deviations of the daily a posteriori RMS m_0 for the LEO-integrated solutions and the reference (GPS-only) solution computed for the time span 14 January 2022 - 13 February 2022.

Table 6.2: A posteriori RMS m_0 of LEO-integrated solutions

ID	A posteriori RMS m_0
REF	1.01±0.01 mm
A	1.04±0.02 mm
B	1.07±0.03 mm
C	1.08±0.04 mm
D	1.10±0.03 mm
E	2.06±0.55 mm
G	1.02±0.02 mm
H	1.07±0.02 mm

First, it is evident that the GPS-only (REF) solution shows the smallest estimated a posteriori m_0 among the solutions. It can be stated that the estimated observation noise level is at the mm level. The results reveal that integrating LEOs leads to an increase in the estimated observation noise. This is especially already the case for one included LEO (scenario A). When a second LEO is added to the system (scenario B) the estimated a posteriori m_0 is increased. The larger m_0 of scenario C compared to B may be explained by the different GPS receivers mounted on the included satellites (see sect. 2.5), where it has been shown that the observation noise depends on the specific receiver. Another reason can be potentially larger deficiencies in the LEO orbit modeling of Jason-3 compared to Sentinel-3B. Adding a third LEO in scenario D leads again to an increased m_0, which can be interpreted, using together with the estimated m_0 of solution E, that adding further LEOs to the integrated processing systematically increases the estimated observation noise. It is possible to determine which of the included LEOs leads to notable increases in the estimated observation noise. For this purpose, for day 14 January 2022, LEO-integrated solutions were determined, whereby additional LEOs were successively added to the system.

Along with the results for the reference solution, where no LEO is included, Fig. 6.2 shows that the largest increase of the a posteriori RMS results from the integration of the Swarm satellites. It is evident that the integration of an additional satellite, from which its "twin" has already been included, only leads to a comparably small increase in the estimated observation noise, e.g., the addition of Sentinel-3B. For Swarm-C, however, the increase is larger, given that Swarm-A has already been integrated. According to Lück (2022), the explicit modeling of non-gravitational accelerations from Swarm presents a higher level of

complexity compared to other LEO missions. Another plausible cause for the comparably large increase of the estimated observation noise could be erroneous information about the PCO.

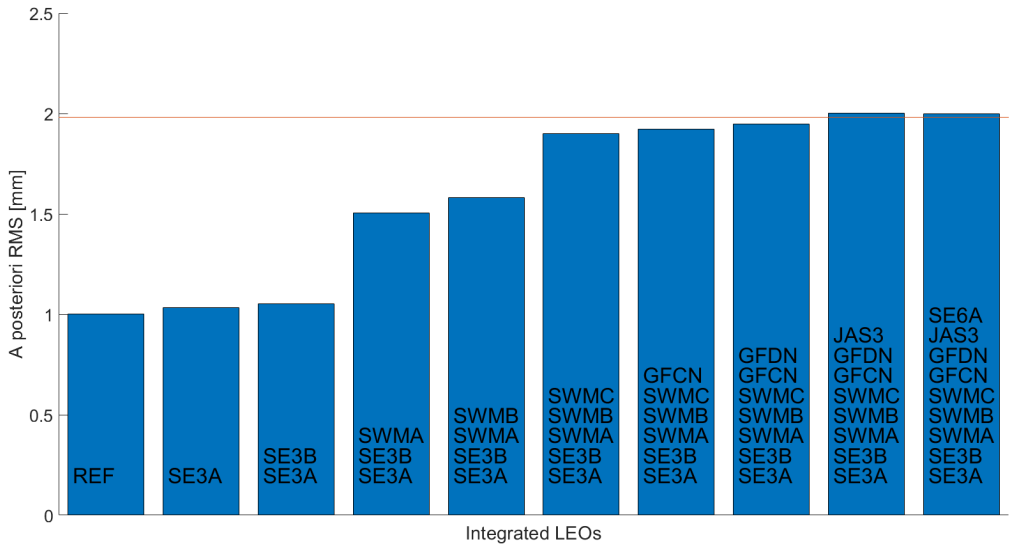

Figure 6.2: A posteriori RMS depending on included LEOs

Peter et al. (2016) demonstrated that a PCO correction for Swarm-A of -10 mm in the U direction is indicated. For Swarm-C Mao et al. (2021) concluded that a PCO correction of -4.85 mm is needed to ensure consistency in the radial leveling between dynamic and kinematic orbit solutions. It was shown by Huang (2022), using a LEO-integrated approach, that noticeable z-PCO correction estimations for Swarm-A, -B, and -C are indicated ranging from -4 mm to 4 mm, whereby a periodic behavior of the estimates is described, assigned to the draconitic period of the LEOs. When the LEO orbit parametrization does not include the estimation of constant acceleration over one arc, as adapted for solution E, false information about satellite-specific properties, e.g., the ARP/PCO, directly maps into the a posteriori RMS. However, a solution, whereby a correction of -10 mm (in U direction) is applied to the Swarm-A PCO only leads to a decrease of the a posteriori m_0 of below 1%. Additionally, a reduction of the constraints for the PCA's may be needed to account for the decreased sampling compared to a LEO-only POD (300 sec vs. 10 sec). Table 6.3 provides the percentual decreases of the a posteriori m_0 for different scenarios, exemplarily for 14 January 2022, where only Swarm-A has been integrated, compared to a (Swarm-A only) integrated solution using the parametrization described in Table 3.2, whereby non-gravitational forces were explicitly modeled and single-receiver ambiguity resolution was applied.

Table 6.3: Decrease of a posteriori m_0 for Swarm-A integrated solutions

Contraints of PCAs	Decrease of m_0
$3{\cdot}10^{-9}$ m/s^2	7%
$3{\cdot}10^{-8}$ m/s^2	6%

The change of the estimated noise in the LEO-integrated processing using adopted PCA constraints, shown in Table 6.3, reveals that LEO orbit characteristic-specific and observation sampling-specific constraints may potentially decrease m_0. This is further discussed in sect. 6.1.4.

The results suggest that the inclusion of LEOs introduces additional sources of observation noise into the system. The present results reveal the complex connection between the integration of LEOs and the influence on the estimated observation noise of the global network solution. The variations of m_0 between the different solutions underline the need for a comprehensive understanding of the LEO orbit modeling to further enhance the integrated processing and to improve the overall accuracy. Adding LEOs to the system

results in an increase in observations and parameters. The explanation for the increased m_0 is that when integrating LEOs into the system the overall increase in model errors is not compensated by the adjustment of additional parameters. The smaller mean value of m_0 for scenario G than for D reveals that single-receiver ambiguity resolution causes an increase in the estimated observation noise. This can be explained by the fact that modeling errors can be absorbed by float ambiguities, which in turn leads to smaller observation residuals, which then map into the estimation of the a posteriori m_0 leading to an increase. From this feature, it can be concluded that the LEO orbit modeling induces increased modeling deficiency of the full system. An increase of the a posteriori m_0 comparing an ambiguity-float and ambiguity-fixed solution can be observed in the LEO-only POD case as well. The explicit modeling of non-gravitational forces leads to an increase of m_0, evident by comparing the mean values of D to H. Assuming that the models for the non-gravitational forces are error-free, the estimation of the a posteriori m_0 would decrease since the number of parameters for the corresponding parametrization is smaller than when these forces are not explicitly modeled. However, the feature of the increasing m_0 can already be observed in a LEO-only POD case. Therefore the increase in the estimated observation noise results as a composition from the difference in the orbit parametrizations for the LEOs and the errors in the non-gravitational force models.

6.1.2 Geodetic parameters

A special focus of this work is the determination of the geodetic parameters, namely the Earth's center-of-mass coordinates and ERPs. The magnitudes of the formal errors are used to represent the potential benefits of integrating LEO observations in terms of observation geometry. The analysis of the estimated values is addressed in sect. 6.5, where a longer time span has been investigated.

6.1.2.1 Earth's center-of-mass coordinates results

The determination of the Z-coordinate of the Earth's center-of-mass location using only data from GPS is challenging (see Sect. 2.7). It is therefore of special interest to determine whether and how much the integration of observations from LEOs allows to improve these parameters. In Fig. 6.3 the formal errors for the estimated Earth's center-of-mass coordinates (X,Y,Z) are shown (mean values and standard deviation of daily formal error estimates).

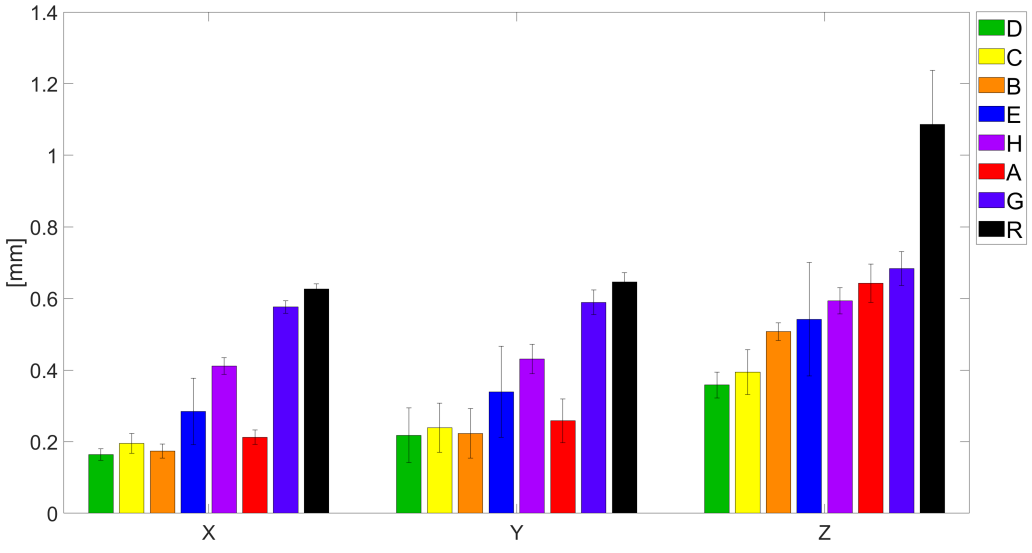

Figure 6.3: Mean values and standard deviation of formal errors of daily estimates of Earth's center-of-mass-coordinates

The labels in Fig. 6.3 are sorted according to the formal error of the Z-coordinate to ease the readability. To identify the impact of integrating LEO observation into the processing, the results for the experiments R, A, B, C, D, and E can be compared. The first feature that can be seen is that the reference solution shows the largest values for all coordinates among all the results. The solution where only one LEO is included (A) shows improvements in terms of formal errors for the estimation of Earth's-center-of-mass coordinates compared to R. This clearly indicates the benefit of the LEO integrated processing, in terms of determining the Earth's center-of-mass coordinates. This can be explained by the increased observation geometry and the imposed physical constraints from the dynamic LEO orbit. Haines et al. (2015) showed that when one LEO is integrated into the determination of a global network solution, the determinability of the Z-coordinate reaches the level of the ones for the X-, and Y-component. The experiment A is most similar to the experimental setup chosen in Haines et al. (2015). It is evident that the formal error for the Z-component of A is similar to the formal errors from the reference solution R of the X- and Y-components. In this regard, the result from Haines et al. (2015) can be confirmed. However, in scenario A the formal errors for X- and Y-coordinates also decreased compared to the reference solution, which did not occur in the experiments shown by Haines et al. (2015). The results of this work go in line with the simulation-based results from Kuang et al. (2015), which reveal that integrating observations from one LEO with an orbit altitude of 1400 km and an inclination of 100° reduces the magnitude of the Z-component formal errors to that of the other two components (X- and Y-component), whereby also the X- and Y-component formal errors show a decrease. This result is also shown by Männel and Rothacher (2017), where an improvement of 20% of the formal errors for all three components is stated, based on experiments using real data and integrating one LEO. The comparison of the results from experiments A and B reveals the influence of including a second LEO in the same orbital plane. The relative improvements from A to B are 18%, 14%, and 21% for the X, Y, and Z-coordinates respectively. This reveals that integrating more than one LEO in the same orbital plane further decreases the uncertainty of the estimated Earth's center-of-mass coordinates, which is caused by the further strengthening of the physical constraint mentioned before. To answer the question of whether the addition of an alternative second LEO in a different orbital plane further improves the results, the relative improvements from A to C can be analyzed and result to be 8%, 8%, and 39%. These results show that the observability of the Z-coordinate of the Earth's center-of-mass clearly benefits more from the inclusion of an additional LEO in a different orbital plane than adding another LEO in an already covered orbital plane. It can also be stated here that, in contrast to the formal error of the Z-component, the determinability of the other two coordinates is better for solution B, with two LEOs in the same orbital plane, than for solution C. This indicates the benefit of the specific orbital geometry of the integrated LEOs (98.6° inclination for both LEOs) of scenario B. When analyzing the solutions D and E two effects become evident: Having three LEOs in the system in three different orbital planes (D) leads to improvements in the observability of the Earth's center-of-mass coordinates with relative improvements, compared to the reference solution R, of 74%, 66%, and 67% for X, Y, and Z-coordinates respectively. Special attention has to be put on the results from experiment E, where observations from 9 LEOs have been included. The formal error for the Z-component is larger than for the solutions where two or three solutions were integrated, and for the X- and Y-component the values even exceed the results of the experiment where only one LEO has been integrated (A). This shows that incorporating a comparably large number of LEOs into the processing can potentially lead to an increase in the formal error of the estimated Earth's center-of-mass coordinates. According to eqn. (3.12), the formal error is a composition of the estimated observation noise m_0 and the square root of the respective diagonal elements of the cofactor matrix ($\sqrt{q_{ii}}$) which is determined by the observation geometry and parametrization of the system. It is, therefore, possible to assess whether the increased formal error results from the approach of integrating LEOs and the associated parametrization itself or from the capability to properly model the additional data.

In Fig. 6.4 the square root of the cofactors $\sqrt{q_{ii}}$ for the Earth's center-of-mass coordinates are shown. It is evident that the solution E, where the most LEOs were integrated, shows the smallest square root of the cofactors for all three components. It can therefore be concluded that the observation geometry and the parametrization of the scenario are superior compared to the other experimental setups, as a result of the multiple orbital planes included. This goes in line with the finding from Huang et al. (2020), where a clear correlation between the number of orbital planes and the quality of GPS orbits was found in the LEO-integrated processing, with the larger number of orbital planes being beneficial. The results

of the experiments shown in this work reveal that this finding also applies to the Earth's center-of-mass coordinates.

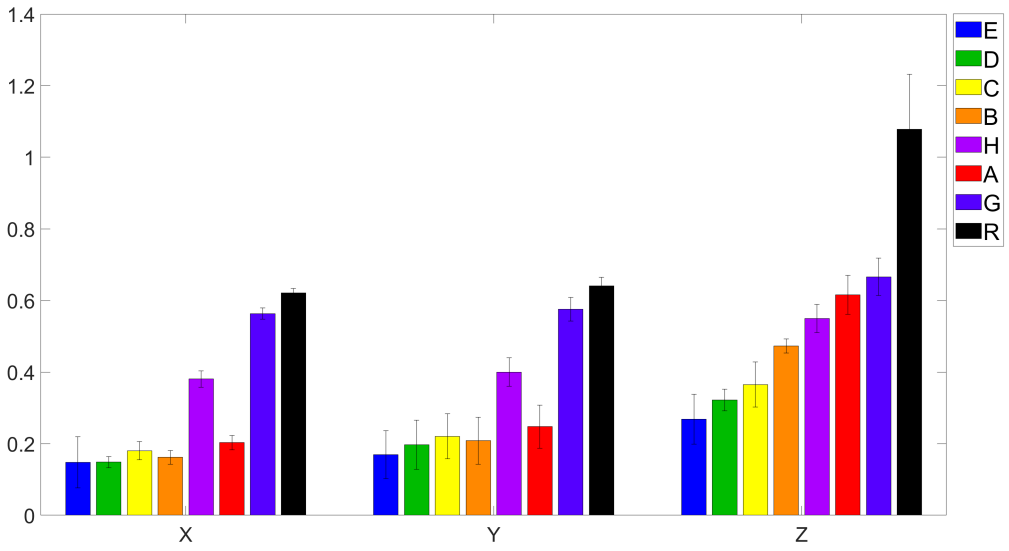

Figure 6.4: Mean values and standard deviation of square root of the cofactors of daily estimates of Earth's center-of-mass-coordinates

For the estimation of the Earth's center-of-mass coordinates, the adapted procedure of single-receiver ambiguity resolution for the LEOs is crucial. This can be read in Fig. 6.3 when comparing the results of experiments G and D. When ambiguity-fixing is applied (for the LEO observations), the formal errors decrease by 72%, 63%, and 48% for the X, Y, and Z-coordinates respectively (from G to D). The Z-component of solution G still exhibits an improvement compared to R, whereby X- and Y-coordinate formal errors show a comparably small improvement. Since, as shown in Fig. 6.4, the square root of the cofactor of these parameters is larger for the ambiguity-float solution than for the ambiguity-fixed solution while the observation geometry is identical, it is possible to conclude that the additional ambiguity (float) parameters can interfere with Earth's center-of-mass coordinates estimation by absorbing the signal.

The effect of explicitly modeling non-gravitational forces for the LEOs, and therefore also adopting a different orbit parametrization (see Table 3.2), can be analyzed by comparing H to D. It is evident that for the formal errors of all three components of the Earth's center-of-mass coordinates, solution D outperforms solution H. The explicit modeling of non-gravitational forces plays therefore a crucial role in the LEO-integrated processing. The results of the Z-component in Figs. 6.3 and 6.4 for H show smaller values than for the one-LEO solution A, which indicates that the increased geometry from scenario A to H compensates for the neglect of the non-gravitational force modeling (and the adapted parametrization). For the X-, and Y-coordinates, however, it is clearly evident that the computation of a global network solution, including the estimation of the Earth's center-of-mass coordinates, using the adopted LEO-integrated approach, demands the explicit modeling of these forces, since the square root of the cofactors show a clear degradation of solution H compared to A. From geometrical reflections, it can be concluded that the altered LEO orbit parametrization in terms of estimated constant accelerations over one arc for the LEOs of solution H leads to interference of these parameters with the Earth's center-of-mass coordinates estimates.

6.1.2.2 Earth rotation parameter estimates

The earlier studies that have investigated the integration of LEO observations into the computation of a global network solution so far, described in sect. 2.7, did not put a special focus on the determination of the ERPs. The validation of the determined parameters can therefore not be done by comparing the quality to the one of previous studies. However, Hugentobler and Beutler (2003) stated an improvement in

the formal accuracy of the pole coordinates estimates in a simulation study. The formal errors (shown in Fig. 6.5) serve as quality indication for the estimated ERPs. Additionally, a comparison was made between the resulting Earth rotation parameters (ERPs) and the combined reference solution C04 (Bizouard et al., 2019), which is consistent with the ITRF14 (shown in Fig. 6.7).

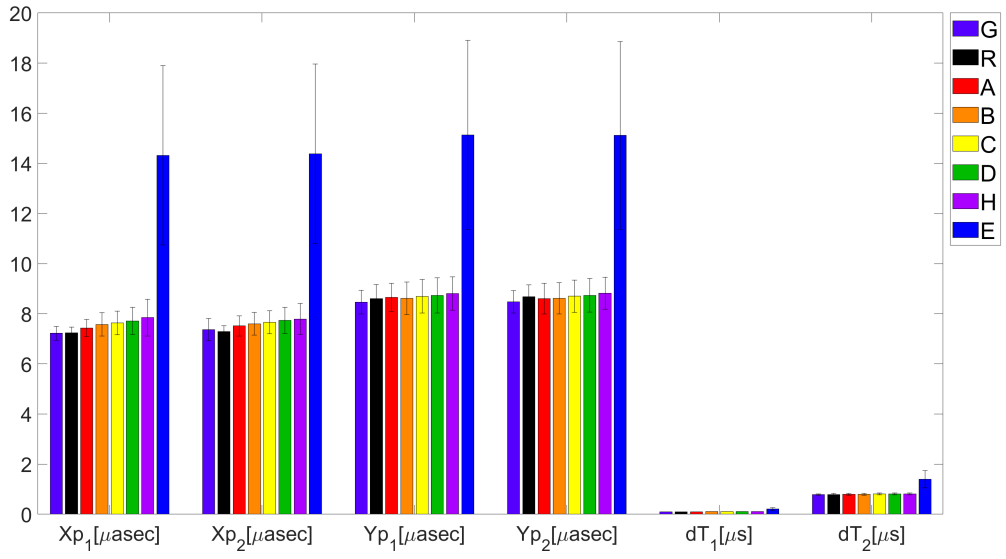

Figure 6.5: Mean values and standard deviation of formal errors of daily estimates of Earth rotation parameters

In Fig. 6.5 the labels are sorted according to the formal error of the estimated Xp_1. The formal errors of the ERPs resulting from the reference solution (R) are always among the smallest for all estimated parameters. For the X-pole coordinates, only the value for G (for Xp_1) is smaller than the one from the reference solution. For the estimated Y-pole coordinates G, A, and B show smaller formal errors, whereby the difference to the reference solution is comparably small. These results show that the integration of LEOs into the processing does not provide beneficial information in terms of formal errors of the ERPs. It seems to be of particular disadvantage if multiple LEOs are integrated, since with the increasing number of integrated LEOs, the formal errors increase, with its maximum values for the E solution. The differentiation of the constituents of the formal error, namely estimated observations noise and geometry and parametrization reveals that the already mentioned comparably large estimated observation noise for solution E dominates the results shown in Fig. 6.5. The square root of the cofactors for the ERPs for the different experimental setups are shown in Fig. 6.6. It is evident that the estimated Y-pole coordinates' square root of the cofactor of solution E shows a clear improvement compared to the other solutions. This is a result of the enlarged observation geometry by the inclusion of LEOs in additional orbital planes, which goes in line with the identical finding for the estimated Earth's center-of-mass coordinates. For the estimated X-pole coordinate, however, the influence of different numbers of integrated LEOs, and therefore orbital planes, is comparably small.

Integer ambiguity resolution for LEO-GPS observations is crucial for ERP parameters, which goes in line with the analysis of the Earth's center-of-mass coordinates. For ERPs, the solution where the ambiguities for the LEO observations are float (G), shows the smallest formal errors among all LEO-integrated solutions. This points out, that ambiguity-fixing introduces stiffness to the system, which may cause formal errors for certain parameters to be larger. Since ambiguity-fixing should in theory increase the quality of the solution, it is important to investigate whether the estimated parameters reflect the poorer observability indicated by the formal errors. The square root of the cofactors of the ERPs, shown in Fig. 6.6, reveal that the parametrization of solution G does not allow for a decrease of the uncertainty of the estimated ERPs to the same extent as the ambiguity-fixed solutions. It can therefore be concluded that the increased estimation of observation noise leads to larger formal errors for solution D than for G, whereby float ambiguities weaken the square root of the cofactor of the ERPs.

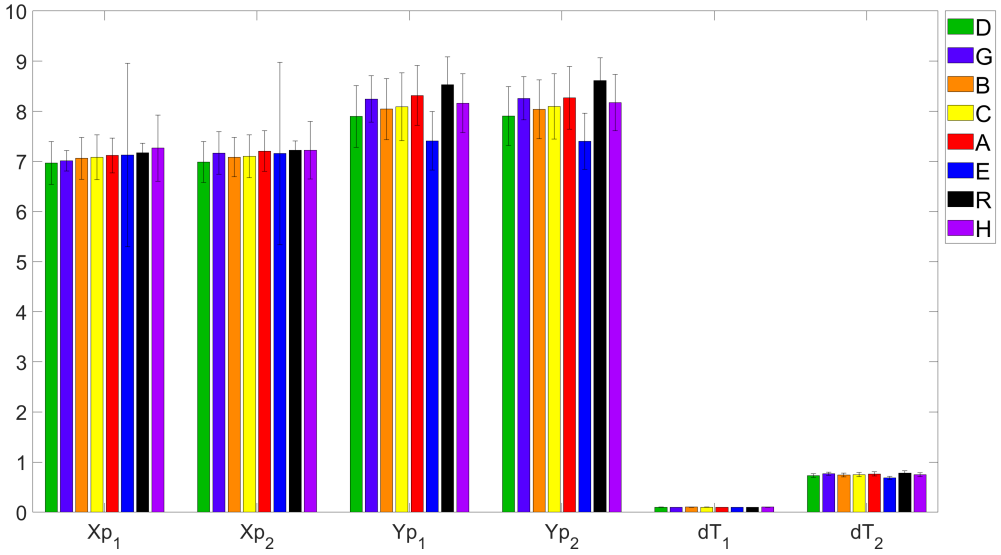

Figure 6.6: Mean values and standard deviation of square root of the cofactors of daily estimates of Earth rotation parameters

Solution H shows the largest formal errors, apart from solution E, which is clear evidence that also for the estimation of ERPs, the explicit modeling of non-gravitational force modeling of the LEO orbit determination is noticeable. However, the difference to solution D, which consists of the same setup in terms of integrated LEOs and only differs by this feature, is marginal. It can therefore be stated, that for the determinability of the ERPs, non-gravitational force modeling is not decisive according to the analysis of the formal errors. The comparison of the square root of the cofactors in Fig. 6.6 reveals that solution D leads to improvement compared to H in terms of certainty of the estimated ERPs. This effect results from the different orbit parametrization of the LEOs for these two solutions, whereby the additional estimated constant accelerations, set up for the LEOs in solution H, compete with the ERP estimates.

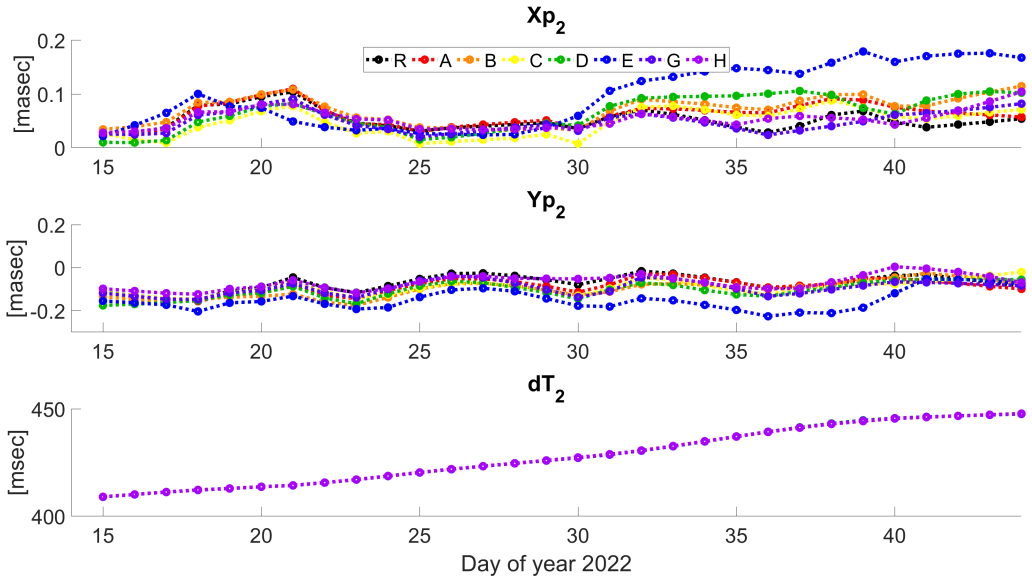

Figure 6.7: Comparison of estimated ERPs to C04 reference values

Figure 6.7 shows differences of the estimated ERPs (Xp_2, Yp_2, and dT_2) to the C04 reference solution, whereby the subscript refers to the second set of ERP estimates from a one-day solution (see Table 3.2). It is clearly visible that different values result for the individual solutions illustrating the influence of integrating

LEOs into the processing. The X- and Y-Pole estimates of solution E are notably off the others, which is evident by the large differences. It can be concluded, that including a comparably large number of LEOs with modeling problems may lead to a remarkable change in the derived ERPs, namely X- and Y-pole coordinates.

Table 6.4: Comparison of estimated Earth rotation parameters to C04 reference values, mean values, standard deviation

ID/ERP	X-pole [masec]	Y-pole [masec]	dT [msec]
R	-0.0705±0.0497	0.0401±0.0695	428.52±13.16
A	-0.0793±0.0529	0.0604±0.0721	427.75±12.88
B	-0.0833±0.0565	0.0759±0.0766	428.49±13.18
C	-0.0811±0.0565	0.0732±0.0787	427.74±12.88
D	-0.0973±0.0540	0.0805±0.0748	428.48±13.17
E	-0.1422±0.0845	0.1262±0.0828	428.44±13.15
G	-0.0820±0.0556	0.0666±0.0718	427.07±12.72
H	-0.0744±0.0520	0.0435±0.0744	426.43±12.96

In Table 6.4 it is evident, that the reference solution shows the smallest mean values and standard deviation of the estimated ERPs in terms of the comparison to the C04 reference solution. In line with the results from Fig. 6.5, the more LEOs are integrated, the larger the mean values of the ERP differences. This is evident when comparing the statistics for the solutions A-D, whereby the mean values and standard deviations increase when an additional LEO is integrated into the system. Remarkable is that the addition of a second LEO to a one-LEO scenario (B and C) shows the effect of having the additional LEO in the same or another orbital plane as the first LEO. The solution C shows a smaller mean value than B which again points to the relevance of including multiple LEOs in different orbit planes, as it has been extensively investigated and shown by Huang et al. (2020). The results of the estimated dT_2 parameter have to be treated with caution because this parameter is dependent on the a priori value, because of the constraints applied to dT_1, as shown in Table 3.2. This causes the characteristics shown in Fig. 6.7, whereby for dT_2 the differences to the C04 reference solution are not distinguishable for the different experiments. However, a clear drift is visible. There are issues with LOD series derived from GPS data because unmodeled instabilities in satellite orbits are resulting in unpredictable and strong drifts in the LOD (Bizouard and Gambis, 2009).

It is revealed that the more LEOs are integrated the larger the bias to the reference solution of the estimated pole-coordinates. The reason for this correlation between increasing mean values of ERP differences and the number of integrated LEOs in the integrated solutions is that integrating LEOs with similar orbit characteristics, namely inclinations, leads to a systematic bias. It was shown by Geisser (2023), in an analysis based on SLR, that the imbalance of contributions from satellites in either prograde or retrograde orbits may lead to systematic biases in the estimation of ERPs. The experimental setups for which the results are shown here consist of an imbalance, as well. This also explains the smaller mean values of solution C compared to B, because in scenario C the two integrated LEOs have different inclinations (98.60° and 66.04°), while in scenario B two LEOs are integrated with the same inclination, which lead to an increase of the bias. A similar result was derived by Scaramuzza et al. (2018) for a GNSS-only analysis, whereby the use of different constellations of orbital planes has been investigated. A beneficial impact on the results (in terms of differences to the C04 reference solution) was shown when constellations were chosen to have an equal number of satellites in prograde and retrograde orbits with different inclinations each. It can therefore be concluded that the estimation of ERPs in the LEO-integrated approach has to be treated with caution when an imbalance of inclinations of the integrated LEOs is present.

The influence of ambiguity-fixing for the LEO observations on the estimated ERPs in the LEO integrated processing approach is evident in Table 6.4, whereby solution G shows smaller biases compared to solution D. This goes in line with the formal errors and the square root of the cofactors of these solutions for the ERPs, where the changes w.r.t the GPS-only solution are smaller for solution G. Since these changes are smaller this means that the integration of LEO observations may have a smaller impact on the determined parameters, which is, in turn, evident by the smaller biases.

The explicit modeling of non-gravitational forces for the LEOs is crucial according to the statistics given in Table 6.4. Solution H, where these forces are not explicitly modelled shows the smallest mean value compared to all other LEO-integrated solutions. This reflects the results from the square root of the cofactors shown in Fig. 6.6, where this solution shows a degradation compared to solution D, whose experimental setup includes the same observation geometry. It can be concluded from these results, that when the non-gravitational forces are explicitly modeled, and the parametrization of the LEO orbits is chosen accordingly, the influence of the LEO observations on the resulting ERPs is larger compared to when not explicitly modeling non-gravitational forces. This results in different biases in the differences to the C04 reference series, whereby the result for scenario H is similar to the GPS-only solution. This can be explained by the feature that the imposed physical constraints by the dynamic nature of the LEO are weakened by the chosen parametrization for scenario H.

Table 6.5: Comparison of estimated Earth rotation parameters from GPS-only to LEO-integrated solution, mean values

X-pole 1	X-pole 2	Y-pole 1	Y-pole 2	dT 1	dT 2
9.3 μasec	3.8 μasec	-32.1 μasec	22.2 μasec	-4·10^{-4} μs	-1.7 μs

Hugentobler et al. (2005) showed the effect of the inclusion of a LEO into the determination of a global network solution, including the estimation of ERPs. The differences between the estimated ERPs for the reference solution and the LEO integrated solution are stated to be of the order of a few ten μasec for the X- and Y-pole coordinates and up to 10 μsec for LOD (dT). In the present experiment, the differences between the solutions have the same order of magnitude. This can be seen by exemplarily analyzing the mean values of the differences of the ERP results from R and D shown in Table 6.5. The strong constraint used for dT_1 leads to almost zero differences in the corresponding estimates of the different solutions.

6.1.2.3 Ground station coordinates

A central component of a global network solution is the determination of the coordinates of ground stations from which observations have contributed to the computations. Directly comparing the resulting coordinates to a reference solution is not meaningful due to the fact that the reference solution can never represent the effective truth. Thus, the quality metric of repeatability is utilized. In this context, the variance of the coordinates estimation of each individual included ground station is determined, whereby a low variance indicates high stability. As the 24-hour solutions are computed independently, this becomes a fundamental characteristic for assessing the reliability of the applied methodology of the LEO-integrated processing. The repeatability values are presented in horizontal (North/East) and vertical (Up) components. Dach et al. (2011) report a repeatability of 2-3 mm for the horizontal components, with values of up to 5 mm possible for certain stations in a weekly GNSS-only determined network solution. This is consistent with Ferland and Piraszewski (2009), where the same magnitude for repeatabilities in the horizontal components and additionally 7 mm for the vertical component are stated.

In Fig. 6.8, the repeatabilities for the included ground stations are depicted, considering only those stations that contributed observations for at least half of all processed days. Furthermore, the stations are ordered based on their repeatabilities (in the respective direction) of the reference solution in ascending order. The plot reveals that for different solutions, the repeatabilities for the same station can vary noticeably. The aforementioned magnitude of repeatabilities from Dach et al. (2011) and Ferland and Piraszewski (2009) can be confirmed by the analysis of the results from this work which are in the order of 1-2 mm and 4-5 mm in mean in North/East and Up directions respectively. Among the LEO-integrated solutions, solution A exhibits the highest mean and standard deviation in North and Up components. In the North direction, in addition to solution A, solutions D and E show higher mean values than the reference solution, whereby the standard deviations are notably smaller than that of the reference solution. In the horizontal components, all other solutions display smaller mean values and standard deviations compared to the reference solution, with solution G exhibiting the smallest mean values, respectively. For the Up component, all solutions, except solution A, show smaller mean values and standard deviations than the reference solution. This is a

clear indication that the determination of ground station coordinates benefits from integrated LEO-GPS observations. Further insight into the quality of the determined ground station coordinates is provided by the relative improvement of repeatabilities of LEO-integrated solutions compared to the GPS-only solution.

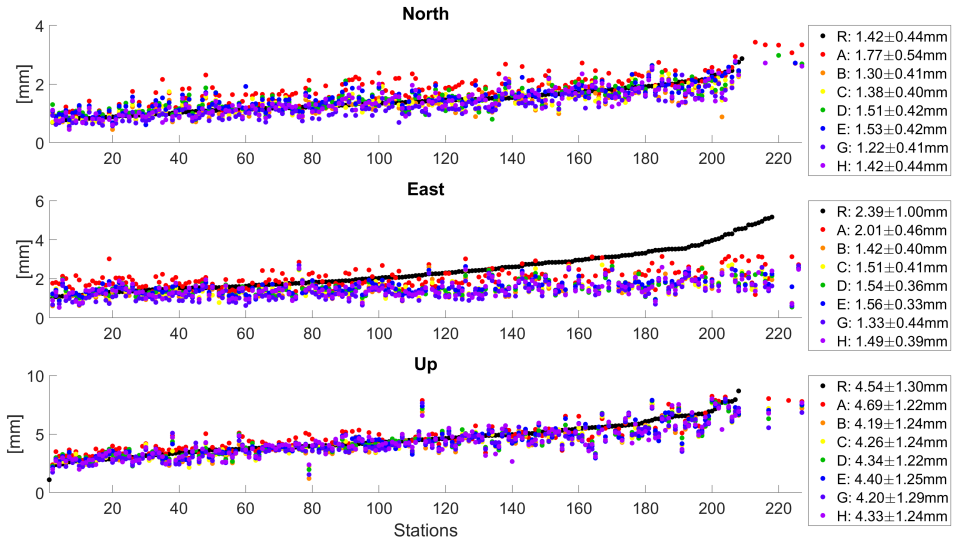

Figure 6.8: Repeatability of ground station coordinates

From Table 6.6, it becomes evident that the setups represented by solutions B, C, and G lead to systematic improvements in the repeatabilities of station coordinates in all components. Thus, it appears that incorporating two LEOs yields better results than integrating only one (solution A) or more than two LEOs, as there is a slight degradation in the North component for 3 LEOs (Solution D), as well as for scenario E. Notably, the repeatability of the horizontal East component benefits from integrated LEO-GPS observations. It can be read in Table 6.6 that ambiguity-fixing plays a crucial role. Ambiguity-fixing seems to degrade the determination of ground station coordinates (as seen in the comparison between D and G), which can be attributed to the fact that float ambiguities allow for better compensation of modeling errors of the forces acting on the LEOs. The explicit modeling of non-gravitational forces (as seen in the comparison between D and H) also appears to play a role, as the North component is notably degraded for Solution D. In this context, the reasoning can be found in the altered parametrization in the form of not estimated constant accelerations for the LEOs which results to have a negative impact on the station coordinates stability, via the estimated GPS orbit solutions.

Table 6.6: Mean relative improvement of ground station coordinates repeatability

ID/Component	North	East	Up
A	-23.7%	4.7%	-4.5%
B	6.3%	33.8%	7.2%
C	1.4%	29.3%	6.0%
D	-7.7%	26.4%	3.7%
E	-9.2%	24.0%	2.5%
G	12.4%	37.6%	7.3%
H	-0.5%	29.4%	4.0%

Figure 6.9 illustrates the ground stations with the largest improvements in repeatabilities. When compared to the utilized network of ground stations (Fig. 2.3), it becomes evident that there is no distinct regional pattern. Some of the stations displaying the most substantial enhancements are moderately isolated; however, this does not hold true for all cases. Therefore, it is not possible to assert that the inclusion of LEO-GPS observations leads to notable benefits from LEO-integrated processing for stations located in areas with sparse station coverage.

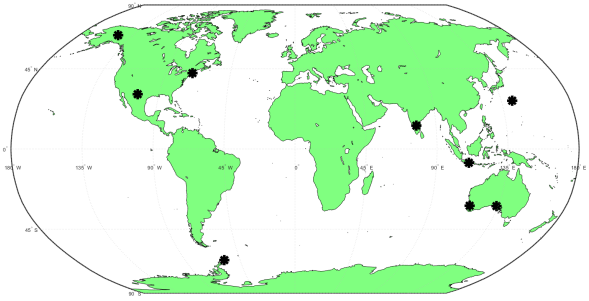

Figure 6.9: Ground stations with the largest improvement of coordinates repeatability

Since the preceding studies on LEO-integrated processing (from Chapter 2.7) do not provide information about resulting ground station coordinates, a direct comparison of results is not possible. Nevertheless, it is possible to state that the statistics of repeatabilities and their improvements, in comparison to the GPS-only reference solution, indicate the advantageous nature of LEO-integrated processing for ground station coordinate determination.

6.1.3 GPS orbit solutions

One part of a global network solution is the resulting orbits for the GNSS satellites. The square root of the cofactors of the estimated GPS osculating elements, shown in Fig. 6.10, indicate the benefit of integrating LEO observations on the determined GPS orbit solutions. For the analyzed period mean values for the square root of the cofactors over all GPS satellites are computed per day, whereby the mean values over all days are shown for the osculating elements. It can be stated that the square root of the cofactors of the reference solution are the largest for all osculating elements. The increased observation geometry, together with the chosen parametrization, leads to superior results for solution E compared to all other solutions. It is evident that the more LEOs are integrated, the smaller the mean square root of the cofactors. The parametrization of solution D leads to improved results compared to G and H, which points out the importance of ambiguity-fixing and explicit non-gravitational force modeling in terms of square root of the cofactors of the GPS osculating elements and goes in line with the identical finding for the Earth's center-of-mass and ERPs and, therefore, affirms the corresponding explanations.

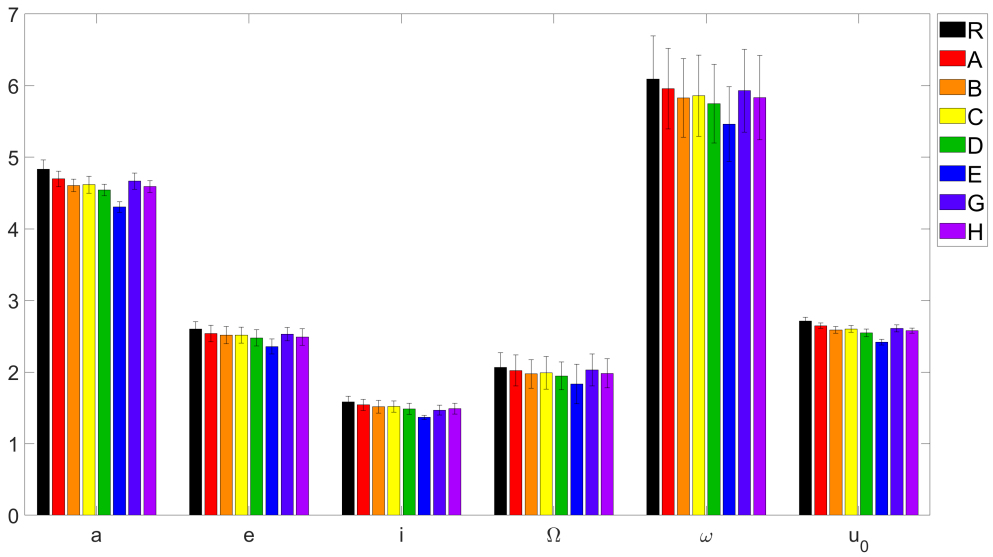

Figure 6.10: Mean values and standard deviation of square root of the cofactors of daily estimates of the GPS osculating elements

As a validation, orbit misclosures (see sect. 3.7.2) are analyzed. When computing orbit misclosures in the terrestrial system, one checks the consistency of the orbits, whereas comparing the satellite positions in the inertial system includes in addition a check of the consistency of the ERPs from both days (Lutz et al.,

2016b). Therefore, the orbit misclosures are computed in the inertial system. For every daily (24-hour arc) solution, the orbit overlaps of two consecutive days are computed. Based on this a mean value and the RMS over all included GPS satellites is computed per day and per spatial direction. In this case, no outlier screening was performed because a visual analysis of the results indicated that it was not necessary.

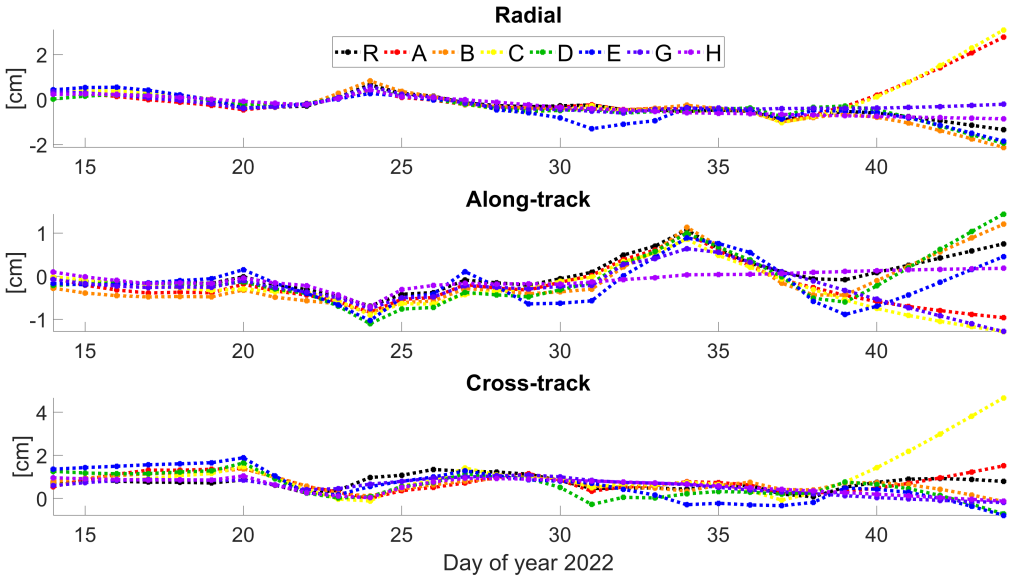

Figure 6.11: GPS orbit misclosures, daily mean values

Figure 6.11 shows the results for the performed experiments in terms of daily mean values, whereby the corresponding statistics, mean values, and standard deviations of daily values are given in Table 6.7. Additionally, the mean values of daily RMS values are given in Table 6.7 as well. The large differences evident at the end of the investigated time period are an artifact by means that only the GPS orbit misclosures show comparably larger values than for the other days. Because no other parameter type shows a notable change in this time period, these days were not excluded from the analysis. The comparably large orbit misclosures cannot be aligned to one specific GPS satellite or a group of GPS satellites.

Table 6.7: GPS orbit misclosures statistics, values in [cm]

ID	R, mean	A, mean	C, mean	R, RMS	A, RMS	C, RMS
R	-0.27±0.48	-0.02±0.44	0.67±0.59	3.61±0.49	3.07±1.15	2.39±0.34
A	-0.25±0.51	-0.16±0.49	0.69±0.48	3.63±0.58	3.13±1.19	2.42±0.44
B	-0.30±0.57	-0.23±0.55	0.72±0.45	3.82±0.61	3.20±1.04	2.54±0.52
C	-0.27±0.58	-0.17±0.49	0.64±0.75	3.83±0.54	3.30±1.29	2.46±0.40
D	-0.27±0.58	-0.20±0.54	0.62±0.66	3.91±0.64	3.30±1.14	2.42±0.42
E	-0.31±0.84	-0.25±0.66	0.58±0.81	4.31±0.72	4.24±1.11	2.87±0.54
G	-0.18±0.45	-0.16±0.47	0.68±0.38	3.59±0.51	3.08±1.24	2.39±0.36
H	-0.13±0.39	-0.13±0.37	0.61±0.45	3.68±0.41	2.78±0.97	2.16±0.34

The results of the GPS orbit misclosures point out that a clear benefit from including LEO observations in terms of the resulting GPS orbit solutions is not evident. For some LEO integrated solutions the resulting mean values are smaller than for the reference solution, e.g., in the radial direction for A, G, and H and in the cross-track direction for C, D, E, and H. For the RMS, for G in radial, for H in along-track, and for H in cross-track direction, smaller statistical values results than for the reference solution R. It is not possible to identify a correlation between the number of included LEO (or the orbital planes) and the quality of the resulting GPS orbit solutions in terms of orbit misclosures. An important statement that can be made based on the results from Table 6.7 is that the LEO-integrated solutions G and H show smaller mean and RMS values than the reference solution for certain spatial directions.

Table 6.8: GPS orbit misclosures statistics, CODE finals, values in [cm]

ID	R, mean	A, mean	C, mean	R, RMS	A, RMS	C, RMS
CODE	0.64±0.65	-0.59±6.12	0.25±0.27	2.54±2.69	1.20±1.40	4.94±4.19

Table 6.8 provides the statistics for the analyzed quality measure resulting from the CODE final 1-day GPS orbit solutions (Dach et al., 2023). The comparison to the values presented in Table 6.7 reveals:

- Radial and along-track orbit misclosures mean values are generally smaller for the GPS orbit solution derived from the experiments in the present work.
- Cross-track direction mean value is notably better for CODE solutions.
- Radial and along-track RMS values are about 50% larger for the solutions derived in this work.
- The cross-track RMS value from LEO integrated processing is superior to the one resulting from the CODE final orbit solutions, caused by outliers of the CODE solution on three days. When these outliers are removed, the mean RMS in the cross-track direction of the CODE orbit misclosures is reduced to 2.8 cm and has, therefore, the same order of magnitude as the results from this work.
- The standard deviations of the along-track mean, the radial RMS, and the cross-track RMS from the CODE orbit misclosures are larger than for the orbit solution derived in this work.

The points mentioned in the list above lead to the conclusion that the reference solution computed in the frame of this work is already of very high quality. Since the differences in statistical measures of orbit misclosures resulting from the LEO integrated solutions to the reference solution are smaller than the difference to the CODE orbit misclosures mean and RMS values, it is feasible to state that the integration of LEO observations into the computation of a global network solution may be useful in terms of resulting GPS orbit solutions, since from the statistics in Table 6.7 no clear preference can be read of but the square root of the cofactors shown in Fig. 6.10 reveal the improved observation geometry.

It is important to note here, that for the shown GPS orbit misclosures the solutions G and H are superior compared to the other LEO-integrated solutions. In particular for specific spatial directions an improvement is visible compared to the reference solution R. This indicates that ambiguity-fixing, by introducing additional stiffness to the system, may partially deteriorate the resulting GPS orbit solutions in the presence of model deficiencies. This can be read in Table 6.7 by comparing G to D, whereby the result of the orbit misclosures favors the ambiguity-float solution. This confirms the conclusion from the simulation-based study by Hugentobler and Beutler (2003), whereby an influence of systematic errors of the integrated LEO orbits on the GPS orbits, caused by the correlation with the ambiguity parameters, is stated.

Since solution H shows smaller values than D, the modeling of non-gravitational forces for the LEOs is crucial when the resulting GPS orbit solutions are analyzed in terms of orbit misclosures. In this scenario, it appears to be beneficial when these forces are not explicitly modeled and the parametrization is chosen accordingly for the LEO orbit. This is an important hint that for the determined GPS orbits, the additional geometry due to the LEO observations is even more important than the additional physical constraints. The study carried out by Huang et al. (2020) showed a clear benefit of incorporating LEO observations in terms of orbit comparisons to the IGS final orbit solutions. To compare the results of the present work to these findings, an orbit comparison of the resulting solutions of the experiments to the CODE 3-day final solutions (Dach et al., 2023) is carried out.

Table 6.9 shows mean values and standard deviation for daily RMS values of orbit comparisons of the solutions to the CODE 3-day final orbits. The findings do in general not match the ones stated in Huang et al. (2020), which means, that no notable improvement can be found when observations from (multiple) LEOs are integrated into the processing. Two important points may cause this issue:

- Huang et al. (2020) used a much smaller station network (see sect. 2.7), which causes the LEO observations to influence the resulting GPS observations to a larger extent.
- The CODE final solution serves as a priori information in this work. This may cause that the more the experimental setup differs from the determination of this solution (e.g., by introducing LEO observations) the more the resulting orbit solution is shifted.

Table 6.9: GPS orbit comparisons statistics, mean of daily RMS values

ID	Radial [mm]	Along-track [mm]	Cross-track [mm]	3D [mm]
R	13.1±2.5	18.8±8.2	13.3±2.2	15.9±4.7
A	13.0±2.7	18.6±7.9	13.5±2.5	15.8±4.6
B	13.4±3.5	18.8±7.4	14.1±2.6	16.2±4.5
C	13.9±2.7	20.1±8.2	14.0±2.5	17.1±4.8
D	14.3±2.6	20.1±7.2	14.6±2.7	17.4±4.2
E	16.3±5.1	21.4±7.0	15.7±2.8	18.5±4.7
G	13.0±2.5	18.8±8.3	13.4±2.4	15.9±4.7
H	13.0±2.1	17.4±7.3	13.3±2.6	15.2±4.2

The first point results from the fact that the absolute changes of the orbit comparisons with respect to the reference are at a maximum level of half the magnitude as the results shown by Huang et al. (2020). The second point is evident by the increasing values in Table 6.9 for increasing numbers of integrated LEOs. It is important to note here, that this orbit comparison does not allow drawing a conclusion about which of the orbit solutions is of superior quality, but serves to compare the findings to earlier research in this field. In line with the results from the orbit misclosures, the experimental setups of G and H appear to result in orbit solutions that are in general the closest to the CODE final solutions, partially better than R. Therefore the findings about the influence of ambiguity-fixing and explicitly modeling non-gravitational forces can be confirmed, namely that the corresponding parametrizations alters the influence of the integrated LEO observations because modeling deficiencies and physical constraints may be absorbed by the additional parameters to a larger extent. Lutz et al. (2016a) stated 3D orbit misclosure RMS values of 65 mm - 72 mm (depending on the analyzed time period) for 24h-arc solutions. The 3D-RMS value for solution R is 43 mm (median), whereby the basis are daily 3D-RMS values over all satellites. It can therefore be confirmed that the GPS orbit quality of the reference solution from this work is comparably high. The smallest 3D-RMS of orbit misclosures from LEO-integrated solution results from scenario H with 38 mm, followed by scenario C with 41 mm. This result underlines that the parametrization of solution H leads to orbits of superior quality, while the solutions where non-gravitational forces are explicitly modeled for the LEOs exhibit larger rigidity which influences the GPS orbit solutions to show larger orbit misclosures. This confirms the potential of the propagation of LEO orbit modeling errors into GPS orbits, as already identified by Visser and Van den IJssel (2000).

6.1.4 LEO orbit solutions

In the present work, the orbit precision of the LEO satellites plays a central role. So far, earlier studies related to this field (see sect. 2.7) have not investigated (or reported) the impact of the LEO-integrated processing on the resulting LEO orbits to a large extent. To analyze the corresponding results, orbit misclosures are analyzed and compared to results stemming from a classical LEO-only POD using fixed GPS products. For the sake of clarity only for one experimental setup, and only one LEO the results are shown. The chosen experimental setup for which the LEO orbits are analyzed consists of the integration of LEO-GPS observations from Sentinel-3A, Jason-3, and GRACE FO-C (scenario D), whereby the orbit solutions for Sentinel-3A and GRACE-FO are analyzed. Figure 6.12 shows orbit misclosures in the three spatial directions for Sentinel-3A.

Results from three different solutions are shown:

- AIUB: Independently derived orbit solutions, which are provided for comparison purposes in the frame of the Copernicus POD Quality Working Group (Fernandez and Femenias, 2014). They are known to be of appropriate quality compared to external solutions[1]. The orbit is parametrized by six initial osculating elements and PCAs, valid for 6 min and constrained to $5{\cdot}10^{-10}$m/s^2, whereby single-receiver ambiguity resolution is performed and non-gravitational forces are explicitly modeled. A 10 sec observation sampling is used for the POD.
- Reference: LEO-only POD solution, whereby the resulting orbit serves as a priori orbit for the LEO-integrated processing. The solution does not include single-receiver ambiguity resolution. Explicit non-gravitational force modeling is applied, whereby a 10 sec observation sampling is used.
- Final: The final LEO orbit solution resulting from the elaborated LEO-integrated approach.

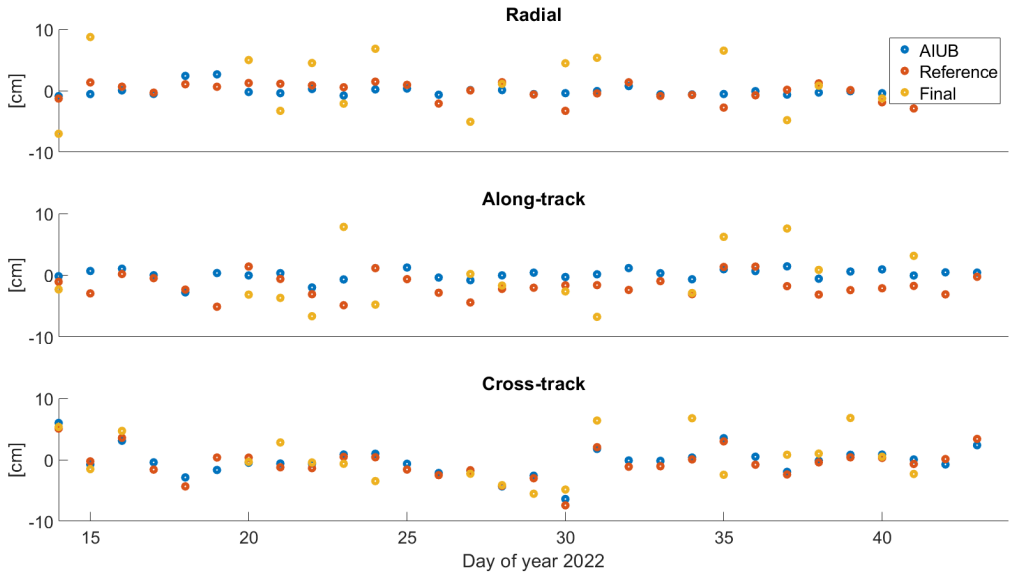

Figure 6.12: Sentinel-3A orbit misclosures

Firstly, the difference in the results of the AIUB solution compared to the reference solution is addressed. The degradation of the reference solution compared to the AIUB solution can be explained when considering the findings of sect. 4.2.2.2 that the difference between ambiguity-float and ambiguity-fixed orbit solutions in terms of orbit misclosures has the same magnitude as it is evident in Fig. 6.12. This degradation of the reference solution compared to the AIUB solution therefore allows to confirm the finding from Fig. 4.13, namely that ambiguity-fixing leads in general to smaller orbit misclosures. The other outcome that can be read from Fig. 6.12 is the degradation of the final S3A orbit solution in terms of orbit misclosures when compared to the AIUB or the reference solution. Hugentobler et al. (2005) analyzed the orbit misclosures for the resulting orbit solutions of the integrated LEO and found a minimum value of 3.5 cm for the 3D-RMS of orbit overlap.

Table 6.10: 3D RMS of LEO orbit misclosures from integrated processing

LEO	Minimum [cm]	Median [cm]
Sentinel-3A	0.9	5.2
GRACE-FO C	1.5	7.1
Jason-3	2.3	6.4

[1] https://sentinels.copernicus.eu/web/sentinel/technical-guides/sentinel-1-sar/pod/documentation (Accessed: 13 July 2023)

For experiment D the results in terms of minimum and median values are shown in Table 6.10. It is evident that the minimum 3D RMS values are generally smaller than the result shown by Hugentobler et al. (2005), probably caused by the integration of observations from multiple LEOs, the explicit modeling of non-gravitational forces, and single-receiver ambiguity resolution. The median values, however, go in line with the finding of the orbit misclosures per spatial direction shown in Fig. 6.12. The results for solution H reveal that explicit modeling of non-gravitational forces is beneficial in terms of orbit misclosures for the resulting LEO orbit solutions, whereby an overall decrease of 14% of the 3D-RMS over all three included LEOs results. Single-receiver ambiguity resolution, however, degrades the resulting LEO orbit solutions, which becomes evident from the analysis of the LEO orbit misclosures from scenario G. On average the 3D-RMS values increase by 25%, which points to potential modeling errors which map into the determination of ambiguities and in turn, by introducing rigidity to the system, affect the LEO orbits in a negative manner.

To obtain more insight into the quality of the derived orbit solutions, as introduced in Sect. 3.7.3, an SLR validation is used as an independent validation technique. For the same orbit solutions for Sentinel-3A analyzed in Fig. 6.12, a SLR validation is carried out. The information needed for the SLR validation (station coordinates, ERPs, Earth's center-of-mass, etc.) is the CODE 3-day final results, which are introduced as fixed.

Table 6.11: SLR validation of Sentinel-3A orbit solutions

	Mean value [mm]	RMS [mm]
AIUB	3.9	8.3
Reference	3.1	9.1
Final	4.1	17.8

The statistics of the SLR validation in Table 6.11 reveals the same conclusion as the computed orbit misclosures, namely that the LEO orbit solutions are degraded when deriving them with the procedure of LEO integrated global network solution determination. This conclusion is driven by the notably higher RMS of the SLR residuals of the performed validation compared to the AIUB and the reference solution. This finding is contrary to the results from Hugentobler et al. (2005), where an SLR validation revealed a statistical improvement using the LEO-integrated approach. However, it is stated that the small amount of data included in the study does not allow for the conclusion that the resulting LEO orbit is of superior quality. The results from the present work show clear evidence that the resulting LEO orbit solution suffers when the LEO-integrated global network solution approach is performed. It is important to note here, that resulting LEO orbits from solutions G and H do not show an improvement in terms of SLR validation compared to the results shown in Table 6.11.

As introduced in sect. 3.7.4, for GRACE-FO an additional validation technique can be used. The KBR validation is carried out for the solution where all LEOs have been incorporated (E) and are compared to the validation resulting from classical LEO-only POD solutions. Also, an independently derived ambiguity-fixed orbit solution is validated, whereby the POD (orbit parametrization) follows the approach for the previously described AIUB Sentinel-3A orbit solutions. This gives further insight into the orbit precision since the SLR validation depends on the underlying reference frame and may therefore cause a blurred picture since the final LEO solutions are computed w.r.t. to the derived reference frame defined by the global network solution.

The results go in line with the statistics provided in Table 6.11 which describes the SLR validation and the orbit misclosures given in Fig. 6.12. It is visible in Fig. 6.13 that the orbit solutions for the two GRACE Follow-On satellites resulting from the LEO integrated processing are less precise than the LEO-only POD solutions. Note that the reference solution has a larger range RMS than the AIUB solution. In this solution (reference), the ambiguities are float, whereby for the AIUB solution single-receiver ambiguity resolution is applied. This finding matches the results from Lasser et al. (2020), where it has been shown that the K-Band residuals for GRACE are significantly larger for ambiguity-float solutions than for ambiguity-fixed solutions. This also holds true for GRACE Follow-On (Martin Lasser, personal communication).

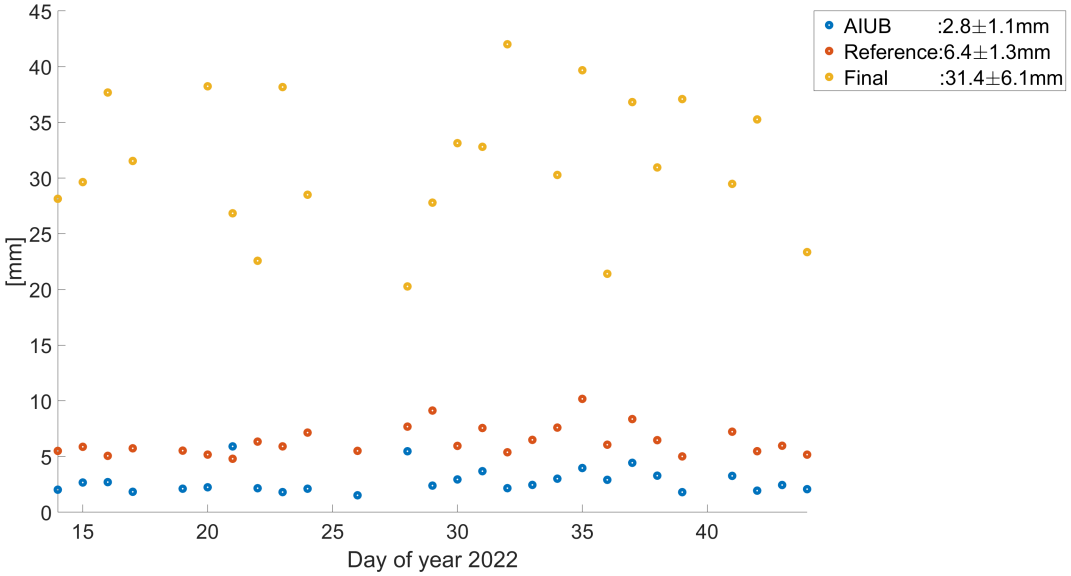

Figure 6.13: K-Band validation, range RMS

The cause for the degradation of the LEO orbits can be partially found in the different observation samplings used for the LEO POD and the LEO-integrated processing (10 sec versus 300 sec). Using these different samplings for the final orbit determination in a LEO-only POD (no integrated processing) of Sentinel-3A causes noticeable differences in resulting orbit misclosures when the same a priori orbit was used, as shown in Fig. 6.14. Compared to a 10 sec sampling, the magnitude of orbit misclosures is on average 2.8 times larger when a 300 sec sampling is used. To ensure consistency between the different samplings, the constraints for the PCAs may need to be reduced from $5{\cdot}10^{-10}$ m/s^2 to $3{\cdot}10^{-9}$ m/s^2 to have the same impact of the pseudo-observations compared to the real observations. This leads to improved results when the 300 sec sampling is used, whereby the magnitude of the orbit misclosures is on average still 2.6 times larger compared to a 10 sec sampling (using $5{\cdot}10^{-10}$ m/s^2 as constraints) and, therefore, 7% smaller to when $5{\cdot}10^{-10}$ m/s^2 and a 300 sec sampling is used.

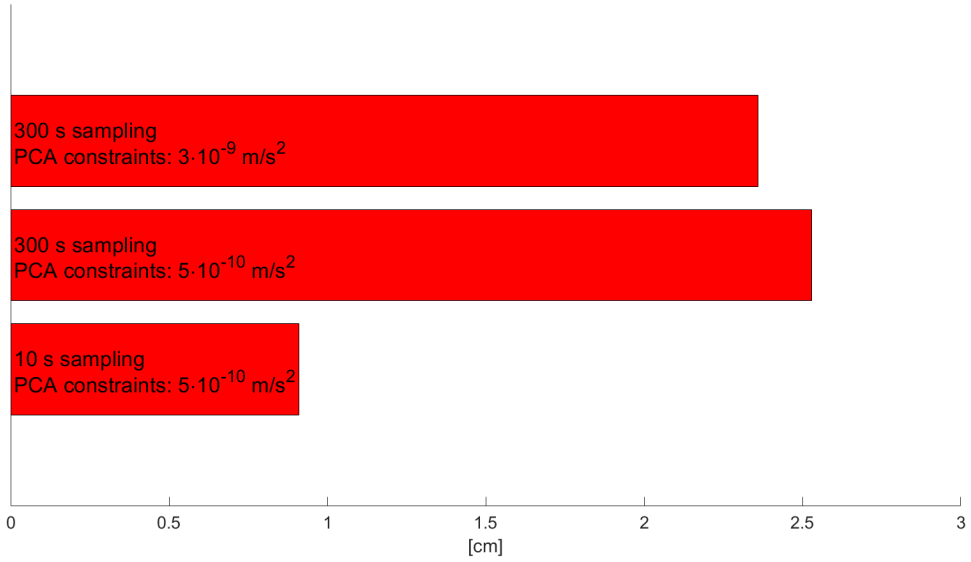

Figure 6.14: 3D RMS of orbit misclosures from LEO POD using different samplings/constraints for PCAs

In Huang (2022) an SLR validation is performed for LEO-only POD orbit solutions (not resulting from the integrated processing), whereby the STDs range from 20.5 mm to 34.9 mm, depending on the LEO.

This reveals, that the LEO orbit solutions resulting from the integrated processing in this work show a superior SLR validation compared to the LEO-only POD results from Huang (2022). Montenbruck et al. (2018a) demonstrates that SLR validations of LEO-only POD solutions for Sentinel-3A lead to STDs below 10 mm, which goes in line with the results of the AIUB and reference solution given in Table 6.11.

To support the statement that the 300 sec sampling causes the LEO orbit deteriorations, a corresponding SLR validation is performed for the LEO-only POD orbit solutions mentioned before. It reveals an increase of the RMS of 52% for the 300 sec sampling solution w.r.t the 10 sec sampling solution. The reduction of the constraints for the PCAs, as mentioned before, leads to a reduction of the RMS of 21% compared to the orbits that are parametrized as in the LEO-integrated approach.

A dedicated experiment for the LEO-integrated processing was designed according to the setup of scenario D, whereby a 120 sec sampling was used. An improvement of a factor of 2.1 for the LEO orbit misclosures is indicated by the results. The SLR validation for Sentinel-3A reveals an improvement of the RMS of 11%. The recapitulation shows that an increase of the observation sampling by the factor 2.5 yields an improvement in the LEO orbit misclosures of 48% and of 11% in the RMS of the SLR validation, which is a clear indication that further increase of the observation sampling potentially leads to LEO orbits of the same precision as from the LEO-only POD. However, due to technical limitations, this has not been performed in this work. The decreased LEO orbit precision, resulting from the experiments of this work, revealed by larger standard deviations for orbit misclosures shown in Fig. 6.12, increased RMS in the SLR validation, and the K-Band validation result is, therefore, caused by the choice of the observation sampling in the integrated processing together with the chosen LEO orbit parametrization in terms of constraints of the PCAs. The reduction of the constraints, however, affects the square root of the cofactors of the estimated geodetic parameters in a negative manner. This is evident from the results described in section 6.1.1, where different orbit parametrizations for the integrated Swarm-A satellite have been tested. The change of the PCAs' constraints from $5{\cdot}10^{-10}$ m/s^2 to $3{\cdot}10^{-9}$ m/s^2 leads to an increase of the square root of the cofactor of the estimated Earth's center-of-mass coordinates of 19%, 5%, and 9% for the X-, Y-, and Z-component respectively.

However, the results of the orbit misclosures, the SLR validation, and the KBR validation indicate that the combined processing and hence the joint determination of the global network solution and the LEO orbit solution result in a degraded orbit precision for the derived LEO trajectories when the experimental design includes a 300 sec sampling. LEO observations make up only a small amount of all observations, so as a result of not assigning higher weights to them systematically, the system may compensate for mismodeling to a large extent by altering the orbit parameters of the integrated LEO satellites. Providing the system is improved in terms of observation residuals (squared), the adjustment process may partially degrade the LEO orbit, while incorporating LEO observations still improves many of the other estimated parameters (Earth's center-of-mass coordinates, ERPs). The result is that LEO-only POD may lead to more high-quality orbits than the LEO-integrated global network determination approach, whereby a higher observation sampling potentially improves the LEO orbit precision.

6.2 Correlation of parameters

In Haines et al. (2015) it has been demonstrated that certain parameters are highly correlated in the determination of global network solutions. This correlation negatively affects the observability of the respective parameters. Consequently, constraints must be imposed on these parameters. As a result, a bias may be introduced into the determination of the solution, which is difficult to quantify. Therefore, it is desirable to create a system in which the correlations between the parameters are minimized to allow as many parameters as possible to be estimated freely. The investigation aims to assess whether LEO-integrated processing enables the reduction of correlations between estimated parameters. In all figures in this section, differences between absolute values of correlations are displayed, whereby the values from a ground station-only processing minus the values resulting from a LEO-integrated solution (solution E) were computed. This implies that positive numbers indicate a decrease in correlation when LEOs are integrated into the processing. The analysis of the correlations between the osculating elements of the GPS satellites and the Earth's center-of-mass reveals that specific correlations between the GPS osculating elements and the Earth's center-of-mass coordinates increase when LEOs are integrated into the processing.

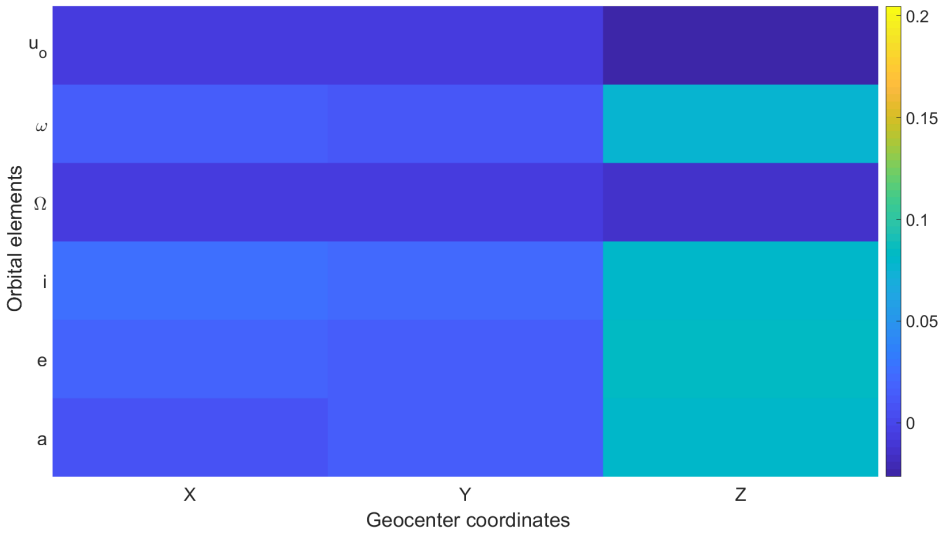

Figure 6.15: Correlation differences of GPS orbital elements and Earth's center-of-mass coordinates for the reference solution and solution E

The correlation of the estimated Z-component of the Earth's center-of-mass and the orbit parameters Ω and u_0 increases for the LEO-integrated solution. The results shown in sect. 6.1.2.1 point out, that the Earth's center-of-mass coordinates can be determined with higher observability, reflected by decreased formal error for LEO-integrated processing. Due to the dynamic nature of the LEO orbits, imposing physical constraints on the system, the integrated-processing approach allows to compensate for the increase of the correlations for the specific pairs of parameters shown in Fig. 6.15 and further increase the determinability of Earth's center-of-mass coordinates.

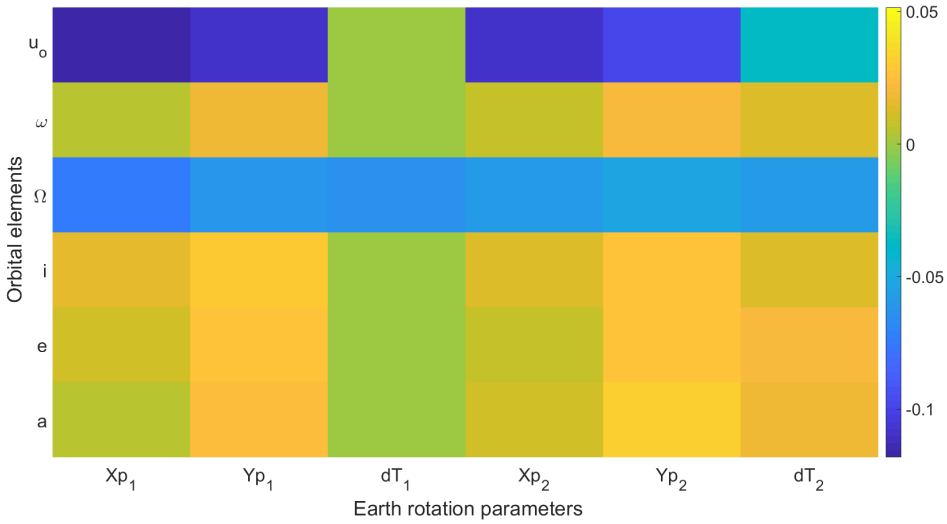

Figure 6.16: Correlation differences of GPS orbital elements and Earth rotation parameters for the reference solution and solution E

Figure 6.16 reveals that the correlations between the GPS osculating elements and the Earth rotation parameters change noticeably when LEO-GPS observations are integrated into the processing. Fig. 6.16 illustrates the change in correlations comparing the GPS-only scenario and the LEO-integrated processing. It is evident that for most of the GPS orbit parameters, a decrease in the correlations results. However, for the GPS orbital element u_0, the correlations to the ERPs increase. The geometrical consideration of this parameter, as clearly evident in Fig. 3.1, points out that this orbit parameter may have a large correlation with the estimated ERPs. This fact can potentially lead to a comparably small change in formal errors for

the LEO-integrated solutions of the ERPs compared to the GPS-only, which were shown in sect. 6.1.2.2. This may be caused by the composition of increased observation geometry due to the additional LEO observations and the contrary additional correlation between the ERPs and the LEO orbital elements, which in turn also influence the GPS orbital elements.

The comparison of the correlations between Earth's center-of-mass coordinates and ERPs, shown in Fig. 6.17, clearly reveals, that a large decorrelation between the estimated Z-component of the Earth's center-of-mass and the Y-pole of the Earth's rotation axis results, when LEO-GPS observations are integrated into the processing. This may be one of the causes for the increase in observability of this component of the Earth's center-of-mass. This is due to the improved observation geometry caused by the orbital inclinations of the LEOs which are not covered by the GPS satellites (see sect. 2.1.1). However, Fig. 6.17 also shows a small increase in correlation between the Yp_2-component of the Earth's center-of-mass and dT_2. This is caused by the correlation of the LEOs ascending nodes (Ω) and dT, which may result in increased correlations of these parameters in the LEO-integrated solutions. The small changes in the correlations between the X-, and Y-component of the Earth's center-of-mass with Xp_1 and Yp_1 respectively, result from the geometrical circumstances that they refer to the same axis each. Remarkable is that the integration of LEO observations leads to a decorrelation of the second set of pole coordinates to the Earth's center-of-mass coordinates, pointing out the benefit of the applied approach in terms of observation geometry.

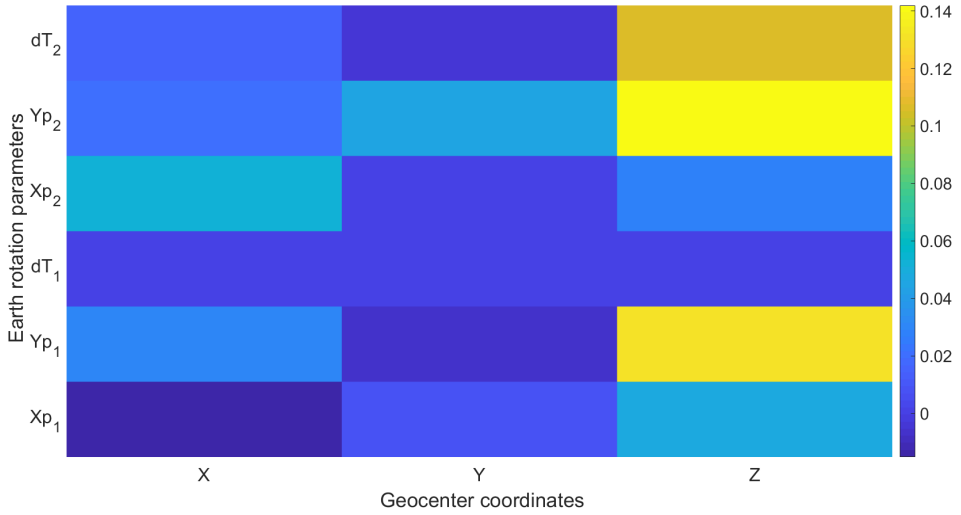

Figure 6.17: Correlation differences of Earth's center-of-mass coordinates and Earth rotation parameters for the reference solution and solution E

6.3 Inclusion of Galileo

The results of the experiments shown in sect. 6.1 were computed using GPS observations solely. Since with Sentinel-6A (see sect. 2.5.3) a LEO is processed and incorporated which collects also observations from Galileo satellites, the extent to compute a multi-GNSS solution is possible. This section describes the results from the dedicated specific experiments from Table 6.1. Three solutions are to be compared within this analysis whereby different satellites were included:

- GPS
- GPS+Galileo
- GPS+Galileo+Sentinel-6A

Very important to state is that for the experiments shown in this section the a priori information mentioned in Table 3.3, namely the GNSS orbits and clocks, the ground station coordinates and clocks, and the ERPs, are not the CODE final products (Dach et al., 2016), but the resulting solutions from a reprocessing campaign (Selmke et al., 2020). This change in a priori information is needed, because the CODE final

products do not include information about Galileo satellites. Theoretically, this may influence the results, but since the results from the experiments from the list above are all based on the same a priori information, the comparison will still reveal the influence of integrating LEO-GNSS observations appropriately. Unfortunately, this makes direct comparisons of the results to the other experiments from Table 6.1 not meaningful. Before the results of these experiments are provided, Table 6.12 gives an overview of the processing details for the different solutions, exemplary for 14 January 2022.

Table 6.12: Multi-GNSS solutions, processing details, 14 January 2022

	GPS	GPS+Galileo	GPS+Galileo+S6A
Number of observations	1152764	1816398	1818532
Number of adjusted parameters	80356	90389	90938
A posteriori RMS	1.001 mm	1.000 mm	1.015 mm

Table 6.12 reveals that the difference in the number of observations and adjusted parameters between the GPS+Galileo-solution and the S6A-integrated solution is smaller than the difference to the GPS-only solution. This underlines the interest in determining whether such a small difference can lead to notable changes in the determined solutions. The focus of the analysis of the results shown in this section is on the estimated geodetic parameters because the results which are shown in sects. 6.1.2.1 and 6.1.2.2 revealed that the integration of LEO observations has the largest impact on these parameters.

6.3.1 Earth's center-of-mass coordinates results

It is clearly evident from the results shown in sect. 6.1.2.1 that incorporation of LEOs into the computation of a global network solution is beneficial for the estimation of the Earth's center-of-mass coordinates, whereby this is especially reflected in the formal errors. The question arises whether this increase of observability can also be achieved by adding satellites, and therefore observations, from another GNSS system. In the frame of the key question of this work, it is then in particular of interest whether the adding of additional observations from a LEO satellite, Sentinel-6A in this case, leads to different results, and whether these are of superior quality. The results for the estimates of the Earth's center-of-mass location are shown in Fig. 6.18.

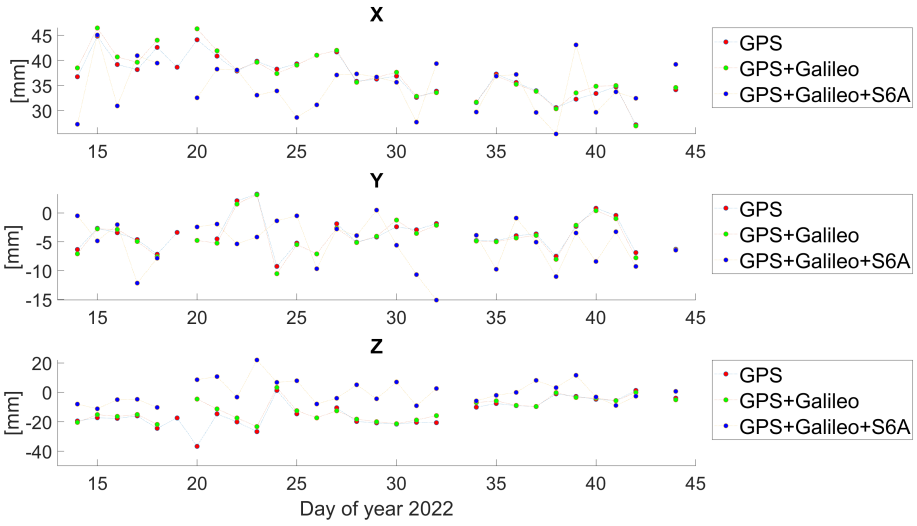

Figure 6.18: Estimated Earth's center-of-mass coordinates

The comparison of the results from the three solutions reveals that the difference between the GPS-only and GPS+Galileo solutions is on the mm level. The solution where additional GNSS observations from Sentinel-6A were incorporated shows notably different estimates. For the estimated Z-component an offset between the LEO integrated solution and the two GNSS-only solutions is apparent.

Table 6.13: Earth's center-of-mass coordinates (Z) differences to an SLR solution

	[mm]
GPS	-17.0±5.7
GPS+Galileo	-15.4±5.2
GPS+Galileo+S6A	-3.5±6.5

Table 6.13 shows mean and standard values of differences between the estimated Z-component of the Earth's center-of-mass coordinates and results derived from an SLR analysis (Geisser, 2023). These reference values are based on 7-day solutions. To obtain comparable estimates a linear interpolation of the reference (SLR) solution was performed and for the determined 24h-arc solutions a median over a seven-element sliding window was used. Since the estimation of the Z-component is heavily affected by modeling errors of the GPS orbits (Meindl et al., 2013) in a GPS-only solution, reliable estimates cannot be derived in such an approach (Sośnica et al., 2013). It is therefore an important result that the mean value of the differences of the Z-component is reduced to a large extent for the LEO-integrated solution, which is caused by the additional observation geometry and the imposed physical constraints by the dynamic nature of the LEO. The standard deviation which is larger for the LEO-integrated solution indicates that the estimates are less stable in relation to the GNSS-only solutions when compared to the SLR-based reference solution. This may be caused by the high sensitivity of the LEO to the Z-component of the Earth's center-of-mass compared to the GNSS satellites, combined with the 24h-arc approach. Therefore a possible way to circumvent this is to perform a long-arc approach, as it is adopted in the SLR reference solution.

The formal errors, as the representative quality metrics for the observability, are shown in Fig. 6.19.

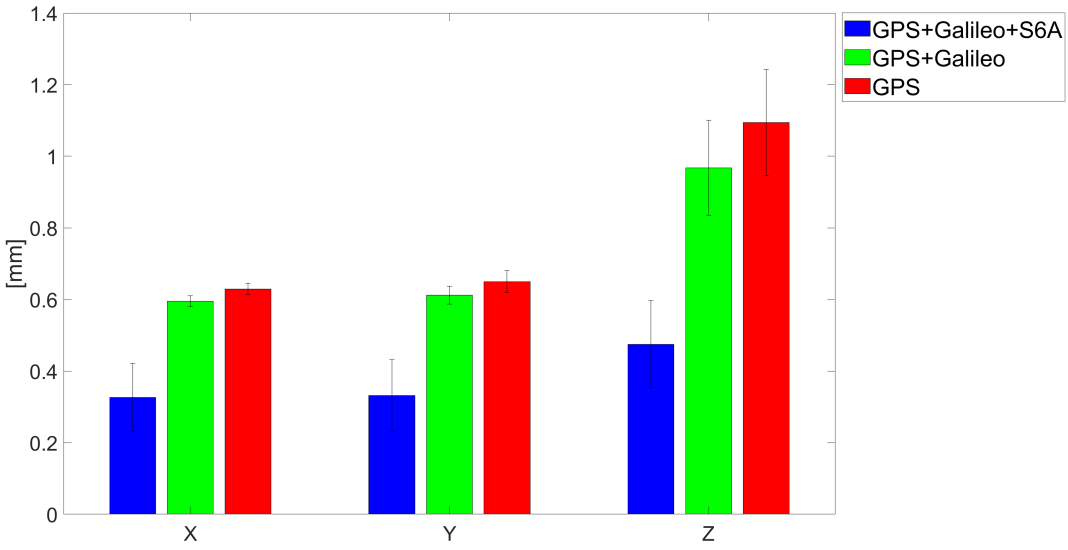

Figure 6.19: Mean values and standard deviation of formal errors of daily estimates of Earth's center-of-mass coordinates

The analysis of the formal errors of the estimated Earth's center-of-mass coordinates clearly reflects the improved observability of this parameter type when LEO-GNSS observations are included in the processing. The LEO-integrated solution shows an improvement of at minimum 45% (X-component compared to GPS+Galileo) with respect to the GNSS-only solutions in all three components. In the experiments carried out a maximum improvement has been found to be 56% for the Z-component when comparing the LEO-integrated solution to the GPS-only solution. Additionally, it is evident that this improvement leads to the formal error of the estimated Z-component being smaller than the ones of the X- and Y-coordinates of the GNSS-only solutions. It is evident that the GPS+Galileo solution outperforms the GPS-only solution in terms of formal errors, whereby the difference between these solutions is comparably small regarding

the improvement of the formal errors resulting from the LEO-integrated solution. These results reveal that integrating LEO observations into the computation of a global network solution leads to a superior observability of the Earth's center-of-mass coordinates, attributed to the imposed physical constraints of the LEOs' dynamic nature.

6.3.2 Earth rotation parameter estimates

It has been shown in Fig. 6.5 that integrating LEO observations may lead to larger formal errors for the estimated ERPs. The multi-GNSS results are evaluated for this quality indication as well and are shown in Fig. 6.20.

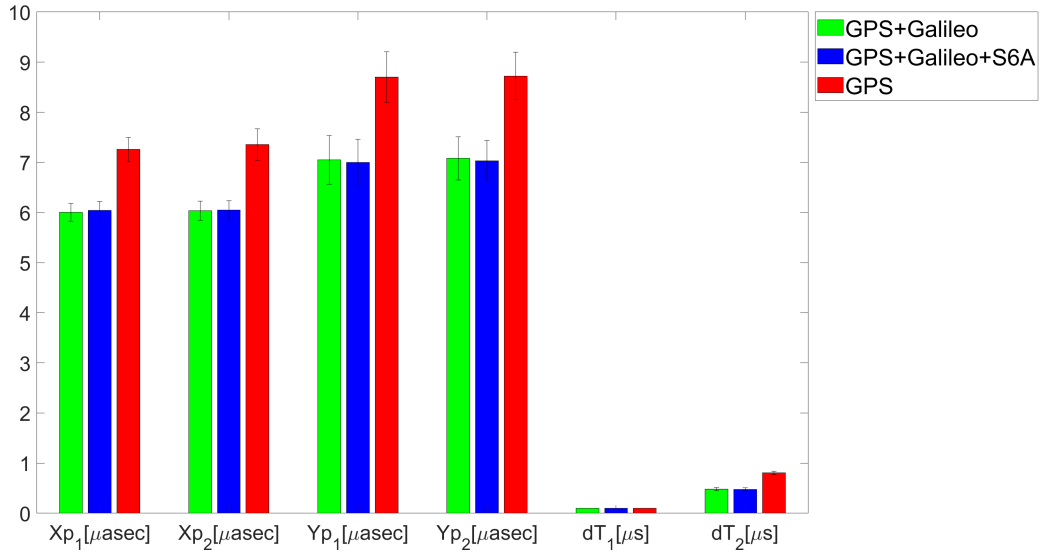

Figure 6.20: Mean values and standard deviation of formal errors of daily estimates of Earth rotation parameters

It is clearly evident that the observability of the determined ERPs notably improves when a multi-GNSS solution is computed. The influence of integrating LEO observations is comparably small, whereby the X-pole coordinates formal errors result in being slightly larger while the Y-pole observability seems to improve. This result goes in line with the findings of resulting from Fig. 6.5, where including observations from only one LEO did not lead to a degradation of the formal errors of the ERPs.

The analysis of the square root of the cofactors shown in Fig. 6.21 reveals that the larger formal errors are caused by the a posteriori m_0, representing the estimation for the observation noise, which is increased for the LEO-integrated solution compared to the GNSS-only solutions (see Table 6.12). It is evident that the additional observation geometry of the included Sentinel-6A satellite leads to smaller square root of the cofactors of the LEO-integrated solution compared to the GPS+Galileo solution.

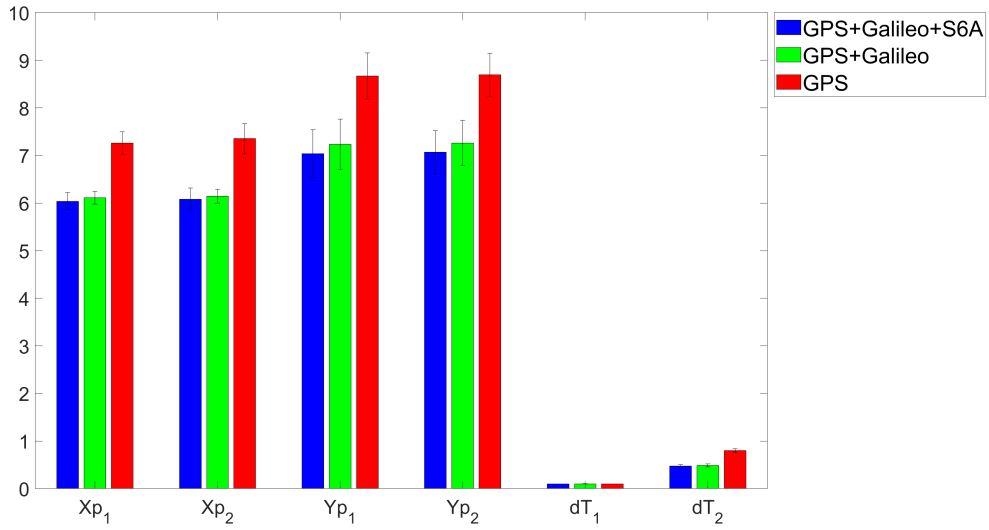

Figure 6.21: Mean values and standard deviation of square root of the cofactors of daily estimates of Earth rotation parameters

6.4 Integration of Spire satellites

Recently, scientifically designed experiments can be carried out using GPS data that was collected by CubeSats operated by Spire Global, which are equipped with dual-frequency GPS receivers (see sect. 2.5.7). The aim of the experiments shown in this section is to determine how incorporating GPS observation data from specific Spire satellites affects the computation of a global network solution. The results shown here serve to further exploit the setup shown in Kobel et al. (2023a). It is of central interest to investigate whether GPS observations from CubeSats with no scientific mission goal can contribute to scientific applications. In the frame of this work, the influence of integrating Spire satellites into the computation of a global network solution is compared to a scientific LEO (SLEO)-integrated solution. The experiment is performed for the time span of 20 May 2020 - 19 June 2020. For this purpose four different solutions are compared:

- GPS
- GPS+Spire
- GPS+SLEO
- GPS+Spire+SLEO

It is important to mention here that for the Spire satellites the procedure of single-receiver ambiguity resolution could not be carried out at the time this investigation took place because the data quality of the code observations does not have the appropriate quality, which is needed for the reliable formation of the Melbourne-Wübbena linear combination (see sect. 3.2.1.3). Due to the very recent possibility of using data from Spire, a sophisticated macro model is not available yet which is needed for explicit modeling of non-gravitational forces (see sect. 3.3), which makes it necessary to choose the reduced-dynamic orbit parametrization by estimating constant accelerations over one arc in all three spatial directions and constrain the PCA's to $5 \cdot 10^{-9}$nm/s^2. In order to keep the comparison between the different solutions fair, the parametrization for the scientific LEO is chosen to be the same, whereby non-gravitational forces are not explicitly modeled and no ambiguity-fixing is applied.

6.4.1 LEO-only POD results

We first evaluate the quality of GPS observations obtained from the GPS receivers aboard the included LEOs in order to determine the potential utility of these observations for determining a global GPS network solution.

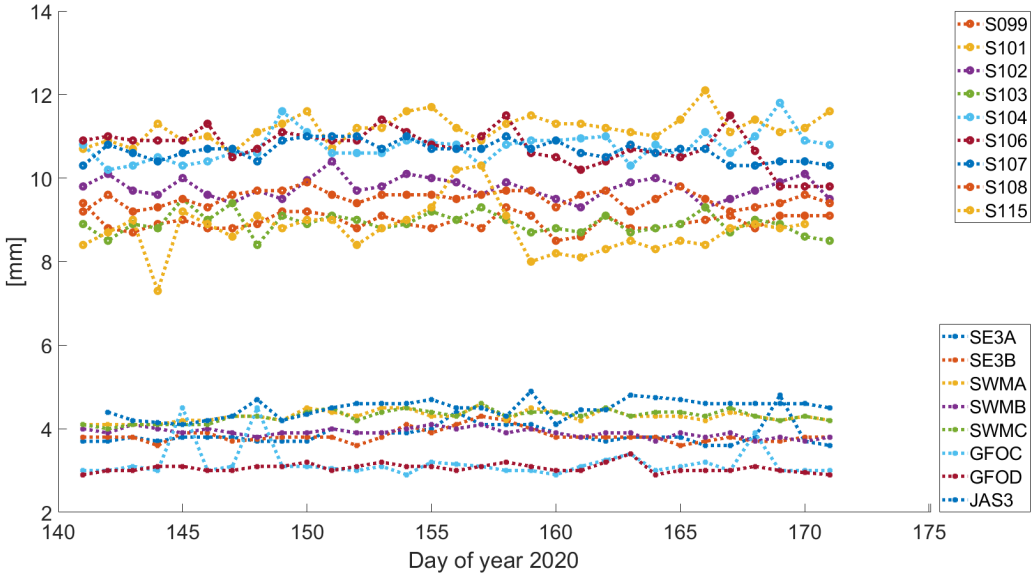

Figure 6.22: Daily RMS values of ionosphere-free phase residuals of different LEO missions

To assess this, a POD of all the included SLEOs and Spire satellites is carried out, whereby the resulting phase RMS are shown in Fig. 6.22. For all LEOs, PCV maps are applied, which were determined based on in-flight data using the residual stacking approach. Using the phase RMS as a measure of data quality, Spire satellite observation quality is compared to results from a POD of LEOs with scientific mission goals. In Fig. 6.22, the phase RMS indicate that the performance of a POD for LEOs with scientific mission objectives is superior to that of Spire satellites, whereby the magnitudes confirm the findings of Arnold et al. (2023b). Additionally, for the two GRACE Follow-on satellites the RMS is always the lowest, whereas for Jason-3 the Phase RMS is the largest compared to the other included scientific LEOs. Since the POD setup by means of orbit parametrization is chosen to be identical for all included LEO satellites, together with differences in data quality, leads to small differences in the resulting phase RMS for the scientific LEOs. LEO-specific parametrization, tuned to the specific orbit characteristics (orbit height and inclination), whereby has the potential to further improve the quality of the POD.

6.4.2 Earth's center-of-mass coordinates results

To allow for a comparison with the results shown in sect. 6.1.2.1, the estimated Earth's center-of-mass coordinates are presented along with their formal errors.

The estimates shown in Fig. 6.23 reveal the influence of integrating LEO-GPS observations on the estimated Earth's center-of-mass coordinates for the different scenarios. From the estimates of the X-, Y-, and Z-component itself it is not possible to identify a superior solution. A key insight is presented in the results of Z-component estimates. For example, the reference solution (GPS-only) shows a systematic offset from zero. The GPS+Spire solution exhibits an offset, although it is partly smaller, but still clearly evident. There is no systematic offset from zero anymore in the GPS+SLEO solution. It is clear from these results that the inclusion of observations from SLEOs influences the resulting Z-component of the Earth's center-of-mass coordinates more strongly than GPS observations from Spire. The solution including all Spire + SLEOs is close to the GPS+SLEO solution, which indicates that Spire-GPS observations are less influential in determining the Earth's center-of-mass coordinates than SLEO-GPS observations, due to the smaller variety of the orbit characteristics (inclination and altitude) of the included satellites. In order to avoid degrading the statistical results, results from three days have been identified as outliers and excluded from the analysis (DOY: 59/61/64).

Table 6.14 shows mean and standard values of differences between the estimated Earth's center-of-mass coordinates and results derived from an SLR analysis (Geisser, 2023). It is evident, that the GPS+Spire-integrated solutions have the largest mean values for the Y- and Z-component of the Earth's center-of-mass

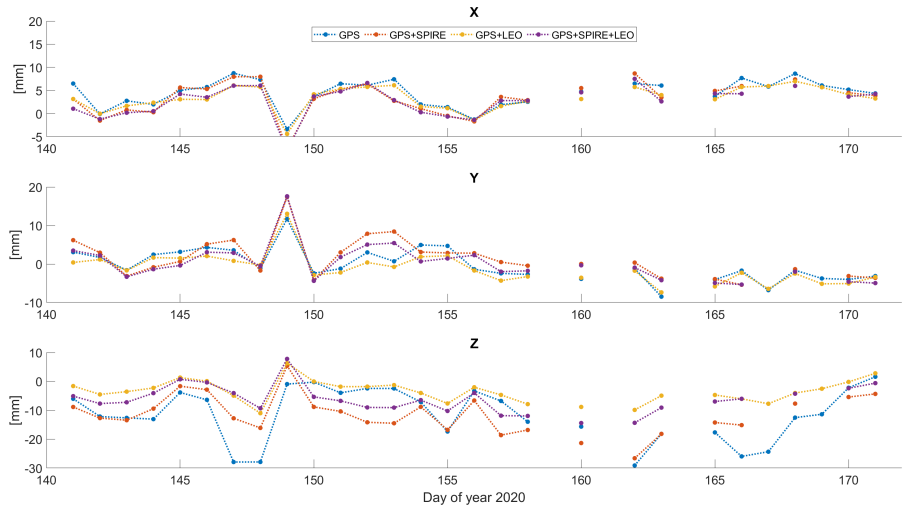

Figure 6.23: Estimated Earth's center-of-mass coordinates

differences. The GPS+SLEO solution outperforms the GPS+Spire solution in terms of mean and standard deviation for all components, whereas the GPS+SLEO+Spire solution shows results that lie between the GPS+Spire and GPS+SLEO solutions with smaller standard deviations than the GPS+Spire solution, highlighting the beneficial influence of the SLEO observations. It is possible to conclude that the integration of GPS observations from SLEOs leads to Earth's center-of-mass estimates of superior quality in terms of differences to the reference time series, whereby single-receiver ambiguity resolution and explicit modeling of non-gravitational forces were not applied for the SLEOs in these experiments. Adding GPS observations from Spire does not lead to systematic improvements in the differences. However, a longer time span has to be examined to evaluate long-term stability.

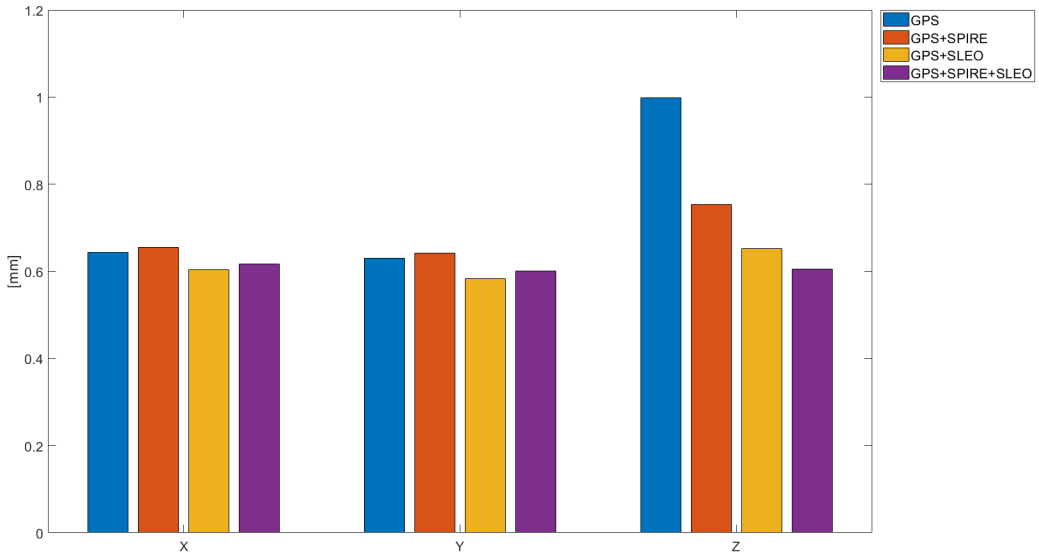

Figure 6.24: Mean values and standard deviation of formal errors of daily estimates of Earth's center-of-mass coordinates

It is evident that the mean values of formal errors, as shown in Fig. 6.24, reflect these benefits in a noticeable manner, particularly the Z-coordinate determination. In the scenario where only the Spire satellites are integrated, the result is notably improved compared to the reference solution, but when

Table 6.14: Earth's center-of-mass coordinates differences

Solution/Component	X [mm]	Y [mm]	Z [mm]
GPS	1.6±3.2	3.2±4.4	-11.8±9.0
GPS+Spire	0.7±3.8	4.8±5.2	-12.6±6.6
GPS+SLEO	0.2±3.6	2.1±3.7	-3.9±4.1
GPS+Spire+SLEO	0.1±3.4	3.5±4.6	-7.0±5.0

observations from SLEOs are included, the results are superior, while the GPS-only solution shows the largest values. This clearly illustrates the benefit of LEO-integrated processing. It is evident that the formal errors for the X-and Y-components of the GPS+Spire solution are larger than for the GPS-only solution.

The analysis of the square root of the cofactors of these parameters, shown in Fig. 6.25 reveals that the reason for the larger formal errors of the GPS+Spire solution, compared to the GPS-only solution, can be found in the increase of the estimate of the observation noise for the GPS+Spire solution, which is probably caused by the comparably poor observation data quality shown by the phase RMS resulting from a LEO-only POD in Fig. 6.22. The GPS+Spire+SLEO solution shows the smallest square root of the cofactor among all solutions, indicating the improvement of observation geometry and parametrization in terms of Earth's center-of-mass coordinate estimation.

The inclusion of Spire-GPS observations notably contributes to the estimation of the Earth's center-of-mass coordinates in terms of observability. However, the GPS observations from the LEOs with scientific mission goals influence the resulting estimates to a larger extent. One reason for this is the much more diverse orbit characteristics of the scientific LEOs compared to the Spire satellites which were integrated in the experiments of this work, which leads to smaller square root of the cofactors of the Earth's center-of-mass estimates. The study conducted by Arnold et al. (2023b) suggests that alternative orbit parametrizations for the Spire satellite can potentially improve the orbit quality, which, in turn, may also improve the results of the Earth's center-of-mass estimates resulting from the LEO-integrated global network determination approach.

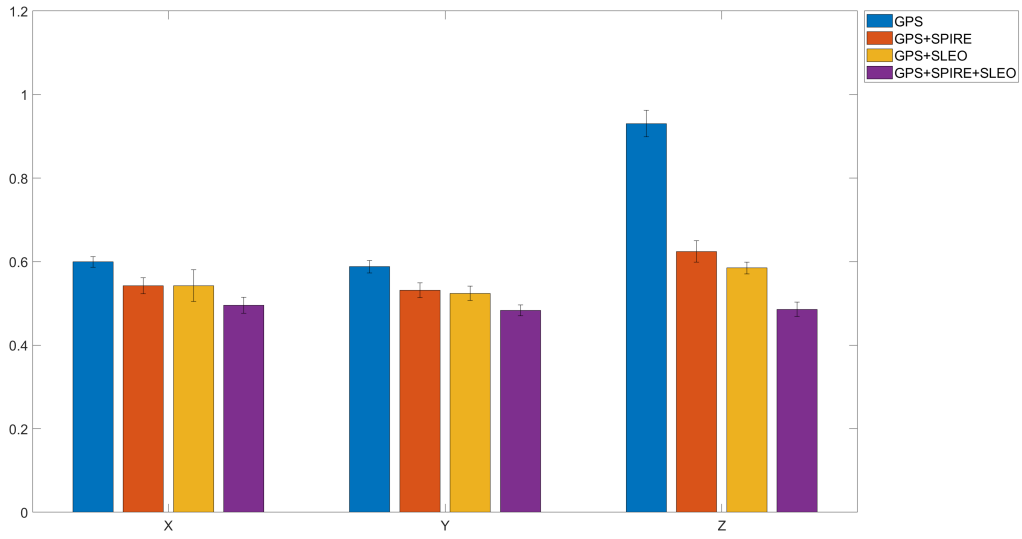

Figure 6.25: Mean values and standard deviation of square root of the cofactors of daily estimates of Earth's center-of-mass coordinates

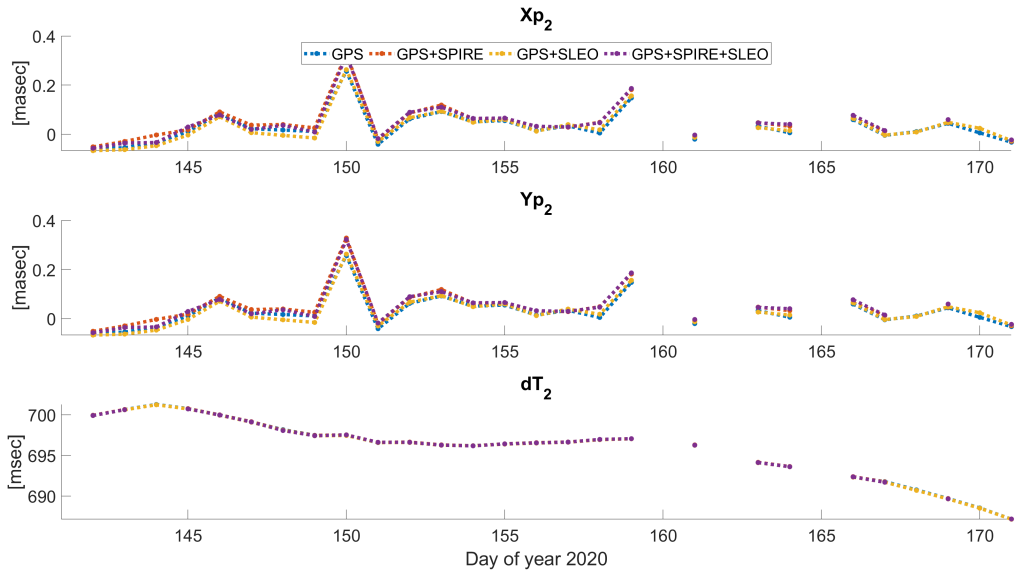

Figure 6.26: Comparison of estimated ERPs to C04 reference values

6.4.3 Earth rotation parameter estimates

The resulting ERPS were compared to the combined reference solution C04, which is consistent with the ITRF2014. As shown in Fig. 6.26, GPS observations from LEOs appear to have a minor impact on the ERP (Xp_2, Yp_2, and dT_2) estimates, since the differences between the individual solutions are small compared to the magnitude of the estimates. The differences between the GPS+Spire and GPS+LEO solutions show an overall difference of 14% for the Xp_2 estimate in terms of standard deviation. The estimation of the Yp_2 coordinate exhibits smaller changes caused by the integration of LEO observation. The GPS+SLEO solution shows an increase of 3% of the standard deviation with respect to the GPS-only solution. The largest deviations in terms of standard deviation w.r.t. the GPS-only solution show the GPS+Spire and GPS+Spire+LEO solutions with an increase of 18% and 19% respectively for Yp_2. A difference of below 1% for the individual estimated values for dT_2 results for all computed solutions indicates that the integration of LEO-GPS observations does not notably affect the estimation of this parameter, which is caused by the strong constraint applied to dT_1 (see Table 3.2).

Based on the square root of the cofactors shown in 6.27, it appears that integrating additional GPS-LEO observations does improve the observability of ERPs due to the increased observation geometry, with the GPS+Spire+LEO solution demonstrating a clear improvement in the square root of the cofactor of ERPs in the frame of a global network solution determination. As shown before, a bias in the pole estimates in LEO-integrated solutions may result caused by the integration of multiple LEOs with similar, and in this case even identical, inclinations.

6.4.4 Ground station coordinates

To determine the internal consistency of the derived ground station coordinates a Helmert transformation is computed referring to the IGS14 solution (Rebischung and Schmid, 2016). A daily RMS over all ground stations is computed per spatial direction (North/East/Up), whereby an outlier rejection is performed on the level of 50 mm. The mean values over the daily RMS values are shown in Fig. 6.28. It is evident, that the LEO-integrated solutions show smaller RMS values than the GPS-only solution for all spatial directions. The results of the RMS of the Helmert transformation, in comparison to the GPS-only reference solution, indicate the advantageous nature of LEO-integrated processing for ground station coordinate determination in terms of consistency with the IGS14 reference solution. It can also be stated that the inclusion of observations from scientific LEOs is more favorable than integrating Spire satellites, based on the smaller median RMS values for the North and Up directions.

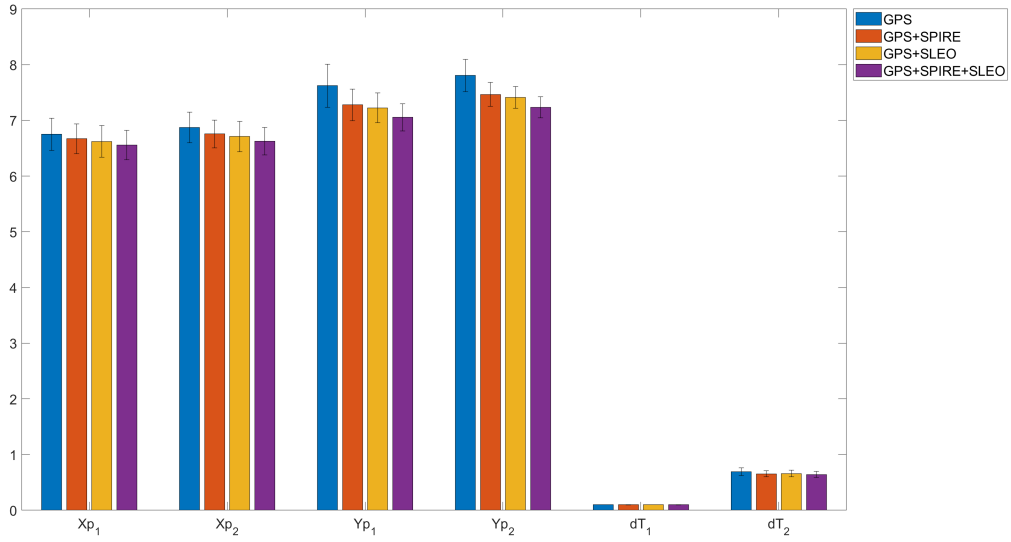

Figure 6.27: Mean values and standard deviation of square root of the cofactors of daily estimates of Earth rotation parameters

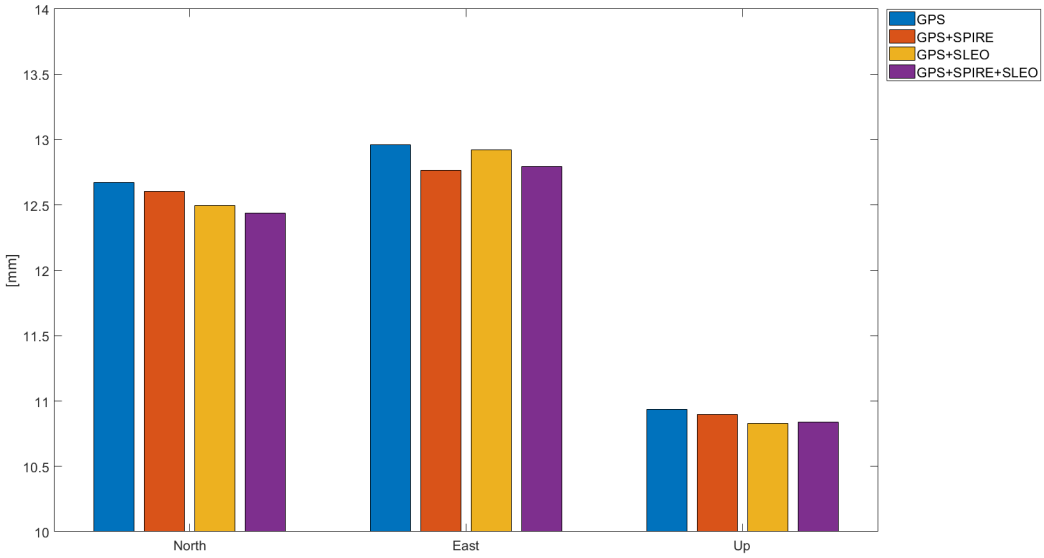

Figure 6.28: RMS of Helmert transformation of ground station network

6.4.5 GPS orbit solutions

The quality of the GPS orbits is assessed by computing orbit misclosures at the day boundaries of two consecutive orbital arcs in the inertial system. In Table 6.15 median values of daily RMS values are shown, whereby one RMS per day is computed over all satellites. It is evident that incorporating GPS observations from LEOs can provide advantages in determining GPS orbit solutions. For the GPS+Spire solution, the median RMS value is smaller than for the reference solution, which points out a slight improvement of the GPS orbit solutions. The resulting GPS orbits of the GPS+SLEO and GPS+Spire+SLEO solutions clearly outperform ground GPS-only processing, indicating the advantageous impact of SLEO observations on the GPS orbit solutions. The increased observation geometry and global coverage due to the integration of LEO observations may lead to more continuous observations and therefore more accurate orbit determination for

Table 6.15: Median of daily GPS orbit misclosures

Solution	RMS [mm]	Improvement (w.r.t. GPS-only)
GPS	70.2	-
GPS+Spire	68.2	3%
GPS+SLEO	66.5	5%
GPS+Spire+SLEO	66.5	5%

GPS satellites. It can therefore be concluded that for the determined GPS orbits, the additional geometry due to the LEO observations is more important than the additional physical constraints imposed by the dynamical nature of the LEOs. Since the included Spire satellites have the same orbit characteristics in terms of inclination (apart from S115), the observation geometry is not increased to the same extent as for the SLEO-included scenarios, which causes the GPS+SLEO and GPS+Spire+SLEO solutions to show the best performance in terms of GPS orbit misclosures. A benefit of estimating ambiguities as float numbers, as it has been adopted for the solutions presented in this section, is to potentially compensate for mismodeling of various sources. It is evident that the 3D orbit disclosure RMS values are generally larger than for the solutions shown in sect. 6.1, which indicates that the processed time span highly influences the statistics. However, the magnitudes of the resulting orbit misclosures from the solutions presented in this section of about 70 mm go in line with the findings by Lutz et al. (2016a).

6.4.6 LEO orbit solutions

To assess the quality of the derived orbit solutions for the Spire and scientific LEO satellites, orbit misclosures are analyzed and compared for the final solutions resulting from the LEO-integrated processing, along with LEO orbits resulting from a classical POD.

Table 6.16: RMS of LEO and Spire orbit misclosures

Solution	LEO [mm]	Spire [mm]
LEO POD	28	79
GPS+Spire	-	141
GPS+SLEO	116	-
GPS+Spire+SLEO	109	141
GPS+SLEO (AF)	149	-
GPS+SLEO (AF+NG)	92	-

It is evident from Tab. 6.16 that the orbit solutions derived for scientific LEOs are notably more accurate than those for Spire satellites based on RMS values of orbit misclosures, which confirms the findings of Arnold et al. (2023b). The orbit misclosures of the final orbit solutions of the integrated processing, shown in Table 6.16, clearly reveal a degradation of the computed LEO and Spire trajectories compared to the results of the LEO-only POD. The computed orbit misclosures are up to five times larger for the final LEO orbit solutions than for the LEO-only POD results, whereby the SLEO orbit solutions clearly outperform the Spire satellite orbit solutions in terms of orbit misclosures. This result goes in line with the findings of the experiments shown in sect. 6.1, whereas the same reasoning for the degradation of the derived LEO orbits compared to LEO-only POD results applies, namely the choice of the observation sampling.

6.5 Analysis of long time series

An analysis of a longer time series of geodetic parameters, which in this work are the Earth's center-of-mass coordinates and ERPs, may be useful to quantify their precision. Certain characteristics of these parameters can only be quantified when a sufficiently long time series is available. The estimated parameters from two solutions, computed for 1 January 2020 - 31 December 2022, are compared: the reference (GPS-only) solution and a solution with Sentinel-3A, GRACE FO-C, and Jason-3 integrated (see Table 6.1).

6.5.1 Earth's center-of-mass coordinates estimates

This section compares the estimated Earth's center-of-mass coordinates results with those shown by Männel and Rothacher (2017), where GPS-only and LEO-integrated solutions are analyzed. Männel and Rothacher (2017) showed that the variations in the X and Y components are smaller than 3 cm, but the ones of the Z component can be up to 10 cm, primarily due to unresolved (float) ambiguities. Also Brockmann (1997) demonstrates that ambiguity-fixing improves the Earth's center-of-mass coordinates estimation by a factor of 3, based on GPS-only results. The LEO-integrated solution computed by Männel and Rothacher (2017) has reduced variations by a factor of 2 for all components compared to the GPS-only solution.

The results of the present work, shown in Fig. 6.29, reveal a different result. The differences in maximum variations of the estimated Earth's center-of-mass coordinates between the GPS-only and GPS+LEO solutions are smaller as shown in Männel and Rothacher (2017). The variations are 1.9 cm, 2.4 cm, and 7.3 cm for the X-, Y-, and Z-component respectively for the GPS-only solution, whereas for the GPS+LEO solution, the variations are 1.6 cm, 2.2 cm, and 7.1 cm. This represents a reduction of 22%, 11%, and 3% for the X-, Y-, and Z-component respectively. The result therefore shows that the inclusion of LEO observations helps to stabilize the long-term estimation of the Earth's center-of-mass estimation compared to a GPS-only solution. However, the influence of these observations is notably smaller as shown in the study from Männel and Rothacher (2017). While in this work, the ground station network consists of 240 stations, the study conducted by Männel and Rothacher (2017) is based on a 53 ground station network. Naturally, the integration of LEO observations has a larger impact on the solution using a smaller number of ground stations. Together with the different adopted arc lengths, Männel and Rothacher (2017) used 7-day arcs, this represents the reason for this smaller improvement resulting from the experiments of this work.

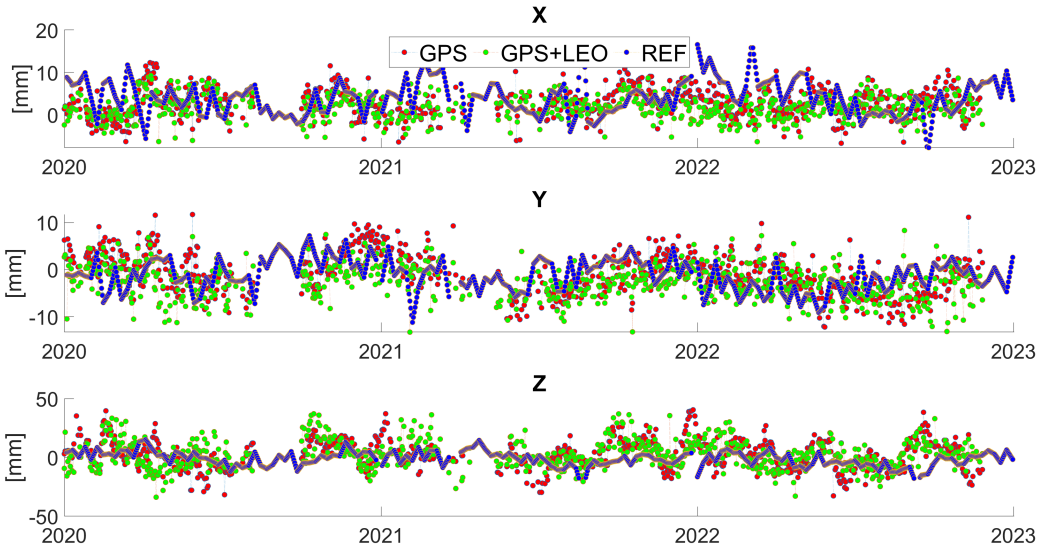

Figure 6.29: Earth's center-of-mass coordinates

For the time periods 7 August 2020 - 30 September and 14 April 2021 - 14 May 2021, severe data issues (related to the ground station network) have been detected, leading to a removal of the results of these days for the analysis. For this time period, the covariance matrix is not positive definite, which means that not all eigenvalues are larger than zero, whereby comparably small sample sizes can lead to non-positive definite matrices, especially when estimating complex models with many parameters. Also, outliers or extreme values in the data can affect the covariance matrix and lead to non-positive definiteness.

The plots in this section also show an external solution derived from the analysis of SLR data (Geisser (2023)), which serves as a reference. This solution shows smaller variations in the Z-component of about 3.3 cm, whereas for the X-, and Y-component the variations are similar to those from the GPS-only and

GPS+LEO solution. Also, this reference solution uses a 7-day arc processing strategy and differs therefore from the GPS-only and GPS+LEO solutions from this work.

The amplitude spectrum (introduced in Chapter 3.7.5) provides valuable insights into the periodicities and amplitudes of the estimated parameters. Männel and Rothacher (2017) shows that the LEO-integrated solution leads to most periodicities having smaller amplitudes than the GPS-only solution.

In the solutions of this work, the amplitude spectrum shown in Fig. 6.30 reveals a more complex influence of integrating LEO observations as described by Männel and Rothacher (2017). In each subplot, the periods with the highest amplitudes are marked correspondingly. In the LEO-integrated solutions by Männel and Rothacher (2017), a signal with a 150-day periodicity is visible, which is not clearly distinguishable in the GPS-only solution, which is probably due to LEO orbit characteristics. It is stated that including multiple LEOs causes LEO-specific characteristics to disappear when they have different orbit characteristics, resulting in further improvements in the Earth's center-of-mass estimation. This raises the question of whether the estimations in this work reveal the draconitic periodicities of the integrated LEOs. Capdeville et al. (2021) shows that the draconitic orbit period of Jason-3 is 59 days, which is not apparent in the amplitude spectrum (Fig. 6.30), however, at 122 days, which is approximate twice the length of the draconitic period, a significant amplitude can be observed for the Z-component. The draconitic period of Sentinel-3A, which is 182 days (Strugarek et al., 2019), overlaps with the semi-annual periodicity and is therefore not clearly distinguishable. However, the LEO-integrated solutions' Z-component amplitude spectra clearly reveal that the Sentinel-3A draconitic orbit period does not map to the estimation, since no large amplitude is evident at this period. It can therefore be stated that when integrating multiple LEOs with different orbit characteristics, the influence of LEO draconitic periods on the estimation of the Earth's center-of-mass coordinates can be reduced, taking into account the results shown by Männel and Rothacher (2017) using a one-LEO scenario.

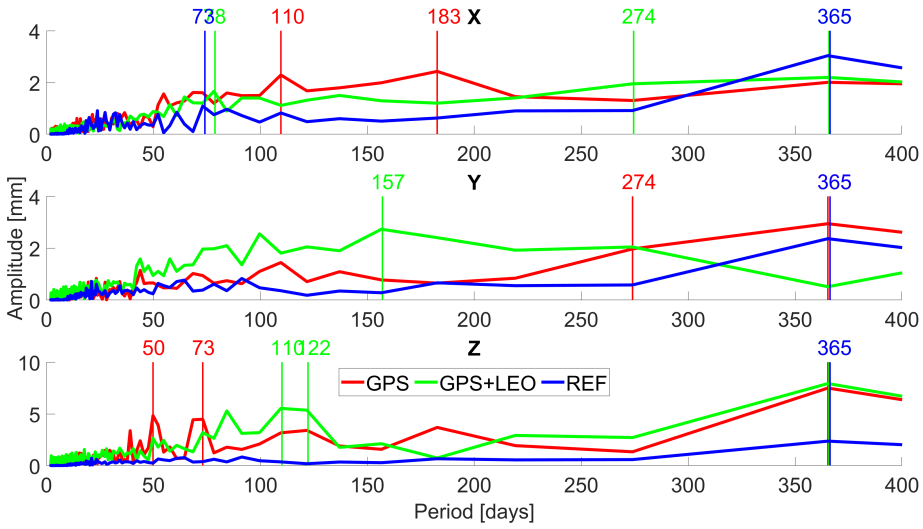

Figure 6.30: Amplitude spectrum of Earth's center-of-mass coordinates

Männel and Rothacher (2017) showed that annual signals and their high-order harmonics, which have a strong connection to the GPS satellites' draconitic orbit period (351.4 days), are reduced when LEOs are included in the processing. However, the analyzed time series (also 3 years) is too short to distinguish between annual and draconitic signals. For all solutions shown in Fig. 6.30, including the reference solution stemming from a SLR processing, and for all components a strong annual signal is present, apart from the GPS+LEO solutions estimate of the Y-component. The semi-annual signal has a notably lower amplitude for the GPS+LEO solution than for the GPS-only solution for the X-, and Z-components, whereby for the Y-component this signal is partly overlapped from a dominant signal with 157 days period in the GPS+LEO solution. In the solutions of this work, it is feasible to state that annual signals have the largest amplitudes, whereby periodicities stemming from the draconitic orbit period of GPS satellites are probably

hidden in the annual signals. However, the signals are dominantly expressed at 365 days and not at 351 days, which goes in line with the SLR-based solution. The absence of the annual signal of the Y-component of the GPS+LEO solution may be caused by a strong semi-annual signal near the peak evident at 157 days period.

Table 6.17: Amplitude of annual Earth center-of-mass motion

	X	Y	Z
GPS (this work)	2.0 cm	2.9 cm	7.5 cm
GPS+LEO (this work)	2.2 cm	0.5 cm	7.9 cm
GPS (Männel and Rothacher, 2017)	4.5 cm	2.6 cm	12.6 cm
GPS+LEO (Männel and Rothacher, 2017)	3.2 cm	4.0 cm	5.9 cm

Table 6.17 reveals that the influence of integrating LEO-GPS observations into the processing on the estimates of the Earth's center-of-mass is notably higher in the setup from Männel and Rothacher (2017), potentially caused by the much smaller ground network used. The amplitudes for the X-, and Y-components are in general smaller for the solutions derived in the frame of the present work. The larger amplitude of the Z-component of the GPS+LEO solution compared to the results of Männel and Rothacher (2017) may be a result of the length of the arc chosen in the setup. It is worth noting that the result of the GPS-only solution for the Z-component is already improved, showing the benefit of the comparably large ground station network.

6.5.2 Earth rotation parameter estimates

The studies presented in sect. 2.7 about LEO-integrated processing have not provided detailed information about the effects on ERP estimations. The estimated ERPs from this work are compared to the C04 reference series.

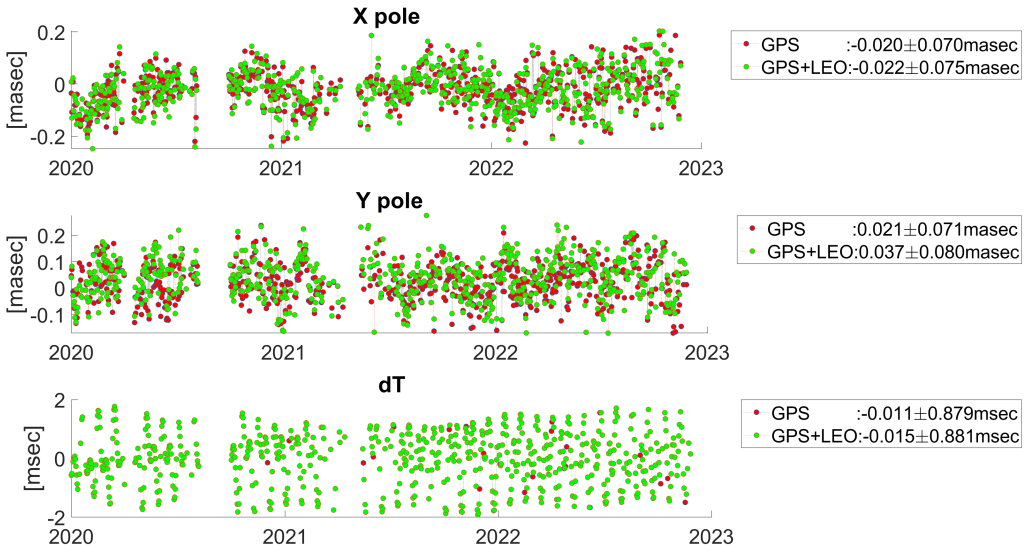

Figure 6.31: Comparison of estimated ERPs to C04 reference values

The study by Shen et al. (2015), based on SLR data from LAGEOS, also shows ERP differences to the C04 reference series. Compared to the results of this work, the ERPs from LEO-integrated processing exhibit 4 times smaller RMS differences for the Xp_2- and Yp_2 coordinates, while those for dT_2 are 10 times larger. This is because dT_2 is influenced by dT_1, which is a constrained parameter in the LEO-integrated solution and heavily dependent on the a priori value. The differences reveal an increased bias of the LEO-integrated solution compared to the GPS-only solution, which can be attributed to the inclinations of the integrated

LEOs which confirms the findings shown in Table 6.4. Since the integrated LEOs have inclinations of 98.60°, 89.00°, and 66.04°, the bias is not expressed to a large extent. As shown by Zajdel et al. (2020) the extension of a 24h processing strategy to a long-arc approach could be beneficial in terms of resulting ERPs, also in the LEO-integrated global network determination approach.

Recall: Experiments were performed to investigate the impact of integrating GNSS observations from LEOs on the resulting global network solution, with special regard to the influence of explicit modeling of non-gravitational forces and ambiguity-fixing for the LEOs. The observation residuals of the experiments show that the reference solution with no LEO observations and the solution with only one LEO incorporated have the smallest RMS, while float ambiguities for LEO observations cushion modeling errors to a larger extent than fixed ambiguities, and explicitly modeling non-gravitational forces in the LEO POD leads generally to larger residuals. The integration of observations from LEOs improves the square root of the cofactors of the geodetic parameters, namely Earth's center-of-mass coordinates and ERPs, whereby fixing ambiguities, and explicit modeling of non-gravitational forces for LEOs play a crucial role in the LEO integrated processing. The inclusion of multiple LEOs with similar orbit characteristics leads to a systematic bias in the estimated pole coordinates. The ground station coordinates determination profits from the inclusion of LEOs in the processing. The resulting GPS orbits of LEO integrated solutions are superior compared to ground station-only processing, when ambiguities remain float and no explicit modeling of non-gravitational forces for LEOs is applied. Orbit overlaps, SLR validation, and KBR validation show significant degradation of the final LEO orbit solutions compared to LEO-only POD results, which can be attributed to the chosen observation sampling. Including Sentinel-6A GNSS observations led to improvements in the Earth's center-of-mass coordinates and ERPs observabilities over using only GPS or GPS+Galileo, while the GPS+Galileo solution outperforms the GPS-only solution. The phase RMS of LEO-only POD procedures show that the data quality and the chosen orbit parametrization for Spire satellites are not as good as for scientific LEOs. The estimated Earth's center-of-mass coordinates and their formal errors reveal that the inclusion of GPS observations from scientific LEO influences the results more than the ones from Spire, although the integration of Spire satellites leads to an improvement of the observability of the geodetic parameters as well. The impact of the inclusion of GPS observations from Spire and scientific LEOs on the resulting GPS orbit solutions was shown to be beneficial in terms of orbit misclosures. The integration of LEO-GPS observations stabilizes the Earth's center-of-mass estimation by reducing its variations, whereby the influence on periodicities and their amplitudes is found to be more complex.

Chapter 7

Summary

The incorporation of data from GNSS receivers based on LEO satellites notably helps in the computation of a global network solution. This allows the determination of trajectories for both LEOs and GNSS satellites, as well as the estimation of geodetic parameters, such as Earth's center-of-mass coordinates, ERPs, and ground station coordinates. In this work, use was made of the fact that GNSS observations from LEO satellites can provide information about areas that are not covered by ground stations. To assess the key question of this work, an integrated processing scheme is employed, including the establishment of NEQs for stations and LEOs, combining these NEQs, estimating ambiguities, and computing final solutions. A review of existing publications provided valuable insights into similar scientific questions and diverse experimental setups.

The method of least-squares is employed for estimating unknown parameters by minimizing the sum of weighted squared errors using design and normal equation matrices. To address difficulties in describing some unknown parameters sufficiently through observations and to limit the influence of known correlations between parameters, pseudo-observations are introduced in the LSQA to constrain these parameters, e.g., the ERP dT_1 which need to be fixed to a priori.

To determine a satellite's trajectory accurately, it is essential to consider all forces acting on it. The process of integer ambiguity resolution plays a crucial role in the POD of LEO satellites. The reduced-dynamic orbit parametrization compensates for mismodeled or unmodeled forces using additional parameters. Some experiments of this work involve modeling forces acting on a satellite, including solar radiation pressure, Earth radiation pressure, and aerodynamic forces, which are more complex for LEO satellites than for GNSS satellites. To determine the precision of orbit solutions, quality metrics such as orbit comparisons, SLR validation, and orbit overlaps at arc boundaries were employed.

Within this work, PCO corrections for LEO receivers were estimated, whereby using single-receiver ambiguity solution was applied. Results reveal offsets in the Up-direction for certain satellites, indicating potential inaccuracies in the macro model or in the provided satellite-specific characteristics. The application of estimated PCO corrections results in reduced-dynamic orbit solutions of superior quality. These results imply, that a rigorous determination of PCO corrections should be performed in-flight for LEO GNSS antennas, either in a LEO-only POD approach or within the LEO-integrated global network determination.

Special attention is given to potential difficulties associated with the satellite design of Jason-3. This includes changes in attitude mode depending on the β-angle, incomplete GPS antenna coverage, and rotating solar panels. The Jason-3 POD results indicate poorer GPS data quality than for Sentinel-3A, with integer ambiguity resolution having a lower success rate and larger residuals from code and phase observations. Different strategies, including ambiguity-fixing and explicit non-gravitational force modeling, improve the precision of the Jason-3 orbit solutions. SLR validation shows that the quality of computed orbits outperforms the reference solution. Various approaches for determining a PCV map and PCO corrections result in notable variations for different attitude modes, with an iterative manner of PCO estimation allowing for further improvement of resulting orbit precision. Possible explanations for these findings are:

- Complex signal propagation patterns may lead to different phase center variations depending on the antennas' orientation due to the satellites' rotation.
- Satellite-specific characteristics are not as accurate as necessary, whereby the erroneous information is indicated by the performed experiments.
- The Jason-3 satellites' attitude may be not adequate enough. In turn, this means the provided quaternions are systematically off from the real orientation of the satellite bus, whereby further research is needed to confirm this hypothesis.

Especially the last point is worth investigating in future research, because this feature may appear for other LEO satellites as well, e.g., for Sentinel-6A, as it has been shown by Desai et al. (2022) and Montenbruck et al. (2022).

Experiments were conducted to investigate the impact of integrating GNSS observations from LEOs on the resulting global network solution, particularly considering the influence of explicit modeling of non-gravitational forces and ambiguity-fixing for the LEOs. The precision of satellite positions and their onboard atomic clocks plays a crucial role in determining a global network solution. GPS satellites are equipped with precise atomic clocks (Pock, 2015), while for the LEO satellites, this is not the case which may cause larger clock instabilities compared to GPS satellites' clocks. Combining data from various sources, such as LEO satellites and ground-based observatories, introduces additional uncertainties and error sources. Coherently combining data from multiple systems requires careful consideration of potential biases and discrepancies between the data. Since LEOs are moving fast compared to ground stations, the observation times are shorter, which can affect the ambiguity resolution. The fixing of ambiguities can revoke the system the possibility to weaken modeling errors, which can in turn then negatively influence the resulting solution.

Observation residuals demonstrate that the reference GPS-only solution and the solution with only one LEO incorporated have the smallest RMS, with float ambiguities for LEO observations cushioning modeling errors to a larger extent than fixed ambiguities. Explicit modeling of non-gravitational forces for the LEO orbit modeling generally leads to larger residuals due to the adoption of tighter constraints on empirical parameters.

Integrating observations from LEOs improves the determination of Earth's center-of-mass coordinates, as evidenced by a decrease in formal errors, with the fixing of ambiguities and explicit modeling of non-gravitational forces playing a crucial role. The increased observational geometry due to the integration of LEO satellite observations from different orbital planes, enhances the overall coverage and diversity of the system. By explicitly modeling non-gravitational forces, additional physical constraints due to the LEOs dynamic nature are imposed to the system. Due to the orbital characteristics of the integrated LEOs, the sensitivity of the Z-component of the Earth's center-of-mass is increased compared to a GPS-only solution. Consequently, both the corresponding formal errors and the estimates from the LEO-integrated processing are superior to a GPS-only solution. LEO satellites are at relatively close distances to the Earth's surface, making their orbits sensitive to small perturbations. Resolving ambiguities accurately ensures that the satellite positions are determined with high precision, which is essential for accurately estimating the Earth's center-of-mass coordinates. Ambiguity-fixed solutions for LEOs ensure consistency among different observations and between multiple epochs, whereby consistent solutions contribute to a more reliable and stable estimation of the Earth's center-of-mass over time.

While including up to three LEOs leads to only a small change in the estimation of the Earth rotation parameters, including multiple LEOs results in larger formal errors of derived X- and Y-pole coordinates, caused by the increased m_0 representing the estimated observation noise. The estimated square root of the cofactors for the ERPs indicate the benefit of integrating LEO observations in terms of observational geometry. A systematic bias in the estimated pole coordinates results due to the imbalance of integrated LEOs being in either prograde or retrograde orbits.

A superior quality of ground station coordinates determination is achieved through the inclusion of three LEOs in the processing, using ambiguity-float GPS-LEO observations.

The resulting GPS orbits of LEO integrated solutions outperform ground station-only processing when ambiguities remain float, and no explicit modeling of non-gravitational forces for LEOs is applied. This is a result of the improved observational geometry, global coverage, and a larger number of observations. The estimation of ambiguities as float numbers allows for more compensation for mismodeling of various sources. Therefore, single-receiver ambiguity resolution for LEOs introduces additional stiffness to the full system. When non-gravitational forces are explicitly modeled for LEO satellites, the parametrization is adjusted. This modified parametrization includes tighter constraints on the PCAs, which are usually employed to compensate for modeling inaccuracies. Consequently, this methodology introduces increased stiffness to the system, leading to adverse effects on the precision of the resulting GPS orbits in the conducted experiments. Additionally, errors in the determination of non-gravitational forces for LEOs can propagate into subsequent GPS orbit computations. As a result, errors may accumulate over time, leading to less accurate orbit solutions.

Orbit overlaps, SLR validation, and KBR validation show degradations of final LEO orbit solutions compared to LEO-only POD results. By not systematically assigning higher weights to LEO observations, the system allows for compensating for mismodeling heavily at the expense of LEO orbit parameters. In this work, the assumption that observations from LEOs are more or less accurate than those from ground stations was not investigated and could be subject to further research. The LSQA may partially degrade the LEO orbit, as long as it improves the overall system in terms of observation residuals. Consequently, it is plausible that many of the estimated parameters are improved through the integration of LEO observations, while the LEO orbit deteriorates. The cause for the deteriorated LEO orbit solutions is the choice of the observation sampling of 300 sec, whereby a higher sampling can potentially improve the LEO orbit precision.

Integrating data from multiple GNSS constellations, such as GPS and Galileo, improves the global network determination. Integrating Sentinel-6A GNSS observations improves the observability of Earth's center-of-mass coordinates compared to using only GPS or GPS+Galileo, with the GPS+Galileo solution outperforming the GPS-only solution. Sentinel-6A's unique orbit characteristics contribute to improved global coverage and more favorable observation geometry. Multi-GNSS computation increases the observability of ERPs, whereas the integration of LEO observations has a smaller impact.

Phase RMS values of LEO-only POD procedures indicate that the data quality and orbit parametrization for Spire satellites is worse than for scientific LEOs. The inclusion of GPS observations from scientific LEOs influences the Earth's center-of-mass coordinates more than those from Spire. The quality of derived orbit solutions for Spire satellites is worse than for scientific LEOs. The methods used for data processing in terms of observation sampling and orbit parametrization may need to be tailored to each satellite. Overall, the observed differences in the quality of the results from the integrated processing with Spire and scientific LEOs may be attributed to variations in data quality and satellite characteristics.

The integration of LEO-GPS observations stabilizes the Earth's center-of-mass estimation by reducing its variations in a long-term analysis. The influence on periodicities and their amplitudes is found to be complex and demands further investigation. The resulting ERPs from a LEO-integrated solution for a long-term analysis show a systematic difference to GPS-only and C04 reference results.

7.1 Conclusion and outlook

The experiments carried out in the frame of this work answer the key question:

How does the integration of GNSS data from satellite-based receivers contribute to the computation of a global network solution be it in terms of the determination of LEO and GNSS satellite trajectories, and particularly, the determination of geodetic parameters, like the Earth's center-of-mass coordinates and Earth rotation parameters?

in the following manner:

LEO-integrated global network determination has shown to be an effective tool for obtaining valuable geodetic information. By being closer to the Earth's surface, LEO satellites offer unique observational advantages and complement existing systems like GPS to study the planet Earth. The results showed the potential for further improving the quality of network solutions derived by including LEOs and more than one GNSS system.

Identifying challenges in data quality and processing of LEO satellites is crucial for addressing the limitations and improving the overall accuracy of the estimations. In light of the detailed experiments carried out for Jason-3, one drawback is that there is still room for improvement with regard to LEO POD precision. Acknowledging these challenges encourages further research and development efforts to enhance the reliability of the LEO POD. The importance of explicitly modeling non-gravitational forces and single-receiver ambiguity resolution for LEOs has been revealed by the square root of the cofactors of the determined geodetic parameters. Further research is needed to investigate how different orbit parametrizations for the LEOs affect the computation of global network solutions.

In this work, no experiments were conducted where LEOs were integrated into an operational processing, e.g., carried out by CODE. Even so, the results clearly indicate that integrating LEOs into processing potentially leads to further improvement. As the results show, a higher sampling than 300 sec is needed to ensure an accurate quality of the resulting LEO orbit solution, whereby a reduction in the number of estimated parameters may be needed. This could be achieved by e.g., modeling the GNSS satellite clocks instead of estimating them, as it may be possible for the high-quality clocks onboard the Galileo satellites (Maciuk et al., 2021).

Dedicated experiments are needed to determine the influence of different ground station selections on the global GNSS network determination, whereby machine learning may be useful in optimizing the configuration by taking into account factors such as station density, baseline lengths, and redundancies.

Using observations from LEOs to determine the Earth's center-of-mass coordinates is a significant benefit. A maximum time span of three years was examined in this work. To gain a deeper understanding of the impact of integrating LEOs into the processing, long-term experiments are necessary. Additionally, the results indicate that carrying out dedicated experiments based on a 7-day arc approach could further improve the estimation.

Since it has been found that for certain LEO missions, non-negligible PCO corrections are needed, a rigorous calibration of GNSS transmitter and LEO receiver antennas is necessary to further enhance global LEO-integrated network solutions. This is viewed as the most substantial limitation inherent in this work.

The investigations conducted within the scope of this work lay the foundation for a deeper understanding of the impacts of GNSS data from LEO on worldwide position determinations and geodetic parameter estimation. In conclusion of the present work, promising perspectives emerge for the advancement of global network determination.

A particular focus in the future could be on the potential role of the planned GENESIS mission (Delva et al., 2023) as a groundbreaking step for improving global network solutions. The GENESIS mission, scheduled for launch in 2027, aims to significantly enhance the accuracy and stability of the Terrestrial

Reference Frame. The GENESIS satellite will be placed in an orbit approximately 6000 km above Earth and equipped with precisely calibrated instruments for all four space geodetic techniques contributing to TRF realization: Global Navigation Satellite Systems, Satellite Laser Ranging, Very Long Baseline Interferometry, and Doppler Orbitography and Radiopositioning Integrated by Satellite.

The utilization of GNSS data by GENESIS poses a significant challenge due to the satellite's orbital height, resulting in larger nadir angles seen from the GNSS satellites as compared to ground receivers or those of the LEOs used in this work. Limited reliable information is currently available about the carrier phase patterns of GNSS transmitting antennas at very large nadir angles. A dual-receiver-antenna system will be carried onboard the satellite, composed of a zenith-looking and a nadir-looking antenna (Montenbruck et al., 2023).

Initial experiments are intended to assess the effects of integrating GENESIS observations into global GNSS network solutions. Real or simulated GNSS observations from terrestrial stations will be used, along with simulated GENESIS-GNSS observations. Through comprehensive analyses and investigations, insights will be gained into how the additional GNSS data can assist in achieving a more precise determination of geodetic parameters. In particular, it shall be demonstrated how GENESIS could act as a key player in significantly improving the accuracy and reliability of global network solutions.

Bibliography

K. Abich, A. Abramovici, B. Amparan, A. Baatzsch, B. B. Okihiro, D. C. Barr, M. P. Bize, C. Bogan, C. Braxmaier, M. J. Burke, et al. In-orbit performance of the GRACE follow-on laser ranging interferometer. *Physical Review Letters*, 123(3), 2019. 12, 41

Z. Altamimi, D. Angermann, D. Argus, G. Blewitt, C. Boucher, B. Chao, H. Drewes, R. Eanes, M. Feissel, R. Ferland, et al. The terrestrial reference frame and the dynamic Earth. *Eos, Transactions American Geophysical Union*, 82(25), 2001. 9

Z. Altamimi, X. Collilieux, and L. Métivier. ITRF2008: an improved solution of the international terrestrial reference frame. *Journal of Geodesy*, 85, 2011. 9, 28

Z. Altamimi, P. Rebischung, L. Métivier, and X. Collilieux. ITRF2014: A new release of the International Terrestrial Reference Frame modeling nonlinear station motions. *Journal of Geophysical Research: Solid Earth*, 121(8), 2016. 1, 2

M. J. Angling, O. Nogués-Correig, V. Nguyen, S. Vetra-Carvalho, F.-X. Bocquet, K. Nordstrom, S. E. Melville, G. Savastano, S. Mohanty, and D. Masters. Sensing the ionosphere with the Spire radio occultation constellation. *Journal of Space Weather and Space Climate*, 11, 2021. 13

D. Arnold, O. Montenbruck, S. Hackel, and K. Sośnica. Satellite laser ranging to low Earth orbiters: orbit and network validation. *Journal of Geodesy*, 93(11), 2019. 40, 41, 63

D. Arnold, A. Couhert, O. Montenbruck, C. S. Kobel, E. Saquet, H. Peter, F. Mercier, and A. Jäggi. Systematic errors in Satellite Laser Ranging validations of microwave-based low Earth orbit solutions. *Presented at COSPAR 44th Scientific Assembly, PSD.1-0017-22*, 2022. 55

D. Arnold, T. Grombein, L. Schreiter, V. Sterken, and A. Jäggi. Reprocessed precise science orbits and gravity field recovery for the entire GOCE mission. *Journal of Geodesy*, 97(7), 2023a. 31

D. Arnold, H. Peter, X. Mao, A. Miller, and A. Jäggi. Precise orbit determination of Spire nano satellites. *Advances in Space Research*, 72(11), 2023b. 102, 104, 107

J. Aschbacher and M. P. Milagro-Pérez. The European Earth monitoring (GMES) programme: Status and perspectives. *Remote Sensing of Environment*, 120, 2012. 10

A. Auriol and C. Tourain. DORIS system: the new age. *Advances in Space Research*, 46(12), 2010. 10

W. Bertiger, S. D. Desai, A. Dorsey, B. J. Haines, N. Harvey, D. Kuang, A. Sibthorpe, and J. P. Weiss. Sub-centimeter precision orbit determination with GPS for ocean altimetry. *Marine Geodesy*, 33(S1), 2010. 53

G. Beutler. *Methods of Celestial Mechanics*. Springer, 2005. ISBN 3-540-40749-9, 3-540-40750-2. 5, 30, 31

G. Beutler, E. Brockmann, W. Gurtner, U. Hugentobler, L. Mervart, M. Rothacher, and A. Verdun. Extended orbit modeling techniques at the CODE processing center of the international GPS service for geodynamics (IGS): theory and initial results. *Manuscripta geodaetica*, 19(6), 1994. 15

G. Beutler, A. Jäggi, L. Mervart, and U. Meyer. The celestial mechanics approach: theoretical foundations. *Journal of Geodesy*, 84, 2010. 31

C. Bizouard and D. Gambis. The combined solution C04 for Earth orientation parameters consistent with international terrestrial reference frame 2005. In *Geodetic Reference Frames: IAG Symposium Munich, Germany, 9-14 October 2006*. Springer, 2009. 85

C. Bizouard, S. Lambert, C. Gattano, O. Becker, and J.-Y. Richard. The IERS EOP 14C04 solution for Earth orientation parameters consistent with ITRF 2014. *Journal of Geodesy*, 93(5), 2019. 83

G. Blewitt. Basics of the GPS technique: observation equations. *Geodetic applications of GPS*, 1, 1997. 6

G. Blewitt. Self-consistency in reference frames, geocenter definition, and surface loading of the solid Earth. *Journal of Geophysical Research: Solid Earth*, 108(B2), 2003. 9

G. Blewitt, Z. Altamimi, J. Davis, R. Gross, C.-Y. Kuo, F. G. Lemoine, A. W. Moore, R. E. Neilan, H.-P. Plag, M. Rothacher, et al. Geodetic observations and global reference frame contributions to understanding sea-level rise and variability. *Understanding sea-level rise and variability*, 2010. 2

E. Brockmann. Combination of solutions for geodetic and geodynamic applications of the Global Positioning System (GPS). *Geodätische-Geophysikalische Arbeiten Schweiz*, 55, 1997. 24, 108

S. Bruinsma. The DTM-2013 thermosphere model. *J. Space Weather Space Clim*, 2015. 68

A. Buis. Milankovitch (orbital) cycles and their role in earth's climate. *NASA Climate*, 27, 2020. 8

H. Capdeville, J.-M. Lemoine, A. Mezerette, and G. Moreaux. DORIS results on Precise Orbit Determination and on geocenter and scale solutions from CNES/CLS IDS Analysis Center contribution to the ITRF2020. In *EGU General Assembly Conference Abstracts*. EGU21–5384, 2021. 109

J. Cappaert. The Spire Small Satellite Network. In *Handbook of Small Satellites: Technology, Design, Manufacture, Applications, Economics and Regulation*. Springer, 2020. 13

E. Cardellach, P. Elósegui, and J. Davis. Global distortion of GPS networks associated with satellite antenna model errors. *Journal of Geophysical Research: Solid Earth*, 112(B7), 2007. 37

L. Cerri, J. Berthias, W. Bertiger, B. Haines, F. Lemoine, F. Mercier, J. Ries, P. Willis, N. Zelensky, and M. Ziebart. Precision orbit determination standards for the Jason series of altimeter missions. *Marine Geodesy*, 33(S1), 2010. 33, 47, 58

L. Cerri, A. Couhert, and P. Ferrage. DORIS satellites models implemented in POE processing, 2018. URL `https://ids-doris.org/documents/BC/satellites/DORISSatelliteModels.pdf`. 49

M. Cheng, J. Ries, and B. Tapley. Geocenter variations from analysis of SLR data. In *Reference frames for applications in geosciences*. Springer, 2013. 9

L. Combrinck. Satellite laser ranging. *Sciences of Geodesy-I: Advances and Future Directions*, 2010. 40

A. Conrad, S. Desai, B. Haines, and P. Axelrad. Extending the GPS IIIA antenna calibration for precise orbit determination of low Earth orbit satellites. *Journal of Geodesy*, 97(4), 2023. 37

E. Cordelli, T. Schildknecht, and A. Vananti. *Improvement of Space Debris Orbits*. PhD thesis, Philosophisch-naturwissenschaftliche Fakultät der Universität Bern, 2017. 23

V. Couderc. Jason-3 characteristics for POD processing. Technical report, CNES, 2015. 47, 49

R. Cullen and R. Francis. The ocean surface topography Jason-CS/Sentinel-6 mission. In *AGU fall meeting abstracts*, volume 2014, 2014. 11

R. Dach and P. Walser. Bernese GNSS Software Version 5.2. *Citeseer*, 2015. i, 8, 21, 23, 30, 31, 44

R. Dach, E. Brockmann, S. Schaer, G. Beutler, M. Meindl, L. Prange, H. Bock, A. Jäggi, and L. Ostini. GNSS processing at CODE: status report. *Journal of Geodesy*, 83, 2009. 6

R. Dach, J. Böhm, S. Lutz, P. Steigenberger, and G. Beutler. Evaluation of the impact of atmospheric pressure loading modeling on GNSS data analysis. *Journal of Geodesy*, 85, 2011. 86

R. Dach, S. Schaer, D. Arnold, E. Orliac, L. Prange, A. Susnik, A. Villiger, and A. Jäggi. CODE final product series for the IGS. *Astronomical Institute, University of Bern*, 2016. 97

R. Dach, I. Selmke, A. Villiger, D. Arnold, L. Prange, S. Schaer, D. Sidorov, P. Stebler, A. Jäggi, and U. Hugentobler. Review of recent GNSS modelling improvements based on CODEs Repro3 contribution. *Advances in Space Research*, 68(3), 2021. 44

R. Dach, S. Schaer, and D. e. a. Arnold. CODE final product series for the IGS. *Astronomical Institute, University of Bern*, 2023. 44, 90

W. Dahmen and A. Reusken. *Nichtlineare Ausgleichsrechnung*, chapter 6, pages 307–329. Springer, 2008. 20

J. J. Degnan. Millimeter accuracy satellite laser ranging: a review. *Contributions of Space Geodesy to Geodynamics: Technology*, 25, 1993. 40

P. Delva, Z. Altamimi, A. Blazquez, M. Blossfeld, J. Böhm, P. Bonnefond, J.-P. Boy, S. Bruinsma, G. Bury, M. Chatzinikos, A. Couhert, C. Courde, R. Dach, V. Dehant, S. Dell'Agnello, G. Elgered, W. Enderle, P. Exertier, S. Glaser, R. Haas, W. Huang, U. Hugentobler, A. Jäggi, O. Karatekin, F. Lemoine, C. Le Poncin-Lafitte, S. Lunz, B. Männel, F. Mercier, L. Métivier, B. Meyssignac, J. Müller, A. Nothnagel, F. Perosanz, R. Rietbroek, M. Rothacher, H. Schuh, H. Sert, K. Sośnica, P. Testani, J. Ventura-Traveset, G. Wautelet, and R. Zajdel. GENESIS: co-location of geodetic techniques in space. *Earth, Planets and Space*, 75(1), 2023. 116

S. Desai, A. Conrad, and B. Haines. GPS-based Precise Orbit Determination of the Sentinel-6 MF and Jason-3 Missions. *Presented at OSTST meeting*, 2022. 114

C. J. Donlon, R. Cullen, L. Giulicchi, P. Vuilleumier, C. R. Francis, M. Kuschnerus, W. Simpson, A. Bouridah, M. Caleno, R. Bertoni, et al. The Copernicus Sentinel-6 mission: Enhanced continuity of satellite sea level measurements from space. *Remote Sensing of Environment*, 258, 2021. 10, 11

E. Doornbos. *Thermospheric density and wind determination from satellite dynamics*. Springer, 2012. 34

D. P. Drob, J. T. Emmert, J. W. Meriwether, J. J. Makela, E. Doornbos, M. Conde, G. Hernandez, J. Noto, K. A. Zawdie, S. E. McDonald, et al. An update to the Horizontal Wind Model (HWM): The quiet time thermosphere. *Earth and Space Science*, 2(7), 2015. 35

J. Dumont, V. Rosmorduc, L. Carrere, E. Picot, N.and Bronner, A. Couhert, A.and Guillot, S. Desai, and J. e. a. Bonekamp, H.and Figa. Jason-3 Products Handbook, 2015. URL `https://www.ospo.noaa.gov/Products/documents/hdbk_j3.pdf`. 11

ESA. *Sentinel-2 User Handbook*. ESA, Sept. 2013. Available at `https://sentinel.esa.int`. 10

ESA. *Sentinel-3 User Handbook*. ESA, Jan. 2017. Available at `https://sentinel.esa.int`. 10

R. Ferland and M. Piraszewski. The IGS-combined station coordinates, earth rotation parameters and apparent geocenter. *Journal of Geodesy*, 83, 2009. 86

J. Fernandez and P. Femenias. Sentinels POD service operations. In *SpaceOps 2014 Conference*, 2014. 92

J. Fernández, H. Peter, E. J. Calero, J. Berzosa, L. J. Gallardo, and P. Féménias. Sentinel-3a: Validation of orbit products at the Copernicus POD service. In *Fiducial Reference Measurements for Altimetry: Proceedings of the International Review Workshop on Satellite Altimetry Cal/Val Activities and Applications*. Springer, 2020. 5

M. Fernández. Sentinel-3A properties for GPS POD. Technical report, GMV-GMESPOD-TN-0027, 11 2019. Technical Report. 33

M. Fernández, H. Peter, D. Arnold, B. Duan, W. Simons, M. Wermuth, S. Hackel, J. Fernández, A. Jäggi, U. Hugentobler, et al. Copernicus Sentinel–1 POD reprocessing campaign. *Advances in Space Research*, 70(2), 2022. 31

J. Fernández-Sánchez, D. Escobar, F. Ayuga, and P. Féménias. Copernicus POD Service Operational Experience. In *14th International Conference on Space Operations*, 2016. 10

C. Flohrer. Mutual validation of satellite-geodetic techniques and its impact on GNSS orbit modeling. *Schweizerische Geodätische Kommission/Swiss Geodetic Commission*, 2008. vii, 40

J. Flury, R. Rummel, C. Reigber, M. Rothacher, G. Boedecker, and U. Schreiber. *Observation of the earth system from space*. Springer, 2006. 1

W. M. Folkner, J. G. Williams, and D. H. Boggs. The planetary and lunar ephemeris DE 421. *IPN progress report*, 42(178), 2009. 44

E. Friis-Christensen, H. Lühr, D. Knudsen, and R. Haagmans. Swarm–an Earth observation mission investigating geospace. *Advances in Space Research*, 41(1), 2008. 12, 13

C. F. Gauss. *Theoria motus corporum coelestium in sectionibus conicis solem ambientium auctore Carolo Friderico Gauss*. sumtibus Frid. Perthes et IH Besser, 1809. 19

L. Geisser. *Generation and Analysis of Satellite Laser Ranging Normal Points for Geodetic Parameter Estimation*. PhD thesis, Philosophisch-naturwissenschaftliche Fakultät der Universität Bern, 2023. 85, 99, 102, 108

V. Girardin. Impact of non-gravitational forces on GPS-based precise orbit determination of low Earth orbiters. *Delft University of Technology*, 2016. 33, 35

GMV. SLR Yearly Report, 2018. URL `https://sentinel.esa.int/web/sentinel/missions/sentinel-3/ground-segment/pod/documentation`. 56

GSA. Galileo IOV and FOC satellite metadata, 2019. URL `https://www.gsc-europa.eu/support-to-developers/galileo-iov-satellitemetadata`. 37

W. Gurtner and L. Estey. RINEX: The receiver independent exchange format version. *Astronomical Institute, University of Berne*, 2006. 9

W. Gurtner and G. Mader. Receiver independent exchange format version 2. CSTG GPS bulletin 3 (3), 1990. 9

R. Haagmans, E. Friis-Christensen, H. Lühr, and G. Hulot. Swarm-the earth's magnetic field and environment explorers. In *AGU Fall Meeting Abstracts*, volume 2004, 2004. 13

S. F. G. Hackel. *Refinement of reduced-dynamic orbit determination for low Earth satellites*. PhD thesis, Technische Universität München, 2019. 13, 34

B. Haines, Y. Bar-Sever, W. Bertiger, S. Byun, S. Desai, and G. Hajj. GPS antenna phase center variations: New perspectives from the GRACE Mission. In *Dynamic Planet*, 2005. 37

B. J. Haines, Y. E. Bar-Sever, W. I. Bertiger, S. D. Desai, N. Harvey, A. E. Sibois, and J. P. Weiss. Realizing a terrestrial reference frame using the Global Positioning System. *Journal of Geophysical Research: Solid Earth*, 120(8), 2015. 7, 16, 37, 81, 95

Y. Hatanaka. A compression format and tools for GNSS observation data, 2008. URL `https://www.gsi.go.jp/common/000045517.pdf`. 9

S. Hilla. The Extended Standard Product 3 Orbit Format (SP3-c), 2010. URL `https://www.epncb.oma.be/ftp/data/format/sp3c.txt`. 9

B. Hofmann-Wellenhof, H. Lichtenegger, and J. Collins. *Global positioning system: theory and practice*. Springer Science & Business Media, 2012. 5

W. Huang. *Enhancing GNSS by integrating low Earth orbiters*. PhD thesis, Technische Universitaet Berlin (Germany), 2022. 6, 18, 79, 94, 95

W. Huang, B. Männel, P. Sakic, M. Ge, and H. Schuh. Integrated processing of ground-and space-based GPS observations: improving GPS satellite orbits observed with sparse ground networks. *Journal of Geodesy*, 94, 2020. 6, 42, 75, 81, 85, 90, 91

U. Hugentobler and G. Beutler. Precise orbit determination and Gravity field modelling: Strategies for Precise Orbit Determination of Low Earth Orbiters Using the GPS. *Space science reviews*, 108(1-2), 2003. 2, 82, 90

U. Hugentobler, A. Jäggi, S. Schaer, and G. Beutler. Combined processing of GPS data from ground station and LEO receivers in a global solution. In *A Window on the Future of Geodesy: Proceedings of the International Association of Geodesy IAG General Assembly Sapporo, Japan June 30–July 11, 2003*. Springer, 2005. 15, 16, 86, 92, 93

C. Hwang, T.-P. Tseng, T. Lin, D. Švehla, and B. Schreiner. Precise orbit determination for the FORMOSAT-3/COSMIC satellite mission using GPS. *Journal of Geodesy*, 83, 2009. 38

A. Jäggi. *Pseudo-stochastic orbit modelling of low Earth satellites using the global positioning system*, volume 73. Schweizerische Geodätische Kommission/Swiss Geodetic Commission, 2007. 9, 30, 44, 45

A. Jäggi and D. Arnold. Precise Orbit Determination. In *Global gravity field modeling from satellite-to-satellite tracking data*. Springer, 2017. 26, 28

A. Jäggi, H. Bock, R. Pail, and H. Goiginger. Highly-reduced dynamic orbits and their use for global gravity field recovery: a simulation study for GOCE. *Studia Geophysica et Geodaetica*, 52, 2008. 31

A. Jäggi, R. Dach, O. Montenbruck, U. Hugentobler, H. Bock, and G. Beutler. Phase center modeling for LEO GPS receiver antennas and its impact on precise orbit determination. *Journal of Geodesy*, 83, 2009. 35, 36, 60

G. Johnston, A. Riddell, and G. Hausler. The international GNSS service. *Springer handbook of global navigation satellite systems*, 2017. 6

A. Johnstone. CubeSat design specification (1U-12U) rev 14 CP-CDS-R14. *The CubeSat Program, Cal Poly SLO*, 2020. 13

G. S. Kelly. *Polar geomagnetism*. The University of Liverpool (United Kingdom), 2013. 13

C. Kobel, D. Arnold, and A. Jäggi. Combination of precise orbit solutions for Sentinel-3A using Variance Component Estimation. *Advances in Geosciences*, 50, 2019. 39

C. Kobel, D. Arnold, and A. Jäggi. Impact of different attitude modes on Jason-3 precise orbit determination and antenna phase center modeling. *Presented at EGU General Assembly Conferenc, EGU21–4831*, 2021. 12, 35, 49, 62

C. Kobel, D. Arnold, and A. Jäggi. Analysis of attitude dependent deficiencies in precise orbit solutions of Jason-3. *Presented at OSTST meeting*, 2022a. 12, 48, 63

C. Kobel, D. Arnold, and A. Jäggi. Estimation of phase center offset corrections for Sentinel satellites. *Presented at EGU General Assembly Conference, EGU22–7136*, 2022b. 35, 73

C. Kobel, D. Arnold, M. S. Kalarus, A. Villiger, and A. Jäggi. Including of Sentinel-6A multi-GNSS observations into global GNSS solutions. *Presented at COSPAR 44th Scientific Assembly, PSD.1-TW-285*, 2022c. 6

C. Kobel, D. Arnold, M. S. Kalarus, A. Villiger, and A. Jäggi. Impact of incorporating SPIRE CubeSat GPS observations in a global GPS network solution. *Presented at EGU General Assembly Conference, EGU23–12153*, 2023a. 13, 101

C. Kobel, M. S. Kalarus, D. Arnold, and A. Jäggi. Impact of incorporating Spire CubeSat GPS observations in a global GPS network solution. *Advances in Space Research, Manuscript submitted*, 2023b. 2

K. Koch. *Parameterschätzung und Hypothesentests in linearen Modellen*. Dümmler typoscripts Geodäsie / Vermessungswesen. Dümmler, 1980. 19

K.-R. Koch. *Parameter estimation and hypothesis testing in linear models*. Springer Science & Business Media, 1999. 21

R. P. Kornfeld, B. W. Arnold, M. A. Gross, N. T. Dahya, W. M. Klipstein, P. F. Gath, and S. Bettadpur. GRACE-FO: the gravity recovery and climate experiment follow-on mission. *Journal of Spacecraft and Rockets*, 56(3), 2019. 12

D. Kuang, Y. Bar-Sever, and B. Haines. Analysis of orbital configurations for geocenter determination with GPS and low-Earth orbiters. *Journal of Geodesy*, 89, 2015. 16, 17, 81

J. B. Kuipers. *Quaternions and rotation sequences: a primer with applications to orbits, aerospace, and virtual reality*. Princeton university press, 1999. 38

A. Kvas, J. M. Brockmann, S. Krauss, T. Schubert, T. Gruber, U. Meyer, T. Mayer-Gürr, W.-D. Schuh, A. Jäggi, and R. Pail. GOCO06s–a satellite-only global gravity field model. *Earth System Science Data*, 13(1), 2021. 44

K. Lambeck and A. Cazenave. Long term variations in the length of day and climatic change. *Geophysical Journal International*, 46(3), 1976. 8

F. W. Landerer, F. M. Flechtner, H. Save, F. H. Webb, T. Bandikova, W. I. Bertiger, S. V. Bettadpur, S. H. Byun, C. Dahle, H. Dobslaw, et al. Extending the global mass change data record: GRACE Follow-On instrument and science data performance. *Geophysical Research Letters*, 47(12), 2020. 12

M. Lasser, U. Meyer, D. Arnold, and A. Jäggi. Stochastic noise modelling of kinematic orbit positions in the Celestial Mechanics Approach. *Advances in Geosciences*, 50, 2020. 31, 93

D. Laurichesse, F. Mercier, J.-P. Berthias, P. Broca, and L. Cerri. Integer ambiguity resolution on undifferenced GPS phase measurements and its application to PPP and satellite precise orbit determination. *Navigation*, 56(2), 2009. 53

D. A. Lavallée, T. Van Dam, G. Blewitt, and P. J. Clarke. Geocenter motions from GPS: A unified observation model. *Journal of Geophysical Research: Solid Earth*, 111(B5), 2006. 9

F. Lemoine, H. Capdeville, P. Stepanek, N. Zelensky, and D. Pavlis. Mitigation of Non-conservative Force Model Error. *IDS Analysis Working Group Meeting*, 2019. 64

M. J. Lighthill. *An introduction to Fourier analysis and generalised functions*. Cambridge University Press, 1958. 41

M. Liu, Y. Yuan, J. Ou, and Y. Chai. Research on attitude models and antenna phase center correction for Jason-3 satellite orbit determination. *Sensors*, 19(10), 2019. 11

C. Lück. *Large-scale mass redistribution in the Earth system from synergistic use of Swarm data*. PhD thesis, Universitäts-und Landesbibliothek Bonn, 2022. 78

S. Lutz, M. Meindl, P. Steigenberger, G. Beutler, K. Sośnica, S. Schaer, R. Dach, D. Arnold, D. Thaller, and A. Jäggi. Impact of the arc length on GNSS analysis results. *Journal of Geodesy*, 90, 2016a. 40, 91, 107

S. Lutz, M. Meindl, P. Steigenberger, G. Beutler, K. Sośnica, S. Schaer, R. Dach, D. Arnold, D. Thaller, and A. Jäggi. Erratum to: Impact of the arc length on GNSS analysis results. *Journal of Geodesy*, 90, 2016b. 88

K. Maciuk, J. Kudrys, B. Skorupa, and Z. Malkin. Testing the product quality of Galileo and GPS on-board oscillators. *Measurement*, 167, 2021. 116

F. Maiwald, S. T. Brown, T. Koch, L. Milligan, P. Kangaslahti, E. Schlecht, A. Skalare, M. Bloom, V. Torossian, J. Kanis, et al. Completion of the AMR-C instrument for Sentinel-6. *IEEE Journal of Selected Topics in Applied Earth Observations and Remote Sensing*, 13, 2020. 11

Z. Malkin. On comparison of the Earth orientation parameters obtained from different VLBI networks and observing programs. *Journal of Geodesy*, 83, 2009. 8

B. Männel and M. Rothacher. Geocenter variations derived from a combined processing of LEO-and ground-based GPS observations. *Journal of Geodesy*, 91, 2017. 6, 17, 81, 108, 109, 110

X. Mao, D. Arnold, V. Girardin, A. Villiger, and A. Jäggi. Dynamic GPS-based LEO orbit determination with 1 cm precision using the Bernese GNSS Software. *Advances in Space Research*, 67(2), 2021. 31, 33, 34, 35, 79

M. Meindl, G. Beutler, D. Thaller, R. Dach, and A. Jäggi. Geocenter coordinates estimated from GNSS data as viewed by perturbation theory. *Advances in Space Research*, 51(7), 2013. 9, 99

W. G. Melbourne. The case for ranging in GPS-based geodetic systems. In *Proceedings of the first international symposium on precise positioning with the Global Positioning System*. US Department of Commerce Rockville, Maryland, 1985. 27

U. Meyer, Y. Jean, A. Kvas, C. Dahle, J.-M. Lemoine, and A. Jäggi. Combination of GRACE monthly gravity fields on the normal equation level. *Journal of Geodesy*, 93, 2019. 31

O. Montenbruck and E. Gill. *Satellite Orbits: Models, Methods, and Applications*. Physics and Astronomy online library. Springer, 2000. 34

O. Montenbruck, M. Garcia-Fernandez, Y. Yoon, S. Schön, and A. Jäggi. Antenna phase center calibration for precise positioning of LEO satellites. *GPS solutions*, 13, 2009. 35

O. Montenbruck, S. Hackel, and A. Jäggi. Precise orbit determination of the Sentinel-3A altimetry satellite using ambiguity-fixed GPS carrier phase observations. *Journal of Geodesy*, 92(7), 2018a. 10, 28, 31, 34, 51, 55, 67, 68, 95

O. Montenbruck, S. Hackel, J. van den IJssel, and D. Arnold. Reduced dynamic and kinematic precise orbit determination for the Swarm mission from 4 years of GPS tracking. *GPS Solutions*, 22(3), 2018b. 33

O. Montenbruck, S. Hackel, M. Wermuth, and F. Zangerl. Sentinel-6A precise orbit determination using a combined GPS/Galileo receiver. *Journal of Geodesy*, 95(9), 2021. 11, 67, 72

O. Montenbruck, M. Wermuth, and S. Hackel. Cross-calibration of the TRIG and PODRIX GNSS receivers onboard Sentinel-6A, 2022. 114

O. Montenbruck, P. Steigenberger, S. Thoelert, D. Arnold, and G. Bury. GNSS visibility and performance implications for the GENESIS mission. *Journal of Geodesy*, 97(10), 2023. 117

Y. J. Morton, F. van Diggelen, J. J. Spilker Jr, B. W. Parkinson, S. Lo, and G. Gao. *Position, navigation, and timing technologies in the 21st century: Integrated satellite navigation, sensor systems, and civil applications, volume 1*. John Wiley & Sons, 2021. 1, 35

J. Moyard, A. Couhert, F. Mercier, S. Houry, H. Ait Lakbir, and C. Masson. CNES POE-F precise orbit performances for the current altimeter missions. *Presented at OSTST*, 2019. 55, 65

A. Noureldin, T. B. Karamat, and J. Georgy. *Fundamentals of inertial navigation, satellite-based positioning and their integration*. Springer Science & Business Media, 2012. 5

M. R. Pearlman, J. J. Degnan, and J. M. Bosworth. The international laser ranging service. *Advances in Space Research*, 30(2), 2002. 41

H. Peter, D. Arnold, A. Jäggi, and J. van den IJssel. Investigation on systematic offsets between different Swarm orbit solutions. *Presented at ESA Living Planet Symposium, EART-133*, 2016. 79

H. Peter, A. Jäggi, J. Fernández, D. Escobar, F. Ayuga, D. Arnold, M. Wermuth, S. Hackel, M. Otten, W. Simons, et al. Sentinel-1A–First precise orbit determination results. *Advances in Space Research*, 60 (5), 2017. 35, 62

H. Peter, J. Fernández, and P. Féménias. Copernicus Sentinel-1 satellites: sensitivity of antenna offset estimation to orbit and observation modelling. *Advances in Geosciences*, 50, 2020. 67, 68, 69, 70

H. Peter, U. Meyer, M. Lasser, and A. Jäggi. COST-G gravity field models for precise orbit determination of Low Earth Orbiting Satellites. *Advances in Space Research*, 69(12), 2022. 40

G. Petit, B. Luzum, et al. IERS conventions. *IERS Technical Note*, 36(1), 2010. 28, 44

C. Pock. Low Earth Orbit Determination for GNSS Radio Occultation with Aspects of Uncertainty Estimation. *Wegener Center Verlag*, 2015. 114

P. Rebischung and R. Schmid. IGS14/igs14. atx: a new framework for the IGS products. *Presented at AGU fall meeting*, 2016. 44, 105

P. Rebischung, R. Schmid, and T. Herring. Upcoming switch to IGS14/igs14.atx. IGSMAIL-7399, 2016. URL `https://lists.igs.org/pipermail/igsmail/2016/001233.html`. 37

B. W. Remondi. *Using the Global Positioning System (GPS) phase observable for relative geodesy: Modeling, processing, and results (Satellite, Timing)*. The University of Texas at Austin, 1984. 5

H. J. Rim, B. E. Schutz, P. Abusali, and B. D. Tapley. Effect of GPS orbit accuracy on GPS-determined Topex/Poseidon orbit. In *Proceedings of Ion GPS*, volume 8. Institute of Navigation, 1995. 2

R. Rummel, H. Drewes, W. Bosch, and H. Hornik. Towards an integrated global geodetic observing system (IGGOS). In *IAG Section II Symposium Munich, October 5-9, 1998. IAG Symposia 120, Springer, Berlin*, 2000. 1

N. Saeed, A. Elzanaty, H. Almorad, H. Dahrouj, T. Al-Naffouri, and M.-S. Alouini. CubeSat Communications: Recent Advances and Future Challenges. *IEEE Communications Surveys Tutorials*, 2020. vii, 6

R. Savcenko and W. Bosch. EOT11a-empirical ocean tide model from multi-mission satellite altimetry. *DGFI Report No. 89*, 2012. 44

S. Scaramuzza, R. Dach, G. Beutler, D. Arnold, A. Sušnik, and A. Jäggi. Dependency of geodynamic parameters on the GNSS constellation. *Journal of Geodesy*, 92, 2018. 85

S. Schaer, A. Villiger, D. Arnold, R. Dach, L. Prange, and A. Jäggi. The CODE ambiguity-fixed clock and phase bias analysis products: generation, properties, and performance. *Journal of Geodesy*, 95, 2021. 28

R. Scharroo, H. Bonekamp, C. Ponsard, F. Parisot, A. von Engeln, M. Tahtadjiev, K. de Vriendt, and F. Montagner. Jason continuity of services: continuing the Jason altimeter data records as Copernicus Sentinel-6. *Ocean Science*, 12(2), 2016. 11

R. Schmid and M. Rothacher. Estimation of elevation-dependent satellite antenna phase center variations of GPS satellites. *Journal of Geodesy*, 77, 2003. 37

R. Schmid, M. Rothacher, D. Thaller, and P. Steigenberger. Absolute phase center corrections of satellite and receiver antennas: Impact on global GPS solutions and estimation of azimuthal phase center variations of the satellite antenna. *GPS solutions*, 9, 2005. 37

R. Schmid, R. Dach, X. Collilieux, A. Jäggi, M. Schmitz, and F. Dilssner. Absolute IGS antenna phase center model igs08. atx: status and potential improvements. *Journal of Geodesy*, 90, 2016. 37

I. Selmke, R. Dach, D. Arnold, L. Prange, S. Schaer, D. Sidorov, P. Stebler, A. Villiger, A. Jäggi, and U. Hugentobler. CODE repro3 product series for the IGS. *Astronomical Institute, University of Bern*, 2020. 6, 42, 44, 97

Y. Shen, J. Guo, C. Zhao, X. Yu, and J. Li. Earth rotation parameter and variation during 2005–2010 solved with LAGEOS SLR data. *Geodesy and Geodynamics*, 6(1), 2015. 110

K. J. Sośnica. *Determination of Precise Satellite Orbits and Geodetic Parameters using Satellite Laser Ranging*, volume 93. Schweizerische Geodätische Kommission/Swiss Geodetic Commission, 2015. 6

K. J. Sośnica, A. Jäggi, D. Thaller, R. Dach, G. Beutler, and C. Baumann. SLR-derived terrestrial reference frame using the observations to LAGEOS-1/2, Starlette, Stella, and AJISAI. In *18th International Workshop on Laser Ranging*, 2013. 99

J. Spits. Total Electron Content reconstruction using triple frequency GNSS signals. *ULiège-Université de Liège*, 2012. 6

G. Strang and K. Borre. *Linear algebra, geodesy, and GPS*. Siam, 1997. 5

D. Strugarek, K. Sośnica, D. Arnold, A. Jäggi, R. Zajdel, G. Bury, and M. Drożdżewski. Determination of global geodetic parameters using satellite laser ranging measurements to sentinel-3 satellites. *Remote sensing*, 11(19), 2019. 109

M. Tamazin. *High Resolution Signal Processing Techniques for Enhancing GPS Receiver Performance*. PhD thesis, Queen's University Kingston, Ontario, Canada, 03 2015. vii, 5

P. J. Teunissen and O. Montenbruck. *Springer handbook of global navigation satellite systems*, volume 10. Springer, 2017. 1, 5

D. Thaller. *Inter-technique combination based on homogeneous normal equation systems including station coordinates, Earth orientation and troposphere parameters*. PhD thesis, Technische Universität München, 2008. 22

Torge, Wolfgang. *Geodäsie*. Walter de Gruyter, 2002. 1

Y. Viertel, P. Freeborn, M. Poetsch, and A. Zorina. Individual Adapter Solutions for Multi-Spacecraft Launches on Rockot. *Presented at 28th Annual AIAA/USU Conference on Small Satellites*, 2014. 12

A. Villiger, S. Schaer, R. Dach, L. Prange, A. Sušnik, and A. Jäggi. Determination of GNSS pseudo-absolute code biases and their long-term combination. *Journal of Geodesy*, 93, 2019. 28

A. Villiger, R. Dach, S. Schaer, L. Prange, F. Zimmermann, H. Kuhlmann, G. Wübbena, M. Schmitz, G. Beutler, and A. Jäggi. GNSS scale determination using calibrated receiver and Galileo satellite antenna patterns. *Journal of Geodesy*, 94, 2020. 38

P. Visser and J. Van den IJssel. GPS-based precise orbit determination of the very low Earth-orbiting gravity mission GOCE. *Journal of Geodesy*, 74, 2000. 91

J. Wang. *Integrated processing of GNSS and VLBI on the observation level*. Technische Universitaet Berlin (Germany), 2021. 9

E. W. Weisstein. Taylor series. *https://mathworld. wolfram. com/*, 2004. 20

H. Y. Wen, G. Kruizinga, M. Paik, F. Landerer, W. Bertiger, C. Sakumura, T. Bandikova, and C. McCullough. *Gravity Recovery and Climate Experiment Follow-On (GRACE-FO) Level-1 Data Product User Handbook*. Technical Report JPL D-56935 (URS270772), NASA Jet Propulsion Laboratory/California Institute of Technology, Pasadena, CA, USA, 2019. 12

B. A. Wielicki, B. R. Barkstrom, E. F. Harrison, R. B. Lee III, G. L. Smith, and J. E. Cooper. Clouds and the Earth's Radiant Energy System (CERES): An earth observing system experiment. *Bulletin of the American Meteorological Society*, 77(5), 1996. 33, 34

G. Wubbena. Software developments for geodetic positioning with GPS using TI 4100 code and carrier measurements. In *Proceedings 1st international symposium on precise positioning with the global positioning system*. US Department of Commerce, 1985. 27

G. Wubbena, M. Schmitz, G. Mader, and F. Czopek. GPS Block II/IIA satellite antenna testing using the automated absolute field calibration with robot. In *Proceedings of the 20th International Technical Meeting of the Satellite Division of The Institute of Navigation (ION GNSS 2007)*, 2007. 37

Y. Xia, X. Liu, J. Guo, Z. Yang, L. Qi, B. Ji, and X. Chang. On GPS data quality of GRACE-FO and GRACE satellites: Effects of phase center variation and satellite attitude on precise orbit determination. *Acta geodaetica et geophysica*, 56, 2021. 38

G. Xu and Y. Xu. Applications of GPS theory and algorithms. In *GPS: Theory, Algorithms and Applications*. Springer, 2016. 5, 6

J. Yang, J. Zhang, and C. Wang. Sentinel-3A SRAL global statistical assessment and cross-calibration with Jason-3. *Remote Sensing*, 11(13), 2019. 10

L. Young. JPL GNSS receivers, past, present, and future. *Pasadena, CA: Jet Propulsion Laboratory, National Aeronautics and Space*, 2017. 11

T. P. Yunck. Orbit determination. *Progress in Astronautics and Aeronautics*, 164, 1996. 1

R. Zajdel, K. Sośnica, G. Bury, R. Dach, and L. Prange. System-specific systematic errors in earth rotation parameters derived from GPS, GLONASS, and Galileo. *GPS Solutions*, 24(3), 2020. 111

S. Zhu, F.-H. Massmann, Y. Yu, and C. Reigber. Satellite antenna phase center offsets and scale errors in GPS solutions. *Journal of Geodesy*, 76, 2003. 37

J. Zumberge, F. Webb, U. Lindqwister, D. J. Lichten, R. Ibanez-Meier, M. Herin, A. Freedman, and G. Blewitt. Geodetic and Atmospheric Measurements GPS Data Analysis for Earth Orientation at the Jet Propulsion Laboratory. *IERS Technical Note*, 16, 1994. 8

Declaration

I declare herewith that this thesis is my own work and that I have not used any sources other than those stated. I have indicated the adoption of quotations as well as thoughts taken from other authors as such in the thesis. I am aware that the Senate pursuant to Article 36 paragraph 1 litera r of the University Act of September 5th, 1996 and Article 69 of the University Statute of June 7th, 2011 is authorized to revoke the doctoral degree awarded on the basis of this thesis.

For the purposes of evaluation and verification of compliance with the declaration of originality and the regulations governing plagiarism, I hereby grant the University of Bern the right to process my personal data and to perform the acts of use this requires, in particular, to reproduce the written thesis and to store it permanently in a database, and to use said database, or to make said database available, to enable comparison with theses submitted by others.

Bern, 21.11.2023